# TURBULENT FLOW AND TRANSPORT MODELING BY LONG WAVES AND CURRENTS

A Dissertation

by

DAE HONG KIM

Submitted to the Office of Graduate Studies of
Texas A&M University
in partial fulfillment of the requirements for the degree of

DOCTOR OF PHILOSOPHY

August 2009

Major Subject: Civil Engineering

# TURBULENT FLOW AND TRANSPORT MODELING BY LONG WAVES AND CURRENTS

A Dissertation

by

DAE HONG KIM

Submitted to the Office of Graduate Studies of
Texas A&M University
in partial fulfillment of the requirements for the degree of

DOCTOR OF PHILOSOPHY

Approved by:

| | |
|---|---|
| Chair of Committee, | Patrick J. Lynett |
| Committee Members, | Robert D. Hetland |
| | Scott A. Socolofsky |
| | Jennifer L. Irish |
| Head of Department, | David V. Rosowsky |

August 2009

Major Subject: Civil Engineering

# ABSTRACT

Turbulent Flow and Transport Modeling by

Long Waves and Currents. (August 2009)

Dae Hong Kim, B.S., Hanyang University, Seoul, Korea;

M.S., Hanyang University, Seoul, Korea

Chair of Advisory Committee: Dr. Patrick J. Lynett

This dissertation presents models for turbulent flow and transport by currents and long waves in large domain.

From the Navier-Stokes equations, a fully nonlinear depth-integrated equation model for weakly dispersive, turbulent and rotational flow is derived by a perturbation approach based on long wave scaling. The same perturbation approach is applied for the derivation of a depth-integrated transport equation. As the results, coherent structures generated by the turbulence induced by the bottom friction and topography can be predicted very reasonably.

The three dimensional turbulence effects are incorporated into the flow model by employing a back scatter model. The back scatter model makes it possible to predict turbulent transport: It contributes to the energy transport and the lateral turbulent diffusion through relying on the turbulent intensity, not by relying on an empirical diffusion constant. The inherent limitation of the depth-integrated transport equation, that is, the limitation for the near field prediction is recognized in the derivation and the numerical simulation.

To solve the derived equation set, a highly accurate and stable finite volume scheme numerical solver is developed. Thus, the numerical solver can predict dispersive and nonlinear wave propagation with minimal error. Also, good stability is achieved enough to be applied to the dam-break flows and undular tidal bores. In

addition, a robust moving boundary scheme based on simple physical conditions is presented, which can extend the applicability area of the depth-integrated models. By the comparison study with experimental data, it is expected that the numerical model can provide high confidence results for the wave and current transformations including shocks and undular bores on complex bathymetry and topography. For the accurate near field transport prediction, a three dimensional transport model in $\sigma$-coordinate coupled with the depth-integrated flow model is developed. Like the other models, this model is also intended for large domain problems, and yet efficient and accurate in the far field and near field together.

To my lovely family

# ACKNOWLEDGEMENTS

Many people have contributed to this research in various ways. First of all, I would like to express my sincere gratitude to my advisor, Dr. Patrick J. Lynett who wanted to make me think scientifically and mathematically. His constant and intellectual advice, and the financial support, highest salary in the department, helped me a lot through the difficult years in doing this research. I would also like to thank Professor Scott Socolofsky and Professor Jennifer Irish of the Department of Civil engineering and Professor Robert Hetland in the Department of Oceanography for their careful review of my dissertation draft and interesting advice. I highly would like to thank professor Moo-Hyun Kim for warm invitations for many dinners at his house and for showing to me an example of sincerity and integrity as a scholar. I would like to thank my lovely wife, Ji-Sook Lim, for her love, support, and patience. She always shows her respect to me. My son, Jonathan Jongdae Kim, you are the sunshine of my life and I will love you from my deep heart forever. Lastly, I appreciate my parents, parents-in-law, and families for their continuous support and encouragement.

# TABLE OF CONTENTS

CHAPTER Page

CHAPTER Page

# LIST OF TABLES

# LIST OF FIGURES

FIGURE Page

FIGURE Page

FIGURE Page

FIGURE Page

FIGURE Page

FIGURE Page

# CHAPTER I
# INTRODUCTION

## I.1. Problem Statement

In natural environment, shallow water flows are ubiquitous with various scales ranging from small scale stream flows to oceanic flows of geophysical scale. In those shallow flows, two dimensional (2D) horizontal large coherent structures related with the rotationality and turbulence are frequently observed as shown in the Figure 1. To understand the motions of these coherent structures is very important because they usually dominate flow patterns and mixing processes of constituent.

The flow and transport models that can accurately simulate these flow motions and the scalar transports can be valuable scientific and engineering tools if those models are based on the reasonable physics and scales.

For the free surface flow simulation in large domain where the water depth is not deep, the depth-integrated or depth-averaged flow models based on long wave scaling are most widely used and still being developed for their efficiency and robustness. Firstly, the shallow water equations models are the most popular engineering tool and widely spread. The reasons are that, in the view of the computational technique, the shallow water equations can be solved very efficiently and stably, and so a lot of various and robust computational methods for the shallow water equations models were developed, such as finite difference method (FDM), finite element method (FEM), and finite volume method (FVM). Also, in the view of results, the free surface can be captured within satisfactory accuracy if the shallow water assumption is valid.

---

The journal model is *Journal of Engineering Mechanics*.

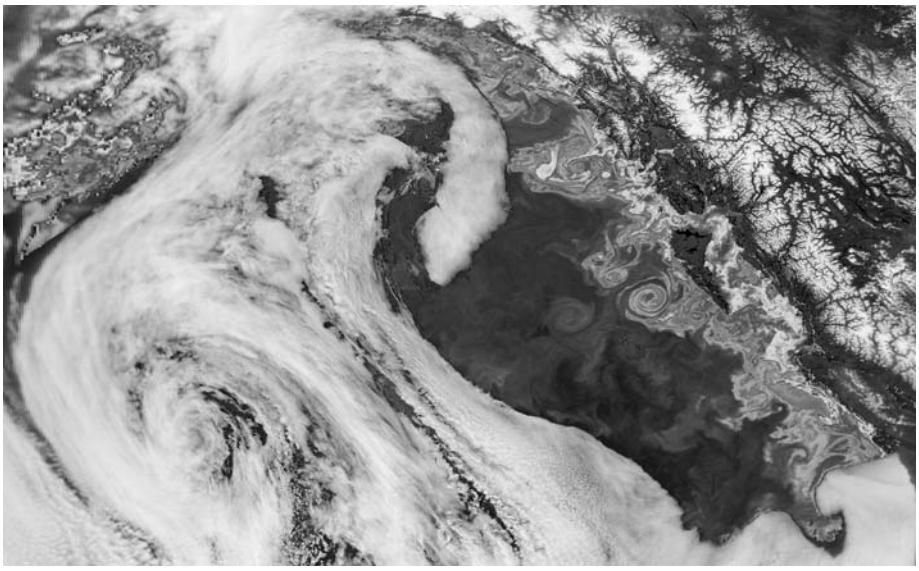

Figure 1. Two dimensional coherent structures in the sea and sky off the Queen Charlotte Islands, Canada (Courtesy NASA SeaWiFS).

Whereas, in the view of physics, they can lose the accuracy when the flow field is dispersive or under nonhydrostatic pressure conditions which are frequently observed in nature, even in shallow water depth areas.

The Boussinesq equations model, one of the depth-integrated equations sets, recently has demonstrated very good capability beyond the limitations of the shallow water equations models. It can be applied to the nonlinear, weakly dispersive and nonhydrostatic pressure fields and excellent results were reported in many literatures. However, in many cases, the potential flow assumption was used for the derivation so that it made hard to apply the Boussinesq equations model to a real flow field, where the flow is rotational and turbulent. In addition that, as an engineering tool, the Boussinesq equations models have some limitations like the stability. Unlike the shallow water equations models, various and stable numerical methods are not yet

developed for the Boussinesq equations, especially in 2D space. Thus it may be valuable to study it further.

Naturally, the three dimensional (3D) numerical model based on the Navier-Stokes equations with turbulent closures can give the most physical and accurate results. However, even till these days, huge computational resources are required so that they may not be practically feasible for large domain simulations. Especially, in cartesian grid system, the free surface crosses the computational grid perpendicularly, and so it brings the difficulty of applying the pressure boundary condition. Sequently, predicting accurate free surface profiles can initiate more difficulties. Besides, the small scale phenomenon that can be captured by only the 3D flow models is often beyond of our interests in many engineering problems. Therefore, the Boussinesq equations model can be a practical and scientific tool if several shortages can be removed and it is used under appropriate assumptions.

The environmental problem is an indispensable and critical issue to every human being. Specifically, to the scientists and engineers in the field of fluid flows, the scalar transport by the flows is the one of the most interesting and important environmental topics. For the similar reasons with the depth-integrated flow model, it would be appreciable to develop a depth-integrated transport equation model with the consistent scales and assumptions of the depth-integrated flow models. Various coupled shallow water equations and depth-averaged transport models were applied to many engineering problems for far field mixing problems. However, because of the inherent limitation of the 2D horizontal model, the efficient modeling for near field mixing is still remaining as an unsolved problem.

## I.2. Overview of the Depth-Integrated Equations

Joseph Boussinesq (1872) firstly derived a equations set nowadays called as "Boussinesq equations" on horizontal bottom. Significant advances have been made in deriving the Boussinesq equations and in developing numerical models in recent years. From the Peregrine (1967) who introduced the weakly nonlinear Boussinesq equations model, almost of the progresses were based on the inviscid flow assumption; the Boussinesq equations were typically derived using the 3D Euler or potential flow equations as a starting point, and resulted in depth-averaged form.

Yoon and Liu (1989) derived a new class of the Boussinesq equations set that included the effect of wave and current interaction. A similar approach was used by Nwogu (1993) through replacing the depth-averaged velocity by the velocity at arbitrary water depth. In his derivation much improved linear dispersive properties was obtained so that the applicable area was extended to the intermediate water depth, $kh \approx 3$, where $k$ is wave number and $h$ is water depth. Recently, Lynett and Liu (2004) proposed a set of equations by piecewise integration of the primitive equations of motion through two arbitrary layers. Up to $kh \approx 6$, very good linear dispersive properties were observed.

For the enhancement of the nonlinear properties, the higher-order nonlinear terms truncated by assuming the weakly-nonlinear phenomena were recovered by Wei et al. (1995), which made possible the simulations of wave propagations with very large amplitude.

To apply the Boussinesq equations model to real fields where the rotationality exist, Chen et al. (2003) introduced the vertical vorticity into the irrotational Boussinesq equations and several ad-hoc viscosity terms, but the equations are incomplete mathematically in 2D space. This inconsistency has been approached in a number of

ways. For example, it was found that by enforcing zero vertical vorticity, all the $z$-dependent terms would disappear, resulting in a solvable, irrotational model (Hsiao et al., 2002). Again, Chen (2006) successfully derived a complete equations set by eliminating the $z$-dependent terms by double-integrating the Boussinesq equations, which resulted in a model that included vertical vorticity, though the horizontal vorticity was not included.

In the view of numerical method, a significant progresses have not been made even these days, especially for the 2D space. Most of the numerical solvers for the fully nonlinear Boussinesq equations are not relatively strong or flexible as much as the shallow water equations solvers. Recently, Erduran et al. (2005) presented a hybrid numerical model comprised of FVM and FDM to solve the Boussinesq equations in one dimensional (1D) space. Tonelli and Petti (2009) extended it to the 2D space. However, no numerical test with severe conditions was provided. Therefore, the development of more robust numerical models and verifications should be encouraged.

### I.3. Objectives

The main objective of this study is to present the depth-integrated flow equations for the analysis of a real flow field in large domain. Thus the equations will have to account the effects of rotationality, viscosity, turbulence and dispersion.

To solve the proposed Boussinesq equations model, a highly accurate and stable numerical method will be developed. To allow wider range of applications in natural topography and bathymetry, robust moving boundary scheme will be added.

For the efficient and accurate numerical simulation of scalar transport in near field and far field together, a depth-integrated transport model and a 3D transport model based on the $\sigma$-coordinate system will be developed. For all the derived equations

and numerical models, various validations will be conducted and discussed.

## I.4. Outline of Dissertation

In Chapter II, from the Navier-Stokes equations, a set of fully nonlinear Boussinesq equations for weakly dispersive, turbulent and rotational fluid flows are derived in conservative form. The numerical methods based on a fourth-order FVM for solving the derived equations are described. For the verifications of the derived equations and the numerical model, four tests including flows with strong coherent structures are presented.

In Chapter III, a depth-integrated flow model with subgrid turbulence closure is presented. With the same approach, a depth-integrated scalar transport equation based on the long wave scales is derived. By coupling the transport model with the flow model which can account the 3D turbulence effects, the turbulent transport by long waves and currents are simulated.

In Chapter IV, a robust moving boundary scheme for the Boussinesq equations model is provided based on simple physical conditions. For the test of the applicability on various engineering problems, several numerical tests under severe conditions such as overtopping, undular bores generated by the dam-break flows and tsunami are simulated.

In Chapter V, a 3D transport model for near field mixing simulation is developed based on the $\sigma$-coordinate grid system.

In Chapter VI, the conclusions of this study are presented. Also included are suggestions for the future and further studies.

# CHAPTER II
# BOUSSINESQ EQUATIONS FOR WEAKLY-DISPERSIVE, TURBULENT AND ROTATIONAL FLOWS

## II.1. Introduction

Boussinesq equation models are a popular choice for the simulation of weakly dispersive free-surface phenomena, such as wind waves in the nearshore area. Significant advances have been made in deriving the Boussinesq type equations and in developing numerical models to solve them in recent years. Nearly all of this progress is based on the inviscid flow assumption; the Boussinesq equations are typically derived using the 3D Euler or potential flow equations as a starting point. One of the common derivation methods is the perturbation approach, with the final equation model cast in depth-averaged form (e.g. Peregrine, 1967). Nwogu (1993) derived a new set of Boussinesq equations by using an arbitrary elevation $z_\alpha$ and extended the applicable water depth to the intermediate water regime. While Nwogu's equation model is depth-integrated, the velocity variables are not in a depth-averaged form, and provide information about the varying vertical flow structure. Wei et al. (1995) extended Nwogu's approach to capture nonlinear-dispersive effects, allowing for the simulation of very large amplitude, weakly dispersive waves. In this study, the models are extended to incorporate friction effects by bottom-generated turbulence through the common quadratic bottom stress. The effects represent a high-order correction to the leading order, shallow-water hydrodynamics, which when consistently applied, allows the model to capture vertical and horizontal vorticity. These model enhancements are important to simulate energy and constituent transport by large 2D coherent structures in coastal flows.

Inclusion of rotationality in the standard Boussinesq model has been the subject of some recent studies. As mentioned above, the Boussinesq model is usually founded on either potential flow or Euler's equations. However, many derivations, including the Euler's-based approach, enforce zero horizontal vorticity. From a strict physical standpoint, if the two horizontal vorticity components are zero, the third must be constant (or zero for practical consideration). Thus, it is difficult to consider an equation model with zero horizontal vorticity, whether derived from Eulers or Navier-Stokes equations, as capable of predicting vertical vorticity. This physical inconsistency has been approached in a number of ways. In the derivation of Hsiao et al. (2002), which is based on Eulers equations, a number of $z$-dependent terms resulted in the final Boussinesq model. As the model is depth-integrated, these residual $z$-dependent terms are mathematically nonsense, implying there is not a unique solution to the Hsiao et al. model. However, it was found that by enforcing zero vertical vorticity, all the $z$-dependent terms would disappear, resulting in a solvable, irrotational model. Chen (2006), faced with a similar issue of $z$-dependent terms, used a different approach. He eliminated the $z$-dependent terms by double-integrating the Boussinesq model, providing a model that included vertical vorticity, although without explicitly including horizontal vorticity. Others have included horizontal vorticity directly, such as Musumeci et al. (2005), who derived a set of Boussinesq-type equations with horizontal vorticity, where the vorticity was solved with a separate transport equation.

To include the effect of the turbulent mixing in the Boussinesq equation model, Chen et al. (1999) used a quadratic bottom friction dissipation term with a current-based subgrid dissipation model. Both terms are added in an ad-hoc manner to the derived, inviscid Boussinesq equations. Hinterberger et al. (2007) presented a "depth-averaged LES" closure, used within a shallow water wave equation model. They

showed that the depth-averaged LES is considerably more economic and can produce results that are generally of sufficient accuracy for practical purposes, compared with the full 3D LES, in shallow flows.

One of the most important characteristics that a numerical model must have is stability, because, in many cases, numerical models are to be applied to real or complex conditions. Recently, approximate Riemann solvers have been widely used with finite volume methods to provide a stable and accurate solution for the analysis of the Euler equations and the shallow water equations. For the Boussinesq equations, Erduran et al. (2005) used the fourth-order MUSCL-TVD scheme and used an approximate Riemann solver to solve leading order terms in 1D space. They used a finite difference scheme to solve the dispersive terms in their numerical model.

In this section, a set Boussinesq equations that include the depth integrated viscosity and associated horizontal and vertical vorticity terms is derived. Hence, the derivation starts from the Navier-Stokes equations. A stable numerical model to solve the derived equations is presented, basically with the fourth-order FVM.

## II.2. Boussinesq Equations with Viscosity Terms

### II.2.1. Dimensionless Governing Equations

The basic approach for including viscous effects into the Boussinesq equations is to derive the governing equations not from Eulers equations but from the Navier-Stokes equations. For the derivation of the approximate, depth-integrated model, a nondimension, or scaling, of the primitive equations is the first step. Consistent with previous Boussinesq-type approaches, it is expected that the leading order solution will be shallow water, and thus a long wave scaling is used. A spatial region is characterized by a typical water depth $h_o$, a horizontal length scale $\ell_o$, wave amplitude

$a_o$, and a time scale $\ell_o/\sqrt{gh_o}$. With these variables, the following dimensionless variables and a parameter can be introduced:

$$(x, y) = \frac{(x', y')}{\ell_o}, \qquad z = \frac{z'}{h_o}, \qquad t = \frac{t'\sqrt{gh_o}}{\ell_o}, \qquad h = \frac{h'}{h_o}, \qquad \zeta = \frac{\zeta'}{h_o},$$
$$(U, V) = \frac{(U', V')}{\sqrt{gh_o}}, \qquad W = \frac{W'}{\mu\sqrt{gh_o}}, \qquad p = \frac{p'}{\rho g h_o}, \qquad \mu = \frac{h_o}{\ell_o} \tag{2.1}$$

where $(x', y')$ denotes horizontal axes, $z'$ is a vertical axis, $t'$ is time, $h'$ is water depth, $\zeta'$ is water surface elevation, $(U', V')$ are horizontal velocities, $W'$ is the vertical direction velocity, and $p'$ is pressure. The $g$ and $\rho$ are a gravitational acceleration and density, respectively. All these variables are dimensional. The $\mu$ is a standard parameter for a scale analysis of long waves.

For this study, due to the depth-integration and resulting loss of flow details in the vertical plane, it will be reasonable to divide the turbulent eddy viscosity into horizontal and vertical components, as is commonly done for shallow mixing studies. The Smagorinsky model (1963) will be used for the horizontal eddy viscosity $\nu_t^{h'}$, that is, $\nu_t^{h'} = (C_s\Delta')^2\sqrt{2S'_{ij}S'_{ij}}$ where $C_s$ is a constant, the $S'_{ij}$ is a strain rate tensor and $\Delta'$ is the grid size. By applying the above scalings to the horizontal eddy viscosity, $\nu_t^{h'}$ can be expressed as

$$\nu_t^{h'} = C_s^2\Delta^2 h_o\sqrt{gh_o}\sqrt{\left(\frac{\partial U}{\partial z}\right)^2 + 2\mu^2\left(\frac{\partial U}{\partial x}\right)^2 + 2\mu^2\left(\frac{\partial W}{\partial z}\right)^2 + \cdots\cdots} \tag{2.2}$$

Equation (2.2) is rewritten in the compact form

$$\nu_t^{h'} = \alpha h_o\sqrt{gh_o}\nu_t^h \tag{2.3}$$

where $\alpha = C_s^2 \Delta^2$. For the vertical eddy viscosity, we presume a shallow flow formulation, where the vertical turbulence is driven by the bottom shear only. Considering that the vertical turbulence is mainly driven by the bottom shear in shallow flows, the vertical eddy viscosity $\nu_t^{v\prime} = C_h H' u'_\tau$ is used, in which the constant $C_h$ is given by $C_h = \kappa/6$ following Elder (1959), the $\kappa$ is the von Karman constant, the $H'$ is the total water depth, and the $u'_\tau$ is the friction velocity. The typical magnitude of the $C_h$ is $O(C_h) \sim 0.1$ and it is expressed with $\beta$. By using the relation $u'_\tau = \sqrt{c_f}|u'| = \sqrt{gH'S'_f}$, the typical magnitude of the roughness coefficient $c_f$ can be determined as $O(c_f) \sim \mu$, in which the $S'_f$ is the energy slope (Chaudhry, 1993). Finally, the nondimensional vertical eddy viscosity can be expressed as

$$\nu_t^{v\prime} = \beta\mu h_o \sqrt{g h_o} H u_\tau = \beta\mu h_o \sqrt{g h_o} \nu_t^v \tag{2.4}$$

Finally, the continuity equation and the Navier-Stokes equations can be scaled with the equations (2.1), (2.3) and (2.4):

$$\nabla \cdot \boldsymbol{U} + \frac{\partial W}{\partial z} = 0 \tag{2.5}$$

$$\frac{\partial \boldsymbol{U}}{\partial t} + \boldsymbol{U} \cdot \nabla \boldsymbol{U} + W \frac{\partial \boldsymbol{U}}{\partial z} + \nabla p = \alpha\mu \nabla \cdot \left(\nu_t^h \nabla \boldsymbol{U}\right) + \beta \frac{\partial}{\partial z}\left(\nu_t^v \frac{\partial \boldsymbol{U}}{\partial z}\right) \tag{2.6}$$

$$\begin{aligned} \mu^2 \frac{\partial W}{\partial t} &+ \mu^2 \boldsymbol{U} \cdot \nabla W + \mu^2 W \frac{\partial W}{\partial z} + \frac{\partial p}{\partial z} + 1 \\ &= \alpha\mu^3 \nabla \cdot \left(\nu_t^h \nabla W\right) + \beta\mu^2 \frac{\partial}{\partial z}\left(\nu_t^v \frac{\partial W}{\partial z}\right) \end{aligned} \tag{2.7}$$

where $\nabla = (\partial/\partial x, \partial/\partial y)$.

### II.2.2. Derivation of the Depth Integrated Momentum Equations

This derivation will be of the perturbation type, and a small parameter assumption must be made. Looking to the vertical momentum equation (2.7), it is assumed that $O(\mu^2) = O(\beta\mu^2) \ll 1$, yielding

$$\frac{\partial p}{\partial z} + 1 = O(\mu^2, \beta\mu^2) \tag{2.8}$$

The above indicates that to leading order, the pressure is hydrostatic, which will permit the standard depth integration to obtain a long wave model. Thus the derived model will be restricted to weakly dispersive waves and flow with weak vertical turbulence and rotation. This step provides significant physical insight into this class of problem, and indicates that in order for the flow to be assumed hydrostatic to leading order, both dispersive and turbulent effects must be weak. Any model that assumes hydrostatic pressure implicitly assumes weak turbulence.

Typically, the perturbation of the inviscid primitive equations is performed using $\mu^2$ as the small parameter. In these inviscid cases, where of course $\alpha = \beta = 0$, the small parameter choice essentially required by the equation (2.8) is clear. This would be the choice when deriving the typical (inviscid) shallow water or Boussinesq-type equations. It is noted that the "true" Boussinesq equations are derived assuming a balance between nonlinearity, or wave amplitude to depth ratio, and frequency dispersion, $\mu^2$, where both effects are considered to be small. The weak nonlinearity assumption is often violated by nearshore wind waves, and can be discarded from the derivation (e.g. Wei et al., 1995). These new fully nonlinear equations are still referred to as Boussinesq or Boussinesq-type equations, despite the fact that they no

longer employ the scaling assumptions associated with their namesake.

Back to the scaling found here, with viscosity, the choice for the expansion parameter is not clear, as either $\mu^2$ or $\mu\beta$ could be used as the small parameter. Mathematically, there is no reason to choose one over the other, as in fact both would result in the same final dimensional equations. For the derivation presentation, $\mu^2$ will be used, and this issue of ambiguity will be addressed later.

Physical values are expanded with power series following

$$f = \sum_{n=0}^{N} \mu^{(2n)} f_n \tag{2.9}$$

where $f = p, U, V, W$ and $\mu^2$ assumed to be small. Substituting this expansion into the equation (2.7) or (2.8) gives $p_o$ as hydrostatic. It follows that $\nabla p_o$ is independent of $z$. This implies that in the horizontal momentum equation, all the other leading order should also be $z$-independent functions (Dellar and Salmon, 2005). Consequently, $\boldsymbol{U}_o$ becomes $\boldsymbol{U}_o(x, y, t)$.

At the water surface and at the bottom, the following boundary conditions $W_\zeta = \partial\zeta/\partial t + \boldsymbol{U}_\zeta \cdot \nabla\zeta$ at $z = \zeta$ and $W_{-h} + \boldsymbol{U}_{-h} \cdot \nabla h = 0$ at $z = -h$ can be applied. The vertical velocity can be expressed with the horizontal velocity terms by integrating the continuity equation, yielding,

$$W_o = -zS - T \tag{2.10}$$

where $S = \nabla \cdot \boldsymbol{U}_o$ and $T = \nabla \cdot (h\boldsymbol{U}_o)$.

With the perturbation analysis, the horizontal vorticity is expressed as

$$\begin{aligned} \frac{\partial \boldsymbol{U}'}{\partial z'} - \nabla W' &= \mu^2 \frac{c_o}{h_o}\left(\frac{\partial \boldsymbol{U}_1}{\partial z} - \nabla W_o\right) + \frac{c_o}{h_o} O\left(\mu^4\right) \\ &= \mu^2 \frac{c_o}{h_o}\boldsymbol{\omega}_1 + \frac{c_o}{h_o} O\left(\mu^4\right) \end{aligned} \tag{2.11}$$

where $c_o = \sqrt{g h_o}$. A vertical profile of $\boldsymbol{U}_1$ can be derived from equation (2.11) through a vertical integration:

$$\begin{aligned} \boldsymbol{U}_1 &= -\frac{1}{2} z^2 \nabla S - z \nabla T + \frac{1}{2} h^2 \nabla S - h \nabla T + \int_{-h}^{z} \boldsymbol{\omega}_1 dz + \boldsymbol{U}_1(-h) \\ &+ O\left(\mu^2\right) \end{aligned} \tag{2.12}$$

such that the horizontal velocity, including high-order terms, becomes

$$\begin{aligned} \boldsymbol{U} = \boldsymbol{U}_o &- \mu^2 \left(\frac{1}{2} z^2 \nabla S + z \nabla T - \frac{1}{2} h^2 \nabla S + h \nabla T\right) + \mu^2 \int_{-h}^{z} \boldsymbol{\omega}_1 dz \\ &+ \mu^2 \boldsymbol{U}_1(-h) + O\left(\mu^4\right) \end{aligned} \tag{2.13}$$

As this derivation will make use of Nwogu's (1993) approach, the horizontal velocity is evaluated at an arbitrary elevation $z = z_\alpha$,

$$\begin{aligned} \boldsymbol{U}_\alpha = \boldsymbol{U}_o &- \mu^2 \left(\frac{1}{2} {z_\alpha}^2 \nabla S + z_\alpha \nabla T - \frac{1}{2} h^2 \nabla S + h \nabla T\right) + \mu^2 \int_{-h}^{z_\alpha} \boldsymbol{\omega}_1 dz \\ &+ \mu^2 \boldsymbol{U}_1(-h) + O\left(\mu^4\right) \end{aligned} \tag{2.14}$$

Subtracting the equation (2.14) from the equation (2.13), $\boldsymbol{U}$ can be expressed in terms of $\boldsymbol{U}_\alpha$.

$$\boldsymbol{U} = \boldsymbol{U}_\alpha + \mu^2 \left\{\frac{1}{2}\left({z_\alpha}^2 - z^2\right)\nabla S + (z_\alpha - z)\nabla T\right\} + \mu^2 \boldsymbol{\Omega} + O\left(\mu^4\right) \tag{2.15}$$

where $\boldsymbol{\Omega} = \int_{z_\alpha}^{z} \boldsymbol{\omega}_1 dz$. For later use, the horizontal velocity can be expressed as $\boldsymbol{U} = \boldsymbol{U}_\alpha + \mu^2 \left( \boldsymbol{U}_1^\phi + \boldsymbol{U}_1^r \right) + O\left(\mu^4\right)$ in which $\boldsymbol{U}_1^r = \boldsymbol{\Omega}$ and $\boldsymbol{U}_1^\phi = \left( U_1^\phi, V_1^\phi \right)$ is defined as

$$\boldsymbol{U}_1^\phi = \frac{1}{2} \left( {z_\alpha}^2 - z^2 \right) \nabla S + (z_\alpha - z) \nabla T \tag{2.16}$$

The vertical profile of pressure is found through integration of the vertical momentum equation. Noting that the vertical distribution of $\nu_t^v$ is independent of $z$ as shown in equation (2.4), the pressure can be expressed as

$$\begin{aligned} p &= \zeta - z \\ &+ \mu^2 \frac{1}{2} \left( z^2 - \zeta^2 \right) \frac{\partial S}{\partial t} + \mu^2 \left( z - \zeta \right) \frac{\partial T}{\partial t} \\ &+ \mu^2 \frac{1}{2} \left( z^2 - \zeta^2 \right) \boldsymbol{U}_o \cdot \nabla S + \mu^2 \left( z - \zeta \right) \boldsymbol{U}_o \cdot \nabla T \\ &+ \mu^2 \frac{1}{2} \left( \zeta^2 - z^2 \right) S^2 + \mu^2 \left( \zeta - z \right) TS \\ &+ O\left( \mu^4, \alpha\mu^3, \beta\mu^4 \right) \end{aligned} \tag{2.17}$$

The next step in deriving the horizontal depth-integrated momentum equation is to express each term of the horizontal momentum equations through $\boldsymbol{U}_\alpha$. These terms, included to elucidate how vorticity and viscosity terms appear, become

$$\begin{aligned} \frac{\partial \boldsymbol{U}}{\partial t} = \frac{\partial \boldsymbol{U}_\alpha}{\partial t} &+ \mu^2 \frac{\partial}{\partial t} \left\{ \frac{1}{2} \left( {z_\alpha}^2 - z^2 \right) \nabla S + (z_\alpha - z) \nabla T \right\} \\ &+ \mu^2 \frac{\partial \boldsymbol{\Omega}}{\partial t} + O\left(\mu^4\right) \end{aligned} \tag{2.18}$$

$$\begin{aligned}\boldsymbol{U}\cdot\nabla\boldsymbol{U}=\boldsymbol{U}_\alpha\cdot\nabla\boldsymbol{U}_\alpha &+ \mu^2\nabla\left[\boldsymbol{U}_\alpha\cdot\left\{\frac{1}{2}\left({z_\alpha}^2-z^2\right)\nabla S+(z_\alpha-z)\nabla T\right\}\right]\\ &+ \mu^2\nabla\left(\boldsymbol{U}_\alpha\cdot\boldsymbol{\Omega}\right)+\mu^2\boldsymbol{\xi}+O\left(\mu^4\right)\end{aligned}\tag{2.19}$$

$$W\frac{\partial\boldsymbol{U}}{\partial z}=\mu^2\left(z^2S\nabla S+zT\nabla S+zS\nabla T+T\nabla T+W_o\boldsymbol{\omega}_1\right)+O\left(\mu^4\right)\tag{2.20}$$

$$\begin{aligned}\nabla p &= \nabla\zeta\\ &- \mu^2\frac{1}{2}\nabla\left(\zeta^2\frac{\partial S}{\partial t}\right)-\mu^2\nabla\left(\zeta\frac{\partial T}{\partial t}\right)+\mu^2\frac{1}{2}\nabla\left(z^2\frac{\partial S}{\partial t}\right)+\mu^2\nabla\left(z\frac{\partial T}{\partial t}\right)\\ &- \mu^2\frac{1}{2}\nabla\left(\zeta^2\boldsymbol{U}_\alpha\cdot\nabla S\right)-\mu^2\nabla\left(\zeta\boldsymbol{U}_\alpha\cdot\nabla T\right)+\mu^2\nabla\left(\frac{1}{2}\zeta^2S^2\right)\\ &+ \mu^2\frac{1}{2}\nabla\left(z^2\boldsymbol{U}_\alpha\cdot\nabla S\right)+\mu^2\nabla\left(z\boldsymbol{U}_\alpha\cdot\nabla T\right)-\mu^2\nabla\left(\frac{1}{2}z^2S^2\right)\\ &+ \mu^2\nabla\left(\zeta TS\right)-\mu^2\nabla\left(zTS\right)\\ &+ O\left(\mu^4\right)\end{aligned}\tag{2.21}$$

$$\alpha\mu\nabla\cdot\left(\nu_t^h\nabla\boldsymbol{U}\right)=\alpha\mu\nabla\cdot\left(\nu_t^h\nabla\boldsymbol{U}_\alpha\right)+O\left(\alpha\mu^3\right)\tag{2.22}$$

$$\beta\frac{\partial}{\partial z}\left(\nu_t^v\frac{\partial\boldsymbol{U}}{\partial z}\right)=\beta\mu^2\frac{\partial\nu_t^v\boldsymbol{\omega}_1}{\partial z}-\beta\mu^2\nu_t^v\nabla S+O\left(\beta\mu^4\right)\tag{2.23}$$

In equation (2.19), $\boldsymbol{\xi}=(\xi^x,\xi^y)$ is defined as

$$\xi^x = V_\alpha \left\{ \frac{\partial \left( U_1^\phi + \Omega^x \right)}{\partial y} - \frac{\partial \left( V_1^\phi + \Omega^y \right)}{\partial x} \right\} - \left( V_1^\phi + \Omega^y \right) \left( \frac{\partial V_\alpha}{\partial x} - \frac{\partial U_\alpha}{\partial y} \right) \quad (2.24)$$

$$\xi^y = U_\alpha \left\{ \frac{\partial \left( V_1^\phi + \Omega^y \right)}{\partial x} - \frac{\partial \left( U_1^\phi + \Omega^x \right)}{\partial y} \right\} + \left( U_1^\phi + \Omega^x \right) \left( \frac{\partial V_\alpha}{\partial x} - \frac{\partial U_\alpha}{\partial y} \right) \quad (2.25)$$

where $(U_\alpha, V_\alpha) = \boldsymbol{U}_\alpha$ and $\Omega^x$ and $\Omega^y$ are defined as $\boldsymbol{\Omega} = (\Omega^x, \Omega^y)$.

The horizontal vorticity term appearing in equation (2.23), namely $\partial \nu_t^v \boldsymbol{\omega}_1 / \partial z$, will be expressed through a shear stress, $\boldsymbol{\tau}$, in the following way:

$$\frac{\partial \nu_t^v \boldsymbol{\omega}_1}{\partial z} = \frac{\partial}{\partial z} \left\{ \nu_t^v \left( \frac{\partial \boldsymbol{U}_1^r}{\partial z} + \frac{\partial \boldsymbol{U}_1^\phi}{\partial z} - \nabla W_o \right) \right\} = \frac{\partial}{\partial z} \left( \nu_t^v \frac{\partial \boldsymbol{U}_1^r}{\partial z} \right) = \frac{\partial \boldsymbol{\tau}}{\partial z} \quad (2.26)$$

If the shear stress is assumed to vary linearly from zero at the water surface to $\boldsymbol{\tau}_b$ at the bottom (Rodi, 1980), then the horizontal vorticity terms can be expressed as

$$\boldsymbol{\omega}_1 = \frac{\partial \boldsymbol{U}_1^r}{\partial z} = \frac{\boldsymbol{\tau}_b}{\nu_t^v} \frac{\zeta - z}{\zeta + h} \quad (2.27)$$

$$\boldsymbol{\Omega} = \int_{z_\alpha}^{z} \boldsymbol{\omega}_1 dz = \frac{\boldsymbol{\tau}_b}{\nu_t^v \left( \zeta + h \right)} \left\{ \frac{1}{2} \left( z_\alpha^2 - z^2 \right) + \zeta \left( z - z_\alpha \right) \right\} \quad (2.28)$$

Equation (2.28) shows that with horizontal vorticity correlated directly, and simply, to the bottom stress, the depth-integrated result is a polynomial "deficit" velocity profile. This rotational velocity component will act to increase the total horizontal velocity near the free surface, and decrease it near the bottom. The justification of

the assumed linear shear stress profile is addressed at the end of the section II.3.2 and its validation is given in section II.5.2.

By substituting the derived equations (2.18)-(2.28) into the equation (2.6) and by substituting $U_o$ into $S$ and $T$ with $U_\alpha$ following Nwogu (1993), the depth-integrated momentum equation becomes:

$$\begin{aligned}
\frac{\partial \boldsymbol{U}_\alpha}{\partial t} &+ \boldsymbol{U}_\alpha \cdot \nabla \boldsymbol{U}_\alpha + \nabla\zeta \\
&- \mu^2 \frac{1}{2}\nabla\left(\zeta^2 \frac{\partial S}{\partial t}\right) - \mu^2 \nabla\left(\zeta \frac{\partial T}{\partial t}\right) + \mu^2\left(\frac{1}{2} {z_\alpha}^2 \frac{\partial \nabla S}{\partial t} + z_\alpha \frac{\partial \nabla T}{\partial t}\right) \\
&- \mu^2 \frac{1}{2}\nabla\left(\zeta^2 \boldsymbol{U}_\alpha \cdot \nabla S\right) - \mu^2 \nabla\left(\zeta \boldsymbol{U}_\alpha \cdot \nabla T\right) + \mu^2 \nabla\left(\frac{1}{2}\zeta^2 S^2\right) \\
&+ \mu^2 \frac{1}{2}\nabla\left({z_\alpha}^2 \boldsymbol{U}_\alpha \cdot \nabla S\right) + \mu^2 \nabla\left(z_\alpha \boldsymbol{U}_\alpha \cdot \nabla T\right) + \mu^2\left(T \nabla T\right) \\
&+ \mu^2 \frac{\partial}{\partial t}\left[\boldsymbol{\psi}\left\{\frac{1}{2}\left(z_\alpha^2 - z^2\right) + \zeta\left(z - z_\alpha\right)\right\}\right] + \mu^2 \nabla\left(\zeta T S\right) \\
&+ \mu^2 \nabla\left(\boldsymbol{U}_\alpha \cdot \left[\boldsymbol{\psi}\left\{\frac{1}{2}\left(z_\alpha^2 - z^2\right) + \zeta\left(z - z_\alpha\right)\right\}\right]\right) \\
&- \mu^2\left(zS + T\right)\left(\zeta - z\right)\boldsymbol{\psi} + \mu^2 \boldsymbol{\xi} \\
&- \alpha\mu\nabla \cdot \left(\nu_t^h \nabla \boldsymbol{U}_\alpha\right) + \beta\mu^2 \nu_t^v \nabla S - \beta\mu^2 \frac{\partial \boldsymbol{\tau}}{\partial z} \\
&= O\left(\mu^4, \alpha\mu^3, \beta\mu^4\right) \qquad (2.29)
\end{aligned}$$

where $\boldsymbol{\psi} = \boldsymbol{\tau}_b / \left\{\nu_t^v \left(\zeta + h\right)\right\}$.

### II.2.3. Elimination of $z$-dependent Terms

Several approaches have been used to eliminate the $z$-dependent terms in the Boussinesq type momentum equations. In Hsiao et al.(2002) and in many publications, irrotational flow assumptions were used to eliminate the terms. Chen et al. (2003) eliminated the $z$ dependency by setting $z = z_\alpha$ in these terms. In this study, the approach proposed by Chen (2006) is used; the equation (2.29) is depth-averaged.

For example, the $\boldsymbol{\tau}$ term can be rewritten by

$$\frac{1}{\zeta+h}\int_{-h}^{\zeta}\frac{\partial\boldsymbol{\tau}}{\partial z}dz=-\frac{\boldsymbol{\tau}_b}{\zeta+h} \tag{2.30}$$

Finally, the depth-integrated momentum equations including viscosity and vorticity effects can be expressed as

$$\begin{aligned}\frac{\partial\boldsymbol{U}_\alpha}{\partial t} &+ \boldsymbol{U}_\alpha\cdot\nabla\boldsymbol{U}_\alpha+\nabla\zeta+\mu^2\left(\boldsymbol{D}+\boldsymbol{D}^\nu+\overline{\boldsymbol{\xi}}+\overline{\boldsymbol{\xi}^\nu}\right)\\ &- \alpha\mu\nabla\cdot\left(\nu_t^h\nabla\boldsymbol{U}_\alpha\right)+\beta\mu^2\nu_t^v\nabla S+\beta\mu^2\frac{\boldsymbol{\tau}_b}{\zeta+h}\\ &= O\left(\mu^4,\alpha\mu^3,\beta\mu^4\right)\end{aligned} \tag{2.31}$$

where

$$\begin{aligned}\boldsymbol{D} &= \frac{1}{2}\nabla\left({z_\alpha}^2\boldsymbol{U}_\alpha\cdot\nabla S\right)+\nabla\left(z_\alpha\boldsymbol{U}_\alpha\cdot\nabla T\right)+\left(T\nabla T\right)\\ &- \frac{1}{2}\nabla\left(\zeta^2\frac{\partial S}{\partial t}\right)-\nabla\left(\zeta\frac{\partial T}{\partial t}\right)+\left(\frac{1}{2}{z_\alpha}^2\frac{\partial\nabla S}{\partial t}+z_\alpha\frac{\partial\nabla T}{\partial t}\right)\\ &- \frac{1}{2}\nabla\left(\zeta^2\boldsymbol{U}_\alpha\cdot\nabla S\right)-\nabla\left(\zeta\boldsymbol{U}_\alpha\cdot\nabla T\right)+\nabla\left(\frac{1}{2}\zeta^2S^2\right)+\nabla\left(\zeta TS\right)\end{aligned} \tag{2.32}$$

$$\begin{aligned}\boldsymbol{D}^\nu &= \frac{(\zeta-h)}{2}\frac{\partial\boldsymbol{\psi}\zeta}{\partial t}-\frac{(\zeta^2-\zeta h+h^2)}{6}\frac{\partial\boldsymbol{\psi}}{\partial t}+\frac{\partial}{\partial t}\left\{\boldsymbol{\psi}\left(\frac{z_\alpha^2}{2}-\zeta z_\alpha\right)\right\}\\ &+ \frac{(\zeta-h)}{2}\nabla\left\{\boldsymbol{U}_\alpha\cdot(\boldsymbol{\psi}\zeta)\right\}-\frac{(\zeta^2-\zeta h+h^2)}{6}\nabla\left(\boldsymbol{U}_\alpha\cdot\boldsymbol{\psi}\right)\\ &+ \nabla\left[\boldsymbol{U}_\alpha\cdot\left\{\boldsymbol{\psi}\left(\frac{z_\alpha^2}{2}-\zeta z_\alpha\right)\right\}\right]\\ &- \boldsymbol{\psi}\left\{\frac{\left(\zeta^2+\zeta h-2h^2\right)S}{6}+\frac{(\zeta+h)\,T}{2}\right\}\end{aligned} \tag{2.33}$$

$\overline{\boldsymbol{\xi}}=\left(\overline{\xi^x},\overline{\xi^y}\right)$ and $\overline{\boldsymbol{\xi}^\nu}=\left(\overline{\xi^{\nu^x}},\overline{\xi^{\nu^y}}\right)$ are given by

$$\begin{aligned}\overline{\xi^x} &= -V_\alpha\left\{\frac{\partial z_\alpha}{\partial x}\left(z_\alpha\frac{\partial S}{\partial y}+\frac{\partial T}{\partial y}\right)-\frac{\partial z_\alpha}{\partial y}\left(z_\alpha\frac{\partial S}{\partial x}+\frac{\partial T}{\partial x}\right)\right\} \\ &- \left(\frac{\partial V_\alpha}{\partial x}-\frac{\partial U_\alpha}{\partial y}\right)\left[\left\{\frac{z_\alpha^2}{2}-\frac{(\zeta^2-\zeta h+h^2)}{6}\right\}\frac{\partial S}{\partial y}+\left\{z_\alpha-\frac{(\zeta-h)}{2}\right\}\frac{\partial T}{\partial y}\right]\end{aligned} \tag{2.34}$$

$$\begin{aligned}\overline{\xi^y} &= U_\alpha\left\{\frac{\partial z_\alpha}{\partial x}\left(z_\alpha\frac{\partial S}{\partial y}+\frac{\partial T}{\partial y}\right)-\frac{\partial z_\alpha}{\partial y}\left(z_\alpha\frac{\partial S}{\partial x}+\frac{\partial T}{\partial x}\right)\right\} \\ &+ \left(\frac{\partial V_\alpha}{\partial x}-\frac{\partial U_\alpha}{\partial y}\right)\left[\left\{\frac{z_\alpha^2}{2}-\frac{(\zeta^2-\zeta h+h^2)}{6}\right\}\frac{\partial S}{\partial x}+\left\{z_\alpha-\frac{(\zeta-h)}{2}\right\}\frac{\partial T}{\partial x}\right]\end{aligned} \tag{2.35}$$

$$\begin{aligned}\overline{\xi^{\nu^x}} &= -V_\alpha\left[\frac{\partial}{\partial x}\left\{\psi^y\left(\frac{1}{2}z_\alpha^2-z_\alpha\zeta\right)\right\}-\frac{(\zeta^2-\zeta h+h^2)}{6}\frac{\partial\psi^y}{\partial x}+\frac{(\zeta-h)}{2}\frac{\partial\psi^y\zeta}{\partial x}\right. \\ &\quad \left.-\frac{\partial}{\partial y}\left\{\psi^x\left(\frac{1}{2}z_\alpha^2-z_\alpha\zeta\right)\right\}+\frac{(\zeta^2-\zeta h+h^2)}{6}\frac{\partial\psi^x}{\partial y}-\frac{(\zeta-h)}{2}\frac{\partial\psi^x\zeta}{\partial y}\right] \\ &- \left(\frac{\partial V_\alpha}{\partial x}-\frac{\partial U_\alpha}{\partial y}\right)\psi^y\left\{\frac{z_\alpha^2}{2}-z_\alpha\zeta+\frac{(2\zeta^2-2\zeta h-h^2)}{6}\right\}\end{aligned} \tag{2.36}$$

$$\begin{aligned}\overline{\xi^{\nu^y}} &= U_\alpha\left[\frac{\partial}{\partial x}\left\{\psi^y\left(\frac{1}{2}z_\alpha^2-z_\alpha\zeta\right)\right\}-\frac{(\zeta^2-\zeta h+h^2)}{6}\frac{\partial\psi^y}{\partial x}+\frac{(\zeta-h)}{2}\frac{\partial\psi^y\zeta}{\partial x}\right. \\ &\quad \left.-\frac{\partial}{\partial y}\left\{\psi^x\left(\frac{1}{2}z_\alpha^2-z_\alpha\zeta\right)\right\}+\frac{(\zeta^2-\zeta h+h^2)}{6}\frac{\partial\psi^x}{\partial y}-\frac{(\zeta-h)}{2}\frac{\partial\psi^x\zeta}{\partial y}\right] \\ &+ \left(\frac{\partial V_\alpha}{\partial x}-\frac{\partial U_\alpha}{\partial y}\right)\psi^x\left\{\frac{z_\alpha^2}{2}-z_\alpha\zeta+\frac{(2\zeta^2-2\zeta h-h^2)}{6}\right\}\end{aligned} \tag{2.37}$$

and $(\psi^x,\psi^y)=\boldsymbol{\psi}$.

The continuity equation is obtained by integrating equation (2.5) with the kinematic bottom and free surface boundary conditions, giving:

$$\frac{\partial\zeta}{\partial t}+\nabla\cdot\left\{(\zeta+h)\,\boldsymbol{U}_\alpha\right\}+\mu^2\left(\mathcal{M}+\mathcal{M}^\nu\right)=O\left(\mu^4\right) \tag{2.38}$$

where

$$\mathcal{M} = -\nabla \cdot \left[ (\zeta + h) \left\{ \left( \frac{(\zeta^2 - \zeta h + h^2)}{6} - \frac{z_\alpha^2}{2} \right) \nabla S + \left( \frac{(\zeta - h)}{2} - z_\alpha \right) \nabla T \right\} \right] \tag{2.39}$$

$$\mathcal{M}^\nu = \nabla \cdot \left[ \boldsymbol{\psi} (\zeta + h) \left\{ \frac{z_\alpha^2}{2} - z_\alpha \zeta + \frac{(2\zeta^2 - 2\zeta h - h^2)}{6} \right\} \right] \tag{2.40}$$

Note that the viscous / rotational modification to the continuity equation is non-zero unless $z_\alpha$ is chosen such that the inner-most bracket of the $\mathcal{M}^\nu$ term is zero. This is a simple quadratic equation solution, and yields a $z_\alpha$ that is a function of time.

### II.2.4. Subgrid Scale Eddy Viscosity Model and Bottom Friction

It is expected that, in the horizontal plane, the depth-integrated model will be able to resolve eddy scales larger than the grid size. For subgrid scale dissipation, the Smagorinsky model is used for the horizontal eddy viscosity, and is given as

$$\begin{aligned} \nu_t^{h\prime} &= \alpha \mu h_o c_o \left[ 2 \left( \frac{\partial U_\alpha}{\partial x} \right)^2 + 2 \left( \frac{\partial V_\alpha}{\partial y} \right)^2 + 2 \left( \frac{\partial W_o}{\partial z} \right)^2 + \left( \frac{\partial V_\alpha}{\partial x} + \frac{\partial U_\alpha}{\partial y} \right)^2 \right]^{1/2} \\ &+ \alpha h_o c_o O\left(\mu^2\right) \end{aligned} \tag{2.41}$$

For the vertical eddy viscosity, equation (2.4) is used, where $C_h = \kappa/6$ following Elder (1959). $\kappa$ is von Karman's constant; a value of 0.4 is used in this study.

To approximate the bottom stress, a quadratic friction equation is used:

$$\tau_b^x = c_f u \sqrt{u^2 + v^2} \ , \qquad \tau_b^y = c_f v \sqrt{u^2 + v^2} \tag{2.42}$$

where the $\tau_b^x$ and $\tau_b^y$ are the bottom stresses in the $x$ and $y$ directions respectively and

$u$ and $v$ are the depth averaged velocities in the $x$ and $y$ directions respectively. The roughness coefficient $c_f = f/4$ (Chen and Jirka, 1995) and $f$ is estimated using the Moody diagram, which here is calculated by the explicit formula given by Haaland (1983).

## II.3. Limiting Cases of Derived Equation Model

### II.3.1. Non-Dispersive, Inviscid Model: $\mu^2 \approx 0; \nu_t^h = \nu_t^v = \tau_b = 0$

Under these assumptions, the model reduces to the standard nonlinear shallow water wave equations:

$$\frac{\partial \boldsymbol{U}_\alpha}{\partial t} + \boldsymbol{U}_\alpha \cdot \nabla \boldsymbol{U}_\alpha + \nabla \zeta = O\left(\mu^2\right) \tag{2.43}$$

$$\frac{\partial \zeta}{\partial t} + \nabla \cdot \left\{ \left(\zeta + h\right) \boldsymbol{U}_\alpha \right\} = O\left(\mu^2\right) \tag{2.44}$$

### II.3.2. Weakly-Dispersive, Inviscid Model: $\mu^2 \ll 1; \nu_t^h = \nu_t^v = \tau_b = 0$

Under these assumptions, the model reduces to the extended Boussinesq equations of Chen (2006), prior to the ad-hoc additions of dissipation sub-models:

$$\frac{\partial \boldsymbol{U}_\alpha}{\partial t} + \boldsymbol{U}_\alpha \cdot \nabla \boldsymbol{U}_\alpha + \nabla \zeta + \mu^2 \left( \boldsymbol{D} + \overline{\boldsymbol{\xi}} \right) = O\left(\mu^4\right) \tag{2.45}$$

$$\frac{\partial \zeta}{\partial t} + \nabla \cdot \left\{ \left(\zeta + h\right) \boldsymbol{U}_\alpha \right\} + \mu^2 \mathcal{M} = O\left(\mu^4\right) \tag{2.46}$$

As shown in Chen (2006), this equation set conserves potential vertical vorticity, although due to the inviscid nature of the model, there is no direct means to generate vorticity. In practical application of the above equations, the addition of dissipation sub-models for bottom friction, subgrid mixing, and breaking provides the vorticity

sources.

It is important now to go back to the original scaling argument (see beginning of section II.2.2). It was mentioned in this earlier discussion that there was no clear reason to choose either $\mu^2$ or $\beta\mu$ as the perturbation expansion parameter. If one derives the inviscid model, given above as equations (2.45) and (2.46), the expansion parameter is clearly $\mu^2$. It is then reasonable to extrapolate that, comparing the inviscid and viscous equations, the new high-order terms appearing in the viscous equations are in fact order $\beta\mu$:

$$\begin{aligned} \frac{\partial \boldsymbol{U}_\alpha}{\partial t} &+ \boldsymbol{U}_\alpha \cdot \nabla \boldsymbol{U}_\alpha + \nabla\zeta + \mu^2\left(\boldsymbol{D} + \overline{\boldsymbol{\xi}}\right) + \beta\mu\left(\boldsymbol{D}^\nu + \overline{\boldsymbol{\xi}^\nu}\right) \\ &- \alpha\mu\nabla\cdot\left(\nu_t^h \nabla \boldsymbol{U}_\alpha\right) + \beta\mu^2\nu_t^v\nabla S + \beta\mu^2\frac{\boldsymbol{\tau}_b}{\zeta + h} \\ &= O\left(\mu^4, \alpha\mu^3, \beta\mu^3, \beta^2\mu^2\right) \end{aligned} \tag{2.47}$$

$$\frac{\partial\zeta}{\partial t} + \nabla\cdot\left\{(\zeta + h)\,\boldsymbol{U}_\alpha\right\} + \mu^2\mathcal{M} + \beta\mu\mathcal{M}^\nu = O\left(\mu^4, \beta^2\mu^2\right) \tag{2.48}$$

Following this argument, the vertical profile of horizontal velocity is now

$$\boldsymbol{U} = \boldsymbol{U}_\alpha + \mu^2\boldsymbol{U}_1^\phi + \beta\mu\boldsymbol{U}_1^r + O\left(\mu^4, \beta^2\mu^2\right) \tag{2.49}$$

and the viscous contribution to the profile is evident. Note that the equation set (2.47) and (2.48), and the velocity profile (2.49), is the weakly-dispersive and weakly-turbulent model, which will be described in more detail in section II.3.4.

### II.3.3. Non-Dispersive, Weakly-Turbulent Model: $\mu^2 \approx 0, O(\alpha\mu) = O(\beta\mu) \ll 1$

Under this set of assumptions, $O(\beta\mu)$ terms are retained as they will be greater than the truncated $O(\mu^2)$ dispersive terms:

$$\begin{aligned} \frac{\partial \boldsymbol{U}_\alpha}{\partial t} &+ \boldsymbol{U}_\alpha \cdot \nabla \boldsymbol{U}_\alpha + \nabla\zeta + \beta\mu\left(\boldsymbol{D}^\nu + \overline{\boldsymbol{\xi}^\nu}\right) \\ &- \alpha\mu\nabla\cdot\left(\nu_t^h \nabla \boldsymbol{U}_\alpha\right) + \beta\mu^2\nu_t^v\nabla S + \beta\mu^2\frac{\boldsymbol{\tau}_b}{\zeta+h} \\ &= O\left(\mu^2, \alpha\mu^3, \beta\mu^3, \beta^2\mu^2\right) \end{aligned} \tag{2.50}$$

$$\frac{\partial\zeta}{\partial t} + \nabla\cdot\left\{(\zeta+h)\,\boldsymbol{U}_\alpha\right\} + \beta\mu\mathcal{M}^\nu = O\left(\mu^2, \beta^2\mu^2\right) \tag{2.51}$$

and the horizontal velocity is

$$\boldsymbol{U} = \boldsymbol{U}_\alpha + \beta\mu\boldsymbol{U}_1^r + O\left(\mu^2, \beta^2\mu^2\right) \tag{2.52}$$

Here, the equations indicate the interesting result that, in a physically consistent context, one cannot simply append a bottom friction term onto the inviscid shallow water wave equations in an attempt to capture dissipative effects. By including a bottom stress, a number of associated terms, all of equal order to the added bottom stress, appear in both the momentum and continuity equations. It is argued that, in any shallow flow where the bottom stress plays a non-negligible role, the equation set given above as (2.50) and (2.51) is the proper model to solve. This set includes both the vertical and horizontal vorticity resulting from the bottom stress.

### II.3.4. Weakly-Dispersive, Weakly-Turbulent Model: $O(\mu^2) = O(\alpha\mu) = O(\beta\mu) \ll 1$

This is the model presented earlier in equations (2.47) and (2.48). This model includes the high-order frequency dispersion correction for free surface waves as well the viscous and rotational correction due to a bottom stress. It is reiterated here that both the frequency dispersion and viscous terms represent corrections to the leading order, shallow water flow. Thus the viscous/rotational effects should mimic those found in very long wave phenomena, such as rivers, tides, storm surges, and some tsunamis. Following this perturbation approach, if one wanted to include the viscous/rotational effects of dispersive waves, such as a wind wave-induced bottom boundary layer, this would be a third-order correction, or a viscous correction to the high-order dispersive terms.

While the eddy viscosity and horizontal vorticity models are simplified, a model with known physical limitations has been derived that includes the bottom friction term commonly added, in an ad-hoc manner, to the inviscid equations. Finally, it is stated that one should take care when adding such ad-hoc models; it is clear from this exercise that (1) it is not necessary to do so - the terms can be included through a consistent derivation from the viscous primitive equations - and (2) one cannot properly add the quadratic bottom friction term without also adding a number of additional terms in both the continuity and momentum equations. Note, however, that additional terms in the continuity equation only exist due to the use of the Nwogu-type approach; use of a depth-averaged velocity formulation would, by definition, result in a continuity equation without high-order terms.

## II.4. Numerical Scheme: Finite Volume Method

From here on, the dimensions are recovered and all dimensional variables are expressed without ‘ ′ ’ for the convenience of expression.

### II.4.1. Conservative Form of Boussinesq Equations

In coastal regions, lakes, and rivers, flow motions can easily become complex. For example, due to bathymetry variations, flow can change from subcritical to supercritical and vice-versa, causing steep fronts and shocks. It is well known that primitive variable or non-conservative schemes will compute shock waves with the wrong strength and the wrong speed of propagation (Toro, 2002).

Conservative schemes are known as a remedy, providing more accurate and stable results. To convert the momentum equations into conservative form, the momentum equation (2.47) is multiplied by the total water depth and continuity equation (2.48) by the horizontal velocity. Assuming that the bottom does not vary in time ($h_t = 0$), the two multiplied equations are added, and after some algebra, a set of conservative Boussinesq equations is obtained:

$$\frac{\partial H}{\partial t} + \frac{\partial HU_\alpha}{\partial x} + \frac{\partial HV_\alpha}{\partial y} + \mathcal{H}_c = 0 \tag{2.53}$$

$$\frac{\partial HU_\alpha}{\partial t} + \frac{\partial HU_\alpha^2}{\partial x} + \frac{\partial HU_\alpha V_\alpha}{\partial y} + gH\frac{\partial \zeta}{\partial x} + H\mathcal{H}_m^x + U_\alpha \mathcal{H}_c = 0 \tag{2.54}$$

$$\frac{\partial HV_\alpha}{\partial t} + \frac{\partial HU_\alpha V_\alpha}{\partial x} + \frac{\partial HV_\alpha^2}{\partial y} + gH\frac{\partial \zeta}{\partial y} + H\mathcal{H}_m^y + V_\alpha \mathcal{H}_c = 0 \tag{2.55}$$

where $H = \zeta + h$ is the total water depth, $\mathcal{H}_m^x$ and $\mathcal{H}_m^y$ are the high-order terms $(O(\mu^2, \alpha\mu, \beta\mu^2))$ of the depth integrated $x$ and $y$ horizontal momentum equations, and $\mathcal{H}_c$ includes the high-order terms of the continuity equation. These are given by

$$(\mathcal{H}_m^x, \mathcal{H}_m^y) = \boldsymbol{D} + \boldsymbol{D}^\nu + \overline{\boldsymbol{\xi}} + \overline{\boldsymbol{\xi}^\nu} - \nabla \cdot \left(\nu_t^h \nabla \boldsymbol{U}_\alpha\right) + \nu_t^v \nabla S + \frac{\boldsymbol{\tau}_b}{\rho H} \tag{2.56}$$

$$\mathcal{H}_c = \mathcal{M} + \mathcal{M}^\nu \tag{2.57}$$

### II.4.2. Time Integration

A standard issue for the extended Boussinesq-type equations, which include first to third-order spatial derivatives, is that the time integration should be fourth-order accurate. This prevents numerical truncation errors of the same form as included derivatives. A third-order Adams-Bashforth predictor and the fourth-order Adams-Moulton corrector scheme are used for the time integration.

The predictor step is

$$\zeta^{n+1} = \zeta^n + \frac{\Delta t}{12}\left(23E^n - 16E^{n-1} + 5E^{n-2}\right) \tag{2.58}$$

$$\begin{aligned} P^{n+1} = P^n \;&+\; \frac{\Delta t}{12}\left(23F^n - 16F^{n-1} + 5F^{n-2}\right) \\ &+\; 2F_1^n - 3F_1^{n-1} + F_1^{n-2} + F_v^p \end{aligned} \tag{2.59}$$

$$\begin{aligned} Q^{n+1} = Q^n \;&+\; \frac{\Delta t}{12}\left(23G^n - 16G^{n-1} + 5G^{n-2}\right) \\ &+\; 2G_1^n - 3G_1^{n-1} + G_1^{n-2} + G_v^p \end{aligned} \tag{2.60}$$

where $P$, $Q$, $E$, $F$ and $G$ are defined as

$$\begin{aligned} P = HU_\alpha + \frac{H}{2}\left(z_\alpha^2 - \zeta^2\right) U_{\alpha xx} &+ H\left(z_\alpha - \zeta\right)\left(hU_\alpha\right)_{xx} \\ &- H\zeta_x\left\{\zeta U_{\alpha x} + \left(hU_\alpha\right)_x\right\} \end{aligned} \tag{2.61}$$

$$\begin{aligned} Q = HV_\alpha + \frac{H}{2}\left(z_\alpha^2 - \zeta^2\right) V_{\alpha yy} &+ H\left(z_\alpha - \zeta\right)\left(hV_\alpha\right)_{yy} \\ &- H\zeta_y\left\{\zeta V_{\alpha y} + \left(hV_\alpha\right)_y\right\} \end{aligned} \tag{2.62}$$

where the subscripts $x$ and $y$ mean the derivatives in the $x$ and $y$ direction, respectively.

$$E = E_{LO} + E_D + E_V \tag{2.63}$$

$$F = F_{LO} + F_D + U_\alpha\left(E_D + E_V\right) \tag{2.64}$$

$$G = G_{LO} + G_D + V_\alpha\left(E_D + E_V\right) \tag{2.65}$$

$E_{LO}$, $F_{LO}$, and $G_{LO}$ are rewritten by

$$E_{LO} = -\frac{\partial HU_\alpha}{\partial x} - \frac{\partial HV_\alpha}{\partial y} \tag{2.66}$$

$$F_{LO} = -\frac{\partial}{\partial x}\left(HU_\alpha^2 + \frac{1}{2}gH^2\right) - \frac{\partial HU_\alpha V_\alpha}{\partial y} + gH\frac{\partial h}{\partial x} \tag{2.67}$$

$$G_{LO} = -\frac{\partial HU_\alpha V_\alpha}{\partial x} - \frac{\partial}{\partial y}\left(HV_\alpha^2 + \frac{1}{2}gH^2\right) + gH\frac{\partial h}{\partial y} \tag{2.68}$$

and $E_D$, $E_V$, $F_D$, $G_D$, $F_1$ and $G_1$ are defined as

$$\begin{aligned} E_D &= \left[H\left\{\left(\frac{1}{6}\left(\zeta^2 - \zeta h + h^2\right) - \frac{1}{2}z_\alpha^2\right)\nabla S + \left(\frac{1}{2}\left(\zeta - h\right) - z_\alpha\right)\nabla T\right\}\right]_x \\ &+ \left[H\left\{\left(\frac{1}{6}\left(\zeta^2 - \zeta h + h^2\right) - \frac{1}{2}z_\alpha^2\right)\nabla S + \left(\frac{1}{2}\left(\zeta - h\right) - z_\alpha\right)\nabla T\right\}\right]_y \end{aligned} \tag{2.69}$$

$$\begin{aligned} E_V = &- \left[H\psi^x\left\{\frac{z_\alpha^2}{2} - z_\alpha\zeta + \frac{(2\zeta^2 - 2\zeta h - h^2)}{6}\right\}\right]_x \\ &- \left[H\psi^y\left\{\frac{z_\alpha^2}{2} - z_\alpha\zeta + \frac{(2\zeta^2 - 2\zeta h - h^2)}{6}\right\}\right]_y \end{aligned} \tag{2.70}$$

$$\begin{aligned} (F_D, G_D) &= H\left[\frac{1}{2}\nabla\left(\zeta^2\boldsymbol{U}_\alpha\cdot\nabla S\right) + \nabla\left(\zeta\boldsymbol{U}_\alpha\cdot\nabla T\right) - \frac{1}{2}\nabla\left(\zeta^2 S^2\right)\right. \\ &- \frac{1}{2}\nabla\left({z_\alpha}^2\boldsymbol{U}_\alpha\cdot\nabla S\right) - \nabla\left(z_\alpha\boldsymbol{U}_\alpha\cdot\nabla T\right) - \left(T\nabla T\right) - \nabla\left(\zeta T S\right) \\ &- \frac{(\zeta - h)}{2}\nabla\left\{\boldsymbol{U}_\alpha\cdot\left(\boldsymbol{\psi}\zeta\right)\right\} + \frac{(\zeta^2 - \zeta h + h^2)}{6}\nabla\left(\boldsymbol{U}_\alpha\cdot\boldsymbol{\psi}\right) \\ &- \nabla\left[\boldsymbol{U}_\alpha\cdot\left\{\boldsymbol{\psi}\left(\frac{z_\alpha^2}{2} - \zeta z_\alpha\right)\right\}\right] \\ &+ \boldsymbol{\psi}\left\{\frac{\left(\zeta^2 + \zeta h - 2h^2\right)S}{6} + \frac{HT}{2}\right\} - \overline{\boldsymbol{\xi}} - \overline{\boldsymbol{\xi}^\nu} \\ &+ \left.\nabla\cdot\left(\nu_t^h\nabla\boldsymbol{U}_\alpha\right) - \nu_t^v\nabla S - \frac{\boldsymbol{\tau}_b}{\rho H}\right] \end{aligned} \tag{2.71}$$

$$F_1 = \frac{H}{2}\left(\zeta^2 - z_\alpha^2\right) V_{\alpha xy} - H\left(z_\alpha - \zeta\right)\left(hV_\alpha\right)_{xy} + H\zeta_x\left\{\zeta V_{\alpha y} + \left(hV_\alpha\right)_y\right\} \tag{2.72}$$

$$G_1 = \frac{H}{2}\left(\zeta^2 - z_\alpha^2\right) U_{\alpha xy} - H\left(z_\alpha - \zeta\right)\left(hU_\alpha\right)_{xy} + H\zeta_y\left\{\zeta U_{\alpha x} + \left(hU_\alpha\right)_x\right\} \tag{2.73}$$

$F_v^p$ and $G_v^p$ are rewritten by

$$\begin{aligned} F_v^p &= \frac{H^n\left(\zeta^2 - \zeta h + h^2 + 3z_\alpha^2\right)^n}{6}\left\{2\left(\psi^x\right)^n - 3\left(\psi^x\right)^{n-1} + \left(\psi^x\right)^{n-2}\right\} \\ &- \frac{H^n\left(\zeta - h - 2z_\alpha\right)^n}{2}\left\{2\left(\psi^x\zeta\right)^n - 3\left(\psi^x\zeta\right)^{n-1} + \left(\psi^x\zeta\right)^{n-2}\right\} \end{aligned} \tag{2.74}$$

$$\begin{aligned} G_v^p &= \frac{H^n\left(\zeta^2 - \zeta h + h^2 + 3z_\alpha^2\right)^n}{6}\left\{2\left(\psi^y\right)^n - 3\left(\psi^y\right)^{n-1} + \left(\psi^y\right)^{n-2}\right\} \\ &- \frac{H^n\left(\zeta - h - 2z_\alpha\right)^n}{2}\left\{2\left(\psi^y\zeta\right)^n - 3\left(\psi^y\zeta\right)^{n-1} + \left(\psi^y\zeta\right)^{n-2}\right\} \end{aligned} \tag{2.75}$$

The corrector step is

$$\zeta^{n+1} = \zeta^n + \frac{\Delta t}{24}\left(9E^{n+1} + 19E^n - 5E^{n-1} + E^{n-2}\right) \tag{2.76}$$

$$\begin{aligned} P^{n+1} = P^n &+ \frac{\Delta t}{24}\left(9F^{n+1} + 19F^n - 5F^{n-1} + F^{n-2}\right) \\ &+ F_1^{n+1} - F_1^n + F_v^c \end{aligned} \tag{2.77}$$

$$\begin{aligned} Q^{n+1} = Q^n &+ \frac{\Delta t}{24}\left(9G^{n+1} + 19G^n - 5G^{n-1} + G^{n-2}\right) \\ &+ G_1^{n+1} - G_1^n + G_v^c \end{aligned} \tag{2.78}$$

where $F_v^c$ and $G_v^c$ are rewritten as

$$\begin{aligned} F_v^c &= \frac{H^{n+1}\left(\zeta^2-\zeta h+h^2+3z_\alpha^2\right)^{n+1}}{6}\left\{(\psi^x)^{n+1}-(\psi^x)^n\right\} \\ &- \frac{H^{n+1}\left(\zeta-h-2z_\alpha\right)^{n+1}}{2}\left\{(\psi^x\zeta)^{n+1}-(\psi^x\zeta)^n\right\} \end{aligned} \tag{2.79}$$

$$\begin{aligned} G_v^c &= \frac{H^{n+1}\left(\zeta^2-\zeta h+h^2+3z_\alpha^2\right)^{n+1}}{6}\left\{(\psi^y)^{n+1}-(\psi^y)^n\right\} \\ &- \frac{H^{n+1}\left(\zeta-h-2z_\alpha\right)^{n+1}}{2}\left\{(\psi^y\zeta)^{n+1}-(\psi^y\zeta)^n\right\} \end{aligned} \tag{2.80}$$

After each predictor and corrector step, $P$ and $Q$ are solved by a matrix solver. Note that the governing equations are solved by a cell averaged finite volume method, so all computed values are cell averaged values. $P$ and $Q$ can be expressed as

$$\begin{aligned} P &= \frac{H}{\Delta x}\left[\int_{x_{i-1/2}}^{x_{i+1/2}} U_\alpha(x)dx+\frac{1}{2}\left(z_\alpha^2-\zeta^2\right)\int_{x_{i-1/2}}^{x_{i+1/2}} U_\alpha(x)_{xx}dx\right. \\ &+ (z_\alpha-\zeta)\int_{x_{i-1/2}}^{x_{i+1/2}}\left\{hU_\alpha(x)\right\}_{xx}dx \\ &\left.- \zeta_x\zeta\int_{x_{i-1/2}}^{x_{i+1/2}} U_\alpha(x)_x dx-\zeta_x\int_{x_{i-1/2}}^{x_{i+1/2}}\left\{hU_\alpha(x)\right\}_x dx\right] \end{aligned} \tag{2.81}$$

$$\begin{aligned} Q &= \frac{H}{\Delta y}\left[\int_{y_{j-1/2}}^{y_{j+1/2}} V_\alpha(y)dy+\frac{1}{2}\left(z_\alpha^2-\zeta^2\right)\int_{y_{j-1/2}}^{y_{j+1/2}} V_\alpha(y)_{yy}dy\right. \\ &+ (z_\alpha-\zeta)\int_{y_{j-1/2}}^{y_{j+1/2}}\left\{hV_\alpha(y)\right\}_{yy}dy \\ &\left.- \zeta_y\zeta\int_{y_{j-1/2}}^{y_{j+1/2}} V_\alpha(y)_y dy-\zeta_y\int_{y_{j-1/2}}^{y_{j+1/2}}\left\{hV_\alpha(y)\right\}_y dy\right] \end{aligned} \tag{2.82}$$

The equations (2.81) and (2.82) yield a tridiagonal matrix and can be solved

efficiently. For $x$ direction,

$$\alpha U_{\alpha}^{i-1} + \beta U_{\alpha}^{i} + \gamma U_{\alpha}^{i+1} = P \tag{2.83}$$

where

$$\alpha = H_i \left\{ \frac{z_\alpha^2 - \zeta^2}{2\Delta x^2} + \frac{(z_\alpha - \zeta)\, h_{i-1}}{\Delta x^2} + \frac{\zeta_x \zeta}{2\Delta x} + \frac{\zeta_x h_{i-1}}{2\Delta x} \right\} \tag{2.84}$$

$$\beta = H_i \left\{ 1 - \frac{z_\alpha^2 - \zeta^2}{\Delta x^2} - \frac{2\,(z_\alpha - \zeta)\, h_i}{\Delta x^2} \right\} \tag{2.85}$$

$$\gamma = H_i \left\{ \frac{z_\alpha^2 - \zeta^2}{2\Delta x^2} + \frac{(z_\alpha - \zeta)\, h_{i+1}}{\Delta x^2} - \frac{\zeta_x \zeta}{2\Delta x} - \frac{\zeta_x h_{i+1}}{2\Delta x} \right\} \tag{2.86}$$

For $y$ direction, a similar procedure is used. The convergence error for the iterative corrector step is defined as $\sum |f^{n+1} - f_*^{n+1}| / \sum |f^{n+1}|$ and it is required to be less than $10^{-4}$.

### II.4.3. Fourth-Order Accuracy Compact MUSCL TVD Scheme for Leading Order Terms

For the calculation of $E_{LO}$, $F_{LO}$ and $G_{LO}$, except for the bottom slope terms $gHh_x$ and $gHh_y$, a fourth-order compact MUSCL TVD scheme (Yamamoto and Daiguji, 1993) is used to construct the interface values as follows:

$$\phi_{i+1/2}^{L} = \phi_i + \frac{1}{6} \left\{ \Delta^* \overline{\phi}_{i-1/2} + 2\Delta^* \widetilde{\phi}_{i+1/2} \right\} \tag{2.87}$$

$$\phi^R_{i+1/2} = \phi_{i+1} - \frac{1}{6}\left\{2\Delta^*\overline{\phi}_{i+1/2} + \Delta^*\widetilde{\phi}_{i+3/2}\right\} \tag{2.88}$$

where

$$\Delta^*\overline{\phi}_{i-1/2} = minmod\left(\Delta^*\phi_{i-1/2}, b\Delta^*\phi_{i+1/2}\right) \tag{2.89}$$

$$\Delta^*\widetilde{\phi}_{i+1/2} = minmod\left(\Delta^*\phi_{i+1/2}, b\Delta^*\phi_{i-1/2}\right) \tag{2.90}$$

$$\Delta^*\overline{\phi}_{i+1/2} = minmod\left(\Delta^*\phi_{i+1/2}, b\Delta^*\phi_{i+3/2}\right) \tag{2.91}$$

$$\Delta^*\widetilde{\phi}_{i+3/2} = minmod\left(\Delta^*\phi_{i+3/2}, b\Delta^*\phi_{i+1/2}\right) \tag{2.92}$$

$$\Delta^*\phi_{i+1/2} = \Delta\phi_{i+1/2} - \frac{1}{6}\Delta^3\overline{\phi}_{i+1/2} \tag{2.93}$$

$$\Delta^3\overline{\phi}_{i+1/2} = \Delta\overline{\phi}_{i-1/2} - 2\Delta\overline{\phi}_{i+1/2} + \Delta\overline{\phi}_{i+3/2} \tag{2.94}$$

$$\Delta\overline{\phi}_{i-1/2} = minmod\left(\Delta\phi_{i-1/2}, b_1\Delta\phi_{i+1/2}, b_1\Delta\phi_{i+3/2}\right) \tag{2.95}$$

$$\Delta\overline{\phi}_{i+1/2} = minmod\left(\Delta\phi_{i+1/2}, b_1\Delta\phi_{i+3/2}, b_1\Delta\phi_{i-1/2}\right) \tag{2.96}$$

$$\Delta\overline{\phi}_{i+3/2} = minmod\left(\Delta\phi_{i+3/2}, b_1\Delta\phi_{i-1/2}, b_1\Delta\phi_{i+1/2}\right) \tag{2.97}$$

$$minmod(i,j) = sign(i)\max\left[0, \min\left\{|i|, sign(i)j\right\}\right] \tag{2.98}$$

$$minmod(i,j,k) = sign(i)\max\left[0, \min\left\{|i|, sign(i)j, sign(i)k\right\}\right] \tag{2.99}$$

in which the coefficients $b_1 = 2$ and $1 \leq b \leq 4$. Additional details of this numerical scheme are described in Yamamoto and Daiguji (1993). By using the constructed interface values, the numerical fluxes are computed by HLLC approximate Riemann solvers (Toro, 2002) on a cartesian grid. The wave speeds of the Riemann solver used in this study are given by

$$S_L = U_L - a_L q_L, \qquad S_R = U_R + a_R q_R \tag{2.100}$$

where the subscripts $L$ and $R$ indicate the left and right computational cells of the interface and $a_L$ and $a_R$ are the long wave celerity. The $q_L$ is given by

$$q_L = \begin{cases} \sqrt{\frac{1}{2}\frac{(H_* + H_L)H_*}{H_L^2}} & , \quad H_* > H_L \\ 1 & , \quad H_* \leq H_L \end{cases} \tag{2.101}$$

where $H_*$ is given by

$$H_* = \frac{1}{g}\left\{\frac{1}{2}(a_L + a_R) + \frac{1}{4}(U_L - U_R)\right\}^2 \tag{2.102}$$

The $q_R$ can be obtained straightforwardly and is given in Toro (2002).

However, in this numerical scheme which combines the Riemann solvers and MUSCL scheme, there can occur unphysical oscillations when applied on rapidly changing bathymetry. One option to mitigate this issue is use of the Surface Gradient Method (Zhou et al. 2001), which can eliminate these oscillations, but requires that the bathymetry varies continuously. In this study, a modified version of the Surface Gradient Method, developed by Kim et al. (2008), is used.

### II.4.4. Finite Volume Discretization for Dispersive Terms

A cell averaged value $\bar{\phi}_i$ is defined as

$$\bar{\phi}_i = \frac{1}{\Delta x}\int_{x_{i-1/2}}^{x_{i+1/2}} \phi(x)dx \tag{2.103}$$

Substituting the cell averaged value into the Taylor series $\phi = \phi_{i+1/2} + x\phi'_{i+1/2} + x^2/2\phi''_{i+1/2} + x^3/6\phi'''_{i+1/2} + x^4/24\phi''''_{i+1/2} + \cdots$, we can express the cell averaged value with the values defined at cell interfaces (Lacor et al., 2004). For example,

$$\bar{\phi}_i = \phi_{i+1/2} - \frac{\Delta x}{2}\phi'_{i+1/2} + \frac{\Delta x^2}{6}\phi''_{i+1/2} - \frac{\Delta x^3}{24}\phi'''_{i+1/2} + \cdots \tag{2.104}$$

where subscript $i$ is the index of a cell and $i + 1/2$ is the index of the right-side cell interface. Through manipulations of Taylor series expansions, the following discretization equations can be derived and used for the discretization of the dispersion

terms:

$$\phi_{i+1/2} = \frac{7\left(\bar{\phi}_{i+1} + \bar{\phi}_i\right) - \left(\bar{\phi}_{i+2} + \bar{\phi}_{i-1}\right)}{12} + O\left(\Delta x^4\right) \tag{2.105}$$

$$\phi'_{i+1/2} = \frac{15\left(\bar{\phi}_{i+1} - \bar{\phi}_i\right) - \left(\bar{\phi}_{i+2} - \bar{\phi}_{i-1}\right)}{12\Delta x} + O\left(\Delta x^4\right) \tag{2.106}$$

$$\phi''_{i+1/2} = \frac{\left(\bar{\phi}_{i+2} + \bar{\phi}_{i-1}\right) - \left(\bar{\phi}_{i+1} + \bar{\phi}_i\right)}{2\Delta x^2} + O\left(\Delta x^2\right) \tag{2.107}$$

## II.5. Validations and Results

### II.5.1. Solitary Wave Propagation

First, the model will be tested for the relatively simple solitary wave propagation over constant depth. This is primarily a check of the numerical accuracy and the effects of the limiter. For a model to predict a permanent-form solitary wave over a long distance of propagation, it must be free of numerical truncation errors. Here, the weakly-dispersive and inviscid model, equations (2.45) and (2.46), are used. The initial wave height is $a = 0.5m$, wave length $L = 14.7m$, and water depth is $h = 1.0m$. The grid size $\Delta x = 0.1m$ and the time step is based on the $CFL$ condition:

$$\Delta t = CFL \times \min\left(\frac{\Delta x}{|u| + \sqrt{gH}}\right) \tag{2.108}$$

with a $CFL = 0.5$. The time step is constant throughout the simulation, with the maximum velocity taken from the initial condition. Four different solitary wave simulations are run, one with no limiter used, and three with varying limiter values from small (large expected numerical dissipation) to high.

Table 1. Properties of the solitary wave simulations, for various limiter coefficient choices. In the table, $\zeta_1$ is the wave height after 15 wavelengths of propagation and $\zeta_2$ is the height after approximately 100 wavelengths. Phase speed error is relative to the no limiter solution.

| | $\zeta_1$ | $\zeta_2$ | $\frac{(\zeta_1-\zeta_2)}{\zeta_1}\times 100\%$ | phase speed error (%) |
|---|---|---|---|---|
| $b_1 = 1.1$ | 0.514 | 0.496 | 3.5 | -0.24 |
| $b_1 = 2.0$ | 0.517 | 0.517 | 0.0 | 0.06 |
| $b_1 = 3.0$ | 0.518 | 0.518 | 0.0 | 0.03 |
| $b_1 = 4.0$ | 0.518 | 0.517 | 0.2 | 0.13 |
| no limiter | 0.518 | 0.518 | 0.0 | 0.00 |

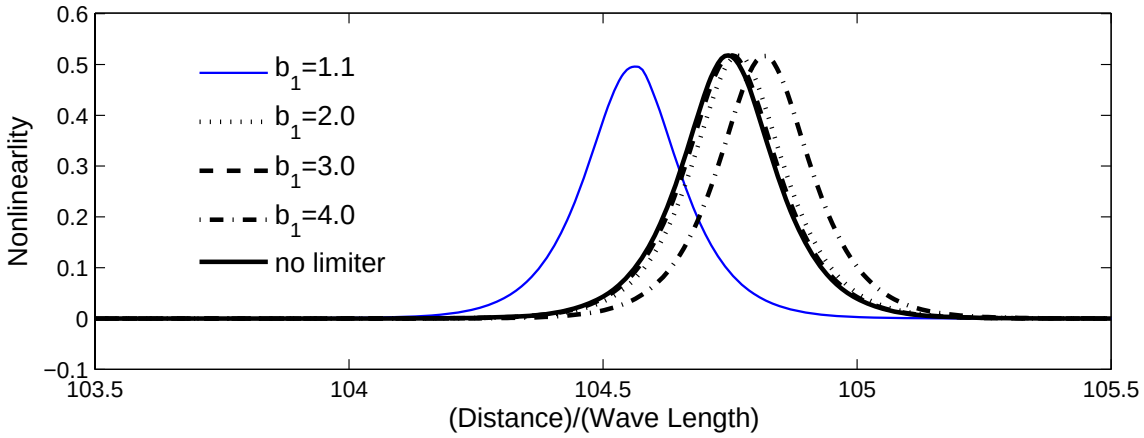


Figure 2. Solitary wave profiles after 104.1 wavelengths of propagation. The various profiles are for different limiter values, shown in the legend.

Figure 2 and Table 1 show the computed results after the solitary wave travels approximately 100 wavelengths. In Table 1, $\zeta_1$ is the computed wave height after the wave travels about 15 wavelengths, or 220 water depths. This value, after 15 wavelengths, is chosen as a reference value due to the well known initial, unsteady behavior of the weakly nonlinear analytical solitary wave solution in the fully nonlinear Boussinesq numerical model (e.g. Wei et al., 1995). The $\zeta_2$ are the computed wave heights after approximately 100 wavelengths of propagation. Although $a = 0.5m$ was used as the initial wave height, as shown in the table, the wave heights increased to $a = 0.514m - 0.518m$ at the beginning of the simulations; again this is expected due to the initial behavior mentioned above, but is also apparently dependent on the limiter. After this initial transition period, the waves maintain a near-constant wave height.

The waves have traveled more than 100 wave lengths in the snapshot shown in Figure 2, 85 after the initial, unsteady period, and so the phase error shown in Figure 2 needs to be divided by 85 to provide a relative value. The maximum phase error is about 20% (0.24% error in phase speed) and the maximum change in free surface height over the 85 wavelengths of travel is 3.5% (or 0.04% per wave period) for the most dissipative limiter.

The solitary phase errors shown in the figure are driven by amplitude differences. When smoothing the solution, the limiters have different behaviors in terms of how they re-distribute the mass of the initial condition. The various limiter choices perform this re-distribution differently, leading to slightly dissimilar wave heights and wave speeds. Thus, while the phase errors provide a good depiction of how the limiter errors can accumulate, the decrease in wave height during the propagation yields a more direct quantification of the dissipative effect of the limiters. The decreases in wave height here are 0.002% per period or less for all but the most dissipative limiter

(b=1.1), and indicate a high level of accuracy and minimal error introduced by the limiters, even for this very nonlinear, steep wave.

### II.5.2. Velocity Profile of Uniform and Steady Flow

In weakly varying shallow flows, such as those driven by a small potential head difference, the horizontal velocity component $\boldsymbol{U}_1^{\phi}$ becomes very small as $\nabla S \approx 0$ and $\nabla T \approx 0$. Hence the vertical profile of the horizontal flow velocity becomes almost constant unless the viscous correction terms are included. A vertically constant velocity profile is unphysical for a steady flow with any bottom shear; such a flow can be described with the well known log-law profile. By including the horizontal vorticity terms, that is, using the equation (2.49), a parabolic velocity profile can be obtained.

In this section, the derived horizontal velocity profile will be analytically compared with the log-law for boundary flows. For this limiting case, the total water depth is assumed constant in time, and the bottom slope is nonzero but negligible. With a steady, uniform, and 1D flow, the depth-integrated velocity profile reduces to:

$$U(z) = U_\alpha + \frac{\tau_b}{2\rho\nu_t^v h}\left(z_\alpha^2 - z^2\right) \tag{2.109}$$

The conventional log-law profile can be presented in a similar format (e.g. Wang et al., 2001)

$$U_{log}(z) = U_{max} + \frac{u_\tau}{\kappa} ln\left(\frac{z+h}{h}\right) \tag{2.110}$$

The $U_\alpha$ in the depth-integrated profile and the $U_{max}$ in the log profile represent free parameters and are chosen to enforce equal vertically-integrated mass flux between the two relations:

$$\int_{-h}^{0} U dz = \int_{z_0}^{0} U_{log} dz = h U_{DA} \tag{2.111}$$

where $U_{DA}$ is the depth-averaged horizontal velocity and $z_0$ is the near-bottom elevation where the log-law velocity goes to zero. For completeness, the various turbulence parameters for this simplified setup are given as follows:

$$\tau_b = \rho c_f U_{DA}^2 \tag{2.112}$$

$$\nu_t^v = \frac{\kappa}{6} h u_\tau \tag{2.113}$$

$$u_\tau = \sqrt{\frac{\tau_b}{\rho}} = U_{DA}\sqrt{c_f} \tag{2.114}$$

where the origins of the $\kappa/6$ coefficient in the equation (2.113) can be found in Elder (1959). With substitution of these expressions in the profile equations, the resulting vertical profiles become a function of only the bottom friction coefficient, $c_f$. Comparisons between equations (2.109) and (2.110) are given in Figure 3 for four different $c_f$ values. In Figure 3(a), for a small $c_f$ value, the profile through most of water column matches very well. Only near the bottom, where the log law quickly approaches zero velocity, is there visible error. The obvious reason for this discrepancy very near to the bottom is that the model derived here does not attempt to resolve the inner boundary layer, which would require a rapidly vertically varying eddy viscosity and enforcement of a no-slip bottom boundary condition. While such modifications are possible, they would make for a significantly more complex equation model. It is reiterated here that the focus of this study was to derive a simple model which explicitly

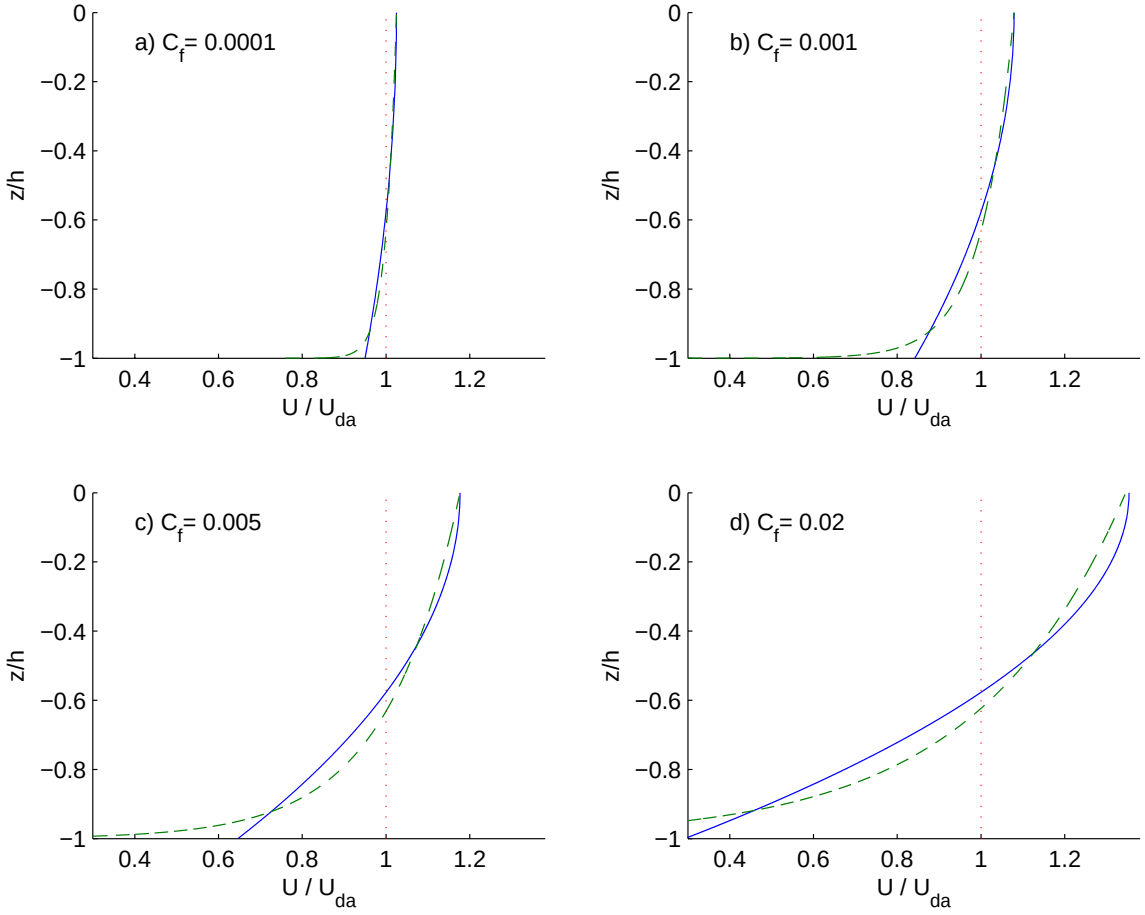


Figure 3. Comparisons of velocity profiles for horizontal uniform flows for four different values of bottom roughness coefficient, $c_f$. In each subplot, the solid line is the velocity profile predicted by equation (2.109), the dashed line is the log-law profile, and the dotted line shows the depth-averaged velocity for reference.

contained the quadratic bottom friction term.

Looking back to Figure 3 and the other presented comparisons, it is clear that the depth-integrated profile error, relative to the total velocity, increases with increasing $c_f$. This is expected under the weakly turbulent assumption, whereby any change to the mean profile due to turbulence should be small. However, even when using a large $c_f$ value, as shown in Figure 3(d), where the turbulence-induced changes to the profile are large, the depth-integrated model provides a reasonable prediction above the inner boundary layer.

### II.5.3. Vortex Street Simulation on a Submerged Conical Island

Lloyd and Stansby (1997b) performed experiments using shallow flows around submerged conical islands with small side slopes. The geometry used in the experiments and inflow and outflow conditions were very simple. However, the flow becomes complex as, on the top of the island, the water surface and velocity varied rapidly and a vortex street was generated at the lee side of the island. In addition, they observed strong vertical mixing just downstream of the apex of the island. As mentioned above, the experimental setup was simple: a conical island was installed $5.0m$ downstream of the inlet in a channel $9.75m$ in length and $1.52m$ in width, and a steady discharge was released at the upstream boundary. The channel and the island were made of marine quality plywood and aluminium, respectively, and the channel bottom was painted to produce uniform surface roughness. More details of the experiments are described in Lloyd and Stansby (1997b).

In this study, the steady discharge velocity is $U = 0.115m/s$, water depth is $h = 0.054m$ and the Reynolds number of the mean flow is $R_e = 6210$ so the flow is in the fully turbulent region. The height and outer radius of the island are $0.049m$ and $0.75m$. Along the upstream numerical boundary an internal source generates the

flow; at the downstream end a sponge layer is used to absorb all outgoing momentum and mass. Convergency of the grid size was tested and when $\Delta x = 0.01 \approx 0.2h$, the computational results were unaffected by further grid reductions. A $CFL = 0.5$ was used. A sensitivity analysis was conducted and $k_s = 0.3mm$ showed the best fit with the experimental data. The $k_s$ of the plywood is $0.6mm$ (French, 1994) and considering the smoothing by the paint, it is a reasonable value. Note that $c_f$ values throughout the domain for this simulation are near 0.01.

Figure 4 shows the water surface elevations and the vorticity distributions at $z = z_\alpha$. The circles depict the submerged island. The coherent structures of the flow seem to be generated reasonably well by the numerical model. Figure 5 shows the numerical velocity field at $z = \zeta$ as well as the experimental field at approximately the same time. In this figure, the equally distributed vertical lines are for reference with the experimental data. Figure 6 shows the measured and computed time series of velocities at the g1 and g2 locations given in Figure 5. The $u_1$ and $v_1$ components are measured at g1, which is at $1.02m$ downstream of the center of the island, and $u_2$ and $v_2$ are measured at g2, which is at $1.02m$ downstream of the island and $0.27m$ away from the centerline. Both cases show good agreement for the period and the magnitude of the velocities. However, for $u_1$, the computed velocity is smaller than the measured data. This numerical model error is also observed in Lloyd and Stansby's 3D computational results. At this location, strong vertical mixing was observed at the downstream of the apex of the island in the experiments, and it is possible that the numerical models are not properly simulating these effects completely.

Figure 7 shows the velocity field at the free surface, $z = \zeta$, and at the bottom, $z = -h$. There are clearly some differences in the velocity patterns, most notably in the magnitude of the velocity vectors, which is expectedly larger at the free surface. There are also some slight differences in the vector directions, although the centers of the

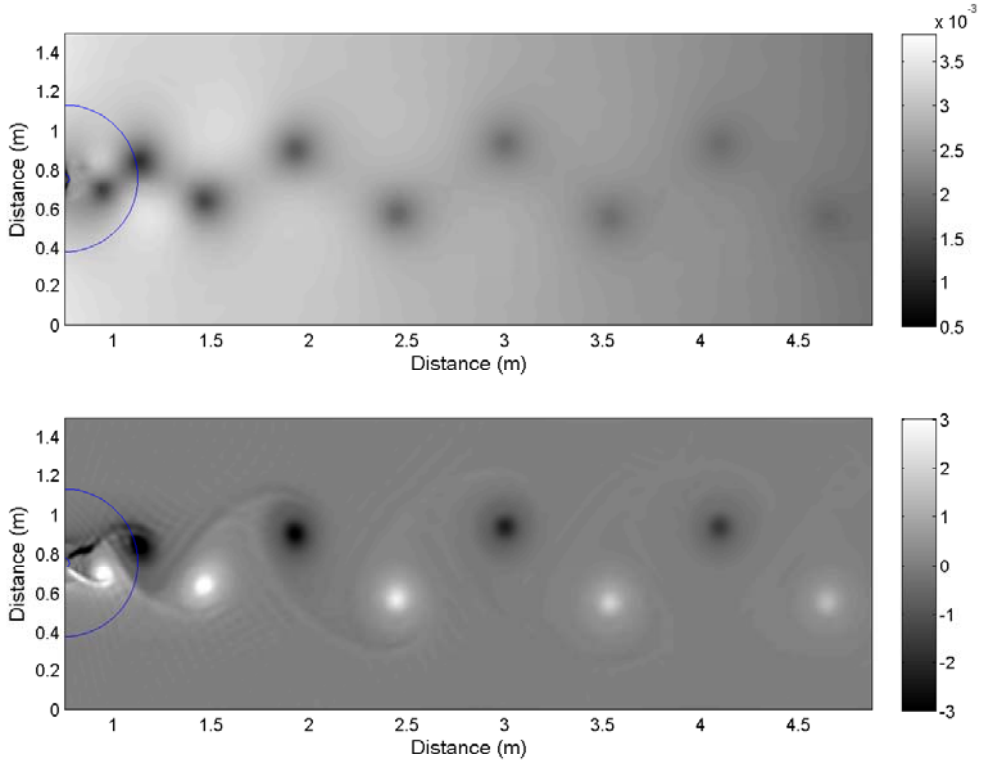


Figure 4. Computed results for Lloyd and Stansby's (1997b) experiment over a submerged island; top: water surface elevations($m$), bottom: vorticity distribution (1/s) at $z = z_\alpha$.

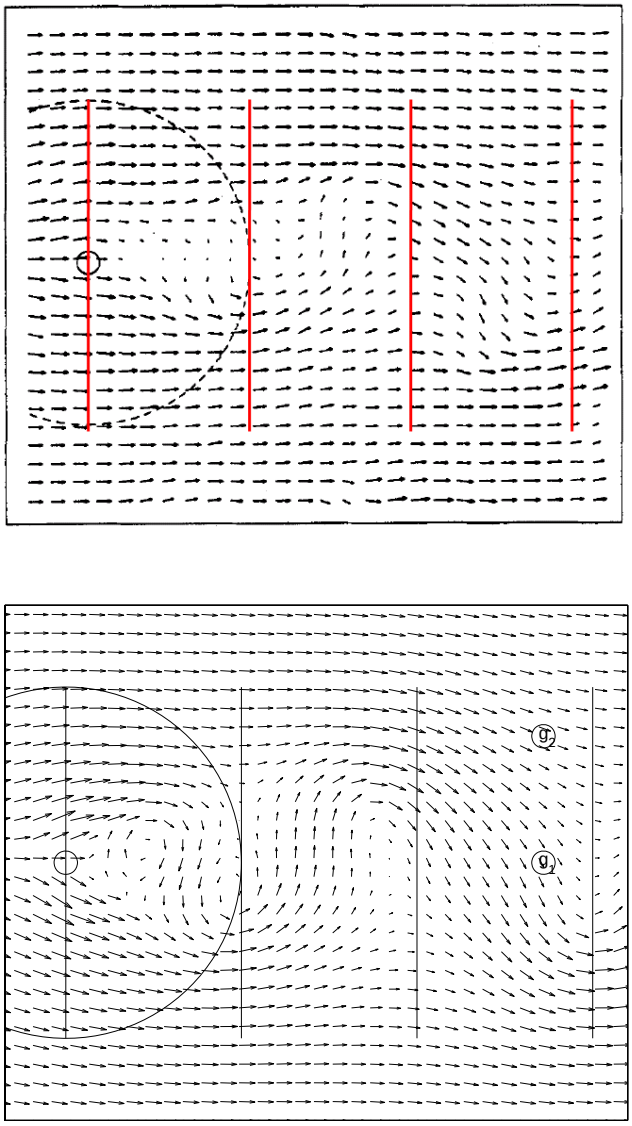


Figure 5. Velocity vector field for Lloyd and Stansby's (1997b) flow over a submerged island at $z = \zeta$; top: experimental, bottom: numerical. The two circled points shown in the numerical plot are the locations of time series shown in figure 6.

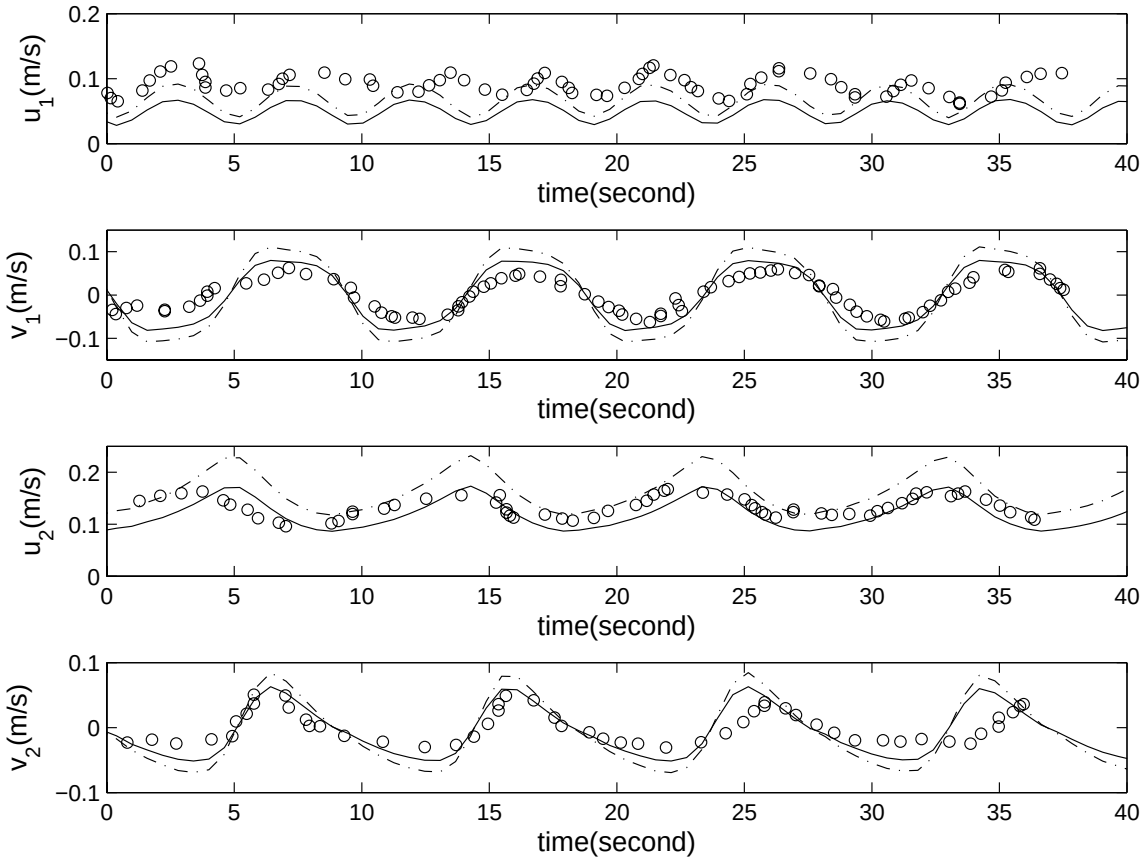


Figure 6. Comparisons of time series of velocities for Lloyd and Stansby's (1997b) experiment over a submerged island; circle: experimental data, solid line: computed velocity at $z = z_\alpha$, dash-dot line: computed velocity at $z = \zeta$. The time series locations are shown in figure 5.

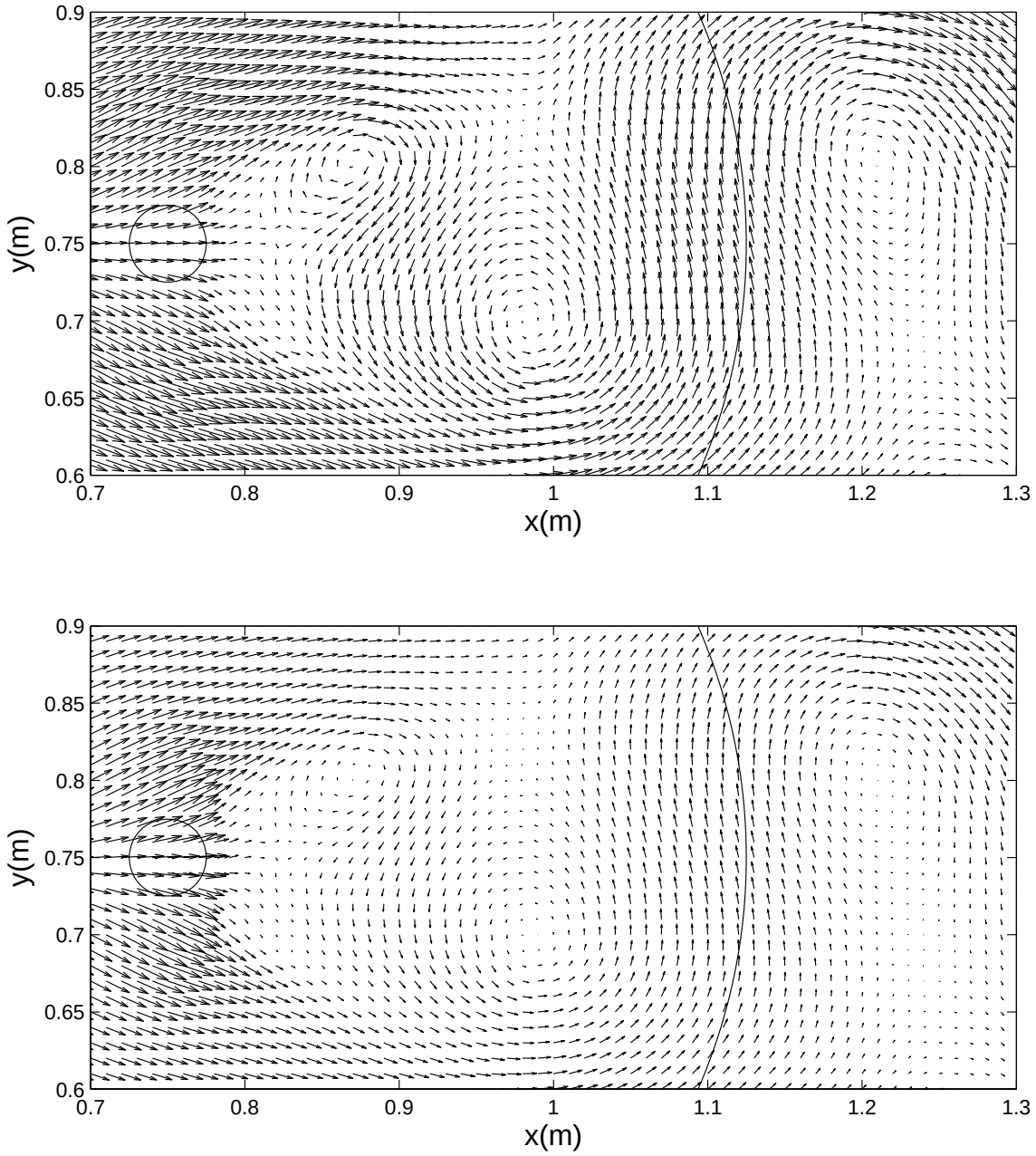


Figure 7. Computed horizontal velocity field for Lloyd and Stansby's (1997b) flow experiment a submerged island; top: at $z = \zeta$, bottom: at $z = \zeta - H$.

eddies do not change location with depth. For evaluation of transport, bed load, etc., it is important that a model be able to predict such vertical changes in the horizontal velocity. Without the horizontal vorticity included here, the velocity profiles would be everywhere almost uniform in the vertical, because the spatial variation of the water surface and horizontal velocity is small.

Figure 8 shows the comparison of the computational results of the fully nonlinear Boussinesq with and without horizontal vorticity effects, as well as the results from the shallow water model, also without horizontal vorticity terms. All results here include the quadratic bottom friction term, with $k_s = 0.3mm$. Thus this comparison will provide some insight into the importance of the high-order dispersive terms and the terms appearing due to the inclusion of the high-order rotational $\Omega$ correction in the horizontal velocity profile, equation (2.49). Comparing the Boussinesq results with and without horizontal vorticity, it is clear that the vorticity terms do not significantly impact the shedding frequency, although they do have a small to moderate effect on the amplitude of the velocity fluctuations. This fluctuation varies from 5% to 50% of the local amplitude.

To assess the importance of frequency dispersion, the Boussinesq and shallow water models should be compared. Here, it is evident that by neglecting the dispersive terms, the shedding frequency changes. The difference is not large; the shallow water model predicts a period approximately 3% shorter than the Boussinesq. This level of error is expected in light of the free surface features shown in Figure 4, which have characteristic length scales on the order of 10 water depths (shallow water wave speed 4% larger than Airy wave speed) and have propagated about one length scale before reaching the measurement locations g1 and g2.

Horizontal vorticity distributions through the center of island in the $x$-$z$ and $y$-$z$ plane are described in Figure 9. Similar to the vertical vorticity shown in Figure

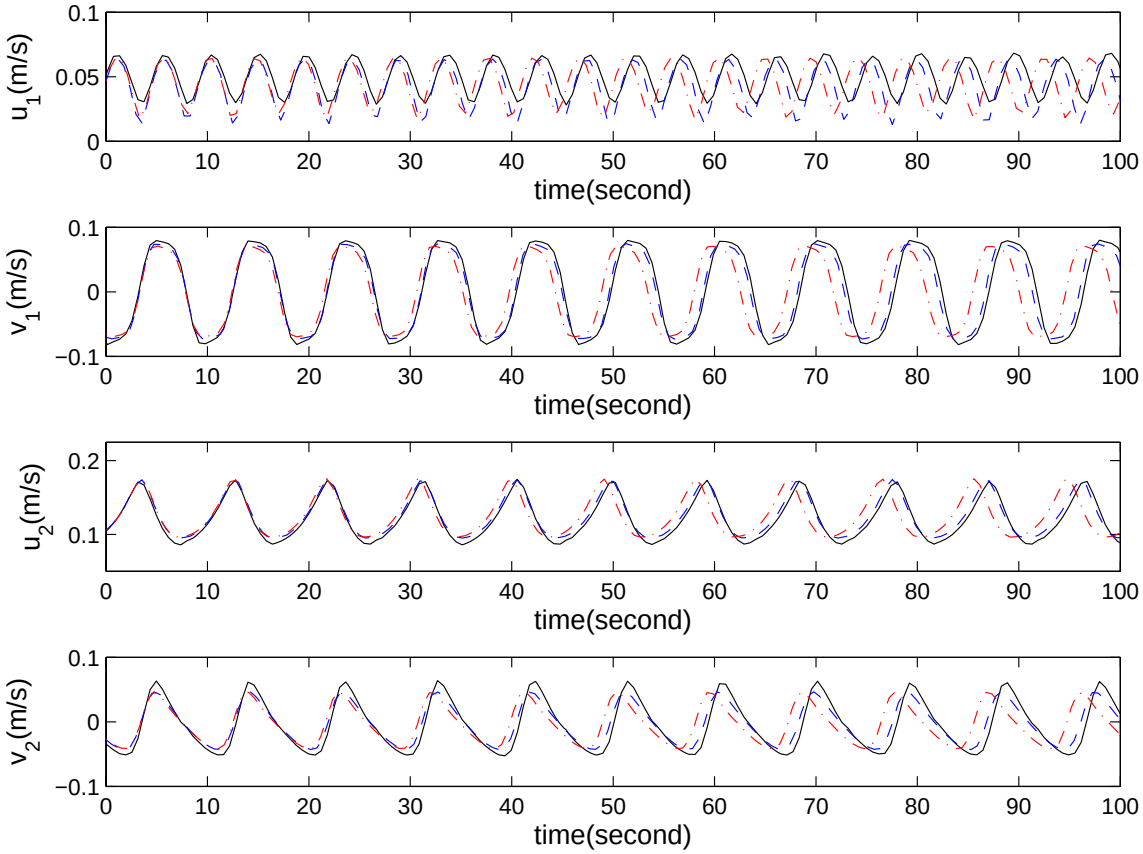


Figure 8. Comparisons of Boussinesq and shallow water model results at time series locations shown in figure 5; solid line: Boussinesq model results with horizontal vorticity terms, dash line: Boussinesq model results without horizontal vorticity terms, dash-dot line: shallow water equations model results.

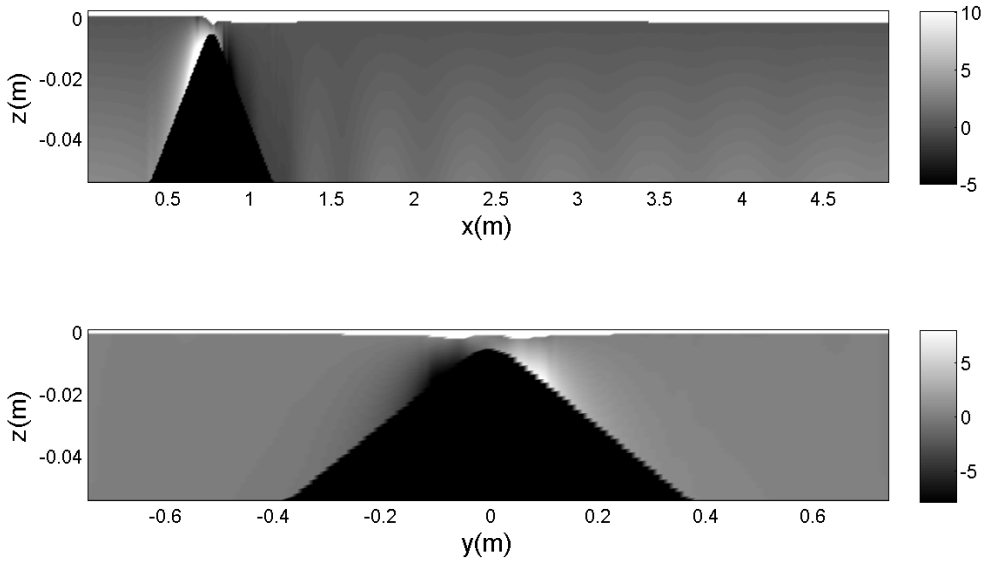


Figure 9. Computed horizontal vorticity distributions ($1/s$) for Lloyd and Stansby's (1997b) flow experiment a submerged island; top: in the $x$-$z$ plane, bottom: in the $y$-$z$ plane. Both profiles intersect the crest of the island.

4, the magnitude of the horizontal vorticity is largest around the apex of the island and decreases downstream. At the downstream end of the island, the horizontal vorticity begins to show a wavy pattern. The pattern matches the pattern of the vertical vorticity in the Figure 4 and it can be regarded as an interaction between the horizontal and vertical vorticity. Generally, because turbulence is mainly generated at the bottom in shallow flows, the magnitude of horizontal vorticity near the bottom will be larger than near the water surface. The numerical results show this pattern. Finally, from the results, it can be concluded that the effects of bottom-induced turbulence in an energetic flow field can be reasonably evaluated with the equations derived here.

### II.5.4. Oscillatory Flow Simulations through Tidal Inlets

Nicolau (2007) and Nicolau et al. (2009) conducted experiments in a laboratory shallow tidal basin in order to characterize the large-scale jet vortices forced by a tidal cycle. At each end of the basin, hydraulic head was given in an oscillatory manner, creating a controlled seiche in the basin. Vortices were created as the flow exited the inlet structures. The width and the length of the basin are $5.48m$ and $14.6m$. At $0.55m$ from both ends, floaters for water surface damping and flow straighteners were installed. The bottom roughness of the basin is given as $k_s = 0.05mm - 0.1mm$ (Carmer, 2005), and correspond to $c_f$ values ranging from 0.007-0.008 for the flows examined here. The tidal period was 55 seconds and the initial water depth $h$ was $0.1m$. The tidal flow discharge varied sinusoidally and the maximum was designed to be $23\ell/s$ in the laboratory experiments. The Reynolds number of the time averaged flow for the half tidal cycle is about 13000. The inlet structures used in the experiment are shown in Figure 10. More details about the basin are described in Carmer (2005) and Nicolau (2007).

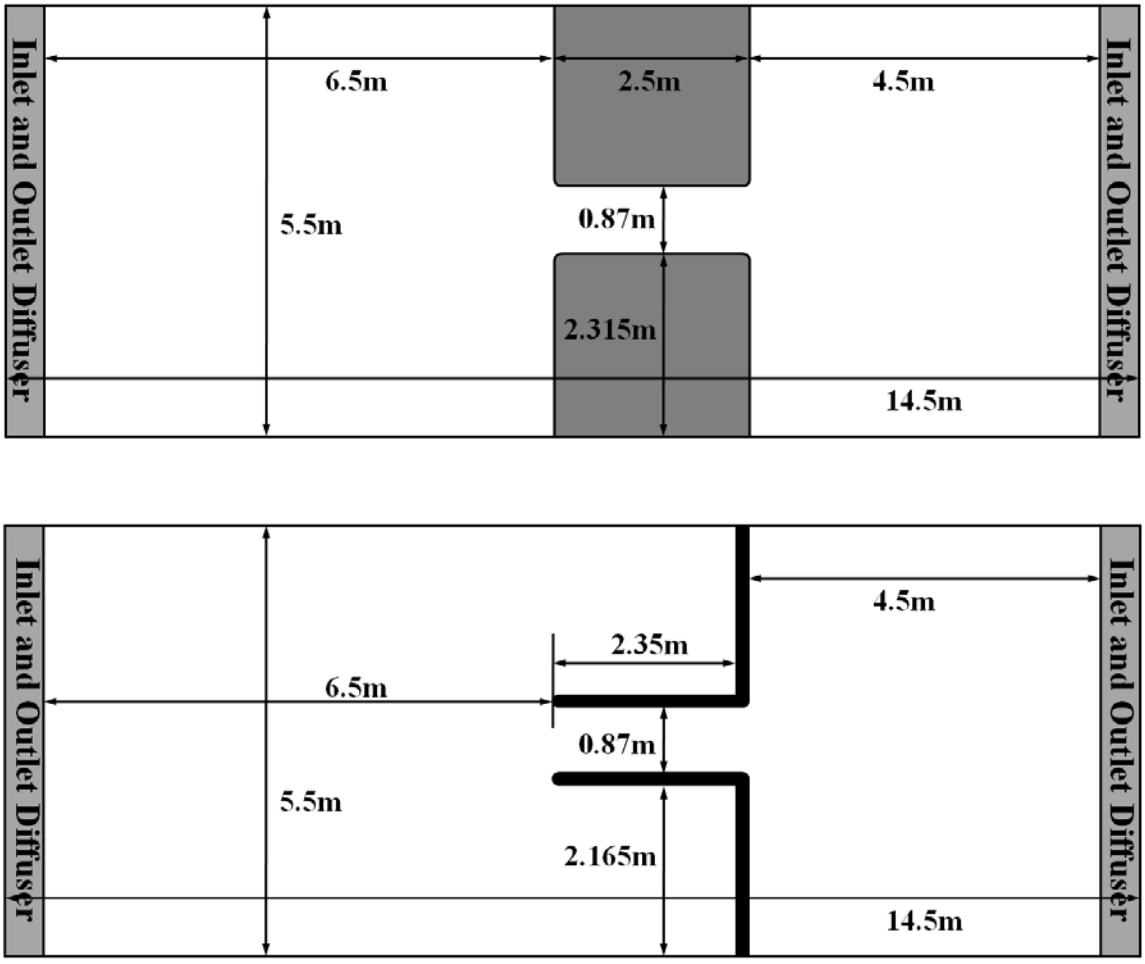


Figure 10. Tidal inlet channels investigated in Nicolau (2007); top: Layout D, bottom: Layout C.

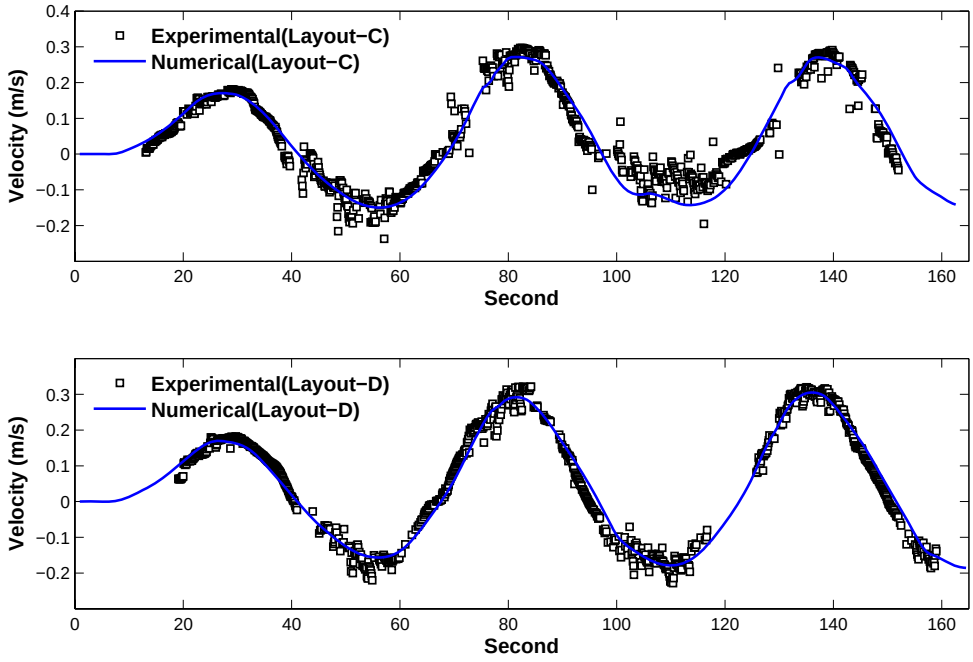


Figure 11. Width-averaged velocity at the mouth of the inlet structures shown in figure 10; top: Layout C, bottom: Layout D.

In this simulation, the numerical seiche is generated by internal source generators placed at both ends of the channel. However, as there were obstacles like screens and floaters at the end sides of the basin, it is difficult to reproduce the experimental flows precisely with a depth-integrated numerical model. Thus to compare the numerical model with the experiment, the computed width-averaged velocity at the mouth of the inlet structure was made similar to the experimental width-averaged velocity, through tuning of the numerical boundary forcing. These velocity comparisons are shown in Figure 11. $CFL = 0.5$ and $\Delta x = 0.2h = 0.02m$ were used in this simulations. The grid size always is smaller than the total water depth, therefore it is expected that the numerical grid is fine enough for the 2D motion to be well resolved (Hinterberger et al., 2007). In the numerical simulations, $k_s = 0.0mm - 0.2mm$ were tested and showed negligible differences, so $k_s = 0.1mm$ was used for all numerical tests, which is also the value recommended by Carmer (2005) for this basin.

Figure 12 shows the computed vorticity and velocity distributions before and after the first tidal period for Layout D. Figure 13 provides a similar series of images taken during the laboratory experiments. Although the timing between the numerical and experimental snapshot are likely slightly different, the overall appearance of the patterns are similar before and after the first tidal period.

Figure 14 shows the traces of the center of first-shed vortex of the experiments and the computed results with respect to time. The $x$ and $y$ locations given in this figure are relative to the inlet corner at which the vortex is generated. The comparisons were done for the vortex generated during the first tidal cycle, as this was the focus of the experiment. The overall agreement is excellent.

As shown in the results, for both types of the inlets examined, it can be concluded that the numerical model can describe the generation mechanism of 2D coherent structures created by a tidal jet, and can predict the flow patterns under unsteady

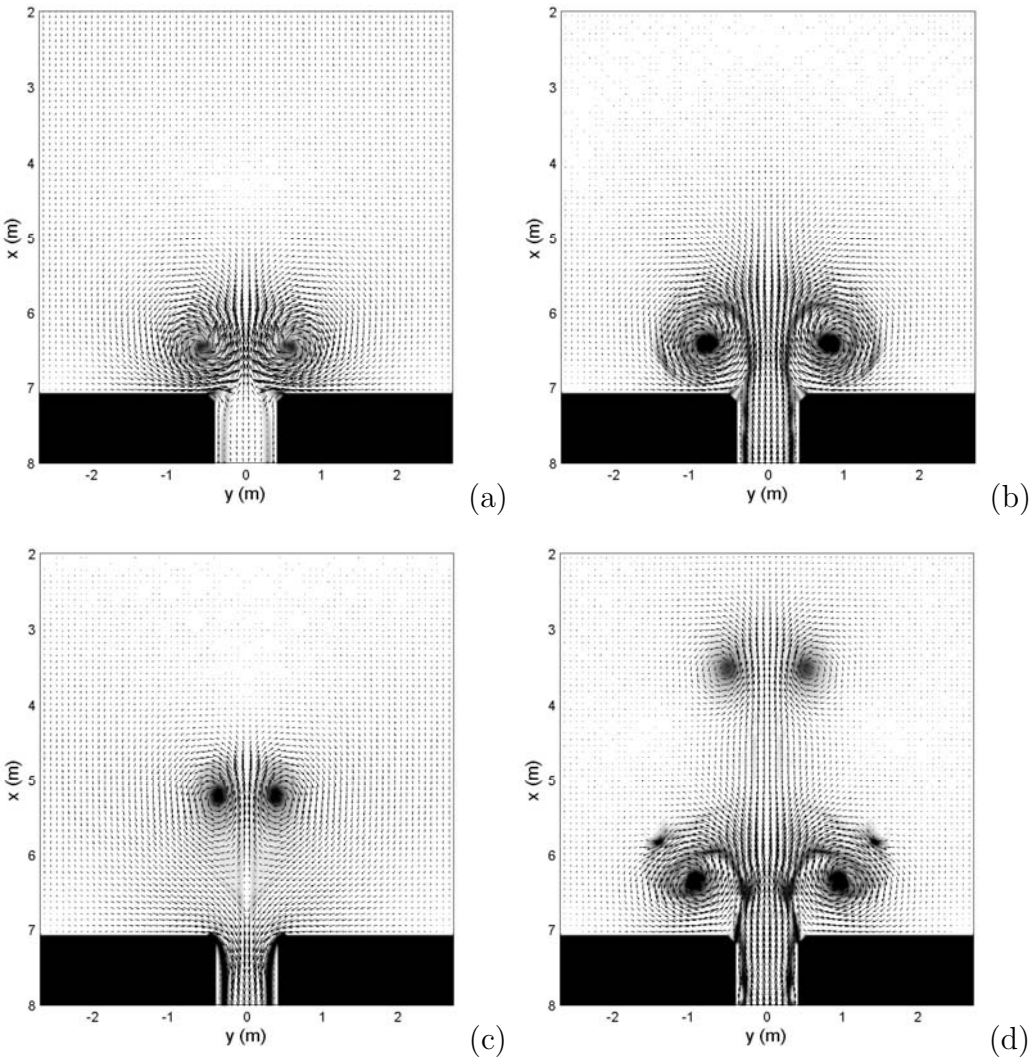


Figure 12. Computed vertical vorticity (absolute value) and free surface horizontal velocity vector distribution at (a)$t = 39$, (b)$t = 90$, (c)$t = 117$, (d)$t = 142$ second, Layout D.

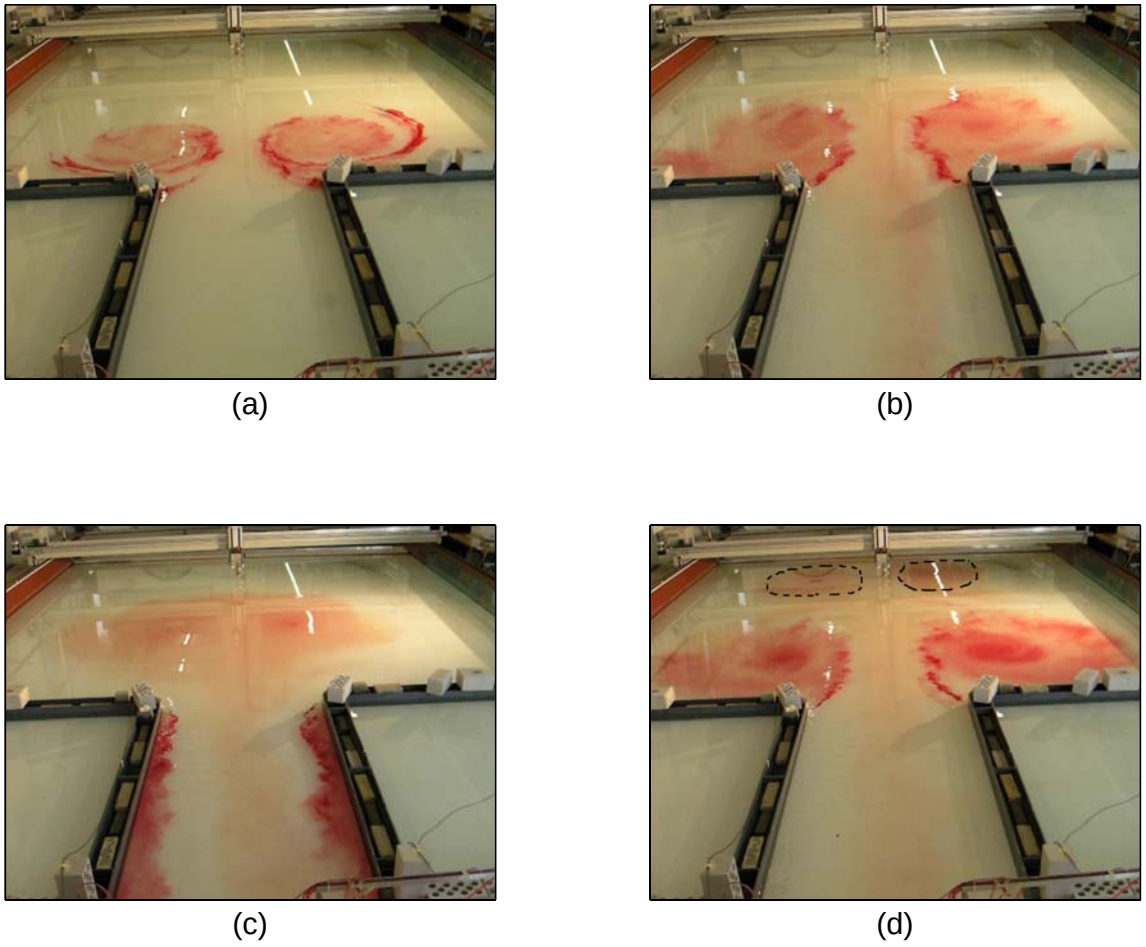


Figure 13. Dye distributions of experiments from Nicolau (2007), Layout D.

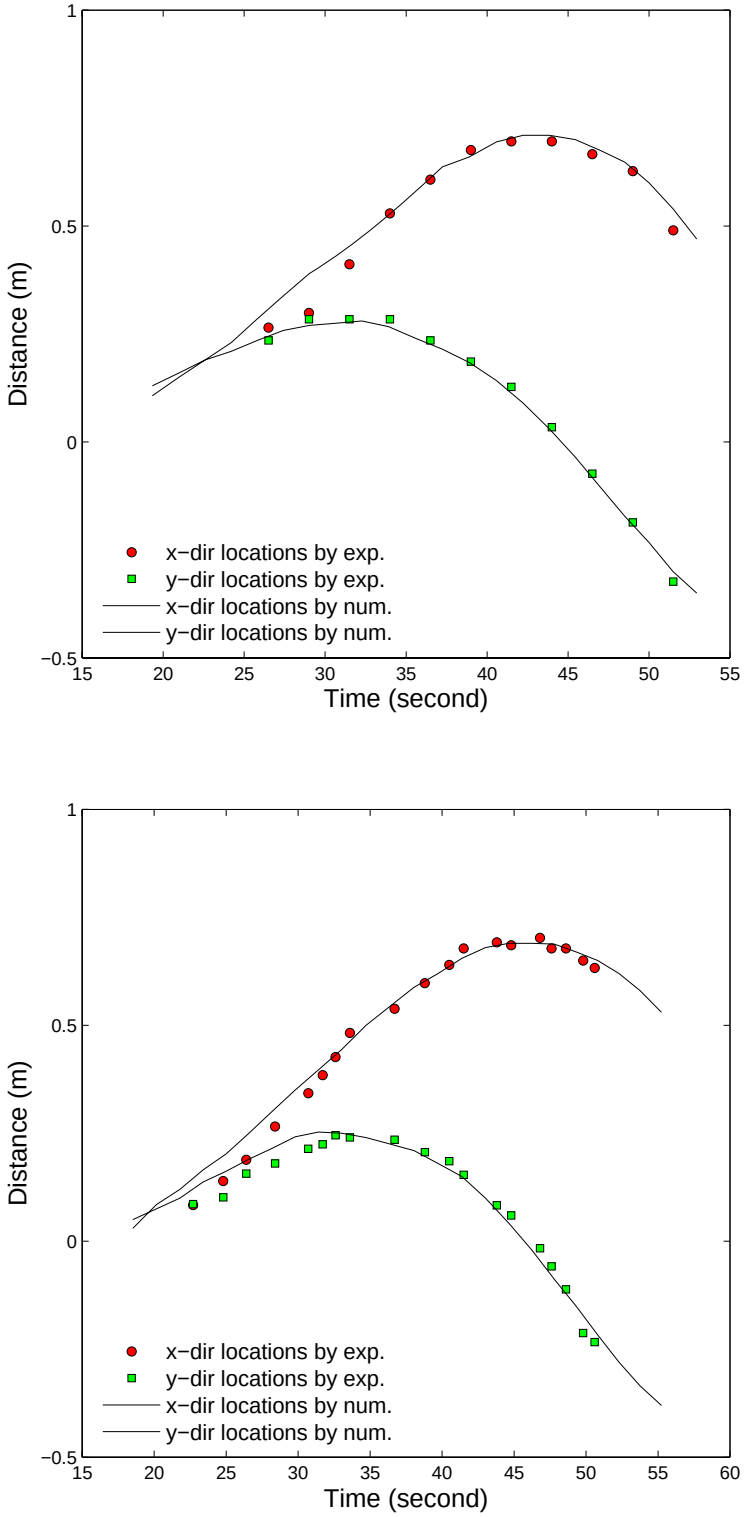


Figure 14. Traces of centers of vortexes, top: Layout D, bottom: Layout C. $x$-dir: longitudinal dir. $y$-dir: width dir. Experimental data from Nicolau (2007).

flow conditions.

## II.6. Summary

From the Navier-Stokes equations, a set of fully nonlinear Boussinesq equations for weakly dispersive, weakly turbulent and rotational fluid flows were derived in conservative form. The model includes the approximate effects of bottom-induced turbulence, in a depth-integrated sense, as a high-order correction. Associated with this turbulence, vertical and horizontal rotational effects are captured. From the derivation interesting results were observed; one should take care when adding ad-hoc models to the flow equations, because it is clear from this exercise that the terms can be included through a consistent derivation from the viscous primitive equations and one cannot properly add the quadratic bottom friction term without also adding a number of additional terms to the depth-integrated governing equations.

A highly accurate and stable numerical model based on the finite volume approach was developed to solve the equations. The numerical method uses a fourth-order MUSCL-TVD scheme to solve the leading order terms. For the high-order terms, a cell averaged finite volume method was implemented.

To verify the derived equations and the numerical model, four verification trials were completed. First, solitary wave propagation was tested as a basic yet fundamental test of the model's ability to predict dispersive and nonlinear wave propagation with minimal numerical error. The computed results showed very small to negligible error in the wave amplitude and phase speed. Thus the finite volume numerical model seems to be able to predict nonlinear and dispersive wave motions very accurately. In the case of steady and uniform flow, the effects of bottom-induced turbulence on the horizontal velocity profile compared well with the log-law boundary velocity profile,

but with increasing error for higher bottom shear stress.

As a more applied validation, flow generating a vortex street was investigated. The computed results seemed to be very reasonable on average, so it can be concluded that the model can analyze the interaction between bottom and flow very reasonably. The last comparison examined the vortex motions created by a tidal jet; simulations showed good overall agreement with the experimental data. Finally, it can be concluded that the provided results show the possible importance of frequency dispersion and horizontal vorticity in turbulent shallow flows, and the derived depth-integrated equations can predict flow patterns, vertical velocity profiles, and coherent structures well.

# CHAPTER III
# TURBULENT TRANSPORT

## III.1. Introduction

In nature, flows are 3D phenomenon. However, in many cases of the geophysical flows, the water depth is limited relative to the horizontal scale so that the horizontal 2D motions dominate the flow structures. In those cases, especially in large domains, the horizontal 2D numerical model can be a practical and accurate tool if the 3D physical properties can be reflected properly into the 2D model. One of the 2D approaches mostly wide spread are the Boussinesq equations and shallow water equations with the long wave scaling derived by perturbation approach or depth averaging.

The Boussinesq equations model can account the dispersive, turbulent and rotational flow properties frequently observed in nature (Kim et al., 2009). Also it has the ability of coupling the currents and waves (Yoon and Liu, 1989) and can predict the nonlinear wave propagations over uneven bottom from deep (or intermediate) water area to shallow water area (Nwogu, 1993 and Wei et al. 1995).

However, during the derivations of a 2D horizontal equation set, some 3D flow features such as the dispersive stresses (Kuipers and Vreugdenhill, 1973) and the effects of the unresolved small scale 3D turbulence are excluded. Consequently, there must be some limitations for predicting the horizontal flow structures which can be originated by the neglected 3D effects. Naturally, the inaccuracy of the flow model is reflected in the results of a transport model.

In order to incorporate the 3D turbulence effects into 2D horizontal flow models, various approaches were proposed. For example, Nadaoka and Yagi (1998) incorporated a subdepth scale turbulence model based on an eddy viscosity into the shallow

water equations. A stochastic BSM proposed by Hinterberger et al. (2007) can account the mechanism of the inverse energy transfer from the unresolved 3D turbulence to the resolved 2D flow motions. Reasonable results were obtained by the proposed methods.

Similar to the flow model, it is required to develop a 2D horizontal scalar transport model that can account the vertical deviations of the concentration and velocity. Taylor (1953) firstly proposed a brilliant method how to reflect the effects of the vertical nonuniformity into the 2D horizontal model. His result, commonly called 'dispersion', was extended to various environmental flow fields by many researchers (Fischer et al., 1979).

For the accurate prediction of transport, an accurate transport numerical solver which can minimize the numerical dispersion, dissipation and diffusion should be developed. Recently, the FVM using approximate Riemann solvers has been developed and applied successfully, for example, Mingham and Causon (2008). The FVM has many advantages. Especially, in the view of eigen structure, the advection equation has the same approximate Riemann solver with the equation of tangential velocity of homogeneous shallow water equations (Toro, 2002). Hence, the exactly same numerical method for the leading-order terms of the Boussinesq equations can be used for the advection terms of the transport equation with consistency.

In this chapter, the turbulent transports by the long waves and currents is investigated. In section 2, the Boussinesq equations with subgrid turbulence closure are introduced. In the next section, a depth-integrated transport equation is introduced. The numerical methods for the transport equation and the test results are briefly presented. The turbulent transport by a plane mixing layer and by bottom topography are presented in the following sections.

## III.2. Depth-Integrated Flow Model for Turbulent Transport

### III.2.1. Dispersive Stress by Velocity Fluctuation $u'$ for Boussinesq Equations

In the 3D space, the filtered continuity and the Navier-Stokes equations for incompressible flow are given by

$$\frac{\partial \overline{u}_i^*}{\partial x_i^*} = 0 \tag{3.1}$$

$$\frac{\partial \overline{u}_i^*}{\partial t^*} + \frac{\partial \overline{u}_i^* \overline{u}_j^*}{\partial x_j^*} + \frac{1}{\rho}\frac{\partial \overline{p^*}}{\partial x_i^*} = \frac{\partial}{\partial x_j^*}\left(2\nu\overline{S_{ij}^*} - \tau_{ij}^*\right) \tag{3.2}$$

where the overbar '$^-$' means the filtering operator. The subscripts $i, j = (1, 2, 3)$. The $x_i^* = (x^*, y^*, z^*)$, where the $(x^*, y^*)$ denote the horizontal axes and the $z^*$ is the vertical axis. The $t^*$ is time and the $u_i^*$ is the velocity tensor, where the $(u^*, v^*)$ are the horizontal velocities and the $w^*$ is the vertical velocity. The $p^*$ is the pressure and the $\rho$ is the density of water. The $\nu$ is the kinematic viscosity of water, the $S_{ij}^*$ is a strain rate tensor and the $\tau_{ij}^*$ is the residual stress tensor.

In this study, for the derivation of the depth-integrated flow equations including the 3D turbulence effects, the perturbation approach with the long wave scaling is used: A typical water depth $h_o$, a horizontal length $\ell_o$, and a time scale $\ell_o/\sqrt{gh_o}$. With these variables, the following dimensionless variables and a parameter can be introduced.

$$(x,y)=\frac{(x^*,y^*)}{\ell_o},\qquad z=\frac{z^*}{h_o},\qquad t=\frac{t^*\sqrt{gh_o}}{\ell_o},\qquad h=\frac{h^*}{h_o},\qquad \zeta=\frac{\zeta^*}{h_o},$$
$$(u,v)=\frac{(u^*,v^*)}{\sqrt{gh_o}},\qquad w=\frac{w^*}{\mu\sqrt{gh_o}},\qquad p=\frac{p^*}{\rho g h_o},\qquad \mu=\frac{h_o}{\ell_o} \tag{3.3}$$

where the $h^*$ is the water depth and the $\zeta^*$ is the water surface elevation. The $\mu$ is the standard parameter for a scale analysis of long waves and its magnitude is assumed to be $O(\mu^2) \ll 1.0$.

As commonly done in shallow flows studies, the turbulent eddy viscosity $\nu_t^*$ is separated into the horizontal and the vertical eddy viscosities. The nondimensional horizontal eddy viscosity is given by

$$\nu_t^h=\frac{\nu_t^{h*}}{\alpha h_o\sqrt{gh_o}} \tag{3.4}$$

where the $\alpha = C_s^2\Delta^2$ is resulted from the $\nu_t^{h*} = (C_s\Delta^*)^2\sqrt{2S_{ij}^*S_{ij}^*}$, (Smagorinsky, 1963) in which the $C_s = 0.2$ is a constant, and the $\Delta^*$ is the grid size. Considering that the vertical turbulence is mainly driven by the bottom shear in shallow flows, the vertical eddy viscosity $\nu_t^{v*} = C_hH^*u_\tau^*$ is used, in which the constant $C_h$ is given by $C_h = \kappa/6$ following Elder (1959), the $\kappa$ is the von Karman constant, the $H^*$ is the total water depth, and the $u_\tau^*$ is the friction velocity. The typical magnitude of the $C_h$ is $O(C_h) \sim 0.1$ and it is expressed with $\beta$. From the relation $u_\tau^* = \sqrt{c_f}|u^*| = \sqrt{gH^*S_f^*}$, the typical magnitude of the roughness coefficient $c_f$ can be determined as $O(c_f) \sim \mu$, in which the $S_f^*$ is the energy slope (Chaudhry, 1993). Finally, the nondimensional vertical eddy viscosity is given by

$$\nu_t^v=\frac{\nu_t^{v*}}{\beta\mu h_o\sqrt{gh_o}} \tag{3.5}$$

With the variables and parameters, the filtered dimensionless form of the continuity equation and the Navier-Stokes equations in the horizontal directions are given by

$$\frac{\partial \overline{u}_i}{\partial x_i} + \frac{\partial \overline{w}}{\partial z} = 0 \tag{3.6}$$

$$\frac{\partial \overline{u}_i}{\partial t} + \frac{\partial \overline{u}_i \overline{u}_j}{\partial x_j} + \frac{\partial \overline{u}_i \overline{w}}{\partial z} + \frac{\partial \overline{p}}{\partial x_i} = \alpha\mu \frac{\partial}{\partial x_j}\left(2\nu_t^h \overline{S_{ij}}\right) + \beta \frac{\partial}{\partial z}\left(2\nu_t^v \overline{S_{ik}}\right) \tag{3.7}$$

henceforth, the index $i, j = (1, 2)$ and the $k = 3$.

A 2D horizontal equations set can be derived by applying depth averaging operator $\widetilde{\phi} = \frac{1}{H}\int_H \phi dz$ to the equations (3.6) and (3.7). However, during the derivations, the dispersive stresses are usually ignored with the assumption of constant velocity profile into the vertical direction like the depth-averaged velocity $\widetilde{u}$ in the Figure 15. Even in the Boussinesq equations that assume the depth-varying velocity like the $U(z)$ in the Figure 15, the fluctuation component $u_i'$ that is important for the prediction of the kinetic energy transport or environmental flows is ignored usually.

In order to consider the 3D turbulence effects by the $u_i'$, Hinterberger et al. (2007) proposed a stochastic BSM for the shallow water equations. The effects can be incorporated into the Boussinesq equations as followings. At first, by integrating the filtered Navier-Stokes equations over the depth, the following equation is obtained.

$$\begin{aligned} \frac{\partial H\widetilde{\overline{u}}_i}{\partial t} &+ \frac{\partial H\widetilde{\overline{u}}_i\widetilde{\overline{u}}_j}{\partial x_j} + H\widetilde{\frac{\partial \overline{p}}{\partial x_i}} \\ &= \alpha\mu \frac{\partial}{\partial x_j}\left(2H\nu_t^h \widetilde{\overline{S_{ij}}}\right) + \beta\left[2\nu_t^v \overline{S_{ik}}\right]_H - \gamma^2 \frac{\partial H D_{ij}\left(\overline{u}\right)}{\partial x_j} \end{aligned} \tag{3.8}$$

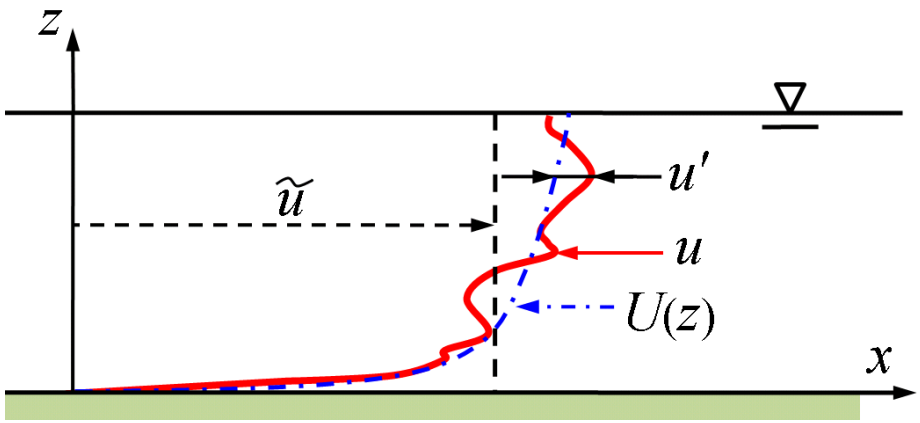


Figure 15. Definitions of velocity notations. $\widetilde{u}$: depth averaged velocity, $u$: real velocity including fluctuating velocity component, $u'$: spatially fluctuating velocity component, $U(z)$: velocity profile neglecting the $u'$.

where the depth averaged velocity is given by

$$\widetilde{u}_i = \frac{1}{H}\int_H \left(U_i + \mu^2 u_i^{\phi} + \beta\mu u_i^{r} + \gamma u_i'\right) dz + O\left(\mu^4, \beta^2\mu^2\right) \tag{3.9}$$

in which the $U_i$ is the horizontal velocity at an arbitrary water depth $z_\alpha$. The $u_i^r$ and the $u_i^\phi$ are the higher-order rotational and irrotational velocity components, respectively (Kim et al., 2009). The newly introduced $\gamma$ is a scale parameter and its magnitude will be determined in a later part. The pressure term is given by $\widetilde{p} = \frac{1}{H}\int_H p(z)dz$, and the $p(z)$ can be obtained by integrating the vertical momentum equation. The dispersive stress $D_{ij}\left(\overline{u}\right)$ is given by

$$
\begin{aligned}
D_{ij}\left(\overline{u}\right) &= \frac{1}{H}\int_H \left(\overline{u}_i - \widetilde{\overline{u}}_i\right)\left(\overline{u}_j - \widetilde{\overline{u}}_j\right) dz \\
&= \mu^2\gamma\left(\widetilde{\overline{u_i^\phi u_j'}} + \widetilde{\overline{u_i' u_j^\phi}}\right) + \beta\mu\gamma\left(\widetilde{\overline{u_i^r u_j'}} + \widetilde{\overline{u_i' u_j^r}}\right) + \gamma^2\widetilde{\overline{u_i' u_j'}} \qquad (3.10)
\end{aligned}
$$

Finally, the momentum equations of the Boussinesq equations that include the dispersive stresses are given by

$$
\begin{aligned}
\frac{\partial H\widetilde{\overline{u}}_i}{\partial t} &+ \frac{\partial H\widetilde{\overline{u}}_i\widetilde{\overline{u}}_j}{\partial x_j} + H\widetilde{\frac{\partial \overline{p}}{\partial x_i}} \\
&= \alpha\mu\frac{\partial}{\partial x_j}\left(2H\nu_t^h\widetilde{\overline{S_{ij}}}\right) + \beta\mu^2 2\nu_t^v\frac{\partial}{\partial x_i}\left(\frac{\partial u_j}{\partial x_j}\right) + \beta\mu^2\tau_i^b \\
&+ \frac{\partial}{\partial x_j}\left[H\left\{\mu^2\gamma\left(\widetilde{\overline{u_i^\phi u_j'}} + \widetilde{\overline{u_i' u_j^\phi}}\right) + \beta\mu\gamma\left(\widetilde{\overline{u_i^r u_j'}} + \widetilde{\overline{u_i' u_j^r}}\right) + \gamma^2\widetilde{\overline{u_i' u_j'}}\right\}\right] \\
&+ O\left(\mu^4, \alpha\mu^3, \beta\mu^4\right) \qquad (3.11)
\end{aligned}
$$

Considering the typical magnitude of the shear stress $\tau_i^b$ which is directly related to the Reynolds stress, we can deduce $\gamma^2 = \beta\mu^2$ from the equation (3.11). Sequently, in the dispersive stresses terms of the equation (3.11), the first and the second terms are relatively smaller than the last term so that only the last term is sustained as below and used for turbulence modeling in this study.

$$
\beta\mu^2\frac{\partial}{\partial x_j}\left(H\widetilde{\overline{u_i' u_j'}}\right) \qquad (3.12)
$$

### III.2.2. Depth-Integrated Model including Subgrid Scale Turbulence Effects (DISGS)

For the convenience of expression, all the dimensional variables are expressed without the superscript '*' after the dimensions are recovered. The overbar '$^-$' for the notation

of the filtering is not expressed from here on either.

Including the dispersive stress terms above derived, the conservative form of the Boussinesq equations with subgrid turbulence closure are given by

$$\frac{\partial \zeta}{\partial t} + \frac{\partial HU_i}{\partial x_i} + \mathcal{M} + \mathcal{M}^{\nu} = 0 \tag{3.13}$$

$$\begin{aligned} \frac{\partial HU_i}{\partial t} \quad &+ \quad \frac{\partial HU_iU_j}{\partial x_j} + gH\frac{\partial \zeta}{\partial x_i} + H\left(D_i + \overline{\xi_i} + D_i^{\nu} + \overline{\xi_i^{\nu}}\right) + U_i\left(\mathcal{M} + \mathcal{M}^{\nu}\right) \\ &- \quad H\frac{\partial}{\partial x_j}\left(2\nu_t^h S_{ij}\right) + 2H\nu_t^v \frac{\partial}{\partial x_i}\left(\frac{\partial U_j}{\partial x_j}\right) + \frac{\tau_i^b}{\rho} - HF_i = 0 \end{aligned} \tag{3.14}$$

in which, the $\mathcal{M}$ and the $\mathcal{M}^{\nu}$ are the second-order terms of the continuity equation. In the momentum equations, the $D_i$ is the dispersion term, the $D_i^{\nu}$ is the horizontal vorticity effect terms, the $\overline{\xi_i}$ is the vertical vorticity term and the $\overline{\xi_i^{\nu}}$ is the vertical vorticity term combined with the horizontal vorticity. More detail expressions of the higher-order terms can be found in the chapter I or Kim et al. (2009).

The $HF_i$ representing the equation (3.12) is implemented by a stochastic BSM proposed by Hinterberger et al. (2007). They assumed that the production rate of 2D kinetic turbulent energy $P_{2D}$ were represented as

$$P_{2D} \sim \frac{P_{3D}}{Re_{\tau}} = \frac{|u_i|^2 \nu \sqrt{c_f}}{H^2} \tag{3.15}$$

where the $Re_{\tau} = u_{\tau}H/\nu$. It can be also expressed like (Alvelius, 1999)

$$P_{2D} \sim F_{rms}^2 \Delta t \tag{3.16}$$

where $\Delta t$ is the time step, $F = F_{rms} \times r$, and the $r$ is a random number with zero mean. Finally, from the relation of the two equations and by introducing a model constant $C_B$, the stochastic BSM model is implemented like

$$F_i = C_B \frac{\sqrt{\widetilde{u}^2 + \widetilde{v}^2}}{H} \sqrt{\frac{\nu\sqrt{c_f}}{\Delta t}} r_i \tag{3.17}$$

### III.3. Depth-Integrated Transport Equation

Basically, the Taylor's analysis is followed to derive the depth-integrated transport equation and the long wave scaling is used for the consistency with the depth-integrated flow equations.

Firstly, by using that the turbulent diffusion can be given by $\nu_t^*/\sigma_t$ and the magnitude of turbulent Schmidt number is $O(\sigma_t) \sim 1.0$, the nondimensional turbulent diffusion coefficients can be given by

$$(D_x, D_y) = \frac{\left(D_x^*, D_y^*\right)}{\alpha h_o \sqrt{g h_o}}, \qquad D_z = \frac{D_z^*}{\beta \mu h_o \sqrt{g h_o}} \tag{3.18}$$

where the $D_x$ and the $D_y$ are the nondimensional horizontal turbulent diffusion coefficients, and the $D_z$ is the nondimensional vertical turbulent diffusion coefficient. Applying the perturbation approach with the equations (3.3) and (3.18), the 3D transport equation is expressed as below on the transformed coordinate $(\tau, \xi, \eta, z)$.

$$\begin{aligned}
\frac{\partial\left(\widetilde{C}+\varepsilon C''\right)}{\partial\tau} &+ \mu^2 u''_\phi \frac{\partial\left(\widetilde{C}+\varepsilon C''\right)}{\partial\xi} + \beta\mu u''_r \frac{\partial\left(\widetilde{C}+\varepsilon C''\right)}{\partial\xi} \\
&+ \mu^2 v''_\phi \frac{\partial\left(\widetilde{C}+\varepsilon C''\right)}{\partial\eta} + \beta\mu v''_r \frac{\partial\left(\widetilde{C}+\varepsilon C''\right)}{\partial\eta} + w\frac{\partial\left(\widetilde{C}+\varepsilon C''\right)}{\partial z} \\
&= \alpha\mu\frac{\partial}{\partial\xi}\left\{D_x\frac{\partial\left(\widetilde{C}+\varepsilon C''\right)}{\partial\xi}\right\} + \alpha\mu\frac{\partial}{\partial\eta}\left\{D_y\frac{\partial\left(\widetilde{C}+\varepsilon C''\right)}{\partial\eta}\right\} \\
&+ \beta\frac{\partial}{\partial z}\left\{D_z\frac{\partial\left(\widetilde{C}+\varepsilon C''\right)}{\partial z}\right\} + O\left(\mu^4, \beta^2\mu^2\right) \qquad (3.19)
\end{aligned}$$

where $C''$ is the deviation of the concentration and the $\varepsilon$ is a small number used for the scale analysis. The $\widetilde{C}$ is the depth averaged concentration so the concentration $C$ is expended as $C = \widetilde{C} + \varepsilon C''$. The velocity deviation $u''$ is defined as $u'' = U(z) - \widetilde{u}$ and has the magnitude of $O\left(\mu^2, \beta\mu\right)$. The $(\tau, \xi, \eta)$ means the transformed coordinate and has the relations with the $(t, x, y)$ as followings

$$\xi = x - \widetilde{u}t, \quad \eta = y - \widetilde{v}t, \quad \tau = t \qquad (3.20)$$

Applying depth averaging operator to the equation (3.19) leaves

$$\begin{aligned}
\frac{\partial\widetilde{C}}{\partial\tau} &+ \frac{\varepsilon\mu^2}{H}\int_H u''_\phi\frac{\partial C''}{\partial\xi}dz + \frac{\varepsilon\beta\mu}{H}\int_H u''_r\frac{\partial C''}{\partial\xi}dz \\
&+ \frac{\varepsilon\mu^2}{H}\int_H v''_\phi\frac{\partial C''}{\partial\eta}dz + \frac{\varepsilon\beta\mu}{H}\int_H v''_r\frac{\partial C''}{\partial\eta}dz + \frac{\varepsilon}{H}\int_H w\frac{\partial C''}{\partial z}dz \\
&= \alpha\mu\frac{\partial}{\partial\xi}\left(D_x\frac{\partial\widetilde{C}}{\partial\xi}\right) + \alpha\mu\frac{\partial}{\partial\eta}\left(D_y\frac{\partial\widetilde{C}}{\partial\eta}\right) + O\left(\mu^4, \beta^2\mu^2\right) \qquad (3.21)
\end{aligned}$$

Subtracting the equation (3.21) from the equation (3.19) results in

$$
\begin{aligned}
\varepsilon\frac{\partial C''}{\partial \tau} &+ \mu^2 u''_\phi \frac{\partial \widetilde{C}}{\partial \xi} + \beta\mu u''_r \frac{\partial \widetilde{C}}{\partial \xi} + \mu^2 v''_\phi \frac{\partial \widetilde{C}}{\partial \eta} + \beta\mu v''_r \frac{\partial \widetilde{C}}{\partial \eta} \\
&+ \varepsilon\mu^2 u''_\phi \frac{\partial C''}{\partial \xi} + \varepsilon\beta\mu u''_r \frac{\partial C''}{\partial \xi} + \varepsilon\mu^2 v''_\phi \frac{\partial C''}{\partial \eta} + \varepsilon\beta\mu v''_r \frac{\partial C''}{\partial \eta} \\
&= \frac{\varepsilon\mu^2}{H}\int_H u''_\phi \frac{\partial C''}{\partial \xi} dz + \frac{\varepsilon\mu^2}{H}\int_H v''_\phi \frac{\partial C''}{\partial \eta} dz \\
&+ \frac{\varepsilon\beta\mu}{H}\int_H u''_r \frac{\partial C''}{\partial \xi} dz + \frac{\varepsilon\beta\mu}{H}\int_H v''_r \frac{\partial C''}{\partial \eta} dz \\
&+ \frac{\varepsilon}{H}\int_H w\frac{\partial C''}{\partial z} dz - \varepsilon w\frac{\partial C''}{\partial z} \\
&= \alpha\mu\varepsilon\frac{\partial}{\partial \xi}\left(D_x \frac{\partial C''}{\partial \xi}\right) + \alpha\mu\varepsilon\frac{\partial}{\partial \eta}\left(D_y \frac{\partial C''}{\partial \eta}\right) + \beta\varepsilon\frac{\partial}{\partial z}\left(D_z \frac{\partial C''}{\partial z}\right) \\
&+ O\left(\mu^4, \beta^2\mu^2\right) \qquad (3.22)
\end{aligned}
$$

Unfortunately, no general solution of the $C''$ of the equation (3.22) can be found because the deviation of the velocity varies into the vertical direction (Fischer et al., 1967). At this point, Taylor (1957) assumed that the balance would be reached so that he could truncate almost of the terms except the second-order advection and the vertical diffusion terms in the equation (3.22). However, in this derivation, all terms are kept temporary and the smaller terms will be truncated based on the scale analysis. Hence, for the brevity, the equation (3.22) is rearranged as following

$$
\begin{aligned}
\mu^2 u''_\phi \frac{\partial \widetilde{C}}{\partial \xi} &+ \mu^2 v''_\phi \frac{\partial \widetilde{C}}{\partial \eta} + \beta\mu\left(u''_r \frac{\partial \widetilde{C}}{\partial \xi} + v''_r \frac{\partial \widetilde{C}}{\partial \eta}\right) - \varepsilon\beta\frac{\partial}{\partial z}\left(D_z \frac{\partial C''}{\partial z}\right) \\
&= \mathcal{O}_1(\varepsilon) + \mathcal{O}_2\left(\varepsilon\mu^2\right) + \mathcal{O}_3(\varepsilon\beta\mu) + O\left(\mu^4, \beta^2\mu^2\right) \qquad (3.23)
\end{aligned}
$$

By integrating the equation (3.23) twice, the $C''$ becomes

$$\begin{aligned}
\beta\epsilon C'' &= \mu^2 \int_{-h}^{z} \frac{1}{D_z} \int_{-h}^{z} \left( u''_{\phi} \frac{\partial \widetilde{C}}{\partial \xi} + v''_{\phi} \frac{\partial \widetilde{C}}{\partial \eta} \right) dzdz \\
&+ \beta\mu \int_{-h}^{z} \frac{1}{D_z} \int_{-h}^{z} \left( u''_{r} \frac{\partial \widetilde{C}}{\partial \xi} + v''_{r} \frac{\partial \widetilde{C}}{\partial \eta} \right) dzdz \\
&+ \mathcal{O}_1(\varepsilon) + \mathcal{O}_2\left(\varepsilon\mu^2\right) + \mathcal{O}_3(\varepsilon\beta\mu) + O\left(\mu^4, \beta^2\mu^2\right) \qquad (3.24)
\end{aligned}$$

Substituting the $C''$ into the equation (3.21), we obtain

$$\begin{aligned}
\frac{\partial \widetilde{C}}{\partial \tau} &= \epsilon \frac{\partial}{\partial \xi} \left( D_{L11} \frac{\partial \widetilde{C}}{\partial \xi} + D_{L12} \frac{\partial \widetilde{C}}{\partial \eta} \right) + \epsilon \frac{\partial}{\partial \eta} \left( D_{L21} \frac{\partial \widetilde{C}}{\partial \xi} + D_{L22} \frac{\partial \widetilde{C}}{\partial \eta} \right) \\
&+ \alpha\mu \frac{\partial}{\partial \xi} \left( D_x \frac{\partial \widetilde{C}}{\partial \xi} \right) + \alpha\mu \frac{\partial}{\partial \eta} \left( D_y \frac{\partial \widetilde{C}}{\partial \eta} \right) - \frac{\varepsilon}{H} \int_H w \frac{\partial C''}{\partial z} dz \\
&+ \mathcal{O}_1\left(\frac{\varepsilon\mu^2}{\beta}\right) + \mathcal{O}_1(\varepsilon\mu) + \mathcal{O}_2\left(\frac{\varepsilon\mu^4}{\beta}\right) + \mathcal{O}_2\left(\varepsilon\mu^3\right) \\
&+ \mathcal{O}_3\left(\varepsilon\mu^3\right) + \mathcal{O}_3\left(\varepsilon\beta\mu^2\right) + O\left(\mu^4, \beta^2\mu^2\right) \qquad (3.25)
\end{aligned}$$

where the $D_{Lij} = -\frac{1}{H} \int_H u''_i \int_{-h}^{z} \frac{1}{D_z} \int_{-h}^{z} u''_j dzdzdz$ is commonly called 'dispersion coefficient', in which the $u''_i$ is the $u''_{\phi i}$ or $u''_{ri}$. The $\epsilon$ is given by $\epsilon = (\mu^4/\beta, \beta\mu^2, \mu^3, \beta\mu^2)$ by the derivation.

As mentioned above, it is not possible to get a general solution for the $C''$. However, under the case of $O(\varepsilon) \ll O(\mu^2, \beta\mu)$, all the $\mathcal{O}$ terms can be neglected fortunately. If $O(\varepsilon) \sim O(\mu^2, \beta\mu)$ then the $\mathcal{O}_1$ term has the same magnitude with the $\epsilon$ terms. Thus, only when the spatial distribution of the $\widetilde{C}$ is steady state and vertically well mixed, the $\mathcal{O}_1$ can be removed, which results in Taylor's analysis. When $O(\varepsilon) \sim O(\mu, \beta)$, the $\mathcal{O}_1$ terms become bigger than $\epsilon$ terms so that should be considered.

Finally, by recovering the dimensions and depth averaging, the depth-integrated

transport equation can be given on the original coordinate as following.

$$\frac{\partial H\widetilde{C}}{\partial t} + \frac{\partial H\widetilde{u}_i\widetilde{C}}{\partial x_i} = \frac{\partial}{\partial x_i}\left(HD_{Lij}\frac{\partial\widetilde{C}}{\partial x_j}\right) + \frac{\partial}{\partial x_i}\left(HD_{xi}\frac{\partial\widetilde{C}}{\partial x_i}\right) \tag{3.26}$$

where the horizontal diffusion coefficients are given by $D_{xi} = \frac{\nu}{S_c} + \frac{\nu_t^h}{\sigma_t}$ with the Schmidt number $S_c = 1000$ (Hinterberger et al., 2007). The $D_{Lij}$ can be derived based on the vertical velocity profile of the Boussinesq equations. After mathematical exercise, it is given by

$$\begin{aligned}
D_{Lij} = & -\frac{\sigma_t}{C_h H^2 u_\tau}\left[\frac{1}{336}\left(\psi_i + \frac{\partial S}{\partial x_i}\right)\left(\psi_j + \frac{\partial S}{\partial x_j}\right)\left(\zeta^7 + h^7\right)\right. \\
& + \frac{1}{48}\left(\psi_i + \frac{\partial S}{\partial x_i}\right)\left(\frac{\partial T}{\partial x_j} - \zeta\psi_j\right)\left(\zeta^6 - h^6\right) \\
& + \frac{1}{30}\left(\frac{\partial T}{\partial x_i} - \zeta\psi_i\right)\left(\frac{\partial T}{\partial x_j} - \zeta\psi_j\right)\left(\zeta^5 + h^5\right) \\
& - \frac{7}{120}\left(\frac{\partial S}{\partial x_i} + \psi_i\right)\left(C_{4j} - C_2\psi_j\right)\left(\zeta^5 + h^5\right) \\
& - \frac{1}{6}\left(\frac{\partial T}{\partial x_i} - \zeta\psi_i\right)\left(C_{4j} - C_2\psi_j\right)\left(\zeta^4 - h^4\right) \\
& - \frac{1}{8}\left(\frac{\partial S}{\partial x_i} + \psi_i\right)\left(C_{5j} - C_3\psi_j\right)\left(\zeta^4 - h^4\right) \\
& + \frac{1}{6}\left(C_{4i} - C_2\psi_i\right)\left(C_{4j} - C_2\psi_j\right)\left(\zeta^3 + h^3\right) \\
& - \frac{1}{3}\left(\frac{\partial T}{\partial x_i} - \zeta\psi_i\right)\left(C_{5j} - C_3\psi_j\right)\left(\zeta^3 + h^3\right) \\
& - \frac{1}{6}\left(\frac{\partial S}{\partial x_i} + \psi_i\right)C_{1j}\left(\zeta^3 + h^3\right) \\
& + \frac{1}{2}\left(C_{5i} - C_3\psi_i\right)\left(C_{4j} - C_2\psi_j\right)\left(\zeta^2 - h^2\right) \\
& - \frac{1}{2}\left(\frac{\partial T}{\partial x_i} - \zeta\psi_i\right)C_{1j}\left(\zeta^2 - h^2\right) \\
& \left. + C_{1i}\left(C_{4j} - C_2\psi_j\right)\left(\zeta + h\right)\right]
\end{aligned} \tag{3.27}$$

where the $C_{1i} \sim C_{5i}$ are given by

$$
\begin{aligned}
C_{1i} &= h\left(C_{5i} - C_3\psi_i\right) - \frac{1}{2}h^2\left(C_{4i} - C_2\psi_i\right) \\
&\quad + \frac{1}{6}h^3\left(\zeta\psi_i - \frac{\partial T}{\partial x_i}\right) + \frac{1}{24}h^4\left(\frac{\partial S}{\partial x_i} + \psi_i\right) \\
C_2 &= \frac{1}{6}\left(2\zeta^2 - 2\zeta h - h^2\right) \\
C_3 &= \frac{1}{6}\zeta h\left(h + 2\zeta\right) \\
C_{4i} &= \frac{1}{6}\left(\zeta^2 - \zeta h + h^2\right)\frac{\partial S}{\partial x_i} + \frac{1}{2}\left(\zeta - h\right)\frac{\partial T}{\partial x_i} \\
C_{5i} &= -\frac{1}{6}h^3\frac{\partial S}{\partial x_i} + \frac{1}{2}h^2\frac{\partial T}{\partial x_i} + C_{4i}h
\end{aligned}
\tag{3.28}
$$

If the flow is uniform and the $\kappa/6 = 0.0667$ then the $\sigma_t = 0.8302\,(\sim O(1))$ makes the dispersion coefficient approach to the $D_L = 5.93hu_\tau$ proposed by Elder (1959) for turbulent flow. It may be a validation for the proposed dispersion coefficient.

## III.4. Numerical Method for the Transport Equation and Verifications

### III.4.1. Fourth-Order Accurate FVM

If the diffusion coefficient is zero, the transport equation becomes a hyperbolic partial differential equation mathematically. Thus the equation should be able to solve a continuous or a discontinuous concentration problem. However, it is hard to solve it numerically without dissipation or dispersive errors if the concentration profile is discontinuous or has a steep gradient. The FVM coupled with Riemann solvers is a good strategy for solving the discontinuous and continuous problems together. Moreover, in the view of eigen structure, the advection equation should have the same approximate Riemann solver with the equation of tangential velocity of homogeneous shallow water equations (Toro, 2002). Hence, the exactly same numerical method for

the flow equations can be used for the transport equation solver.

By integrating the transport equation over a cell, the equation becomes

$$\frac{\partial HC_{i,j}}{\partial t} + \frac{1}{A}\sum \boldsymbol{F}_k \cdot \boldsymbol{L}_k = 0 \tag{3.29}$$

where the subscripts $(i, j)$ are the cell index. The $A$ is a cell area, $\boldsymbol{F}$ is a flux vector evaluated at the cell interface, which is defined as $\boldsymbol{F} = CH\boldsymbol{U}$, $\boldsymbol{U} = (U, V)$, and $\boldsymbol{L}$ is a cell side vector defined as the cell side length multiplied by the outward unit normal vector. In order to construct the $C$ at the interface, a fourth-order compact MUSCL TVD scheme (Yamamoto and Daiguji, 1993) is used as followings.

$$C^L_{i+1/2} = C_i + \frac{1}{6}\left\{\Delta^*\overline{C}_{i-1/2} + 2\Delta^*\widetilde{C}_{i+1/2}\right\} \tag{3.30}$$

$$C^R_{i+1/2} = C_{i+1} - \frac{1}{6}\left\{2\Delta^*\overline{C}_{i+1/2} + 2\Delta^*\widetilde{C}_{i+3/2}\right\} \tag{3.31}$$

where subscript $i + 1/2$ and $i - 1/2$ mean the interfaces and $L$ and $R$ mean the left and right sides of a cell interface and

$$\Delta^*\overline{C}_{i-1/2} = minmod\left(\Delta^* C_{i-1/2}, b\Delta^* C_{i+1/2}\right) \tag{3.32}$$

$$\Delta^*\widetilde{C}_{i+1/2} = minmod\left(\Delta^* C_{i+1/2}, b\Delta^* C_{i-1/2}\right) \tag{3.33}$$

$$\Delta^*\overline{C}_{i+1/2} = minmod\left(\Delta^* C_{i+1/2}, b\Delta^* C_{i+3/2}\right) \tag{3.34}$$

$$\Delta^*\widetilde{C}_{i+3/2} = minmod\left(\Delta^* C_{i+3/2}, b\Delta^* C_{i+1/2}\right) \tag{3.35}$$

$$\Delta^{*}C_{i+1/2} = \Delta C_{i+1/2} - \frac{1}{6}\Delta^{3}\overline{C}_{i+1/2} \tag{3.36}$$

$$\Delta^{3}\overline{C}_{i+1/2} = \Delta\overline{C}_{i-1/2} - 2\Delta\overline{C}_{i+1/2} + \Delta\overline{C}_{i+3/2} \tag{3.37}$$

$$\Delta\overline{C}_{i-1/2} = minmod\left(\Delta C_{i-1/2}, b_1\Delta C_{i+1/2}, b_1\Delta C_{i+3/2}\right) \tag{3.38}$$

$$\Delta\overline{C}_{i+1/2} = minmod\left(\Delta C_{i+1/2}, b_1\Delta C_{i+3/2}, b_1\Delta C_{i-1/2}\right) \tag{3.39}$$

$$\Delta\overline{C}_{i+3/2} = minmod\left(\Delta C_{i+3/2}, b_1\Delta C_{i-1/2}, b_1\Delta C_{i+1/2}\right) \tag{3.40}$$

$$minmod(i,j) = sign(i)\max\left[0, \min\left\{|i|, sign(i)\right\}\right] \tag{3.41}$$

$$minmod(i,j,k) = sign(i)\max\left[0, \min\left\{|i|, sign(i), sign(i)k\right\}\right] \tag{3.42}$$

in which the coefficients $b_1 = 2$ and $1 < b \leq 4$ and more details of this numerical scheme are described in Yamamoto and Daiguji (1993).

By using the constructed interface values, the numerical fluxes are computed by the HLL approximate Riemann solver (Toro, 1997) because in preliminary tests, the HLL solver showed more stable results than the HLLC solver on complex topography if moving boundary is included in the computational domain. The HLL numerical flux is given by

$$\boldsymbol{F}_{i+1/2} = \begin{cases} \boldsymbol{F}_L, & 0 \leq S_L \\ \boldsymbol{F}_*, & S_L \leq 0 \leq S_R \\ \boldsymbol{F}_R, & 0 \geq S_R \end{cases} \tag{3.43}$$

where

$$\boldsymbol{F}_* = \frac{S_R \boldsymbol{F}_L - S_L \boldsymbol{F}_R + S_R S_L \left( \boldsymbol{U}_R - \boldsymbol{U}_L \right)}{S_R - S_L} \tag{3.44}$$

and the $S_L$ and $S_R$ are wave speed, and more details of the HLL approximate Riemann solver is well explained in Toro (1997) and Toro (2002).

For the discretization of the diffusion terms, a FVM is used also. A cell averaged value $\overline{C}_i$ is defined as

$$\overline{C}_i = \frac{1}{\Delta x} \int_{x_{i-1/2}}^{x_{i+1/2}} C(x) dx \tag{3.45}$$

and by substituting the cell averaged value into the Taylor series $C = C_{1+1/2} + xC'_{1+1/2} + x^2/2C''_{1+1/2} + x^3/6C'''_{1+1/2} + x^4/24C''''_{1+1/2} + \cdots$, then the cell averaged value can be expressed with the values defined at cell interfaces (Lacor et al., 2004). For example,

$$\overline{C}_i = C_{i+1/2} - \frac{\Delta x}{2} C'_{i+1/2} + \frac{\Delta x^2}{6} C''_{i+1/2} - \frac{\Delta x^3}{24} C'''_{1+1/2} + \cdots \tag{3.46}$$

where, the subscript $i$ means the index of a cell and $i + 1/2$ means the index of a cell interface. By the combinations of the Taylor series expansions, fourth-order accurate discretization equations can be obtained and used for the discretization of the diffusion terms.

$$C_{i+1/2} = \frac{7 \left( \overline{C}_{i+1} + \overline{C}_i \right) - \left( \overline{C}_{i+2} + \overline{C}_{i-1} \right)}{12} + O\left( \Delta x^4 \right) \tag{3.47}$$

$$C'_{i+1/2} = \frac{15\left(\overline{C}_{i+1} - \overline{C}_i\right) - \left(\overline{C}_{i+2} - \overline{C}_{i-1}\right)}{12\Delta x} + O\left(\Delta x^4\right) \tag{3.48}$$

### III.4.2. Time Integration

Third-order Adams-Bashforth predictor and the fourth-order Adams-Moulton corrector scheme are used for the time integration.

In predictor step,

$$C^{n+1} = C^n + \frac{\Delta t}{12}\left(23T^n - 16T^{n-1} + 5T^{n-2}\right) \tag{3.49}$$

In corrector step,

$$C^{n+1} = C^n + \frac{\Delta t}{24}\left(9T^{n+1} + 19T^n - 5T^{n-1} + T^{n-2}\right) \tag{3.50}$$

where $T$ is given by

$$T = -\frac{\partial HCU_i}{\partial x_i} - \Phi - \Phi^\nu + \frac{\partial}{\partial x_i}\left\{D_{Lij}H\frac{\partial C}{\partial x_j} + \left(\frac{\nu}{S_c} + \frac{\nu_t^h}{\sigma_t}\right)H\frac{\partial C}{\partial x_i}\right\} \tag{3.51}$$

where the $\Phi$ and $\Phi^\nu$ are the products by the dispersion and vorticity effects of the Boussinesq equations. They are given by

$$\begin{aligned}\Phi = \; - \;& \frac{\partial}{\partial x_i}\left[HC\left\{\left(\frac{\zeta^2 - \zeta h + h^2}{6} - \frac{z_\alpha^2}{2}\right)\frac{\partial}{\partial x_i}\left(\frac{\partial U_j}{\partial x_j}\right)\right.\right. \\ + \; & \left.\left.\left(\frac{\zeta - h}{2} - z_\alpha\right)\frac{\partial}{\partial x_i}\left(\frac{\partial hU_j}{\partial x_j}\right)\right\}\right]\end{aligned} \tag{3.52}$$

$$\Phi^\nu = \frac{\partial}{\partial x_i}\left[\psi_i HC\left\{\frac{z_\alpha^2}{2} - z_\alpha\zeta + \frac{(2\zeta^2 - 2\zeta h - h^2)}{6}\right\}\right] \tag{3.53}$$

The convergence error is defined as $\sum |C^{n+1} - C_*^{n+1}| / \sum |C^{n+1}|$ and it is required to be less than $10^{-4}$ to be converged in this study.

### III.4.3. 1D Linear Pure Advection

As a basic test, 1D linear pure advection problem was tested. A composite initial concentration profile is given by

$$C_o(x,0) = \begin{cases} 1, & 1 \le x \le 3 \\ x - 4, & 4 \le x \le 5 \\ -x + 6, & 5 \le x \le 6 \\ \cos\left\{0.5\pi(x-8)\right\}, & 7 \le x \le 9 \\ \exp\left\{-4.5(x-11)^2\right\}, & 10 \le x \le 12 \\ 0, & \text{elsewhere} \end{cases}$$

and it is advected by a uniform velocity of $1.0 m/s$. The uniform grid size $\Delta x = 0.05m$ and the courant number $C_r = 0.5$ were used. Figures 16 show the comparisons of the computed results and the analytical solutions at $t = 20$ second, that is after it was advected 10 time length of the each profile. In the simulation without the limiter, unphysical numerical oscillations were created at the edge of the rectangular shape concentration profile. However, the computed results agree well with the analytic solutions entirely and very limited undershoot below than zero was observed. With the limiter, the unphysical oscillations disappeared from the square shaped concentration. However, the sharp peaks were damped slightly by the limiter in the other profiles.

### III.4.4. 2D Advection and Diffusion

A pure advection problem was tested in a 2D space where the flow is rotating about the center of the domain with a constant angular velocity $0.314 rad/hr$. Thus it

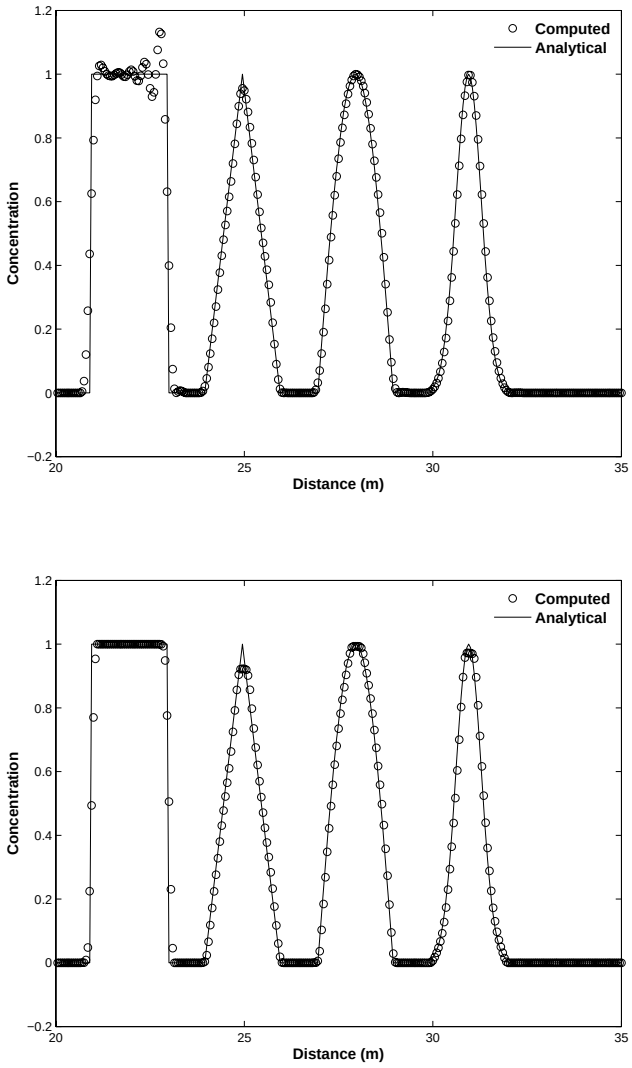


Figure 16. 1D linear advection results at $t = 20s$. Upper: without limiter, lower: with limiter.

rotates one circle per 20 hours. The initial concentration is given by

$$C_o(x,y) = \exp\left\{-\frac{(x-x_c)^2+(y-y_c)^2}{2\sigma^2}\right\} \tag{3.54}$$

where $x_c$ and $y_c$ are $1250m$ and $2500m$ and the $\sigma = 220m$. This advection problem was solved by Man and Tsai (2008) and the same numerical mesh size and computational time step were used here; $100 \times 100$ grids with $\Delta x = \Delta y = 50m$ and $\Delta t = 40$ second. The Figure 17 shows the initial conditions and the computed results at $t = 5$ hour, 30 hour and 55 hour. All the shapes look quite similar and sustained very well for about three circulations. After one circulation (at $t = 20$ hour), the maximum and minimum values are 0.9945 and $-9 \times 10^{-10}$. At $t = 60$ hour, that is, after three circulations, the maximum and minimum values are 0.9828 and $-6 \times 10^{-8}$, respectively. With smaller size grid $\Delta x = \Delta y = 25m$, the maximum and minimum values are 0.9997 and $-1 \times 10^{-10}$ at $t = 20$ hour and 0.9979 and $-7 \times 10^{-9}$ at $t = 60$ hour, respectively. Very small error, especially very small undershoot, was observed, thus it means excellent conservation property of the proposed numerical scheme. The Figure 18 shows the contour of the concentrations at the end of the one and three circulations and with different grid sizes and with different $\Delta t$. All the results are very similar, so it can be concluded that the proposed numerical scheme is not affected by the courant number and the grid size much. In addition, though the flow direction is not parallel or perpendicular to the grids, quite similar agreements with the analytical solutions were obtained. Therefore, the proposed model is expected to produce a good result under complex flow fields with cartesian grid system.

In the same flow field, advection-diffusion problem was tested. In this problem, the $\sigma = 200m$ and the diffusion coefficients $D_x = D_y = 0.1m^2/s$. The $\Delta t = 40$ second and $\Delta x = \Delta y = 50m$ were used as conducted by Man and Tsai (2008). Because the

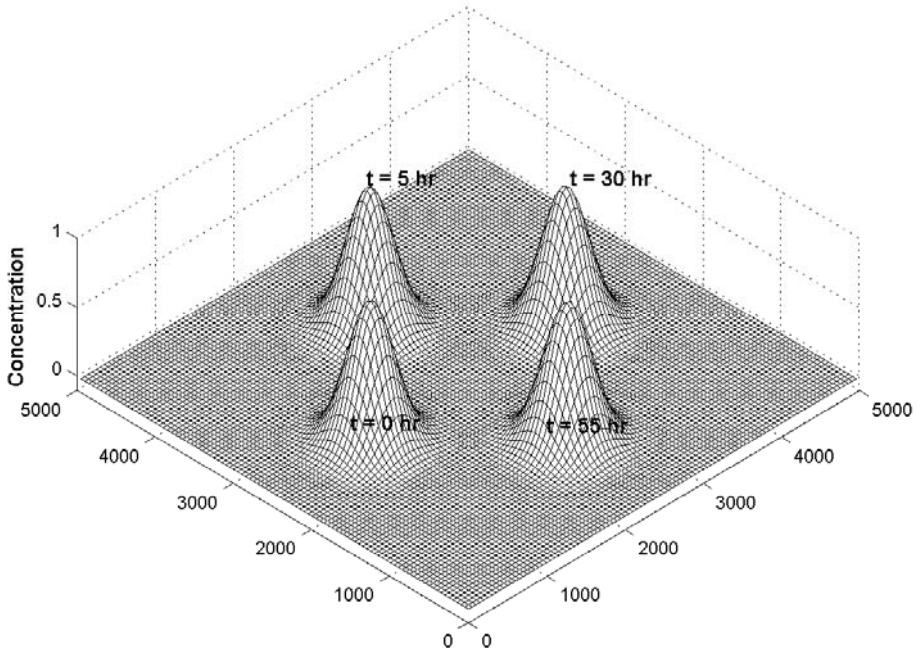


Figure 17. 3D view of computed results of pure advection test.

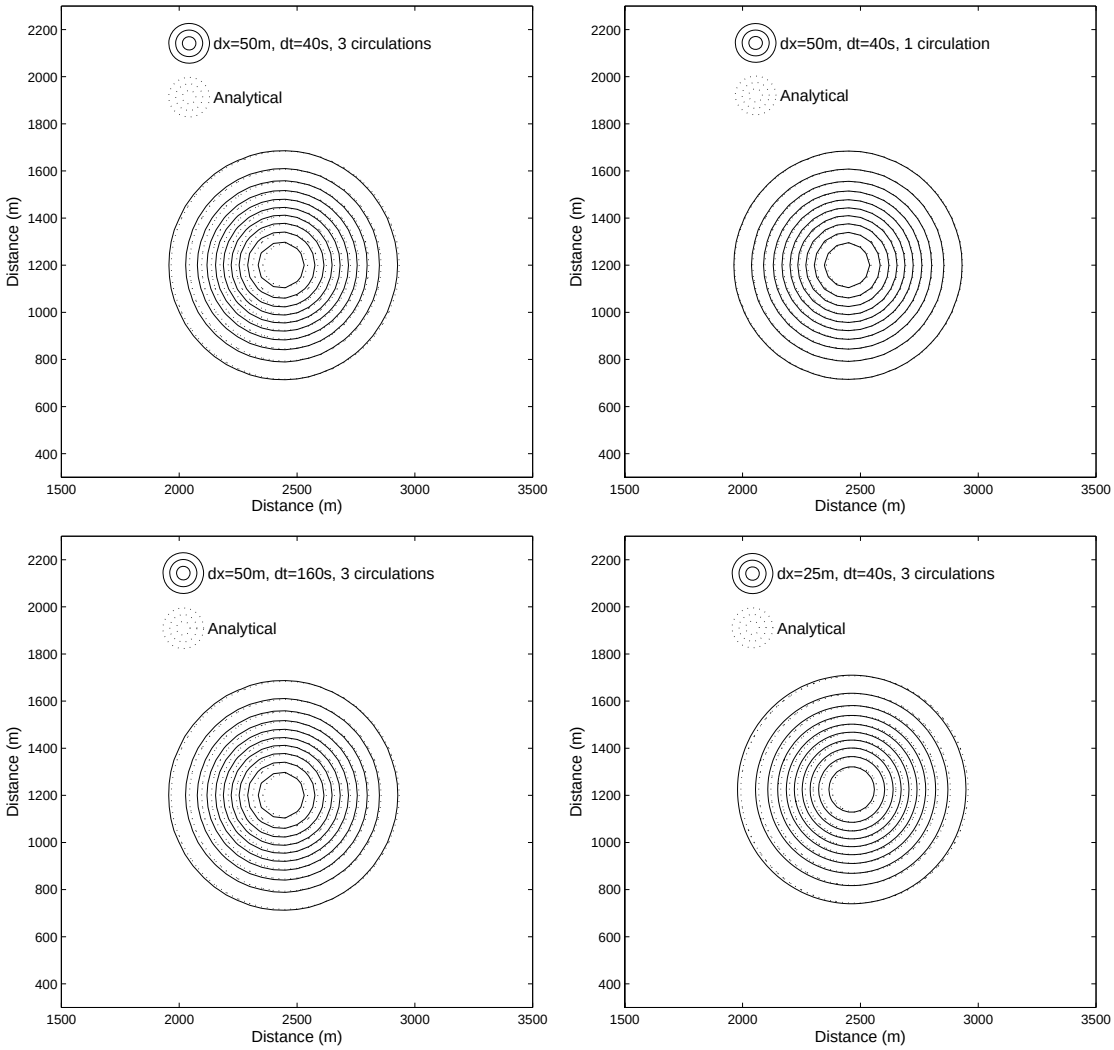


Figure 18. Contours of the concentrations with different computational conditions.

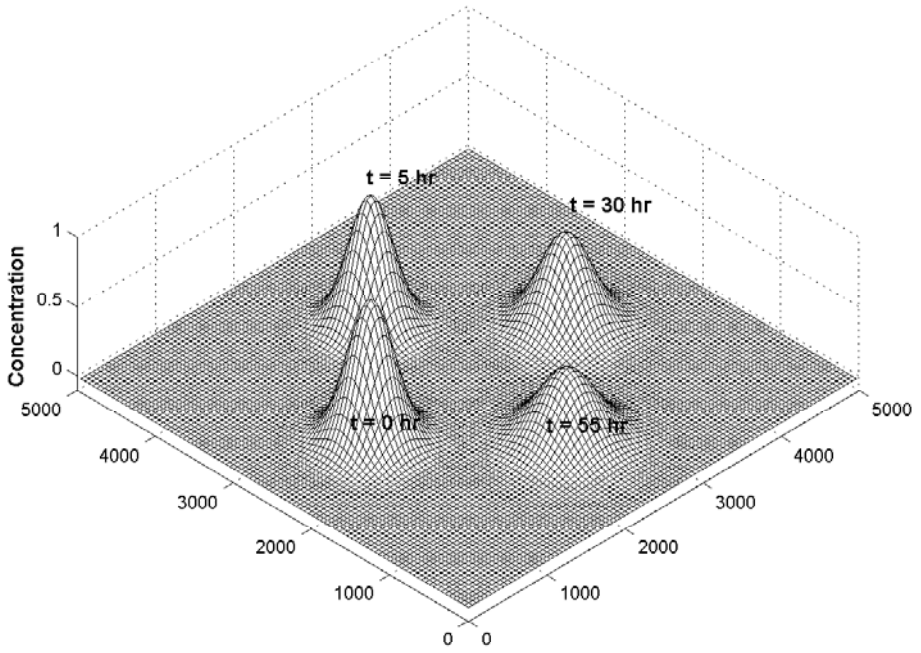


Figure 19. 3D view of computed concentrations of the 2D advection-diffusion test.

diffusion is included, the peak should decrease and the distribution should spread wider as time marches as shown in the Figure 19. The Figure 20 shows the computed and analytical profiles of the concentrations at the end of each circulation. The agreements are pretty good. Therefore the proposed numerical model seems to be good for the prediction of combined advection and diffusion in 2D spaces.

### III.5. Numerical Simulations for Turbulent Transport

Three typical generation mechanisms in shallow flows that lead to the development of 2D coherent structures were identified by Jirka (2001): 'topographical forcing', 'internal transverse shear instabilities' and 'secondary instabilities of base flow'. This

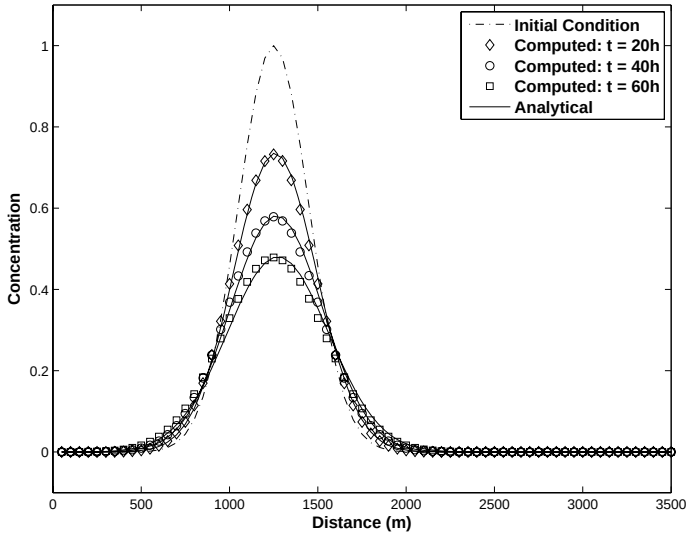


Figure 20. Concentration profiles of the 2D advection-diffusion test.

category is very useful for the validations of a numerical model for the turbulent transport. Especially, for the first two mechanisms, several experiments were studied well and so the results are used in this section. For the verification of quantity, a comparison study with a laboratory experiment is presented, too.

### III.5.1. Turbulent Transport by Internal Transverse Shear Instability

For the validation of the internal transverse shear instabilities, a flow in a plane mixing layer experimentally investigated by Babarutsi and Chu (1998) is simulated with the DISGS model. The dimension of the channel was $0.61m$ wide, $7m$ long and the water depth $h = 0.0296m$. The inflow section was divided halfway by a plate as shown in the Figure 21. At the upstream boundary, the velocity on one side of the plate was $u_1 = 0.111m/s$ and the velocity on the other side was $u_2 = 0.264m/s$, so the overall Reynolds number was about $Re = 5550$. For the numerical simulation,

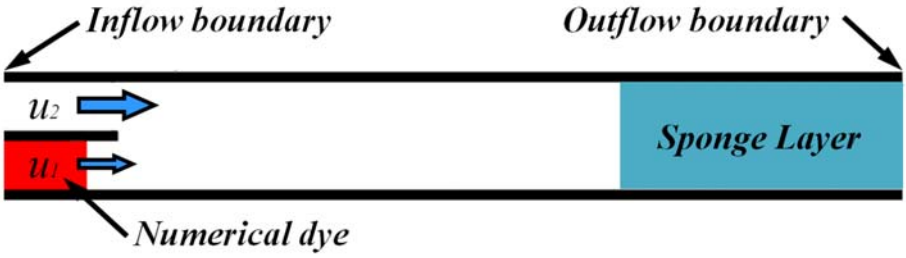


Figure 21. Mixing layer channel (plan view).

the grid size $\Delta x = \Delta y = 0.2h$, the $C_r = 0.5$ and the $C_B = 100$ were used. To minimize the downstream boundary effects, a sponge layer was added additionally at the downstream.

The Figure 22 shows the $\langle u \rangle$ (time mean velocity) and the $u'_{rms}$ (root mean square value of the velocity fluctuation in the streamwise direction) by the DISGS and the measurement. The discrepancy around the downstream end mainly resulted from the different downstream boundary conditions between the experiment and the numerical simulations, and from the freeslip condition at the side walls in the numerical model. However, the computed $\langle u \rangle$, the slope of the $\langle u \rangle$ profile into the transverse direction and the spreading rate of the mixing layer agree well with the experimental data in overall sense. These good agreements are observed again in the comparison of the $u'_{rms}$, so reasonable prediction of the energy transport and scalar mixing by turbulent flow are expected.

However, without the BSM, that is only with the hydrodynamic model, the spreading rate and the slope of the $\langle u \rangle$ do not agree with the experimental data as shown in the Figure 23. Especially, the value of the $u'_{rms}$ is too small and even the tendency is absolutely different: The computational results are continuously getting

bigger as flows toward the downstream unlike the experimental data. The main reason of the overall discrepancies resulted from that the strength of the horizontal shear of the numerical model without BSM is not strong enough to destabilize in the mixing layer. Therefore the 3D turbulence effects that has the magnitude of $\gamma^2$ in the equation (3.11) should be included in the case of destabilization by internal transverse shear.

By the visualization, the transformations of eddies which are physically related with the energy transport are observed. As shown in the Figure 24, the relatively large eddies begin to be generated from about $x = 0.2m$ and they grow bigger till about $x = 1.0m$. After they pass the section $x = 1.5m$, the large eddy is not created any more, the shape of the eddies is not sustained, and its structure becomes very irregular. These development of the eddies can be validated by looking into the 2D turbulent kinetic energy transfer in the Figure 25: In the upstream region, because the eddies coalesce each other around the centerline of the channel, the energy is extracted from the mean flow and it transfers to the large eddies located in the mixing layer. In the downstream region, the eddies break down and the turbulent kinetic energy is spread and dissipated. Considering the Figures 22 ($u'_{rms}$), 24 and 25 together, the validity of the present DISGS model can be recognized. Without the BSM, however, very regular eddy-shaped concentration distribution is observed as depicted in the Figure 24 and the size of the eddies are getting larger as flows to the downstream. In addition, the computational results without the BSM shown in the Figures 23 ($u'_{rms}$) and 25 are inconsistent with the experimental data quantitatively and even qualitatively as well. In conclusion, it is apparent that the BSM plays an important role for the turbulent transport in mixing layers, so it should be included to account the 3D turbulence effects for these cases.

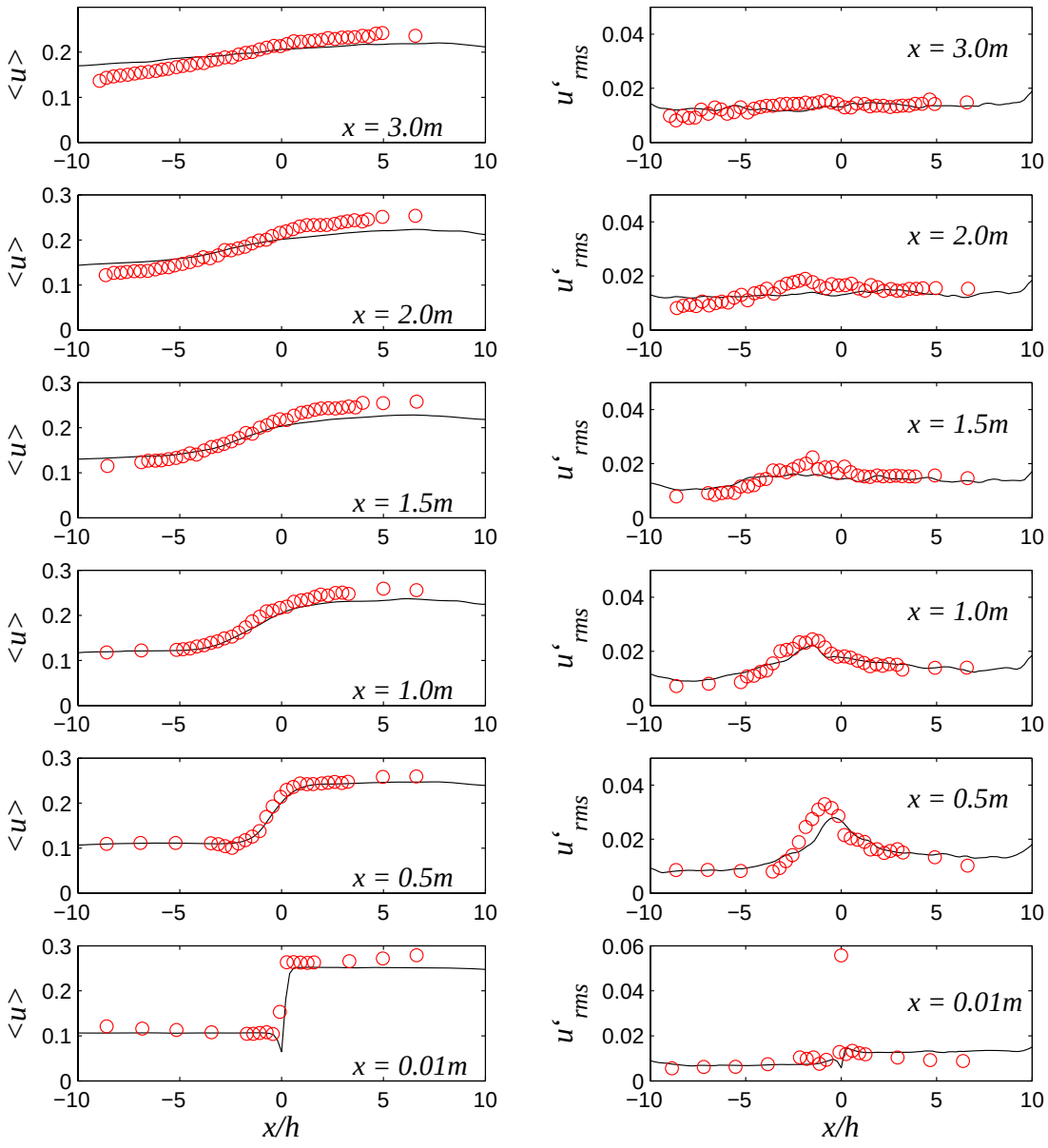


Figure 22. Comparisons of the DISGS results and experimental data. Left: time mean velocity $(m/s)$. Right: root mean square velocity $(m/s)$. Circle: experimental data (by Babarutsi and Chu ,1998), line: numerical results.

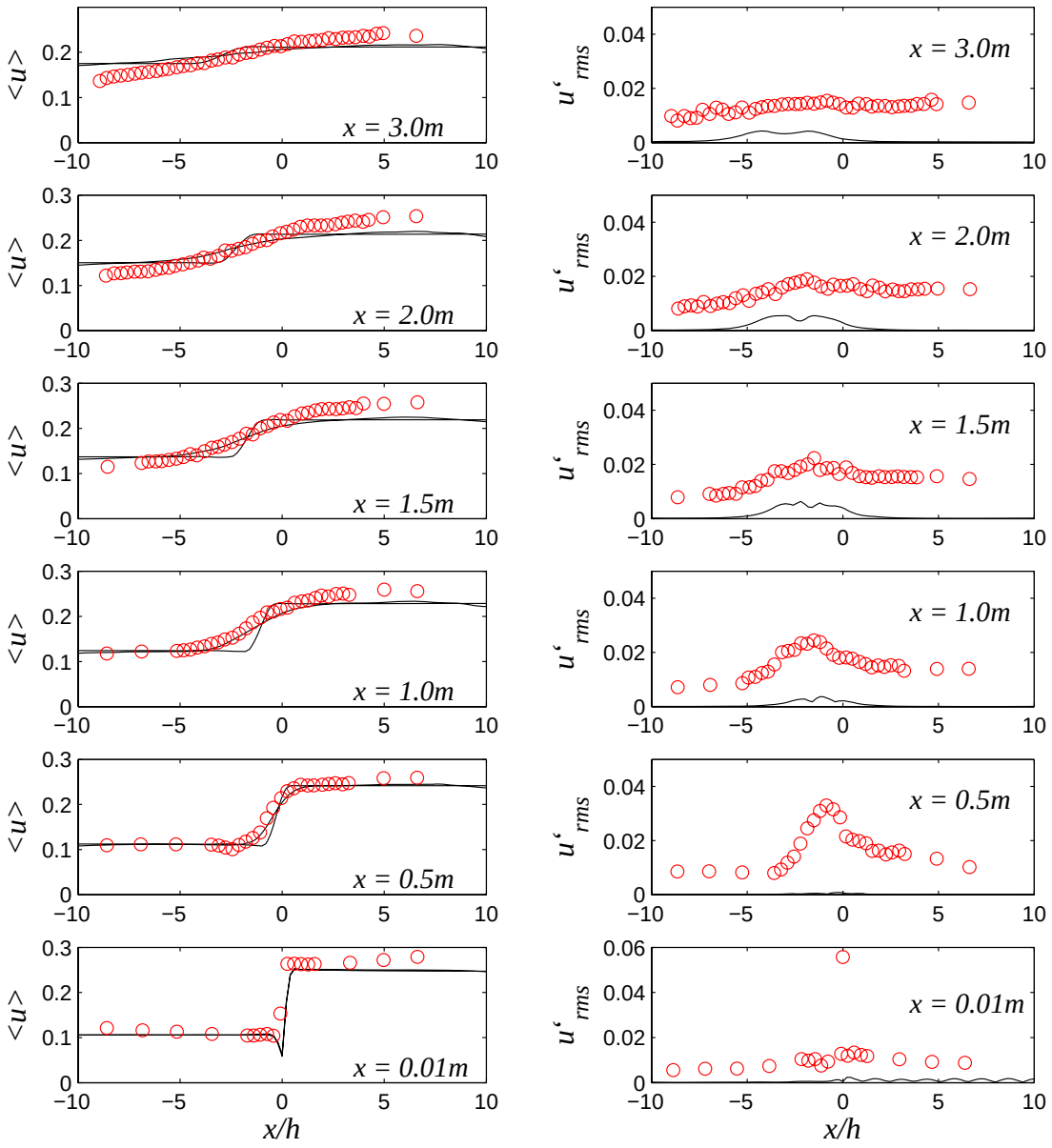


Figure 23. Comparisons of the numerical results without BSM and experimental data. Left: time mean velocity $(m/s)$. Right: root mean square velocity $(m/s)$. Circle: experimental data (by Babarutsi and Chu, 1998), line: numerical results.

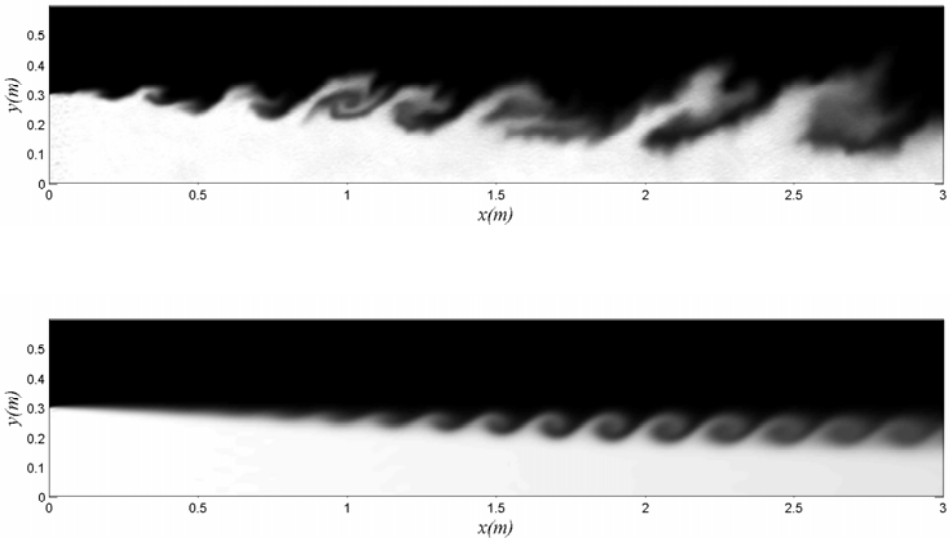


Figure 24. Computed concentration. Upper: by DISGS, lower: without BSM. $x = 0$ represents the locations of the end of the splitting plate.

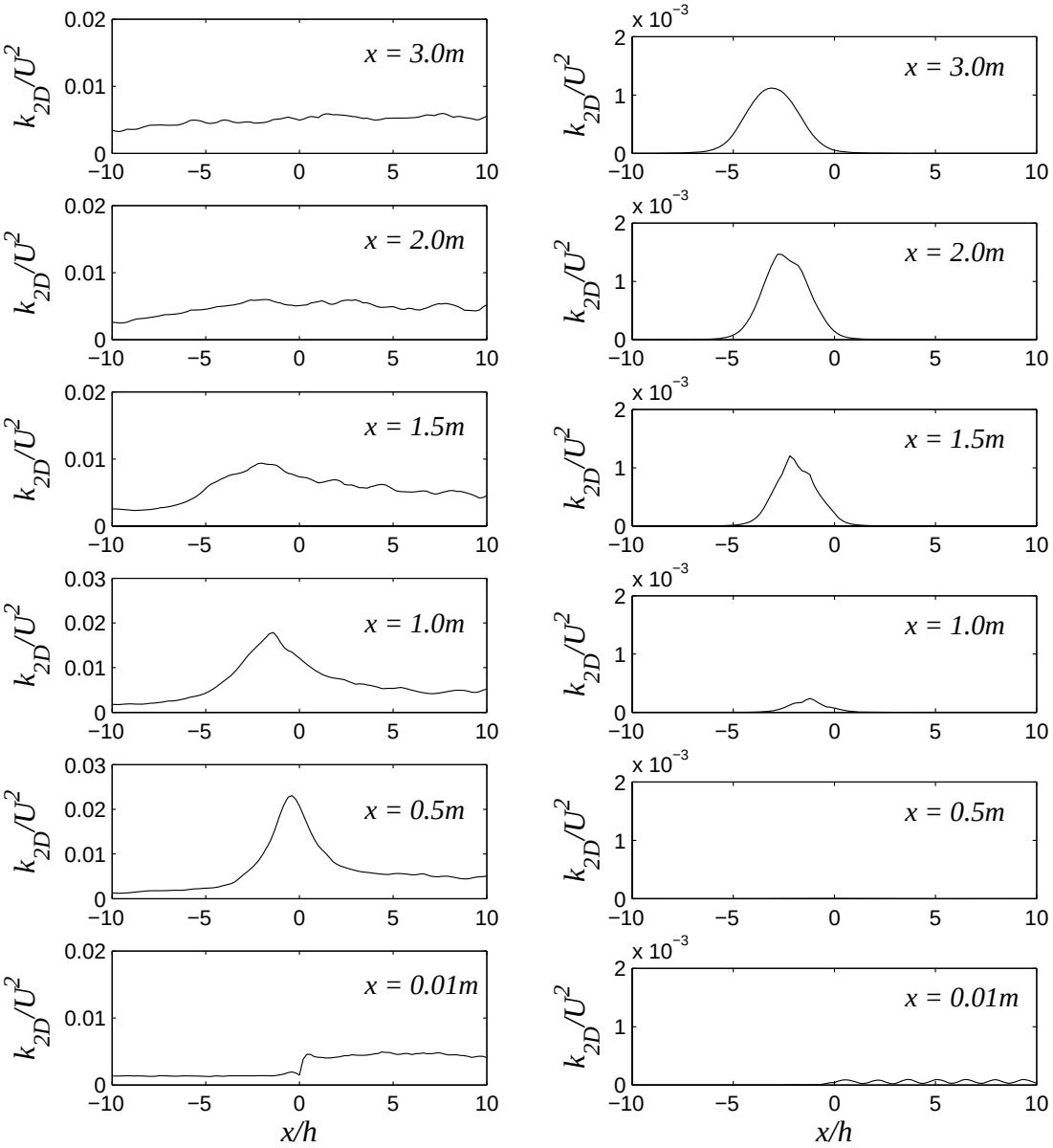


Figure 25. Computed 2D turbulent kinetic energy. Left: DISGS, right: without BSM.

### III.5.2. Comparison to Taylor's Theorem

Rummel et al. (2005) presented the results of an experimental study to determine the magnitude of mixing coefficient for a passive tracer plume in shallow open channel flow. Also they presented two analytical solutions for the near field and far field mixing based on the Taylor's theorem (1921). These results are compared with the numerical simulation results quantitatively in this section.

In the experiment done by Rummel et al. (2005), the channel length was $13.5m$ and the width was $5.5m$. The water depth was $h = 0.025m$ and the velocity was $U = 0.16m/s$, resulting in the $Re = 4000$. The bed friction coefficient was given by $f = 0.029$ from the experiment. The dye was injected through a $0.001m$ diameter tube into the streamwise direction constantly at the middepth. In near field, the analytical solution for lateral diffusion is given by

$$\langle \sigma_y^2 \rangle = \frac{\langle v'^2 \rangle}{U^2} x^2 \tag{3.55}$$

and in far field, it is given by

$$\langle \sigma_y^2 \rangle = 2 \langle v'^2 \rangle t_{iL} \frac{x}{U} \tag{3.56}$$

where the $\sigma_y^2$ is the lateral variance of the concentration and the $\langle v'^2 \rangle t_{iL}$ is the turbulent diffusion coefficient.

From the solutions, we can see that the $\sigma_y/h$ is a function of the transverse turbulent intensity $i_y = \left(\langle v'^2 \rangle / U^2\right)^{0.5}$ and proportional to $(x/h)$ in the near field and proportional to $(x/h)^{0.5}$ in the far field. Hence, numerical results should be related with the $i_y$ and should show the similar proportionality with the analytical solutions in

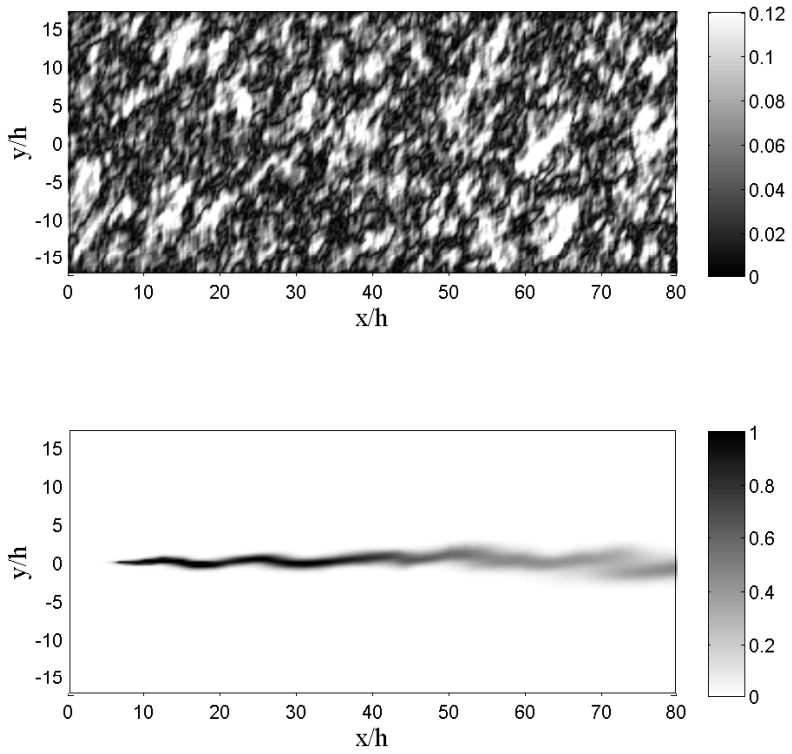


Figure 26. Instantaneous plot of the computed results by DISGS. Upper: turbulent intensity, lower: scalar concentration.

the near and far fields, respectively. In the laboratory experiment, the flow conditions resulted in the $i_y = 0.06$. In the numerical simulation, the $C_B = 70$ resulted in the $i_y = 0.06$ and randomly distributed scalar distribution as shown in the Figure 26.

The Figure 27 shows the characteristic plume half widths by the experiment and the numerical simulation with the $\Delta x = \Delta y = h/3$. In far field ($x/h > 10$), the slope (qualitative characteristic) and the width (quantitative characteristic) agree well each other. In near field, the slopes of the analytic solution and the numerical and experimental data show a little difference. It resulted from the limitation of 2D horizontal model. That is, in near field, the flow in numerical model is still 2D

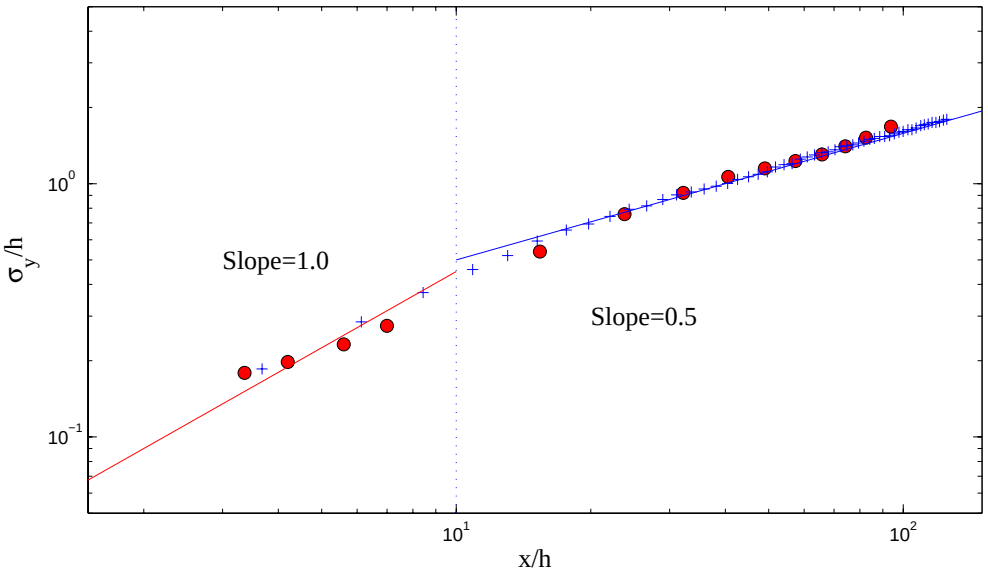


Figure 27. Normalized standard deviation $\sigma_y/h$ of the transverse concentration profiles (Logarithmic plot). Line: analytic (by Rummel et al, 2005), circle: computed, cross: measured (by Rummel et al, 2005).

motion in overall sense, but contains highly 3D small scale turbulence in real spaces which cannot be resolved by a 2D horizontal model. Looking back to the derivation of the depth-integrated transport equation, the $\mathcal{O}_1$ terms in the equation (3.25) were neglected with the assumption of $O(\varepsilon) \ll 1.0$. However, this assumption is not valid physically in the near field. Therefore, a different dispersion model specialized for the near field or a 3D model is required for more accurate near field mixing simulations.

### III.5.3. Mixing by Topographical Forcing

It is greatly important to investigate the effects of topography like islands to flows, because their effects that can cause instability and coherent structures are very strong (Jirka, 2002). Thus in this section, the mixing by the 2D coherent structures generated

by the typical islands is investigated.

For the investigation, the flows studied by a laboratory experiment and numerical model were selected. The laboratory experiment was conducted by Lloyd and Stansby (1997a, 1997b). The experimental setup was: The $0.049m$ high island with 8 degree side slope was installed at the $5.0m$ downstream from the inlet. The channel length was $9.75m$ and the width was $1.52m$. The outer radius and the inner radius of the island were $0.375m$ and $0.025m$, respectively. A steady streamwise flow with velocity $0.115m/s$ was released at the upstream boundary. Two different cases were tested. For the surface piercing island case, the water depth was $0.045m$ and for the submerged island case, it was $0.054m$. Thus the Reynolds numbers are $Re = 5175$ and $Re = 6210$, respectively. For the numerical simulation, the grid size $\Delta x = \Delta y = 0.01m$, the $C_B = 70$ and the $C_r = 0.5$ were used. For the scalar transport simulations, the numerical dye is injected at the $0.5m$ upstream of the island.

The computed results for the surface piercing island by the DISGS model are plotted in the Figure 28. The proposed model generated the large 2D coherent structures very well and their patterns look similar to the snapshot of the dye distributions in the Figure 29. However, in these cases named 'topographical forcing', the main generation mechanism of the 2D coherent structures is the separation from the topography. Thus the 2D coherent structures were also generated very reasonably without the BSM as shown in the Figure 30. Of course, into the Boussinesq equations model without BSM, the subdepth scale turbulence effects by the bottom friction such as the vertical eddy viscosity and the vorticity terms were incorporated.

For the submerged island case, the water depth was so shallow at the apex of the island that the separation was observed at the downstream lip of the horizontal apex and across the upper shoulder (Lloyd and Stansby, 1997b). Thus, the 2D coherent structure can be generated by the topographical forcing. The Figure 31 shows the

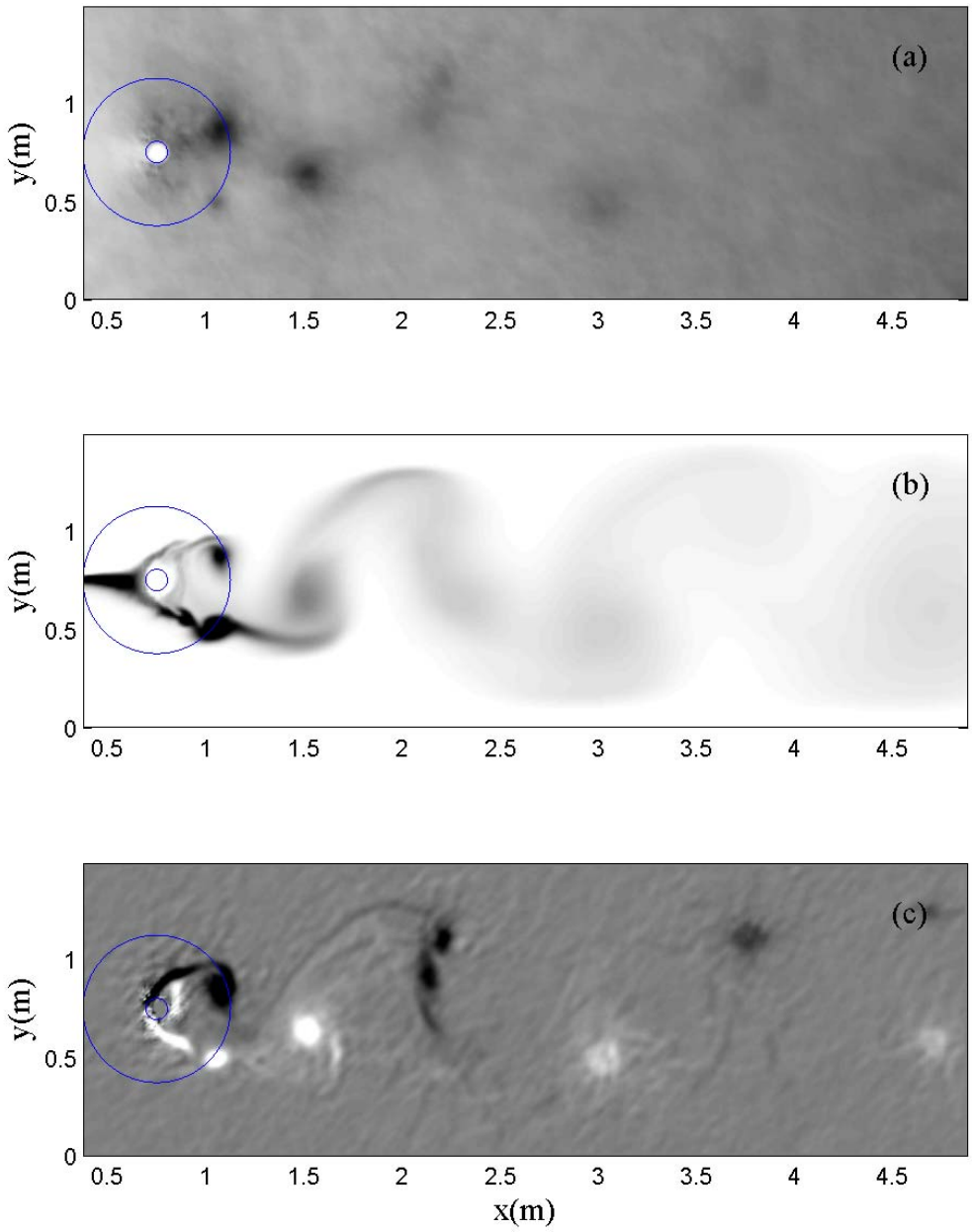


Figure 28. Computed results for surface piercing case by DISGS. (a) water surface elevation, (b) scalar concentration, (c) vertical vorticity.

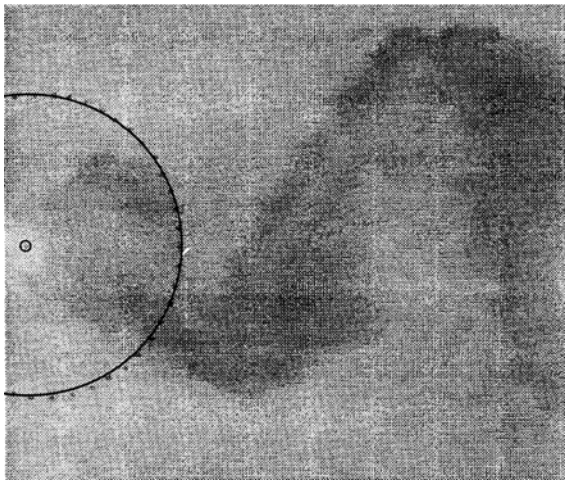

Figure 29. Dye visualization of wakes (by Lloyd and Stansby, 1997a). Surface piercing island case.

computed results by the DISGS model and the computed concentration looks similar to the experimental data in the Figure 32. Similar to the surface piercing case, the 2D coherent structures were generated very reasonably without the BSM as shown in the Figure 33. However, it will be very hard to decide whether the effects of the 3D turbulence is important or not in real applications, because the topography is so arbitrary. Hence it is recommended include the BSM for an important simulation. In conclusion, the proposed DISGS model is expected to be able to predict the mixing by topographical change under and over water surfaces which are very commonly observed in nature.

### III.6. Summary

For the turbulent transport by long waves and currents, the 3D turbulent effects were incorporated by a perturbation approach into the fully nonlinear Boussinesq

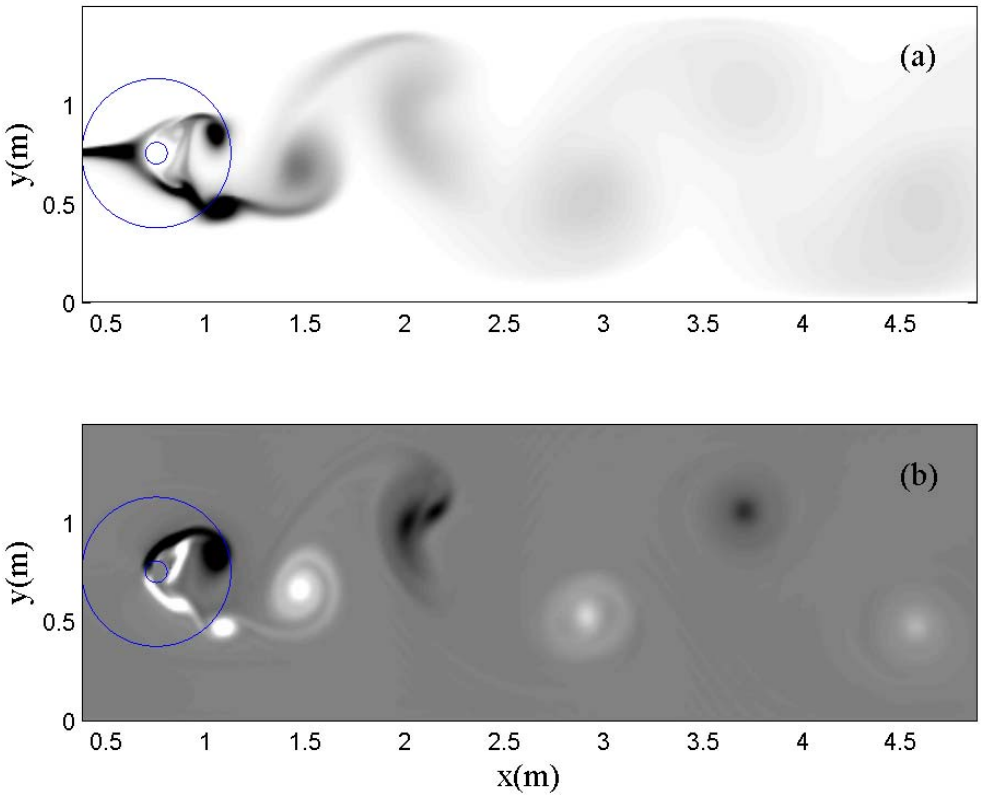


Figure 30. Computed results without BSM for surface piercing island case. (a) scalar concentration, (b) vertical vorticity.

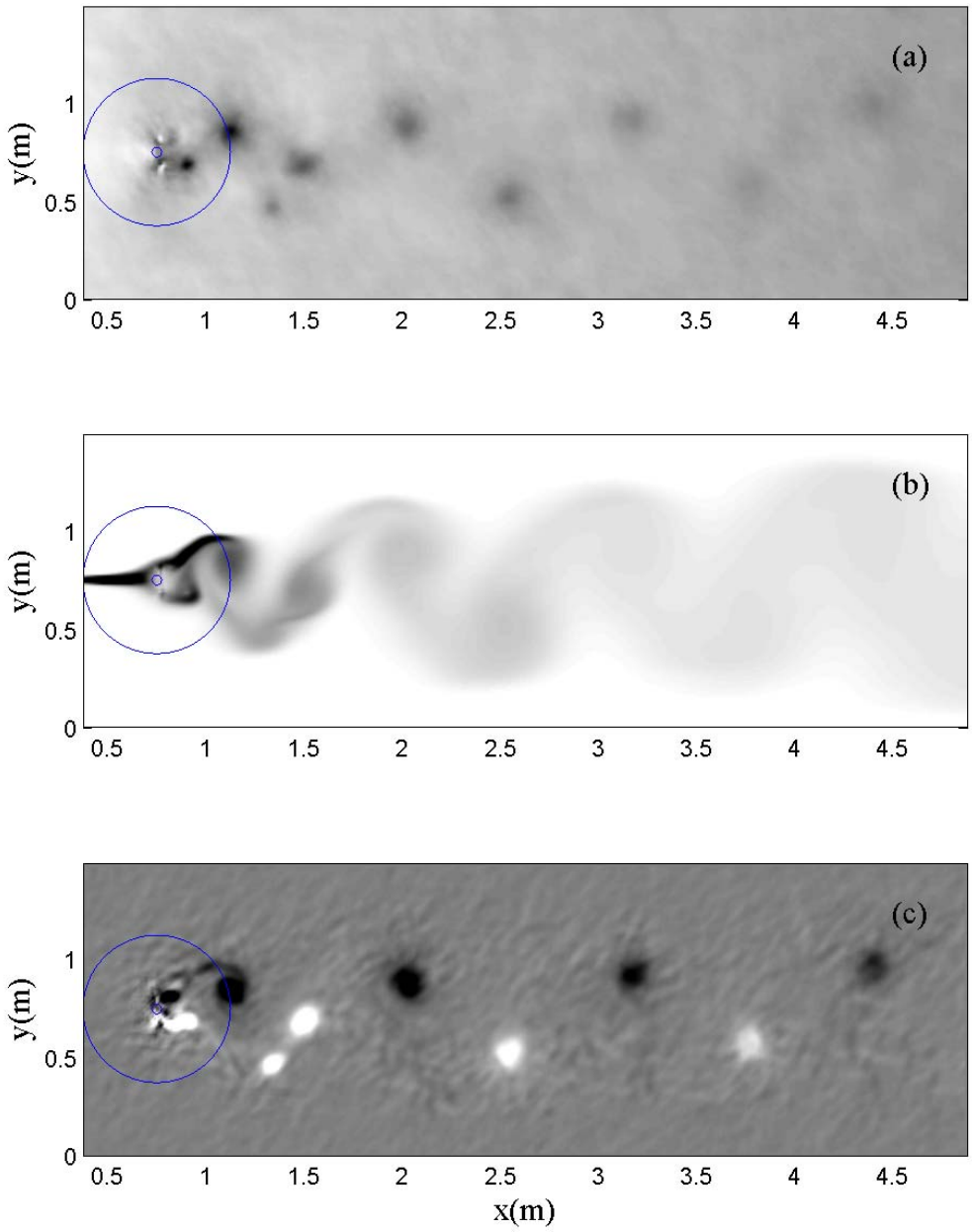


Figure 31. Computed results for submerged case by DISGS. (a) water surface elevation, (b) scalar concentration, (c) vertical vorticity.

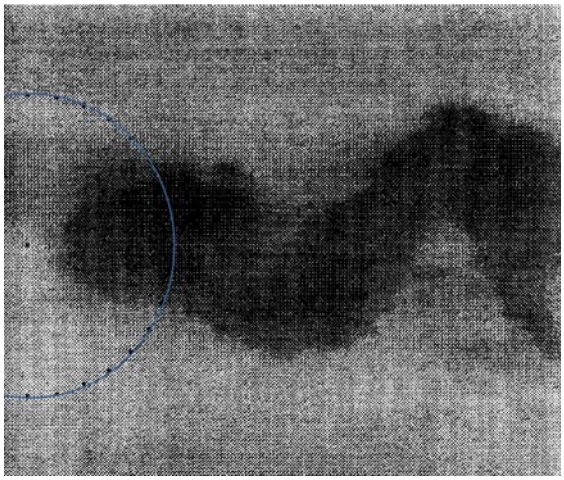

Figure 32. Dye visualization of wakes (by Lloyd and Stansby, 1997b). Submerged island case.

equations which are for weakly dispersive and rotational flow.

A depth-integrated scalar transport equations were derived by the same perturbation approach based on the long wave scaling for consistency. The dispersion coefficient was derived based on the vertical velocity profile of the Boussinesq equations.

The proposed equations were solved by a fourth-order accurate FVM. Several typical tests for the verifications of the scalar transport solver showed very good agreements with analytical solutions. Especially, very little error by numerical dispersion, dissipation and diffusion were detected.

From the mixing layer simulation with the stochastic BSM, the importance of the 3D turbulence effects to the turbulent transport was apparently proved. The comparisons with the Taylor's theorem showed that the proposed depth-integrated transport model coupled with the DISGS model has the consistency with the analytic

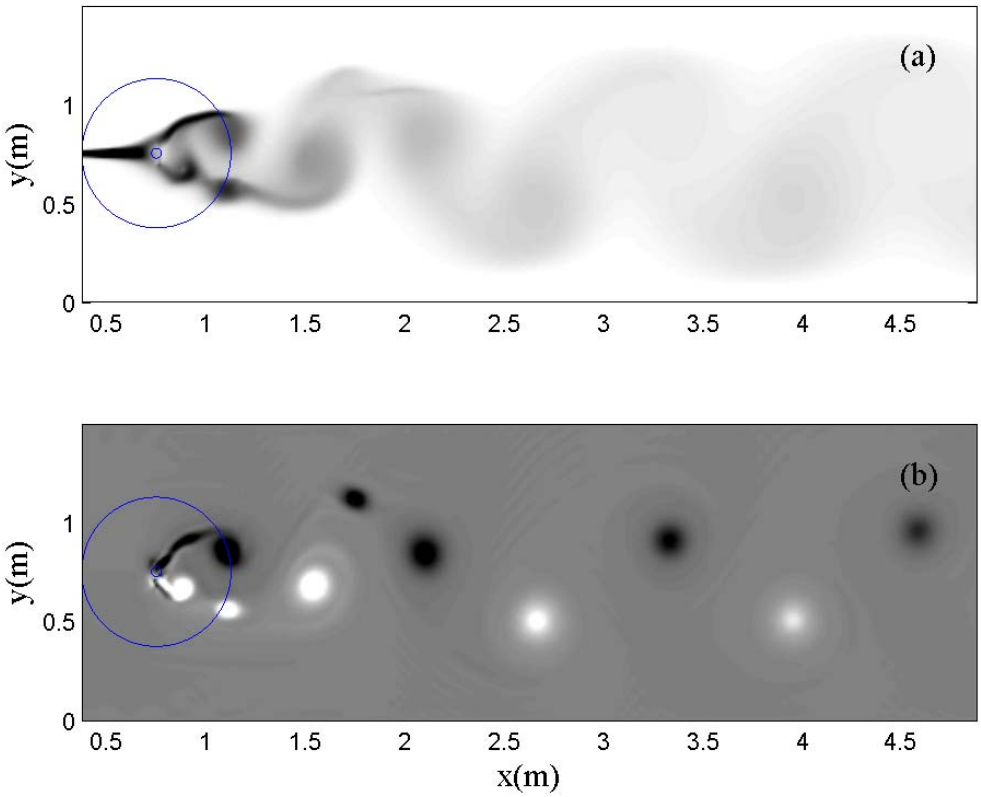


Figure 33. Computed results without BSM for submerged island case. (a) scalar concentration, (b) vertical vorticity.

solutions and the experimental data in far field. From the comparison in near field, the inherent limitation of the 2D horizontal model was recognized. In the simulations of the mixing by the bottom topography, the effects of the 3D turbulence effects were less important than the other cases.

# CHAPTER IV
# TOWARDS ENGINEERING APPLICATIONS: COMPLEX TOPOGRAPHY AND SHOCK CAPTURING

## IV.1. Introduction

In natural environment, somewhere the boundary of water body must interact dynamically with the dry land where we live on. One extreme example is the tsunami. When it is generated by an earthquake, a long wave propagates across the ocean and approaches to nearshore region while transforming itself by interacting with the bottom bathymetry. Over the shorelines, it runs up and sometimes overtops levees or islands, resulting in new waves or shocks regenerated by the overtopped waters or levee breaches. To model such a complex motion of flows, two requisites should be satisfied; a stable moving boundary scheme and a shock capturing scheme.

By many researchers, various moving boundary schemes for shallow water equations models were proposed and compared with experimental data and analytical solutions, for example, Liu et al (1995), Titov and Synolakis (1995), Kim et al. (2004), Kobayashi and Wurjanto (1989) and Hu et al. (2000). Commonly very good agreements were observed in the results. The numerical solvers of the shallow water equations are very stable and accurate for the very long waves within short propagation distance. However, we cannot expect reasonable prediction unless the waves are nondispersive, the waves travel short distance or the pressure is hydrostatic. Hence, we have to seek another solution, the Boussinesq equations model.

Unfortunately, only a few moving boundary schemes focused to runup studies were developed for the Boussinesq equations model and tested, for example, Madsen et al. (1997) and Lynett et al. (2002). Moreover, for the overtopping which

includes run down or re-entrance process, only more limited studies were done like Stansby (2003), who proposed 1D Boussinesq equations model equipped with moving boundary scheme. One possible reason for this is that the Boussinesq equations model, with its attractive ability to simulate dispersive wind waves, generally requires a complex numerical scheme for accuracy, a numerical scheme that does not readily lend itself to capturing the complex flow patterns (e.g flow re-entrance on the lee side of a levee) common with overtopping. Finally, it resulted in the limitations of the practical applications of the Boussinesq modeling.

The undular bores observed at the front of a tsunami or tide in nearshore area can be generated by a collapse of a dam, too. The dam-break flow, usually very long wave, has been important issue to hydraulic engineers from very long time ago, because it can cause a catastrophic disaster. To find the countermeasures, lots of laboratory experiments, mathematical and numerical studies were done by many research groups, for example the IMPACT project (2004), Toro (2002) and Kim et al. (2008).

In a typical study for the dam-break flows, the initial condition is given like the Figure 34(a): Where two stationary water bodies are separated by a dam and the dam is assumed to be removed instantaneously. For the numerical simulation of the dam-break flows, the shallow water equations set was the most popular choice. The shallow water equations model assumes that the pressure is propositional only to the water depth and the vertical velocity is small enough to be ignored. With those assumptions, the shallow water equations model can predict a surge and a rarefaction wave as shown in the Figure 34(b).

However, the undular bores in the Figure 34(c) which cannot be predicted by the shallow water equations model are frequently observed in nature. For example, in the Main-Danube navigation canal, secondary waves with a wavelength of about

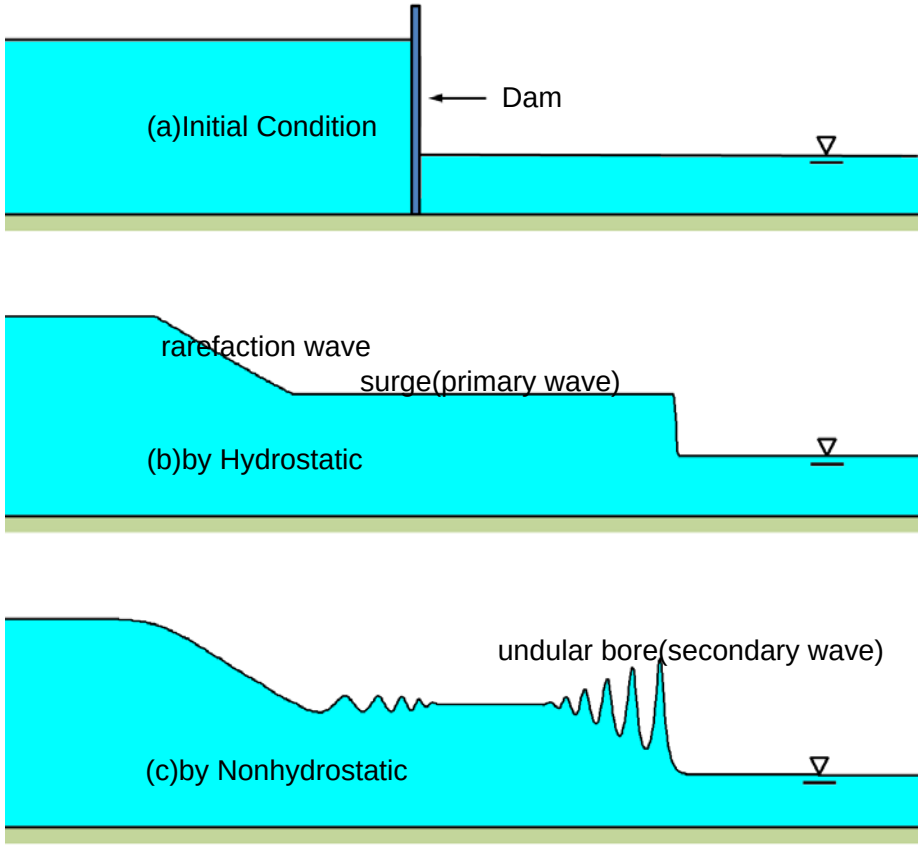


Figure 34. Schematics of water surface profiles in a typical dam-break problem, (a) initial condition, (b) profile by hydrostatic theory, (c) profile by nonhydrostatic theory.

$100m$ and amplitudes of up to $\mp 0.5m$ produced by the operation of lock gates were observed (Treske, 1994). By nature, undular bores can be generated and observed in coastal areas frequently. Tidal bores are regularly observed at many estuaries like the Qiantang River in China and the tsunami wave fission has been observed occasionally. These undular motions can arise many practical engineering problems of the freeboard height, overtopping or inundation. Besides, in the view of numerical methods, its computational condition can be so severe due to the shock.

To simulate the undular bores, the nonhydrostatic effects and shock capturing technique should be considered. Soares (2002) described how the nonhydrostatic effects can generated the undular bores conceptually. Here, it is explained mathematically. During the derivation of the fully nonlinear Boussinesq equations, the pressure term is expressed as

$$\begin{aligned} \frac{p}{\rho} &= \zeta - z + \frac{1}{2}\left(z^2 - \zeta^2\right)\frac{\partial S}{\partial t} + \left(z - \zeta\right)\frac{\partial T}{\partial t} \\ &+ \frac{1}{2}\left(z^2 - \zeta^2\right)\boldsymbol{U}\cdot\nabla S + \left(z - \zeta\right)\boldsymbol{U}\cdot\nabla T \\ &+ \frac{1}{2}\left(\zeta^2 - z^2\right)S^2 + \left(\zeta - z\right)TS \end{aligned} \tag{4.1}$$

As can be seen from the equation (4.1), the pressure depends not only on the water depth but also on the spatial and time variations of many variables like the water velocity and the water depth. Because the dam-break flows and the tidal bores are strongly transient and nonuniform, all the terms of the right hand side of the equation (4.1) cannot be negligible but can be significant under some specific situations.

For the case of the typical dam-break flows which is induced by sudden removal of dam, Mohapatra and Chaudhry (2004) investigated the effect of nonhydrostatic

pressure distribution with a Boussinesq equations model. They solved the equations with a fourth-order explicit FDM. In their results, the computed water surface profiles had undulations when the depth ratio $\epsilon_r$ (initial downstream water depth/initial upstream water depth) was greater than 0.4. Carmo et al. (1993) conducted dam-break flow experiments with the condition of $\epsilon_r > 0.5$ and observed undular bores at the downstream of the dam. They compared the experimental data and the computed results based on a Serre equations model. Mignot and Cienfuegos (2008) applied a 1D Boussinesq equations model including wave breaking energy dissipation to the flows including a shock. However, their applications were not for undular bores.

Undular bores generated by a sudden release of a constant discharge were investigated by Soares and Zech (2002b) with an experiment and a numerical method. They solved the 1D Boussinesq equations with a hybrid (FVM/FDM) numerical scheme. Soares and Guinot (2008) proposed a modified hybrid scheme to solve the Boussinesq equations in 1D space on a horizontal bed. Good agreements were obtained.

Soares and Zech (1998, 2002a) presented a 2D experimental data set and numerical results of a dam-break flow in a channel with a 90-degree bend. Their numerical model was based on the shallow water equations and solved by a FVM. They showed that the 1D approach revealed the expected limitations, while the 2D approach provided more physical prediction and rather satisfactory information. Naturally, as a next progress, a 2D Boussinesq modeling which is stable enough to be applied the dam-break flows is investigated in this study.

In this chapter, a simple but robust moving boundary scheme for Boussinesq modeling is presented. Various verification tests are conducted and the results are discussed. For the test of the applicability to the dam-break flows and undular bores, several benchmark problems are simulated using a fully nonlinear Boussinesq equations model in 1D and 2D spaces.

## IV.2. Moving Boundary Scheme

In this section, a new moving boundary scheme based on simple physical conditions is proposed. Essentially it follows the approach proposed by Liu et al. (1995) except for one condition described below. As shown in Figure 35(a), if the water surface level at $i$ is lower than the level of the dry bed at $i+1$, then the variables at $i+1/2$ are evaluated by assuming that there is a wall at $i+1$. Here the $i$ index represents a spatial cell location. On the other hand, if the water surface level at $i$ is higher than the level of the dry bed at $i+1$, as in Figure 35(b), the water is supposed to flow into the cell $i+1$. Note that this moving boundary scheme assumes discontinuous bottom topography, so the modified surface gradient method that can be applied on discontinuous bottom topography should be used (Kim et al., 2008). Without employing such a method, nonphysical oscillations can be created at the boundary of the wet and dry bed.

A physical constraint is added to the scheme, determined largely from experience in using it. Similar to other moving boundary schemes (e.g. Lynett et al. 2002), some minimum allowable total water depth must be chosen. When the total water depth is very small, the computed velocity can become very large, often due to a poor representation of bottom friction for these cases, causing the required time step for stability to plummet. Here, if the total water depth is less than $\epsilon_h$, then the computed velocity is set to zero. For idealized flow simulations on a simple bottom, $\epsilon_h$ can be less than $1 \times 10^{-6} m$ or less. However, for complex flow simulations, $\epsilon_h = 1 \sim 2 \times 10^{-4} m$ is recommended.

However, for a particular situation, a disconnected case, shown in Figure 36, nonphysical and unstable computations can occur even if the above described moving boundary scheme is implemented correctly. In Figure 36(a), physically, the water at

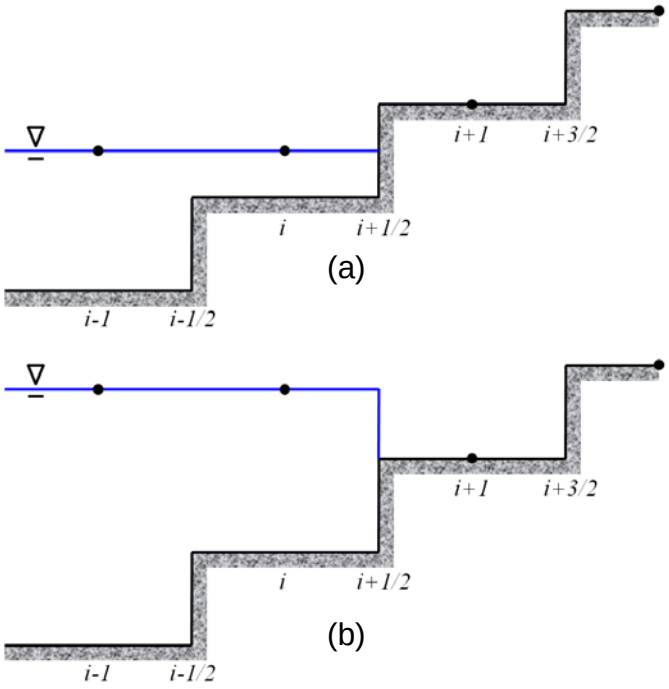


Figure 35. Schematic diagram of moving boundary scheme.

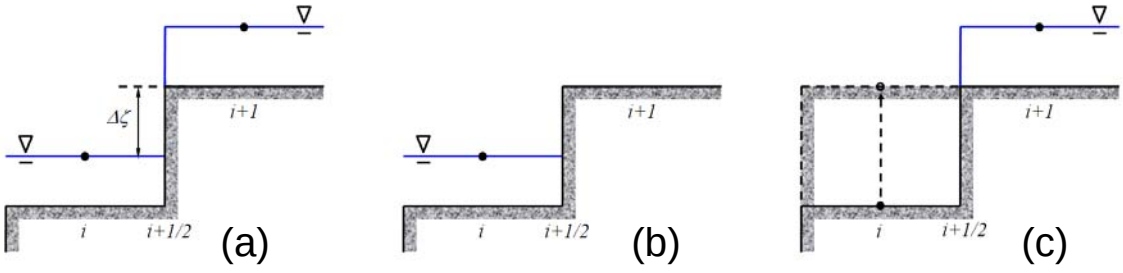


Figure 36. Schematic diagram of moving boundary scheme for disconnected case.

cell at $i$ must not affect the flow at $i+1$, but the water at $i+1$ can affect the flow at $i$. Therefore, in order to reflect this particular situation in the numerical model, the flux at $i+1/2$ is divided into two parts following the Figure 36(b) and (c). The fluxes for each interface side are calculated independently, and then combined. In detail, in one-dimensional space,

1. Divide the case (a) into (b) and (c) as in figure 36.
2. For the case of (b), compute the fluxes for cell $i$ as if there was a vertical wall at $i+1/2$.
3. For the case of (c), assume the bottom level of cell $i$ to be the same with the bottom level of cell $i+1$, and compute the fluxes of the cell $i+1$ (as if on flat bed).
4. Sum the computed fluxes at $i+1/2$ from case (b) and (c), and use that total flux in the application of the governing equations for cells $i$ and $i+1$.

With this moving boundary scheme, all equations are solved directly without extrapolations as used in Lynett et al., (2002), for example. Thus, it is anticipated that physical solutions with less loss of mass can be obtained and overtopping of steep walls can be solved as well.

Small numerical oscillations may be still created at the shoreline where flow is particularly energetic, and is typically due to the dispersive terms, and their high-order expression. To get rid of the unwanted numerical oscillations, a combination of shallow water equations and Boussinesq equations is used. In this study, if one or more of the three cells to the left or three cells to the right have the total water depths less than $\epsilon_h$, the shallow water equations are solved; otherwise Boussinesq equations are employed. This criterion is physically reasonable as, in shallow water, that is

near the shoreline, depth-integrated flow properties can be reasonably predicted by the conventional nonlinear shallow water models. Note that this moving boundary scheme can be applied to the transport equation as well.

## IV.3. Tests of the Moving Boundary Scheme

In this section the performance of the proposed moving boundary scheme is tested. Note that no modification and smoothing of the bathymetry were done for all numerical simulations in this dissertation.

### IV.3.1. Solitary Wave Runup and Rundown

For the verification of the moving boundary scheme, one of the most commonly-compared solitary wave runup and rundown data set, investigated experimentally by Synolakis (1987), is used. In Synolakis' experiments, the beach slope was 1:19.85 and various wave nonlinearities $\varepsilon_n$, the wave height to depth ratio, were tested. To compare with the measurement data, a nonbreaking wave with $\varepsilon_n = 0.04$ and a breaking wave with $\varepsilon_n = 0.28$ are simulated; this solitary wave breaks before reaching the shoreline. For the numerical simulations, $\Delta x = 0.3m$, $C_r = 0.5$ and, for the bottom friction, $k_s = 0.1mm$ were used. During the breaking wave runup simulation, the breaking dissipation term $R_b$ (Kennedy et al, 2000) is incorporated into the momentum equations. The computed results are compared with the measured data by Synolakis (1987) in Figure 37 and Figure 38. The proposed moving boundary scheme produces very good agreement and stable results for both the runup and rundown process. These comparisons provide a measure of confidence that the moving boundary scheme can reproduce well-controlled, small-scale measurements.

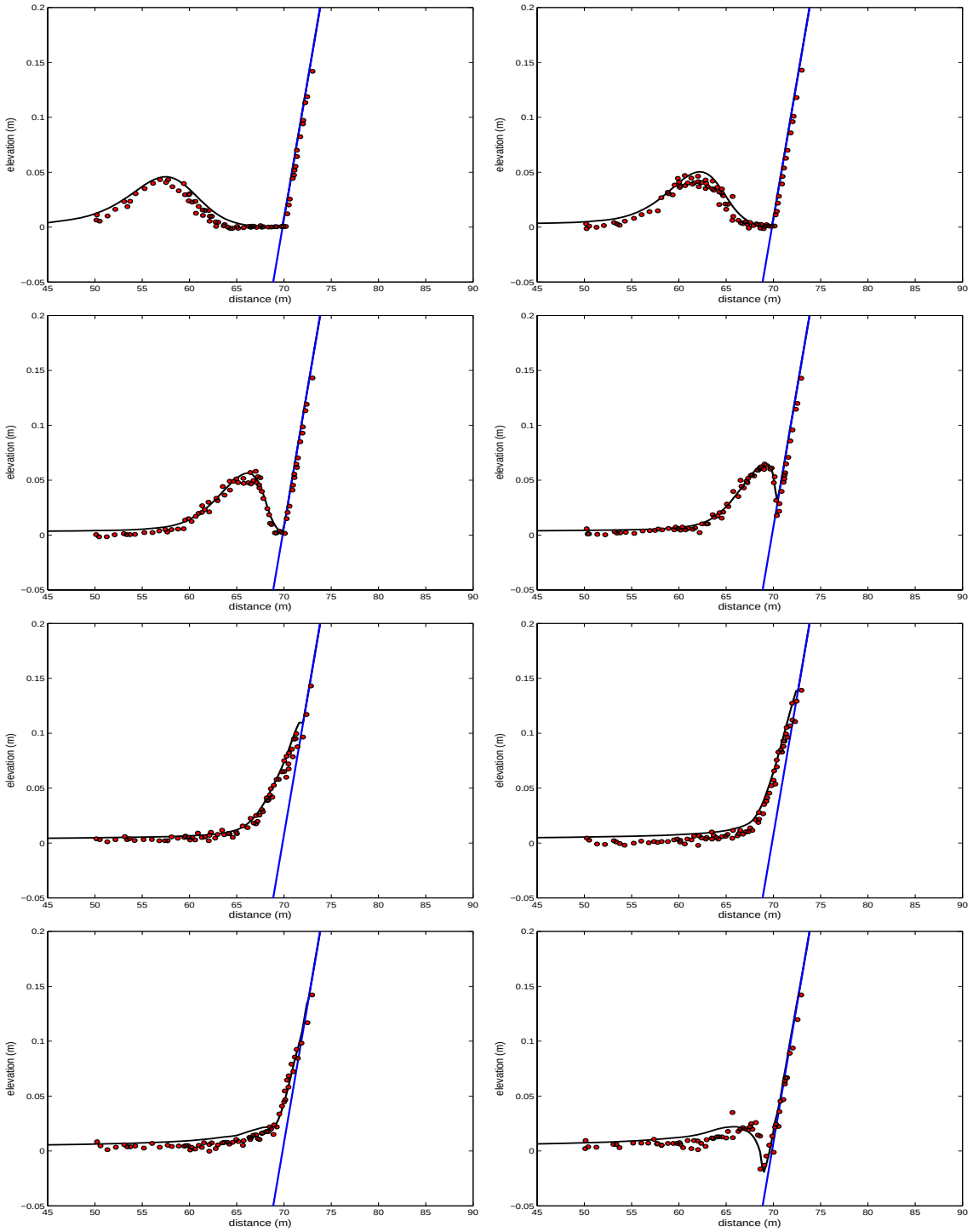


Figure 37. Water surface profiles for runup and rundown process. Nonbreaking case ($\varepsilon_n$=0.04). Line: numerical results, dot: experimental data (by Synolakis, 1987).

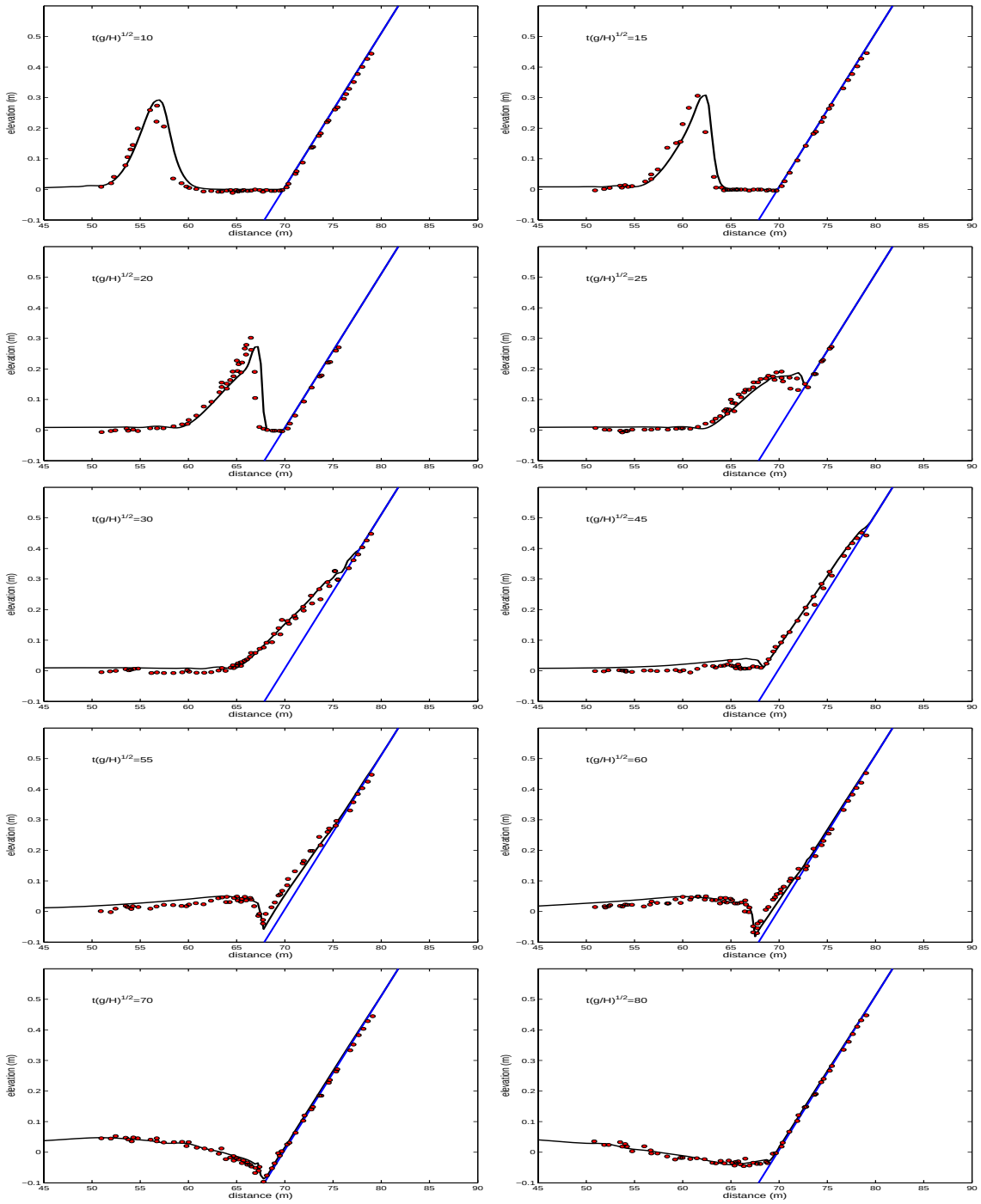


Figure 38. Water surface profiles for runup and rundown process. Breaking case ($\varepsilon_n$=0.28). Line: numerical results, dot: experimental data (by Synolakis, 1987).

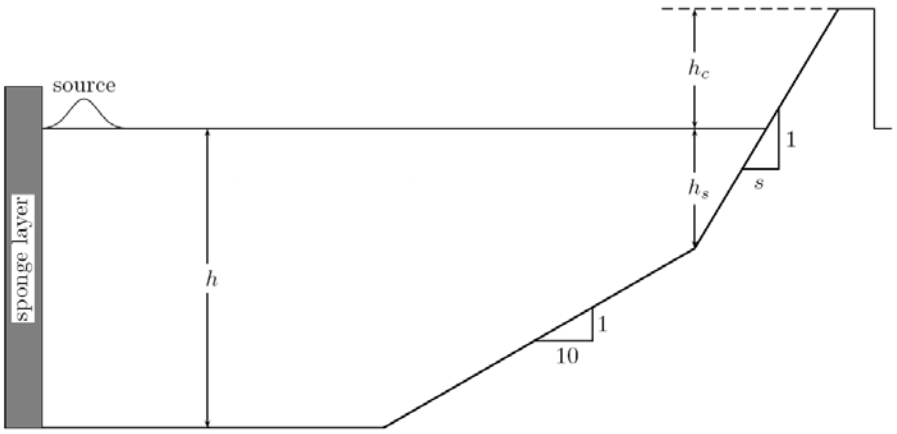


Figure 39. Laboratory experiment setup of BEB.

### IV.3.2. Sinusoidal Wave Overtopping

Here, overtopping experimental data reported in Saville (1955) are compared with computational results. The experiment was conducted by the Beach Erosion Board (BEB). The flume was made of concrete and was $36.6m$ long, $1.52m$ wide, and $1.52m$ deep. At upstream side, a wavemaker was used for sinusoidal wave generation. At the downstream end of the flume, levee structures were built. A structure with slope $1 : s$ was fronted by a fixed $1 : 10$ sloped floor. The setup of the waves and the structures are summarized in the table 2 and the Figure 39.

In the numerical simulations, the sinusoidal wave is generated using an internal source generator combined with the sponge layer on the upstream boundary. $\Delta x = 0.05m$, $C_r = 0.5$, and $k_s = 0.0006m$ are used and the overtopping fluxes are evaluated on the levee crest. The breaking dissipation terms are included in all the computations. For the comparisons, other computed results by the shallow water equations models of Kobayashi and Wurjanto (1989) and Dodd (1998), and the

Table 2. Experimental setup of the BEB sinusoidal wave overtopping.

| Test no. | $h$ (m) | $h_s$ (m) | $h_c$ (m) | $H$ (m) | $T$ (s) | $s$ |
|---|---|---|---|---|---|---|
| 1 | 0.529 | 0.081 | 0.054 | 0.107 | 1.549 | 3.0 |
| 2 | 0.529 | 0.081 | 0.107 | 0.107 | 1.549 | 3.0 |
| 3 | 0.609 | 0.161 | 0.054 | 0.107 | 1.549 | 3.0 |
| 4 | 0.609 | 0.161 | 0.107 | 0.107 | 1.549 | 3.0 |
| 5 | 0.609 | 0.161 | 0.054 | 0.081 | 1.858 | 3.0 |
| 6 | 0.529 | 0.081 | 0.054 | 0.107 | 2.616 | 3.0 |
| 7 | 0.529 | 0.081 | 0.107 | 0.107 | 2.616 | 3.0 |
| 8 | 0.529 | 0.081 | 0.161 | 0.107 | 2.616 | 3.0 |
| 9 | 0.609 | 0.161 | 0.054 | 0.107 | 2.616 | 3.0 |
| 10 | 0.609 | 0.161 | 0.107 | 0.107 | 2.616 | 3.0 |
| 11 | 0.609 | 0.161 | 0.161 | 0.107 | 2.616 | 3.0 |
| 12 | 0.529 | 0.081 | 0.054 | 0.081 | 3.634 | 3.0 |
| 13 | 0.609 | 0.161 | 0.054 | 0.081 | 3.634 | 3.0 |
| 14 | 0.609 | 0.161 | 0.107 | 0.081 | 3.634 | 3.0 |
| 15 | 0.609 | 0.161 | 0.161 | 0.081 | 3.634 | 3.0 |
| 16 | 0.609 | 0.161 | 0.215 | 0.081 | 3.634 | 3.0 |
| 17 | 0.529 | 0.081 | 0.054 | 0.107 | 2.616 | 1.5 |
| 18 | 0.529 | 0.081 | 0.161 | 0.107 | 2.616 | 1.5 |
| 19 | 0.448 | 0.000 | 0.054 | 0.107 | 2.616 | 1.5 |
| 20 | 0.448 | 0.000 | 0.107 | 0.107 | 2.616 | 1.5 |

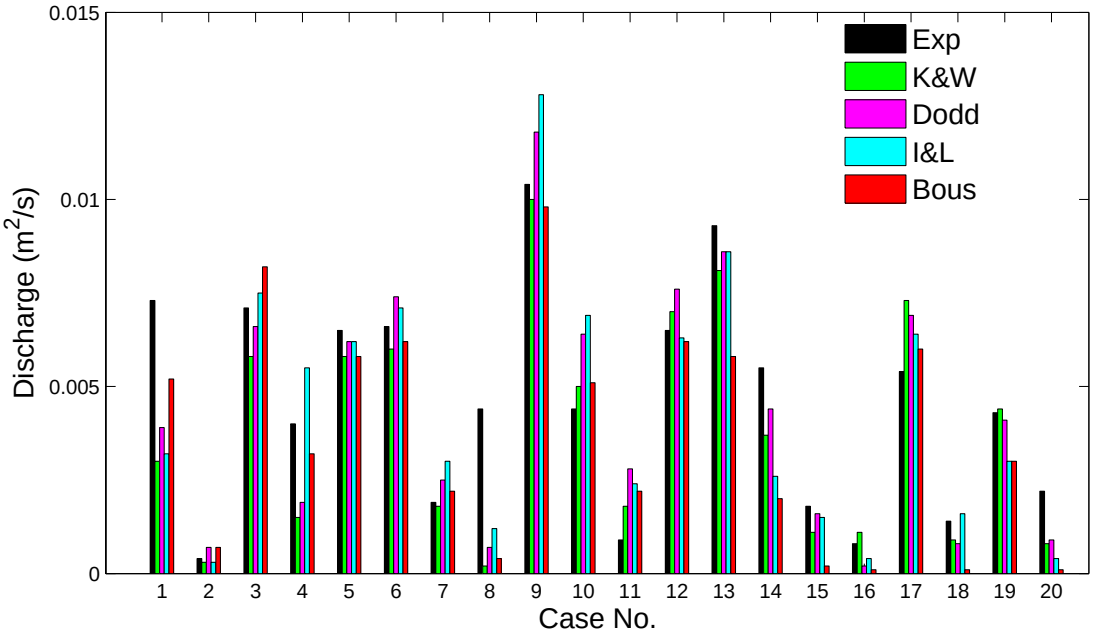


Figure 40. Overtopping fluxes over of the levees. In each group of bars, from left to right, Exp: Saville (1955), K&W: Kobayashi and Wurjanto (1989), Dodd: Dodd (1998), I&L: Sitanggang & Lynett (inpress), Bous: Present study.

Reynolds averaged Navier-Stokes model by Sitanggang and Lynett (inpress) are compared together in Figure 40. In general, all the computed fluxes are in good agreement with the experimental data and consistent with the previously published results.

### IV.3.3. Overtopping and Wave Regeneration at Lee Side

HR Wallingford performed a set of experiments on solitary wave overtopping of levees in 1996. The wave flume used in the experiments was $40m$ long and $0.5m$ wide and filled with water to $h_1 = 0.7m$ at the seaward side of the breakwater and $h_2 = 0.3m$ behind the levee. A levee with $1:4$ seaward slope and $1:2$ leeward slope was built at the right end of the flume, as shown in Figure 41. The height of the levee was

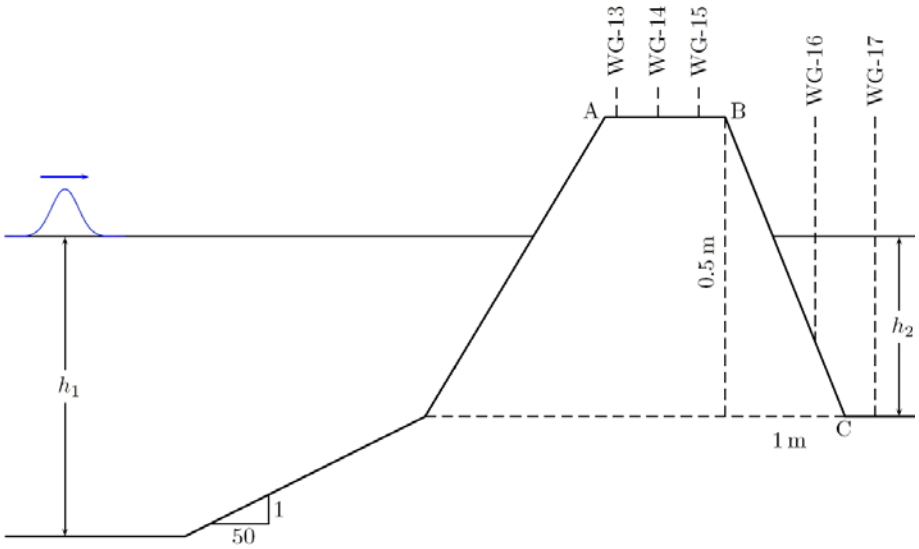


Figure 41. Laboratory experiment setup of HR Wallingford.

$0.5m$ and the width of the crest was $0.16m$, and it was fronted by a 1:50 inclined floor of height $0.4m$. Five gauges were installed on the top of and behind the levee. The first wave gauge (13) was located $0.015m$ behind the leading edge (A), the second gauge (14) and third gauge (15) were installed $0.055m$ and $0.11m$ from the first gauge respectively. The fourth gauge (16) was located $0.72m$ behind the backside edge (B) of the levee. The last gauge was installed $0.44m$ behind the back toe (C) of the levee as given in Figure 41. More details of the experimental setup are given in Dodd (1998).

With the wave gauges located behind the structure, this data set provides the rare opportunity to compare not only the overtopping wave, but the regenerated wave behind. Correct simulation of this regenerated wave is considerably more difficult than capturing runup or even overtopping rates. It requires that the model properly simulate the flow down the backface of the structure as well as the re-entrance of

the overtopping flow into the calm backside water. This latter aspect is the most challenging, and requires a robust and stable method of determining water fluxes in and out of a numerical cell.

Two wave height cases are simulated with the numerical model. The $\Delta x = 0.04m$, $C_r = 0.5$ and $k_s = 0.0006m$ for plywood were used. The computed profiles of the wave overtopping simulation data are shown in Figure 42. The left side figures show the profiles when the waves begin overtopping and the right side figures show the small regenerated wave profiles behind the levee. These profiles are verified by the comparison with the laboratory experimental time series data in Figure 43. Overall agreements of overtopping with gauges 13, 14 and 15 are good. At gauges 16 and 17, on the lee side of the levee, the proposed numerical model predicts the dispersive wave motions accurately, which cannot be observed in shallow water equation based model as described in Dodd (1998). With the comparisons presented here, it is expected that the model will provide high confidence nearshore transformation and overtopping estimates for variable, complex, and steep bathymetry and topography.

## IV.4. Dam-Break Flow Simulations

### IV.4.1. Undular Bore Generation by Sudden Discharge Release

The ability of the Boussinesq equations model for the prediction of the undular bore generated by a sudden release of discharge is investigated. For the verification purpose, a laboratory experiment conducted by Soares and Zech (2002b) was chosen. In the experiment, a sluice gate was installed between the upstream reservoir and the downstream channel as described in the Figure 44. In the downstream channel, six water surface elevation gauges (C0 $\cdots$ C5) were installed. The initial downstream water depth was $h = 0.251m$. They opened the sluice gate partially from the bottom,

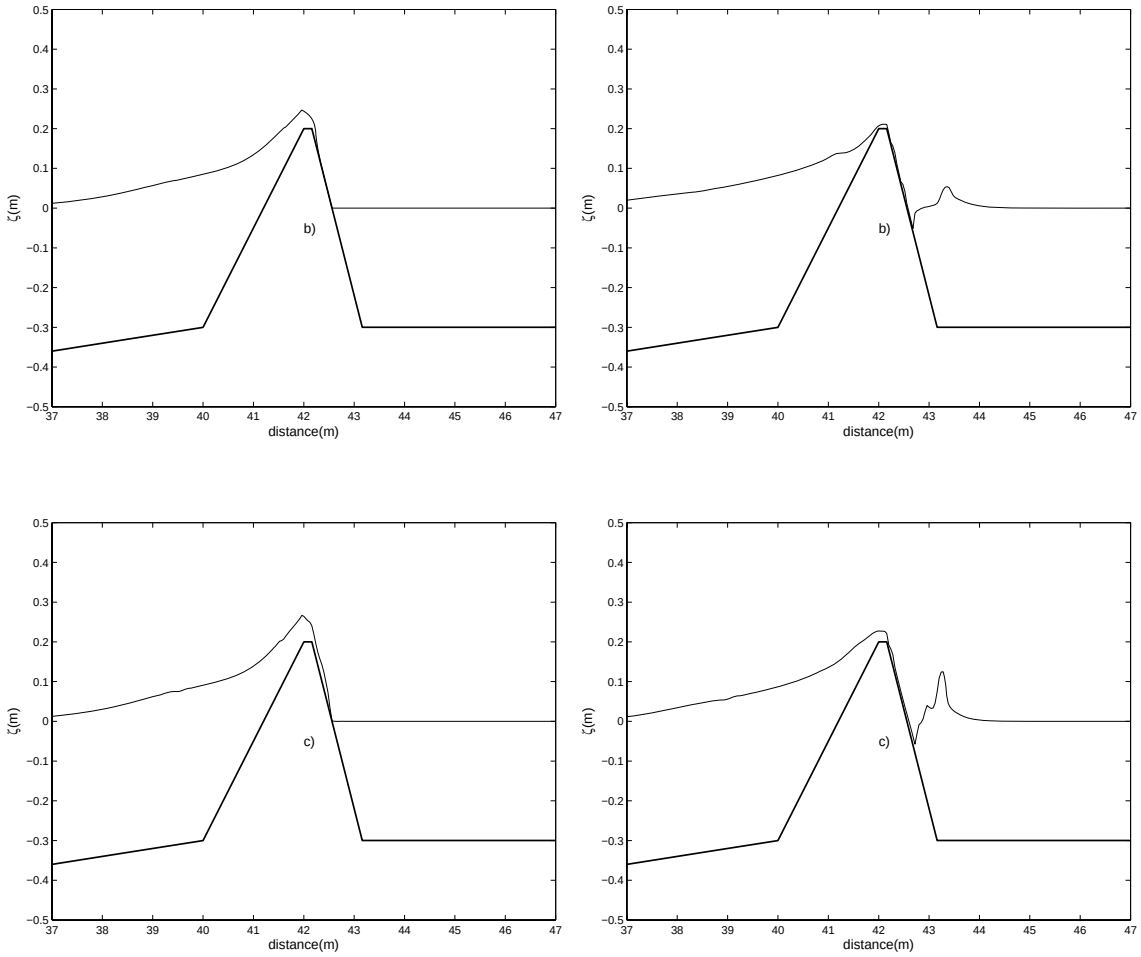


Figure 42. Snapshot of computed water surface profiles. (b) wave heights = $0.10m$, (c) wave height = $0.12m$.

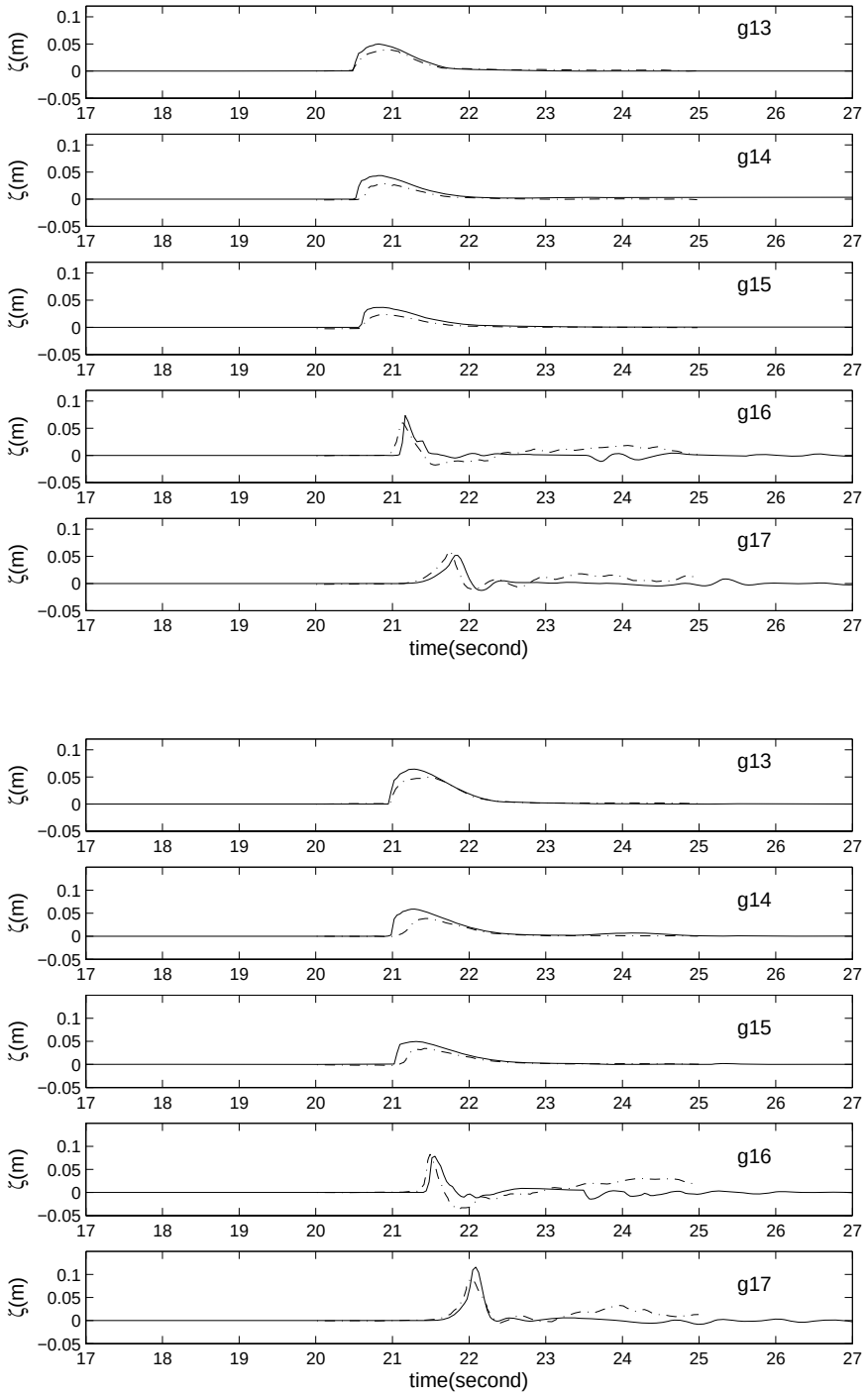


Figure 43. Time series of the water surface elevations. Solid: numerical results, dotted: experimental data, upper: wave height = $0.10m$, lower: wave height = $0.12m$.

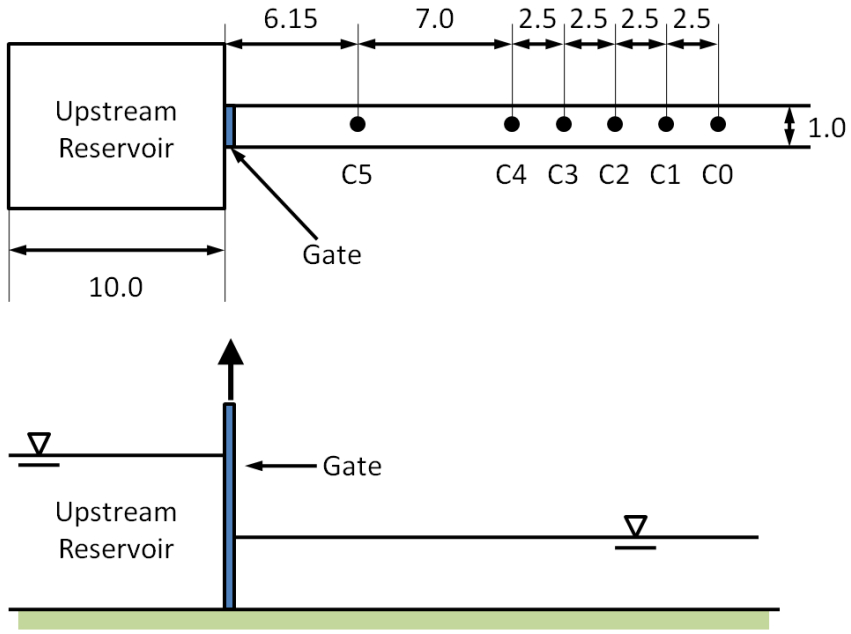


Figure 44. Experimental setup for undular bore propagation (Soares and Zech, 2002b). All units are in meter.

thus a sudden discharge was pushed into the downstream channel instantaneously and constantly. For the numerical simulation, this sudden release from the gate was modeled as a unit discharge $0.059m^2/s$ at the upstream boundary condition as done by Soares and Guinot (2008). The grid size $\Delta x = 0.05m$, the $C_r = 0.5$ and the $k_s = 0.0003m$ were used for the numerical simulation.

The time series of the water surface elevations at the each gauge are plotted in the Figure 45. As can be seen from the figures, the physical properties of the undular bores were captured very reasonably. In addition, the amplitudes and the periods of the waves agree very well with the experimental data quantitatively. Although both numerical models reproduced the undular bores very accurately, the present model

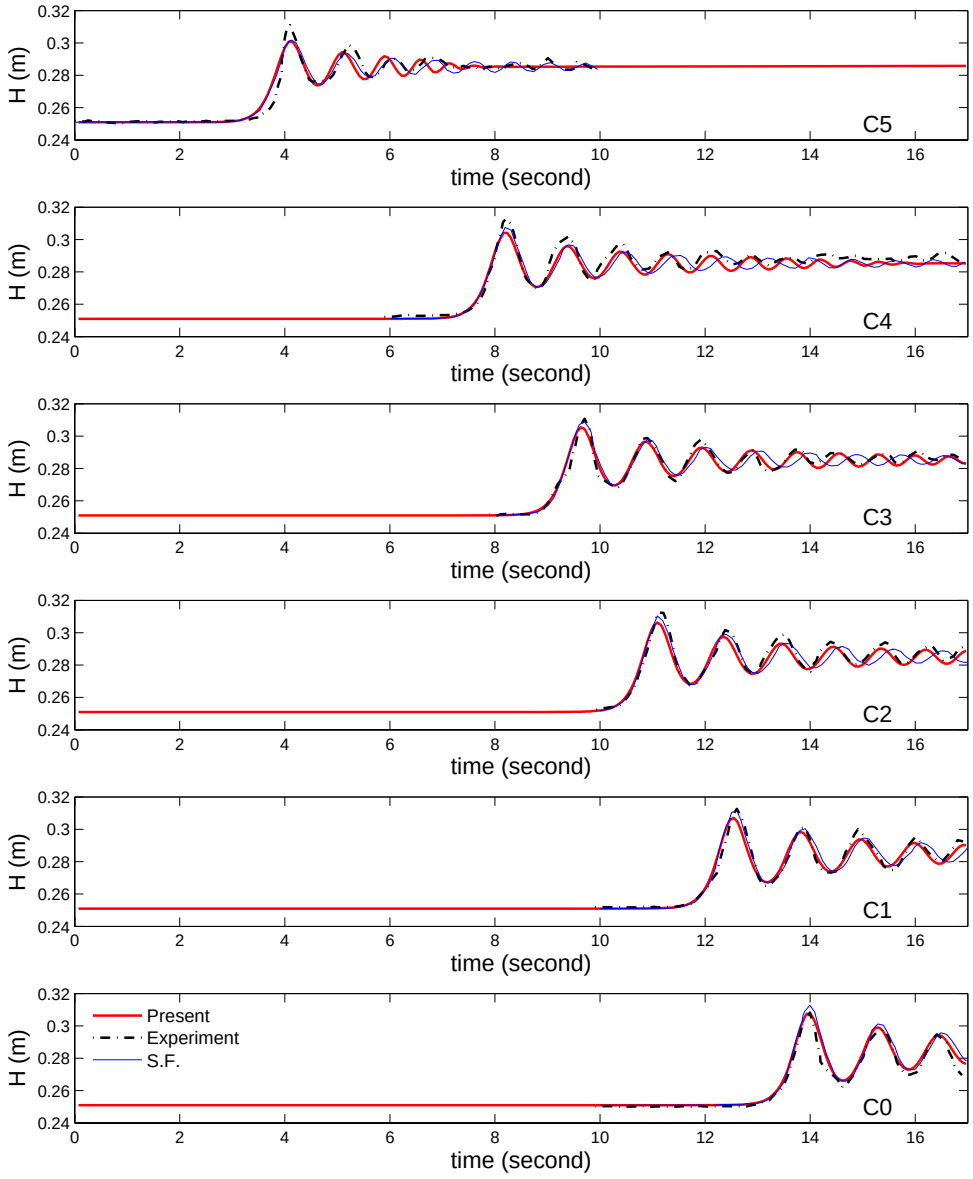


Figure 45. Time series of water surface at each gauge. Present: present study, Experiment: measured data, S.F.: computed by Soares and Guinot (2008).

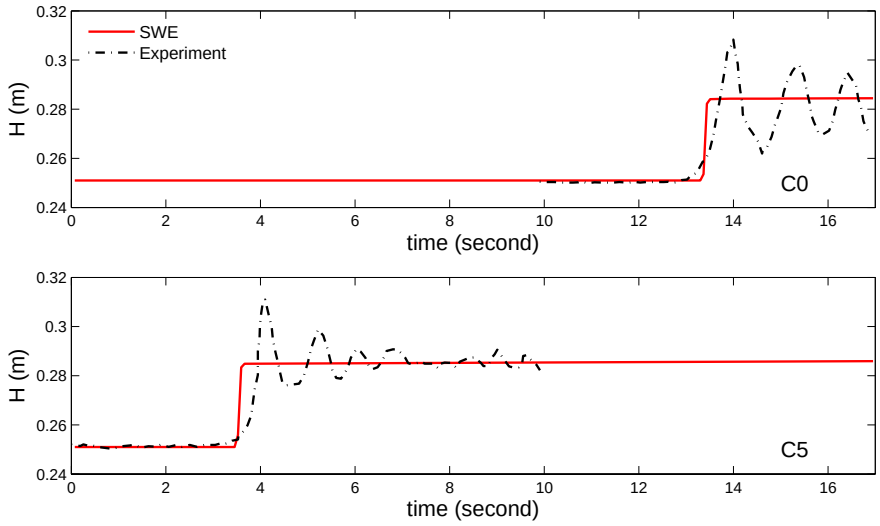


Figure 46. Time series of water surface at gauges. SWE: by shallow water equations model, Experiment: measured data.

showed better agreements with the experimental data for the period, which can be seen clearly at the gauge C2, C3 and C4. It should be mentioned that the time series of the measured data were shifted $-0.1$ second in the figures for easier comparison. The shallow water equations model was applied to solve the same flow. However, as expected, the shallow water equations model failed to generate the secondary waves. As can be seen in the Figure 46, it could generate only the surge. The magnitude of the difference is about 10% based on $H$ and about 40% based on $\zeta$, which values are not negligible in practices. Note that all shallow water equations model used in this study were solved by the exactly same numerical method with the Boussinesq equations model, that is, a fourth-order MUSCL scheme with the HLL approximate Riemann solver.

### IV.4.2. Dam-Break Flows Simulations

In this test, the gate is fully opened instantaneously so that a rarefaction wave is generated and propagates toward the upstream reservoir, which is different with the previous test case. For the verification purpose, an experimental case that showed undular bores (Carmo et al., 1993) was chosen. The experiment was conducted in a $7.50m$ long and flat channel. One water surface level gauge (G1) was installed in the upstream reservoir at $x = 3.85m$ from the upstream end. The other three gauges (G2-G4) were located at $x = 5.25m$, $6.25m$, and $7.25m$, respectively in the downstream channel. The initial upstream reservoir water depth was $0.099m$ and the downstream channel water depth was $0.051m$. For the numerical simulations, $\Delta x = 0.025m$, $C_r = 0.5$ and $k_s = 0.0001m$ were used.

The time series of the water surface elevation are shown in the Figure 47. For the measured data, the numeric values of the $\zeta$ are not given because they were not reported in Carmo et al. (1993). However, it seems that the Boussinesq equations model predicted the oscillatory patterns and the periods of the secondary waves very well. While the shallow water equations model shows different physics with the experimental data due to the inherent limitation, the hydrostatic pressure assumption. The small discrepancy of the arrival timing mainly resulted from the gate opening time ($t_{op}$). To be regarded as an 'instantaneous' opening, the $t_{op}$ should satisfy (Vischer and Harger, 1998).

$$t_{op} \leq 1.25\sqrt{\frac{H_u}{g}} \approx \ 0.13 \tag{4.2}$$

where the $H_u$ is the initial upstream water depth, or should be in the range (by Lauber and Harger, 1998)

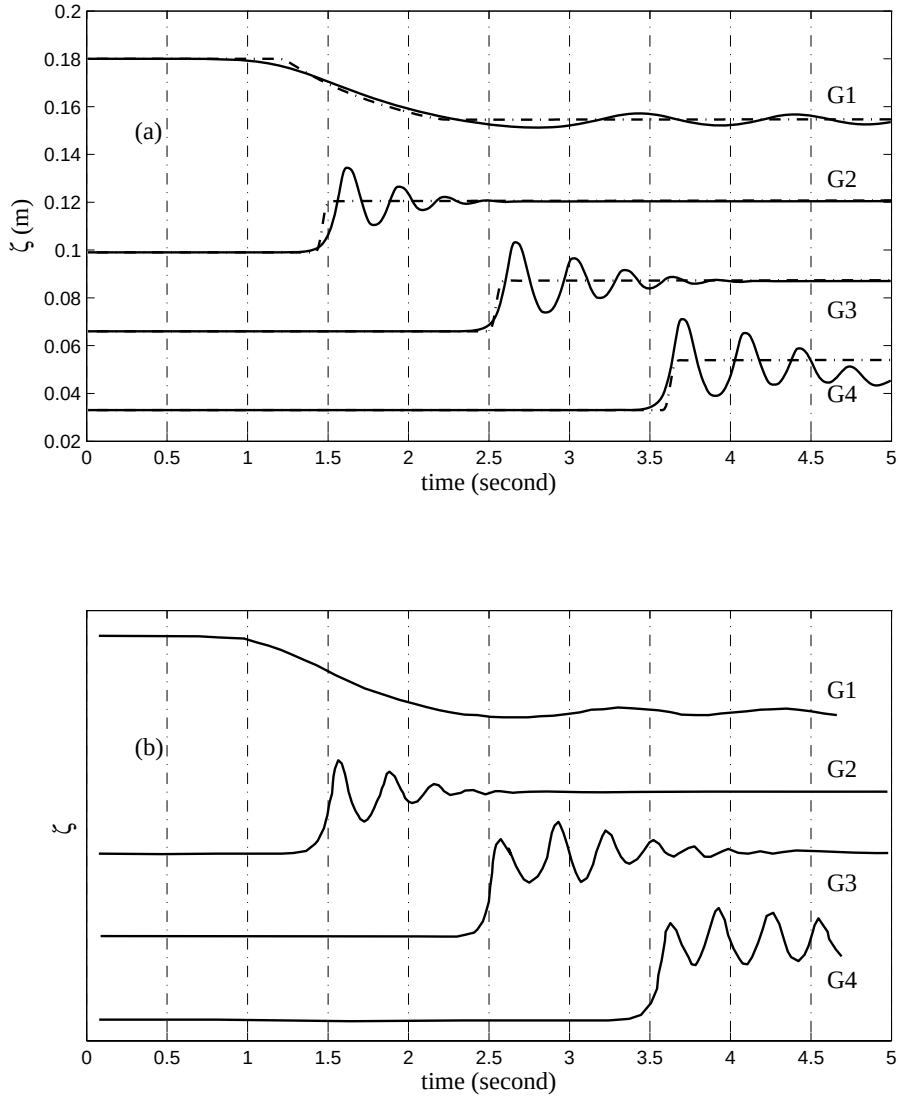


Figure 47. Time series of water surface elevation. (a) computed results. Solid line: by Boussinesq equations model, dotted line: by shallow water equations model. (b) measured data (Carmo et al., 1993). The G1, G2, G3, and G4 are the gauge numbers.

$$t_{op} \leq \sqrt{\frac{2H_u}{g}} \approx 0.14 \tag{4.3}$$

In the numerical simulations $t_{op}$ was assumed to be 0.0 second, but it took about $t_{op} = 0.5$ second in the laboratory experiments, which number is much bigger than the estimated values by the equations (4.3) and (4.4).

The spatial water surface profiles and the velocity distributions are plotted in the Figure 48 and the Figure 49, respectively. The arrival times by the Boussinesq equations model and by the shallow water equations model are very similar. However, there exist non-negligible differences of the water surface elevations and the velocities around the fronts. One more different pattern is detected around the end of the rarefaction wave. As explained with the equation (4.1), the unsteady and nonuniform curvatures shown in the Figures 48 and 49 can cause the nonhydrostatic pressure effects. However, after many simulations it was found that its effect to the flow is not important in overall sense, though not printed here.

### IV.4.3. 2D Dam-Break Flows in a L-Shaped Channel

The dam-break flow experiments in a L-shaped channel conducted by Soares and Zech (1998, 2002a) have been used as a typical benchmark data set for the 2D dam-break flow studies in many literatures. The experimental channel shown in the Figure 50 was composed of a $2.44 \times 2.37m$ size upstream reservoir and a downstream channel with a 90-degree bend. The bottom of the reservoir and the channel were flat but the bottom level of the downstream channel was $0.33m$ higher than the reservoir bottom. The initial water surface elevation of the reservoir was $0.2m$ higher than the channel bottom. For the wet bed case, the total water depth at the downstream channel was $0.01m$. For the dry bed case, it was $0.0m$. For the numerical simulation, the

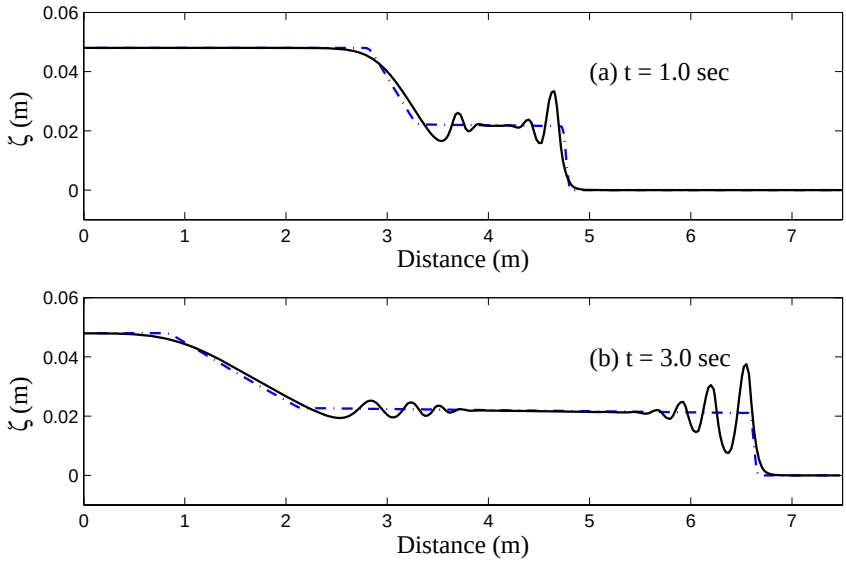


Figure 48. Computed water surface profiles. Solid line: by Boussinesq equations model, dotted line: by shallow water equations model.

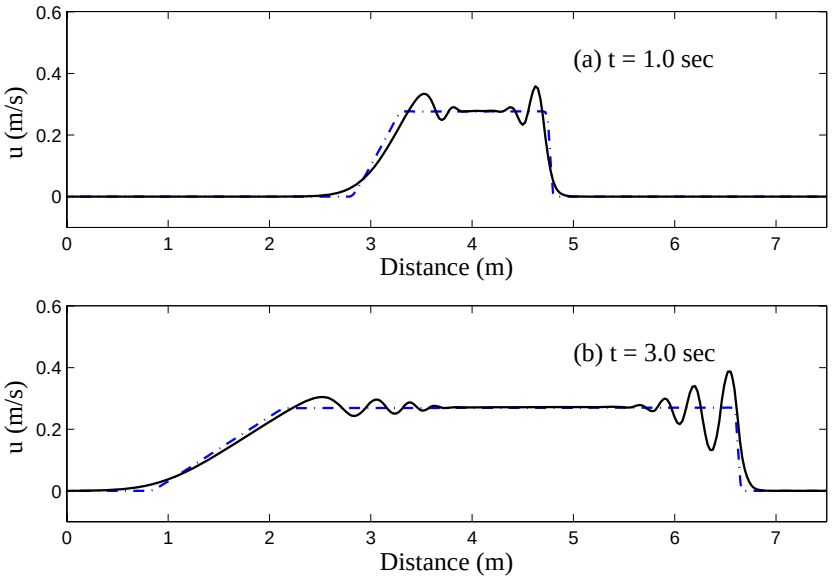


Figure 49. Computed velocity profiles. Solid line: by Boussinesq equations model, dotted line: by shallow water equations model.

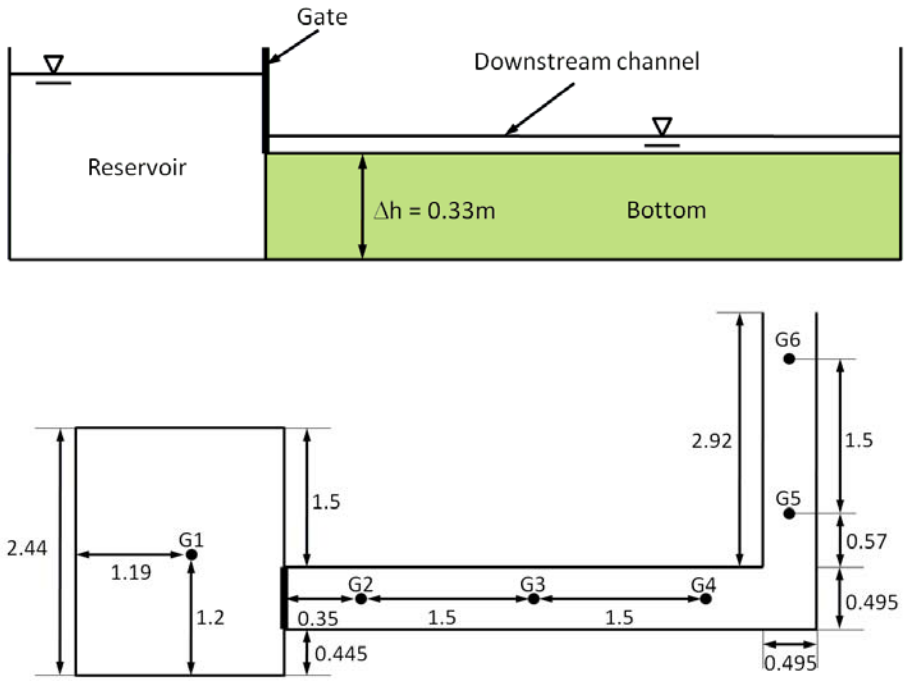


Figure 50. Experimental set up of the L-shaped channel. Upper: side view, lower: plan view. All units are in meter.

$\Delta x = \Delta y = 0.0495m$ and a uniform value of Manning coefficient $n = 0.011$ were used for the entire computational domain as proposed by Soares and Zech (2002a). The Manning friction formula can be applied with $c_f = gn^2/H^{1/3}$. It should be mentioned that the shallow water equations were solved at the dam location for the stability.

The time series of water surface elevations at the gauges are plotted in the Figures 51. Reasonable agreements were obtained as shown in the figures though there are small differences between the measured data and the computed results. There are various reasons that can cause the errors. Firstly, the friction term based on the steady state, that is, Manning's formula was used in the numerical simulations. As tested by Soares and Zech (1998), the computed results were sensitive to the Manning $n$ value.

The use of a frictionless side walls condition can contribute to the discrepancy, too. Especially, the energy losses that can occur at the abrupt contraction between the channel and the reservoir, and at the 90 degree bend were not accounted properly in these simulations. Lastly, because the flows in 3D space were modeled in 2D space in the present modeling, it is natural that there are differences between the computed results and the experimental data.

The second undular peaks at the gauges G2, G3 and G4 in the time series can be explained by the Figure 52 and Figure 53: The suddenly released water flows straightly at the beginning and then blocked by the wall in the bend. For a while, the water is temporary stored and the water surface is increased in the bend. After soon, the part of the stored water in the bend is reversely released to the upstream reservoir. Consequently, the undular bores can be created like the figures. After the part of the flow passes the 90-degree bend, the 2D secondary shocks generated by the reflections between the side walls were captured as shown in the Figure 52 and Figure 53. These patterns are similar to the 2D secondary shock captured in the experiments (by Soares and Zech, 2002a) like the Figure 54. However, in the similar computational studies like Zhou et al. (2004) and Soares-Fraza and Zech (2002a), the 2D secondary shocks were not captured. It should be noted that the secondary shocks are not directly related with the nonhydrostatic pressure effects of the Boussinesq equations. In the numerical results by the shallow water equations model solved by the present numerical method, the 2D secondary shocks were captured also though not printed here. It seems reasonable because, if the ratio $\epsilon_r$ is very small like in the downstream of the 90-degree bend then the nonhydrostatic effects become negligible (Mohapatra and Chaudhry, 2004).

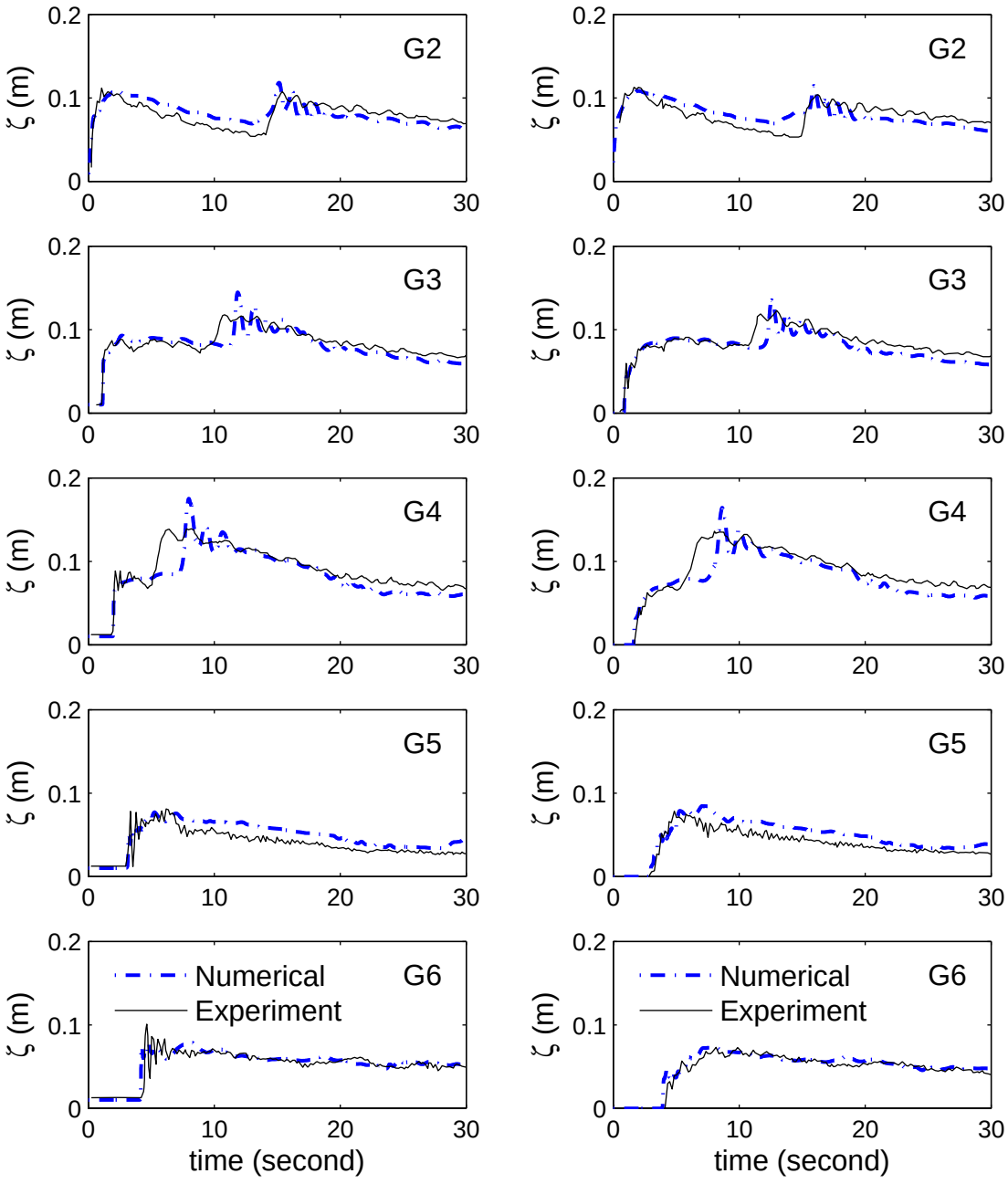


Figure 51. Time series of water surface elevations in the L-shaped channel. left: wet bed case, right: dry bed case. Solid line: numerical results, dotted line: measured data.

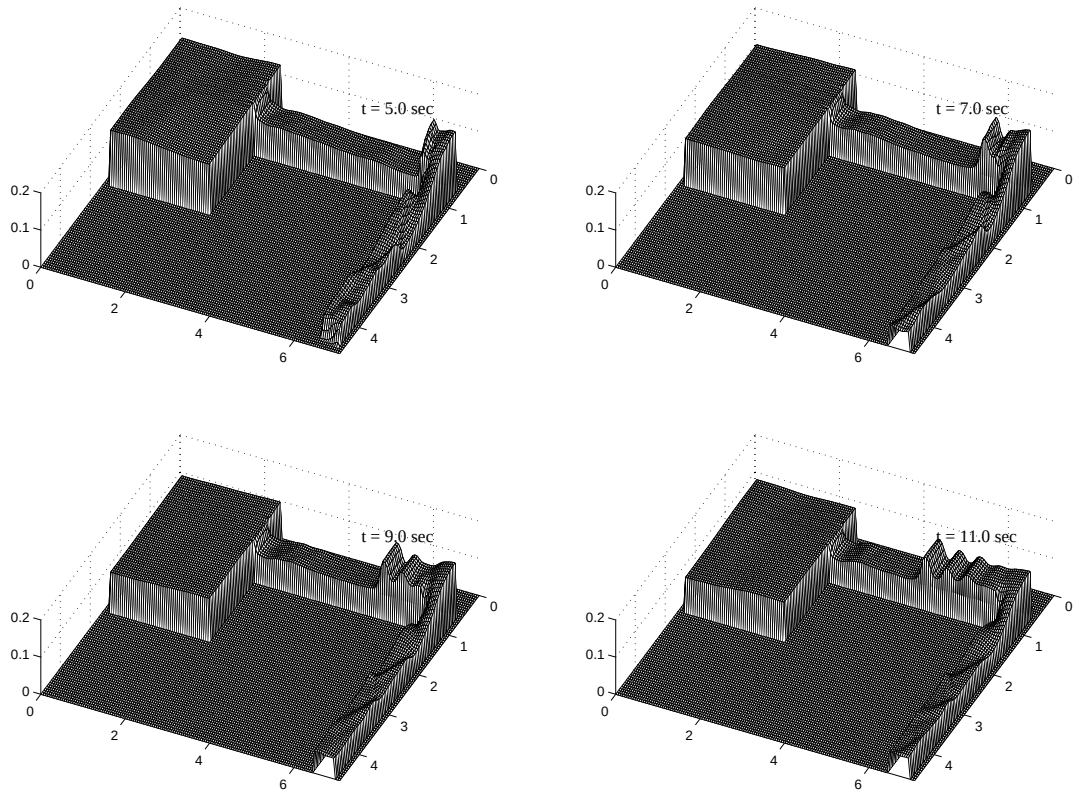


Figure 52. Snapshots of the computed water surfaces of dam break flows (wet bed case). All units are in meter.

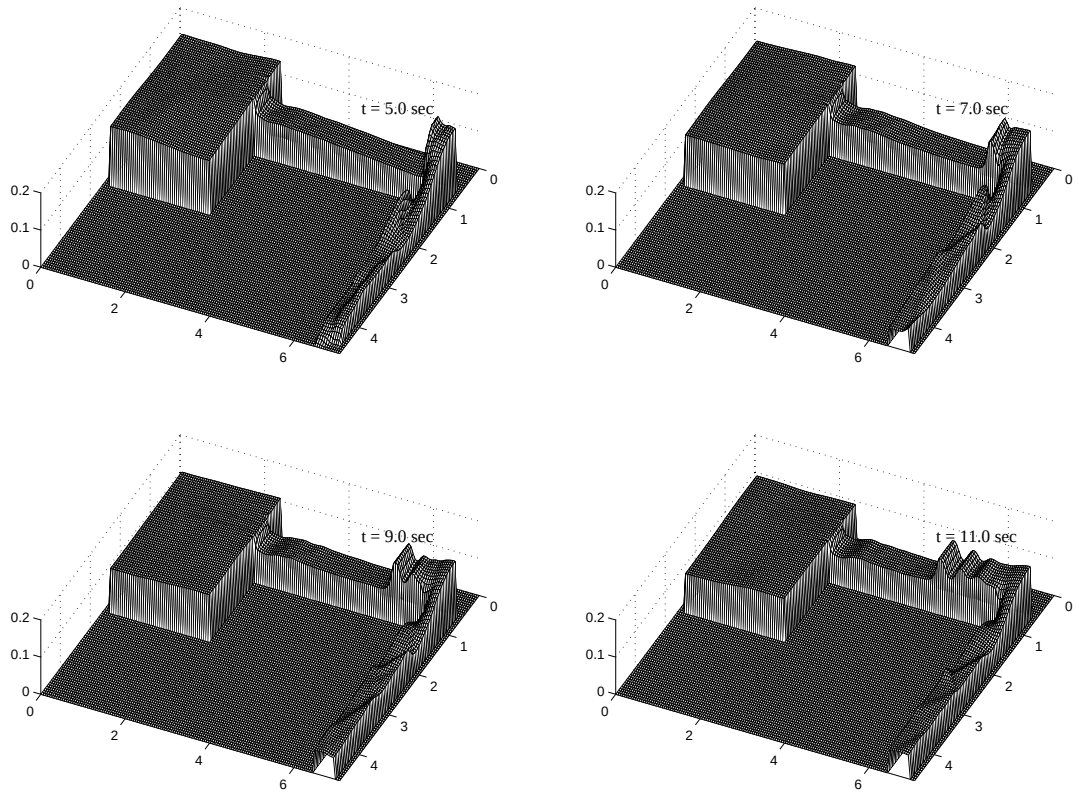


Figure 53. Snapshots of the computed water surfaces of dam-break flows (dry bed case). All units are in meter.

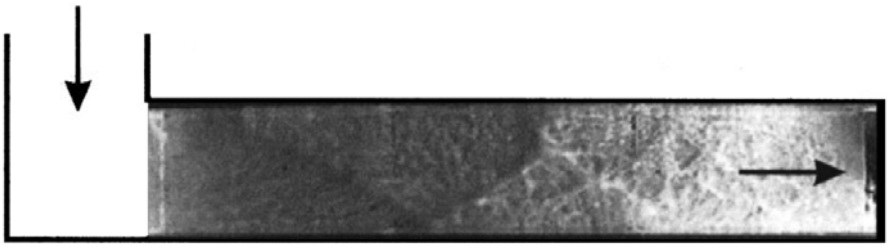

Figure 54. Secondary shock captured in the experiment (Soares and Zech, 2002a).

## IV.5. Undular Bore Simulations

### IV.5.1. Undular Bores Generated by Tsunami Wave Fission

Tsunami, a very long wave, can occur one of the most serious disasters to human society. When it approaches shores, the curvature of the water surface is getting steeper due to the celerity, so the nonhydrostatic pressure effects may become important. Sequently, the undular bores like the soliton fission can be generated in nearshore areas. For example, a fission was observed during the 1983 Nihonkai-Chubu earthquake tsunami in Japan (Shuto, 1985). These waves can occur the harbor oscillation problems or can affect to the runup height which is critical to the evacuation.

An undistorted experimental study on the tsunami soliton fission was carried out in the Large Wave Flume located at Central Research Institute of Electric Power Industry in Japan (Matsuyama et al, 2007). The dimensions of the channel were $205m$ long, $3.4m$ wide and $6.0m$ deep. The bottom geometry of the experiment is depicted in the Figure 55. The tsunami was generated with a sinusoidal wave form at the left boundary like

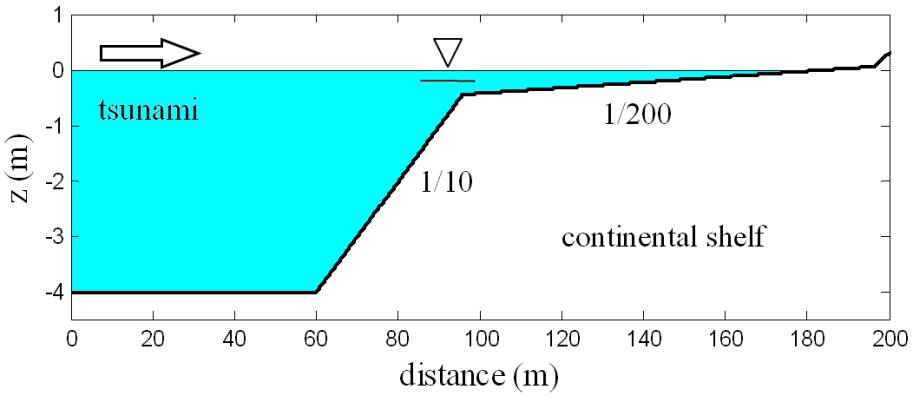


Figure 55. Experimental setup for tsunami wave fission.

$$\zeta = \begin{cases} Asin\left(\frac{2\pi t}{T}\right), & 0 \le t \le T \\ 0, & T > t \end{cases} \tag{4.4}$$

where $A = 0.03$m and the $T = 20$ second. For the numerical simulation, the $\Delta x = 0.075m$, the $k_s = 0.0003m$ and the $C_r = 0.5$ were used.

During the long wave is approaching the shore, the transformation processes of the soliton fission is captured reasonably by the proposed Boussinesq equations model as shown in the Figure 56. For the validation, the time series of the water surfaces were compared in the Figure 57. Very good agreements with the measured data were obtained. The error resulted from mainly the discrepancy of the wave source between the numerical model and the laboratory experiment.

### IV.5.2. Okushri Island Tsunami

On July 12, 1993, a tsunami was generated and attacked the south-west coast of Hokkaido in Japan including Okushri island. Matsuyama and Tanaka (2001) repro-

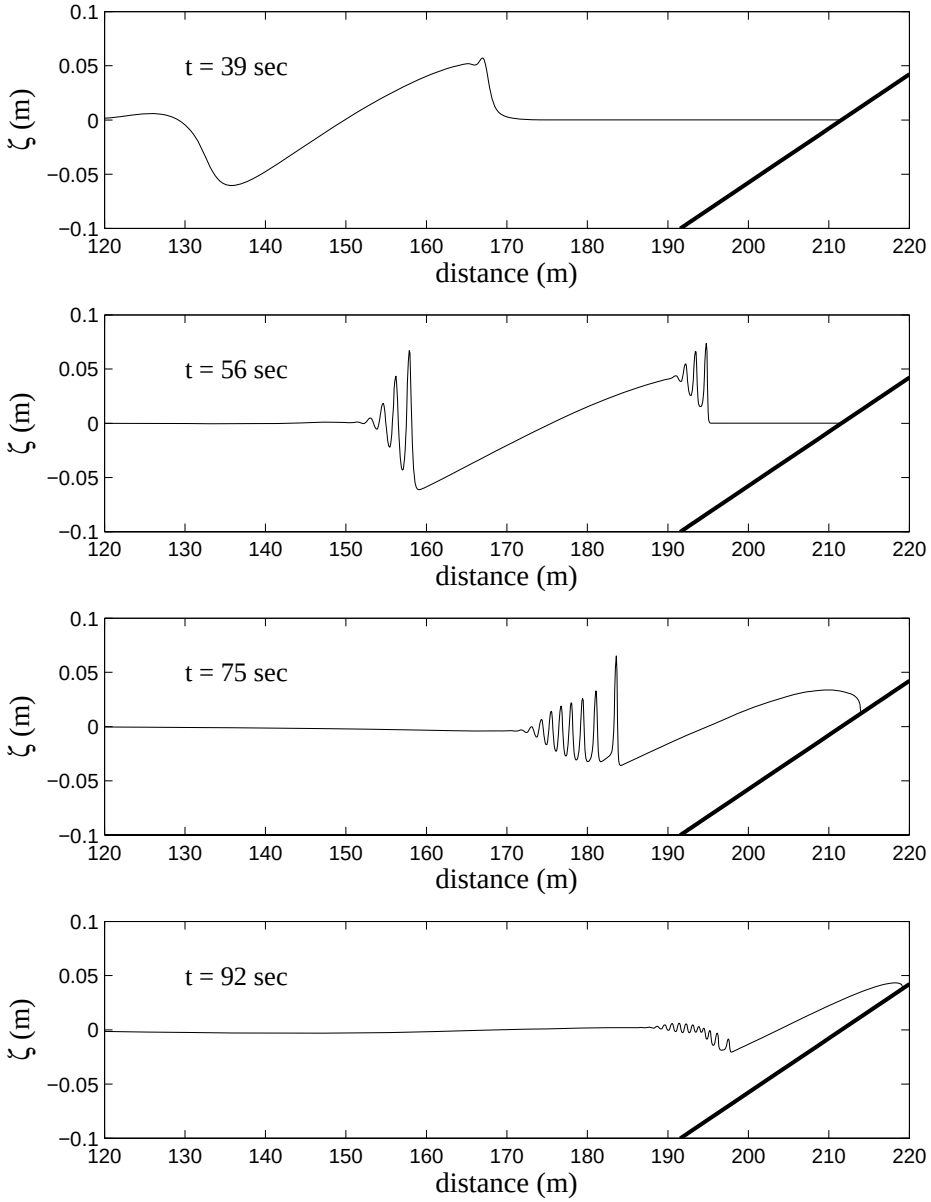


Figure 56. Computed water surface profiles of tsunami wave fission.

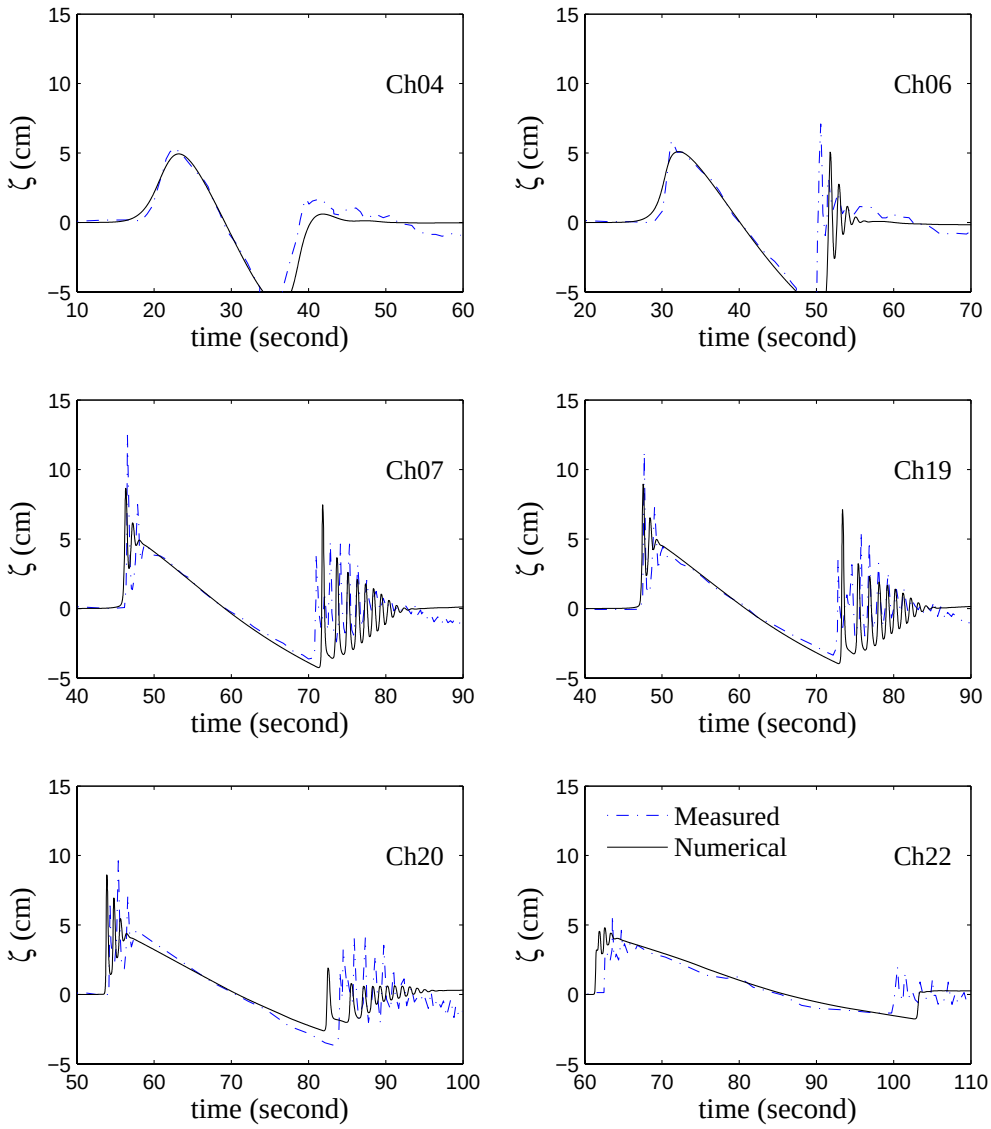


Figure 57. Time series of water surface elevations. Solid line: numerical results. Dotted line: measured data (by Matsuyama et al, 2007).

duced the tsunami in a laboratory for the investigation of the mechanism and the maximum runup height of Okushri tsunami. This experimental data set is a very good benchmark problem in the view of theory and application because the physics and the topography are complex together. Thus, their results (time series of water surface, animation of runup process, boundary condition and bathymetry) were widely spread and used as a benchmark problem.

The topography given by the laboratory data is plotted in the Figure 58. In the domain, there are a submerged (Hira island) and a surface piercing island (Muen island). A complex topography comprised of two small valleys (Monai valley) is located on the shore, where the maximum runup was observed. About $2m$ off from the offshore boundary, there is a submerged vertical cliff, which may create a numerical oscillation in numerical simulation. As shown in the figure, the shoreline is not uniform and so the runup and the rundown processes should be affected by the particular topography. More details about the experiment are in the Matsuyama and Tanaka (2001).

Note that, for the numerical simulations, the topography data were used without any modifications. The boundary conditions given by the experimental data are generated by using internal source and sponge layer at left boundary. At the other boundaries, there are walls. The grid size $\Delta x = \Delta y = 0.014m$, $k_s = 0.001m$ and $C_r = 0.5$ were used, and the breaking terms are included in the numerical simulations.

The computed water surface elevations are shown in the Figure 59. At the beginning, withdrawal seaward direction is observed due to the left side boundary condition. Thus the water surface elevation descends and Muen island is bridged to the shoreline as shown in the figure at $t = 12.9$ second. Next wave from the seaward boundary is propagating toward shoreline and it is separated and bended by Muen island. The dried pathway between Muen island and the shoreline becomes

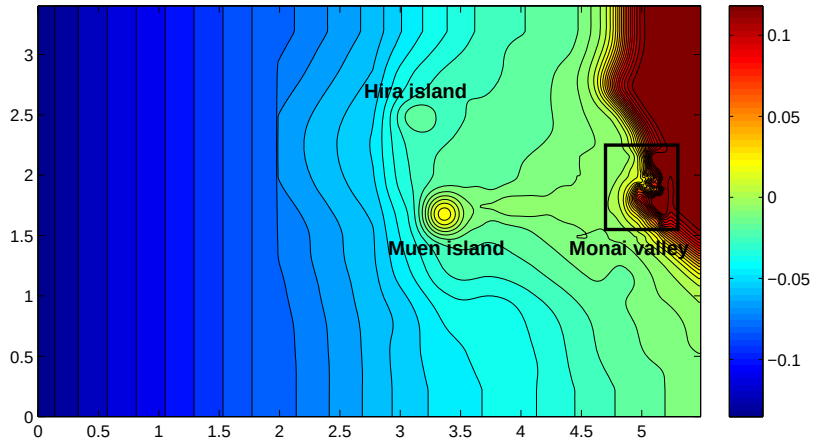


Figure 58. Topography data (Matsuyama and Tanaka, 2001). All units are in meter.

submerged again. After the wave reaches the shoreline, it is reflected and scattered. As shown in the figures from at $t = 16.2$ second, the secondary wave that can be captured by dispersive wave model, is propagated into the entire domain. Note that the wiggle that is parallel to the longshore axis is generated by the submerged vertical cliff located $2m$ off the left boundary.

These secondary waves can be seen obviously in the time series at three locations, ($4.521m$,$1.196m$), ($4.521m$,$1.696m$) and ($4.521m$,$2.196m$). As shown in the Figure 60, the numerical results and the measured data are within good agreements. In the time series, for the first 10 seconds, there are discrepancy between the numerical and experimental data, because the water surface and velocity in the laboratory tank were not zero.

Next, the detail inundation mechanism on Monai valley is described, on which the maximum runup was observed. In the Figure 61(a), the current and wave front are flooding on the dry land. The front reaches firstly just above area of Monai valley like the Figure 61(b). Next, it runs up Monai valley and makes the valley inundated

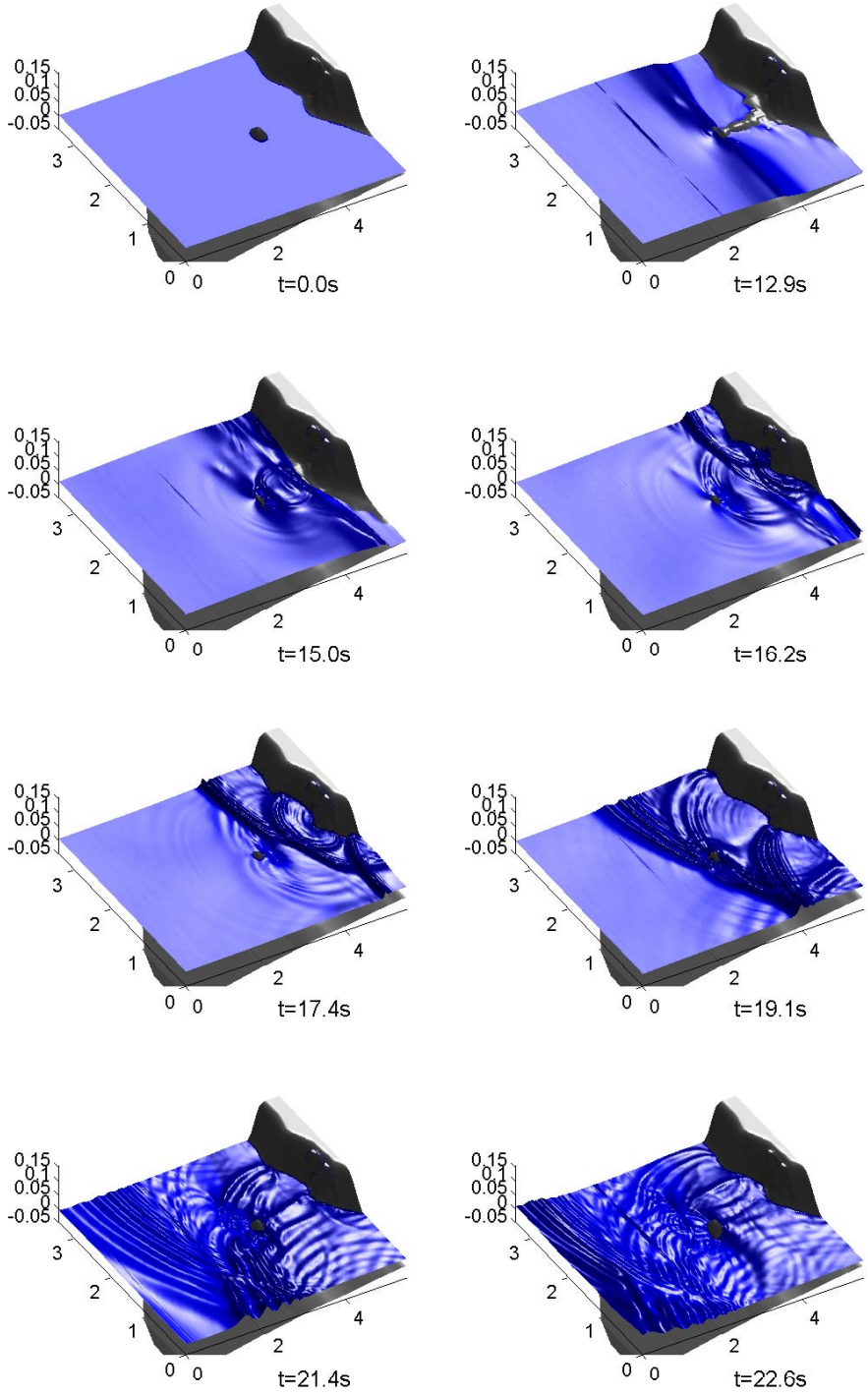


Figure 59. 3D view of the computed water surface elevations. All units are in meter.

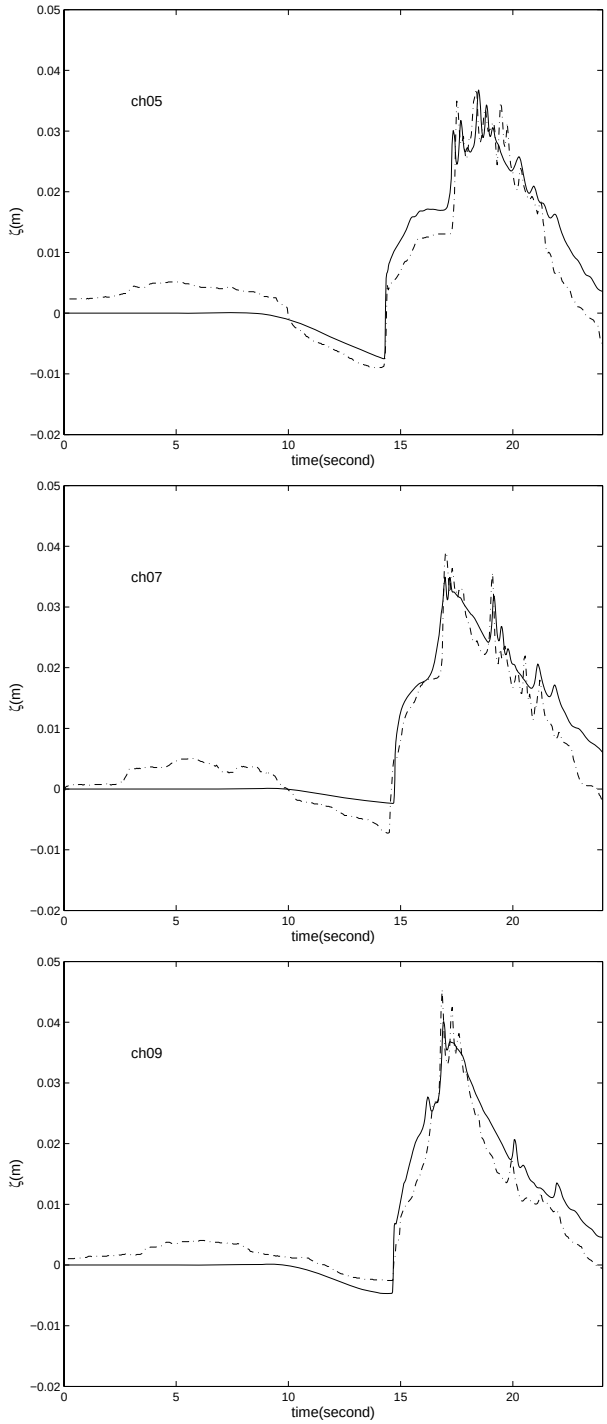


Figure 60. Time series of water surface levels. Solid line: numerical results, dotted: experimental data (Matsuyama and Tanaka, 2001), upper: at gauge no.5 ($4.521m$,$1.196m$), middle: at gauge no.7 ($4.521m$,$1.696m$), bottom: at gauge no.9 ($4.521m$,$2.196m$).

as shown in the Figure 61(c). At final stage, the water retreats as shown in the Figure 61(d). Quite similar runup procedure was observed in the laboratory experiment like the photos in the Figure 61.

Liu et al. (1995) investigated a general process of long wave propagation and transformation around a conical island. When a long wave propagates through an island, it is separated into two parts and the separated waves are partly trapped by shallow water depth area, and so the wave crests bend. The separated waves may collide again at the lee side of the island, and a second runup can be occurred at the lee side of the island. These processes are modeled quite well with the proposed model around Muen island as shown in the Figure 62. In addition, it shows the strong coherent structures at the lee sides of the island during the tide (upper figures) and the ebb (lower figures).

The coherent structure is expressed with vertical vorticity in the Figure 63. As described above, around the surface piercing Muen island strong vertical vorticity is generated mainly by the topography itself. On the submerged Hira island, the strength of the vertical vorticity becomes weaker when the water depth is deep (at $t = 18.6sec$).

## IV.6. Summary

A robust moving boundary scheme based on simple physical conditions was developed. With several experimental data sets, the numerical results showed good agreements. Especially, the re-entrance of the overtopped flow into the lee side of levees, one of the most challenging problem of moving boundary scheme, showed very reasonable agreements with experimental data.

Several typical undular bores generated by dam-break flows and tsunamis were

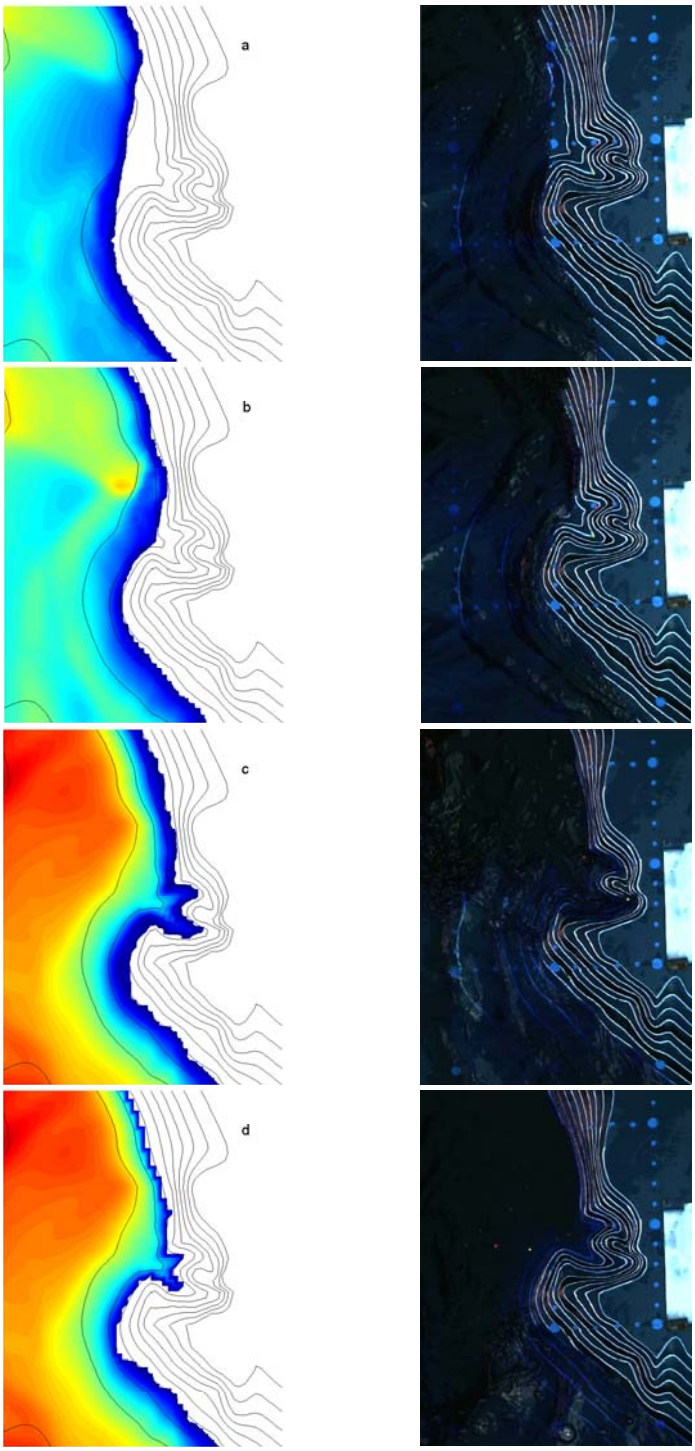


Figure 61. Inundation process around Monai valley. Color represents the water depth. left: numerical results, right: photographs of experiment (by Matsuyama and Tanaka, 2001).

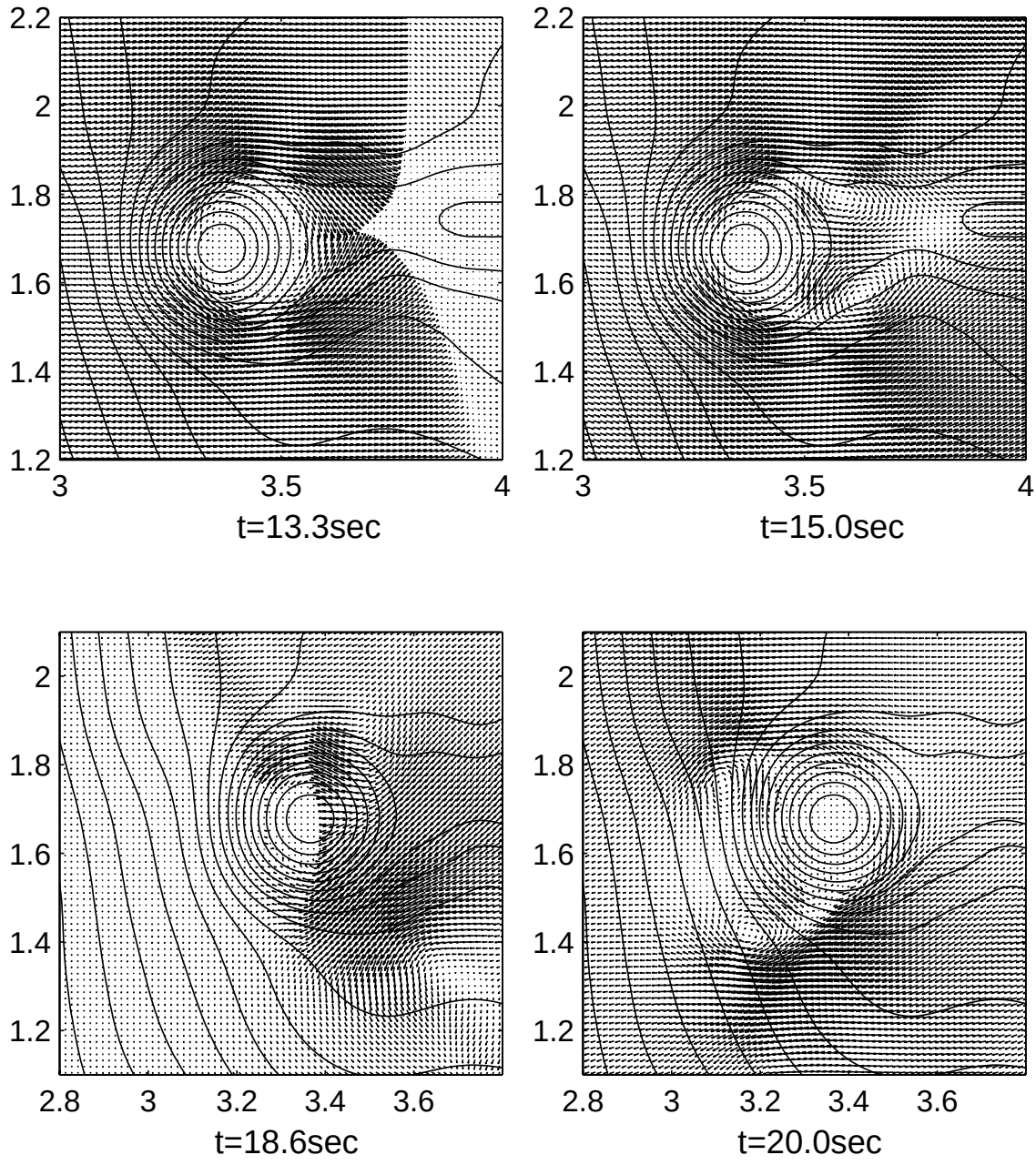


Figure 62. Computed velocity distribution around Muen island. Line: bathymetry contour.

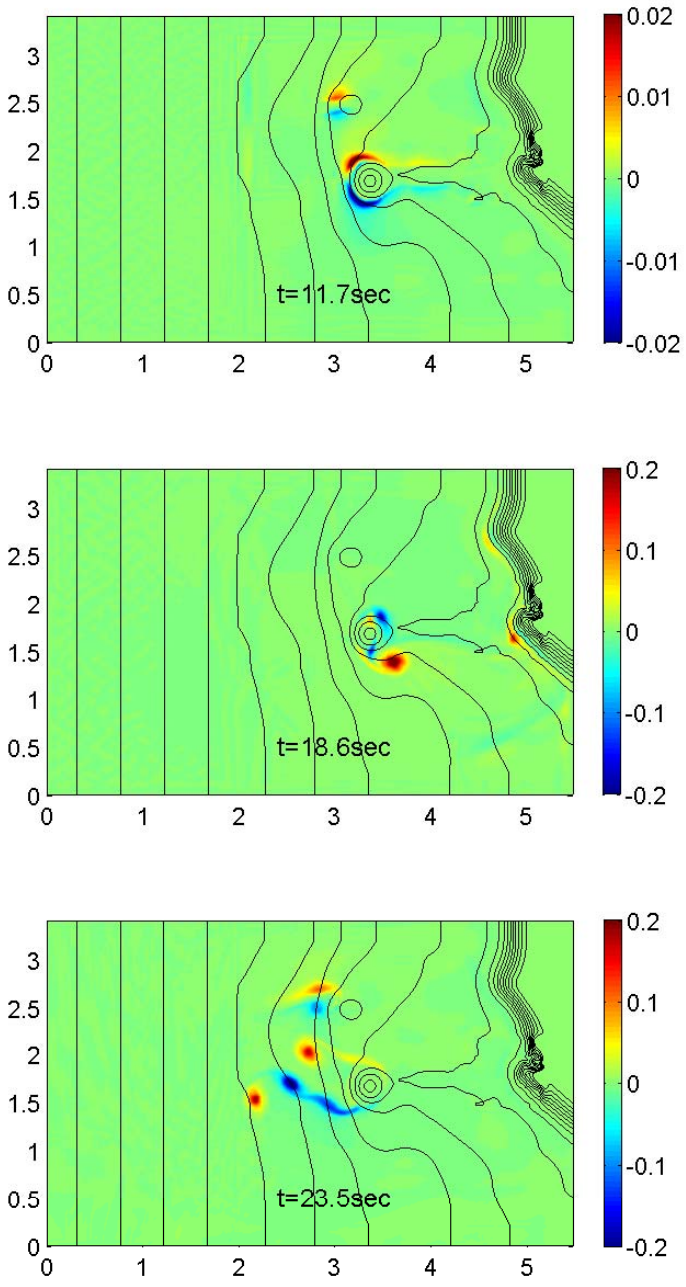


Figure 63. Computed depth-integrated vertical vorticity ($m/s$).

simulated with the nonlinear Boussinesq equations model that can consider the non-hydrostatic pressure effects. From the numerical simulation results, the importance of the nonhydrostatic pressure effects was recognized. In overall sense, accurate and stable computational results were obtained. Thus, it can be regarded as a good tool for the wave and current interaction including shocks and undular bores. In Okushri tsunami simulations, widely used as a benchmark data set, the complex physics and topography of the laboratory experimental flow were very well dealt with the proposed model.

Therefore, with the comparisons presented here, it is expected that the model can provide high confidence wave and flow transformations including shocks and undular bores on complex topography.

# CHAPTER V
# NEAR FIELD TRANSPORT MODELING

## V.1. Introduction

The scalar transport is strongly dependent on flow structures, and so the accurate prediction of the flow structures is critically important for the accurate scalar transport predictions. Various numerical methods for the prediction of free surface flows have been developed and applied as described in the previous chapters. Firstly, the shallow water equations models and the coupled depth-averaged transport equation models are most widely used for large domain problems. They can be solved very efficiently and accurate horizontal flow and concentration fields are obtained by them if the shallow water assumption is valid. However, they can lose the accuracy when the flow field is dispersive or under nonhydrostatic pressure conditions. For those flow fields, 3D Navier-Stokes equations with turbulent closures and 3D transport equation models are the most physical and accurate numerical approach. However, even till these days, they demand huge computational resources so that they are not practical for large domain problems. Especially, in cartesian coordinate system, the free surface crosses the computational grid perpendicularly, and so it brings the difficulty of applying the pressure boundary condition precisely on the free surface (Lin and Li, 2002). To solve this kind of problem, the $\sigma$-coordinate system can be used (Phillips, 1957), which maps a nonuniform vertical domain into a rectangular domain. Thus, if the water surface and the bottom bathymetry are smooth, then it can make the boundary conditions simple and possible for the computational accuracy to be improved.

Using the $\sigma$-coordinate system, Stansby (1997) developed a 3D semi-implicit FVM for shallow water flow with the hydrostatic pressure assumption. Stansby and

Zhou (1998) developed a numerical scheme incorporating nonhydrostatic pressure and they obtained reasonable agreements with experimental data. Lin and Li (2002) developed a 3D numerical model based on the Navier-Stokes equations in a $\sigma$-coordinate system. They reported that some minimum resolution was needed to get accurate results. Yuan and Wu (2004) developed an implicit FDM model in vertical 2D $\sigma$-coordinate. For the real field prediction of saline in a estuary and river, Lee et al. (inpress) developed a width-averaged 2D $\sigma$-coordinate flow and transport models. Their application showed good agreement with the observed field data.

However, the numerical flow model based on $\sigma$-coordinate still requires expensive computational cost and they are restricted by stability criterion originated by the coordinate transformation (Haney, 1996, Lin and Li, 2002). It makes hard to apply the $\sigma$-coordinate model to moving boundary problems like tidal flat and surf zone where the water depth approaches to zero. In addition, the free surface elevation and the bottom bathymetry must be a single function on a horizontal plane even though it solves all three momentum equations for 3D cases. Consequently, it will be very hard to solve accurately the wave breaking and the related strong vertical mixing which are relevantly observed in coastal areas or near hydraulic structures.

Comparing to the $\sigma$-coordinate flow model, the Boussinesq equations model can calculate much efficiently the 3D information of water surface and velocity with continuity equation and only two momentum equations provided that the water depth is not deep. Thus the combination of the Boussinesq equations model and the depth-integrated transport model is very good for the far field prediction. However, the limitation for the near field prediction recognized in the chapter III also exists in the combination of the 2D horizontal models. Therefore, a new combination comprised of the Boussinesq equations model and a $\sigma$-coordinate transport model can be useful for the near field and far field problems in large domain.

In this study, a 3D $\sigma$-coordinate transport model coupled with the Boussinesq equations model is developed. In the next section, the advection-diffusion equation in the $\sigma$-coordinate is derived. Next, the brief explanation about the Boussinesq equations model and the numerical methods are following. In the last part, the validations and various numerical simulations of the developed model are presented.

## V.2. Advection-Diffusion Equation in $\sigma$-Coordinate

### V.2.1. Transformed Advection and Diffusion Terms

In a physical domain $(t^*, x^*, y^*, z^*)$, the advection-diffusion equation is given by

$$\begin{aligned} \frac{\partial C}{\partial t^*} &+ \frac{\partial Cu}{\partial x^*} + \frac{\partial Cv}{\partial y^*} + \frac{\partial Cw}{\partial z^*} \\ &= \frac{\partial}{\partial x^*}\left(D_x \frac{\partial C}{\partial x^*}\right) + \frac{\partial}{\partial y^*}\left(D_y \frac{\partial C}{\partial y^*}\right) + \frac{\partial}{\partial z^*}\left(D_z \frac{\partial C}{\partial z^*}\right) \end{aligned} \tag{5.1}$$

where the $(x^*, y^*)$ represents the horizontal axes and the $z^*$ is the vertical axis. The $t^*$ is the time and the $C$ is the concentration. The $(u, v)$ are the horizontal velocities and the $w$ is the vertical velocity. The $D_x$, $D_y$, and $D_z$ are the diffusion coefficients into the $x^*$, $y^*$ and $z^*$ directions, respectively.

The $\sigma$-coordinate space $(t, x, y, \sigma)$ is defined as followings (Blumberg and Mellor, 1983).

$$t = t^*, \quad x = x^*, \quad y = y^*, \quad \sigma = \frac{z^* + h}{H} \tag{5.2}$$

The grid systems before and after the coordinate transformation by the equation (5.2) are shown in the Figure 64.

To transform the advection-diffusion equation from the physical coordinate to

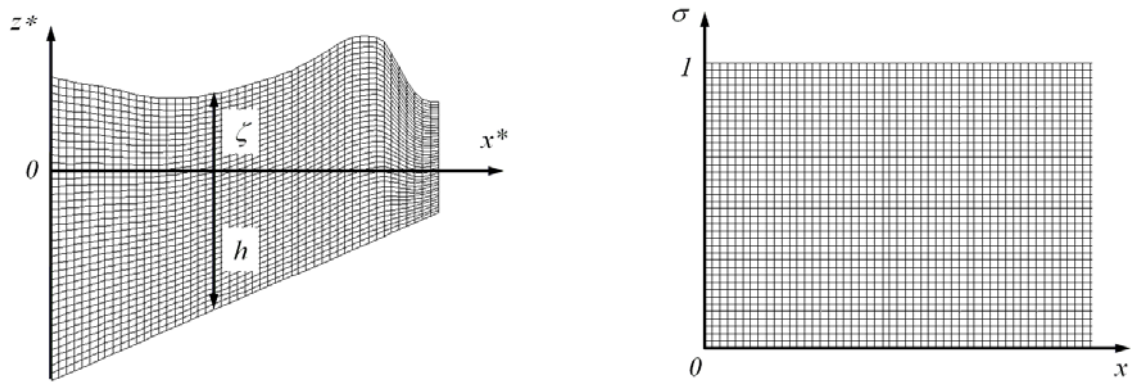


Figure 64. Grid systems in physical domain (left) and $\sigma$-coordinate system (right).

the $\sigma$-coordinate, the chain rule is used as followings

$$\begin{aligned}
\frac{\partial f}{\partial t^*} &= \frac{\partial f}{\partial t} + \frac{\partial f}{\partial \sigma}\frac{\partial \sigma}{\partial t^*} \\
\frac{\partial f}{\partial x^*} &= \frac{\partial f}{\partial x} + \frac{\partial f}{\partial \sigma}\frac{\partial \sigma}{\partial x^*} \\
\frac{\partial f}{\partial y^*} &= \frac{\partial f}{\partial y} + \frac{\partial f}{\partial \sigma}\frac{\partial \sigma}{\partial y^*} \\
\frac{\partial f}{\partial z^*} &= \frac{\partial f}{\partial \sigma}\frac{\partial \sigma}{\partial z^*}
\end{aligned} \tag{5.3}$$

where the $f = f(t^*, x^*, y^*, z^*)$ is a function in the physical domain and the differentiation terms in the right hand side are expressed as

$$
\begin{aligned}
\frac{\partial \sigma}{\partial t^*} &= -\frac{\sigma}{H}\frac{\partial H}{\partial t} \\
\frac{\partial \sigma}{\partial x^*} &= \frac{1}{H}\frac{\partial h}{\partial x} - \frac{\sigma}{H}\frac{\partial H}{\partial x} \\
\frac{\partial \sigma}{\partial y^*} &= \frac{1}{H}\frac{\partial h}{\partial y} - \frac{\sigma}{H}\frac{\partial H}{\partial y} \\
\frac{\partial \sigma}{\partial z^*} &= \frac{1}{H}
\end{aligned}
\tag{5.4}
$$

Substituting the equation (5.3) and the equation (5.4) into the advection terms in physical domain, the advection terms are transformed like

$$
\frac{\partial C}{\partial t} + \frac{\partial Cu}{\partial x} + \frac{\partial Cv}{\partial y} + \frac{\partial Cw_\sigma}{\partial \sigma} \tag{5.5}
$$

where

$$
w_\sigma = -\frac{\sigma}{H}\frac{\partial H}{\partial t} + \frac{u}{H}\frac{\partial h}{\partial x} - u\frac{\sigma}{H}\frac{\partial H}{\partial x} + \frac{v}{H}\frac{\partial h}{\partial y} - v\frac{\sigma}{H}\frac{\partial H}{\partial y} + \frac{w}{H} \tag{5.6}
$$

By applying the chain rule to the diffusion terms, the diffusion terms on the $\sigma$-coordinates can be expressed as

$$
\begin{aligned}
\frac{\partial}{\partial x^*}\left(D_x\frac{\partial C}{\partial x^*}\right) &= \frac{\partial}{\partial x}\left(D_x\frac{\partial C}{\partial x}\right) \\
&+ \frac{\partial}{\partial x}\left\{\frac{D_x}{H}\left(\frac{\partial h}{\partial x} - \sigma\frac{\partial H}{\partial x}\right)\frac{\partial C}{\partial \sigma}\right\} \\
&+ \frac{1}{H}\left(\frac{\partial h}{\partial x} - \sigma\frac{\partial H}{\partial x}\right)\frac{\partial}{\partial \sigma}\left(D_x\frac{\partial C}{\partial x}\right) \\
&+ \frac{1}{H}\left(\frac{\partial h}{\partial x} - \sigma\frac{\partial H}{\partial x}\right)\frac{\partial}{\partial \sigma}\left\{\frac{D_x}{H}\left(\frac{\partial h}{\partial x} - \sigma\frac{\partial H}{\partial x}\right)\frac{\partial C}{\partial \sigma}\right\}
\end{aligned}
\tag{5.7}
$$

$$\begin{aligned}\frac{\partial}{\partial y^*}\left(D_y\frac{\partial C}{\partial y^*}\right) &= \frac{\partial}{\partial y}\left(D_y\frac{\partial C}{\partial y}\right)\\ &+ \frac{\partial}{\partial y}\left\{\frac{D_y}{H}\left(\frac{\partial h}{\partial y}-\sigma\frac{\partial H}{\partial y}\right)\frac{\partial C}{\partial \sigma}\right\}\\ &+ \frac{1}{H}\left(\frac{\partial h}{\partial y}-\sigma\frac{\partial H}{\partial y}\right)\frac{\partial}{\partial \sigma}\left(D_y\frac{\partial C}{\partial y}\right)\\ &+ \frac{1}{H}\left(\frac{\partial h}{\partial x}-\sigma\frac{\partial H}{\partial y}\right)\frac{\partial}{\partial \sigma}\left\{\frac{D_x}{H}\left(\frac{\partial h}{\partial x}-\sigma\frac{\partial H}{\partial y}\right)\frac{\partial C}{\partial \sigma}\right\} \qquad (5.8)\end{aligned}$$

$$\frac{\partial}{\partial z^*}\left(D_z\frac{\partial C}{\partial z^*}\right) = \frac{1}{H^2}\frac{\partial}{\partial \sigma}\left(D_z\frac{\partial C}{\partial \sigma}\right) \qquad (5.9)$$

Multiplying the transformed advection terms and diffusion terms by $H$, the advection-diffusion equation becomes conservative form which has the same numerical property with the Boussinesq equations model proposed in this study.

$$\begin{aligned}\frac{\partial HC}{\partial t} &+ \frac{\partial uHC}{\partial x}+\frac{\partial vHC}{\partial y}+\frac{\partial w_\sigma HC}{\partial \sigma}\\ &= H\frac{\partial}{\partial x}\left(D_x\frac{\partial C}{\partial x}\right)+H\frac{\partial}{\partial x}\left\{\frac{D_x}{H}\left(\frac{\partial h}{\partial x}-\sigma\frac{\partial H}{\partial x}\right)\frac{\partial C}{\partial \sigma}\right\}\\ &+ \left(\frac{\partial h}{\partial x}-\sigma\frac{\partial H}{\partial x}\right)\frac{\partial}{\partial \sigma}\left(D_x\frac{\partial C}{\partial x}\right)\\ &+ \left(\frac{\partial h}{\partial x}-\sigma\frac{\partial H}{\partial x}\right)\frac{\partial}{\partial \sigma}\left\{\frac{D_x}{H}\left(\frac{\partial h}{\partial x}-\sigma\frac{\partial H}{\partial x}\right)\frac{\partial C}{\partial \sigma}\right\}\\ &+ H\frac{\partial}{\partial y}\left(D_y\frac{\partial C}{\partial y}\right)+H\frac{\partial}{\partial y}\left\{\frac{D_y}{H}\left(\frac{\partial h}{\partial y}-\sigma\frac{\partial H}{\partial y}\right)\frac{\partial C}{\partial \sigma}\right\}\\ &+ \left(\frac{\partial h}{\partial y}-\sigma\frac{\partial H}{\partial y}\right)\frac{\partial}{\partial \sigma}\left(D_y\frac{\partial C}{\partial y}\right)\\ &+ \left(\frac{\partial h}{\partial x}-\sigma\frac{\partial H}{\partial y}\right)\frac{\partial}{\partial \sigma}\left\{\frac{D_x}{H}\left(\frac{\partial h}{\partial x}-\sigma\frac{\partial H}{\partial y}\right)\frac{\partial C}{\partial \sigma}\right\}\\ &+ \frac{1}{H}\frac{\partial}{\partial \sigma}\left(D_z\frac{\partial C}{\partial \sigma}\right) \qquad (5.10)\end{aligned}$$

### V.2.2. Boundary Conditions

Applying the chain rule to boundary conditions results in that Dirichlet boundary condition remains the same, but Neumann boundary condition is changed. At the bottom and at the water surface, it is changed like

$$\frac{\partial C}{\partial z^*} = \frac{1}{H}\frac{\partial C}{\partial \sigma} = 0 \tag{5.11}$$

and at the side walls, it is changed to

$$\frac{\partial C}{\partial x^*} = \frac{\partial C}{\partial x} + \left(\frac{1}{H}\frac{\partial h}{\partial x} - \frac{\sigma}{H}\frac{\partial H}{\partial x}\right)\frac{\partial C}{\partial \sigma} = 0 \tag{5.12}$$

Note that the variables in cartesian coordinate will be expressed without the ‘ * ’ from the following section for the convenience of expression.

## V.3. Numerical Methods and Tests for $\sigma$-Coordinate Transport Model

### V.3.1. Numerical Methods

Basically, the same numerical methods for the depth-integrated flow equations and depth-integrated transport equation are used again to solve the 3D $\sigma$-coordinate transport equation.

By integrating the equation over a cell, the equation becomes

$$\frac{\partial HC}{\partial t} + \frac{1}{\mathcal{V}}\sum \boldsymbol{F}\cdot A = 0 \tag{5.13}$$

where $\mathcal{V}$ is a volume of a computational cell, $\boldsymbol{F}$ is a flux vector evaluated at the cell interface, which is defined as $\boldsymbol{F} = CH\boldsymbol{U}$, the $\boldsymbol{U} = (u, v, \omega_\sigma)$, and the $A$ is a cell side

vector defined as the cell side area multiplied by the outward unit normal vector. To solve the advection terms, the fourth-order accurate MUSCL finite volume method (Yamamoto and Daiguji, 1993) with HLL Riemann solver (Toro, 1997) is used. To solve the diffusion terms, fourth-order finite volume discretization equations is used. The third-order Adams-Bashforth predictor and the fourth-order Adams-Moulton corrector scheme are used for the time integration as followings.

In predictor step,

$$C^{n+1} = C^n + \frac{\Delta t}{12}\left(23T^n - 16T^{n-1} + 5T^{n-2}\right) \tag{5.14}$$

In corrector step,

$$C^{n+1} = C^n + \frac{\Delta t}{24}\left(9T^{n+1} + 19T^n - 5T^{n-1} + T^{n-2}\right) \tag{5.15}$$

where the $T$ is given by

$$T = -\nabla \cdot HC\boldsymbol{U} + \nabla \cdot \left(\frac{\nu_t}{\sigma_t} H \nabla C\right) \tag{5.16}$$

The convergence error is defined as $\sum |C^{n+1} - C_*^{n+1}| / \sum |C^{n+1}|$ and it is required to be less than $10^{-4}$ to be converged in this study. More details can be referred to the chapters II and III.

### V.3.2. Advection-Diffusion Tests in $\sigma$-Coordinate System

As a basic numerical test, a pure advection problem is tested. In physical space, the gird has two vertical side boundaries and flat water surface boundary. However, as shown in the Figure 65, the bottom boundary has a sinusoidal curve of

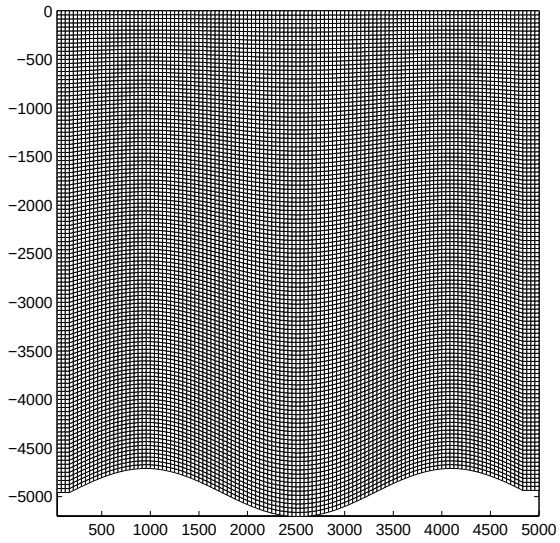


Figure 65. Non-rectangular physical domain for test problem.

$$h\left(x\right) = 250 \times \sin\left(0.002x\right) - 5000 \tag{5.17}$$

so, the wave height of the bathymetry is 10% of the median water depth and the maximum bottom slope becomes $S_b = 0.5$.

The flow is rotating about the center of the domain with a constant angular velocity $0.314 rad/hr$, so it rotates one circle per 20 hours. The initial concentration is given by

$$C_o(x, y) = \exp\left\{-\frac{(x - x_c)^2 + (z - z_c)^2}{2\theta^2}\right\} \tag{5.18}$$

where $x_c = 1250m$ and $z_c = -2500m$ and the $\theta = 220m$. The computational domain is composed of $125 \times 125$ grids with $\Delta x = \Delta y = 40m$ and the $\Delta t = 40$ second is used.

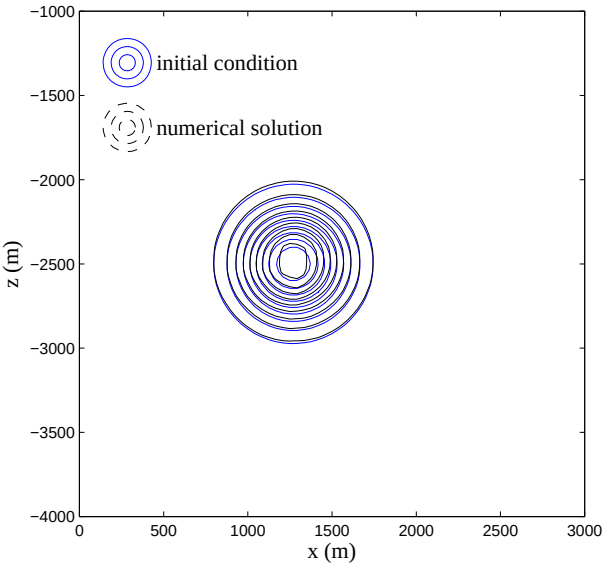


Figure 66. Pure advection test results after one circulation.

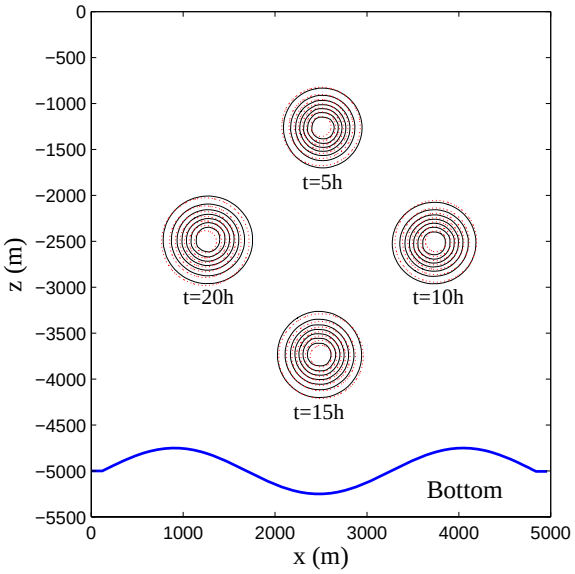


Figure 67. Advection-diffusion test results. Solid line: computational results, dotted line: analytical solutions.

The Figure 66 shows the initial condition and the computed result at $t = 20$ hour. Very close agreement with the analytical solution is obtained.

An advection-diffusion problem was tested in the same flow field and the same computational grid. For the diffusion, the $D_x = D_z = 0.1m^2/s$ were given. In the initial concentration profile equations, the $\theta = 200m$ was used. The Figure 67 shows the comparisons between the analytical solutions (Wang et al., 1999) and the computed results at $t = 5$, $t = 10$, $t = 15$, and $t = 20$ hour. Good agreements with the analytical solutions are obtained in the advection-diffusion test, too.

## V.4. Velocity Profiles and Coupling

In many literatures, successful applications of the Boussinesq equations models have been reported. However, usually the successes were focused to the water surface profiles, not to the vertical profiles of the currents. In near shore areas, although the water depth scale is relatively small to the horizontal length scale, the variations of the velocity into the vertical direction like undertow is not small enough to be neglected. However, it was recognized that the many Boussinesq equations models yielded very poor prediction of undertow flow (Lynett, 2006). Even in a steady flow in a prismatic channel, they would predict vertically constant velocity profiles, physically which is not true. In this study, by including the horizontal vorticity, physically reasonable velocity profile into the vertical direction could be estimated in open channel flows as shown in the section II.5.2.

Based on the $(\zeta, U, V)$ resulted from the Boussinesq equations model, the horizontal velocity at $z$ can be obtained by

$$
\begin{aligned}
u = U &+ \frac{1}{2}\left(z_\alpha^2 - z^2\right)\frac{\partial}{\partial x}\left(\frac{\partial U}{\partial x} + \frac{\partial V}{\partial y}\right) \\
&+ \left(z_a - z\right)\frac{\partial}{\partial x}\left(\frac{\partial hU}{\partial x} + \frac{\partial hV}{\partial y}\right) \\
&+ \psi^x\left\{\frac{1}{2}\left(z_\alpha^2 - z^2\right) + \zeta\left(z - z_\alpha\right)\right\}
\end{aligned} \tag{5.19}
$$

$$
\begin{aligned}
v = V &+ \frac{1}{2}\left(z_\alpha^2 - z^2\right)\frac{\partial}{\partial y}\left(\frac{\partial U}{\partial x} + \frac{\partial V}{\partial y}\right) \\
&+ \left(z_a - z\right)\frac{\partial}{\partial y}\left(\frac{\partial hU}{\partial x} + \frac{\partial hV}{\partial y}\right) \\
&+ \psi^y\left\{\frac{1}{2}\left(z_\alpha^2 - z^2\right) + \zeta\left(z - z_\alpha\right)\right\}
\end{aligned} \tag{5.20}
$$

and the vertical velocity at $z$ is given by

$$
w = -z\left(\frac{\partial u}{\partial x} + \frac{\partial v}{\partial y}\right) - \left(\frac{\partial hu}{\partial x} + \frac{\partial hv}{\partial y}\right) \tag{5.21}
$$

These equations (5.19), (5.20) and (5.21) are transferred to the transport equation solver.

For the verifications of the velocity profile in surf zone where undertows are strong, two comparisons will be presented in this section. Firstly, the laboratory experimental data by Ting and Kirby (1994) are compared with the velocity profile by the equation (5.19). In their experiment, wave train with $0.089m$ wave height and 5.0 second period was generated on horizontal plane with $h = 0.4m$. On opposite side, a 1/35 sloped bottom was installed. For another comparison, the experimental data by Nadaoka and Kondoh (1982) is used. In their experiment, the wave height was $0.219m$, the wave period was 2.34 second, and the water depth was $h = 0.7m$

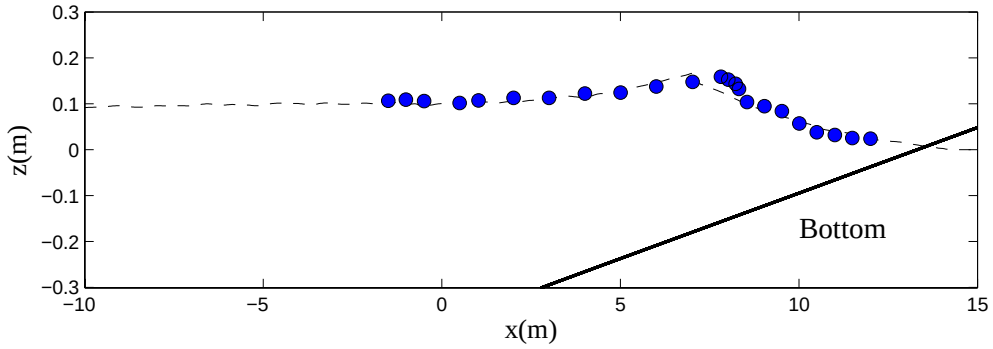


Figure 68. Comparison of the crest level based on the phase averaged water surface elevation. Dots: measured data (by Ting and Kirby, 1994). Line: numerical results.

at the offshore site. The slope of the shore was 1/20. More details of the laboratory experiments are well described in the two literatures.

The Figure 68 shows the crest elevation of the waves based on the phase averaged water surface elevation. As can be seen from the figure, good agreements were obtained. Based on the numerical results, the 3D velocity information can be estimated by the equations (5.19), (5.20) and (5.21). The results are plotted in the Figure 69: Here, the comparisons between the measured data, computed results by Boussinesq equations model and Navier-Stokes equations model with $k - \varepsilon$ turbulence closure (Lin and Liu, 1998) are presented. For the undertow profiles, acceptable agreements with the measured data were obtained. For the wave parts above undertow layer, also good agreements with the Navier-Stokes equations model were obtained. For the Nadaoka and Kondoh's case, the measured data and the numerical results are plotted in the Figure 70. Although some disagreements are observed at $x = 2.14m$ and $x = 3.14m$, they are within good agreements from the bottom to the water surface

in overall sense.

In conclusion, the proposed Boussinesq equations model can present good information of the vertical structure of velocity. Hence good scalar transport prediction is expected by coupling with the $\sigma$-coordinate transport model.

## V.5. Turbulent Transport Simulation in Near Field

### V.5.1. Quantitative Verification in Open Channel Flow

For the quantitative validation purpose, two laboratory experimental cases were simulated numerically with the proposed model. The experiments were done by Nokes and Wood (1988) in a $12m$ long, $0.56m$ wide and $0.43m$ deep channel. The cross section was rectangular and the slope of the bottom was 0.00047. The water depth was $0.05m$ and the streamwise direction velocity was $0.236m/s$ resulting in the $Re = 10700$. The friction factor was estimated $f = 0.0282$ by the experiment.

For all the turbulent transport simulation, the turbulent diffusion coefficients are assumed to be the same with the turbulent eddy viscosities, that is, $D_x = D_y = \nu_t^h/\sigma_t$ and $D_z = \nu_t^v/\sigma_t$, where the turbulent Schmidt number $\sigma_t = 1.0$.

Similar to the results in the section II.5.2, the horizontal vorticity effects related with the bottom shear stress make the horizontal velocity variant into the vertical direction as shown in the Figure 71. The computational results in the Figure 71 are the time averaged data with $\Delta x = \Delta y = 0.025m$ and $\Delta\sigma = 1/21$. Of course, the Boussinesq equations models which are based on potential flow theory or which do not consider the horizontal vorticity effects should have almost constant velocity profile.

At the two different levels (at $\sigma = 0.24$ or $\sigma = 0.57$), the contaminants were released continuously. The instantaneous scalar distribution by the numerical sim-

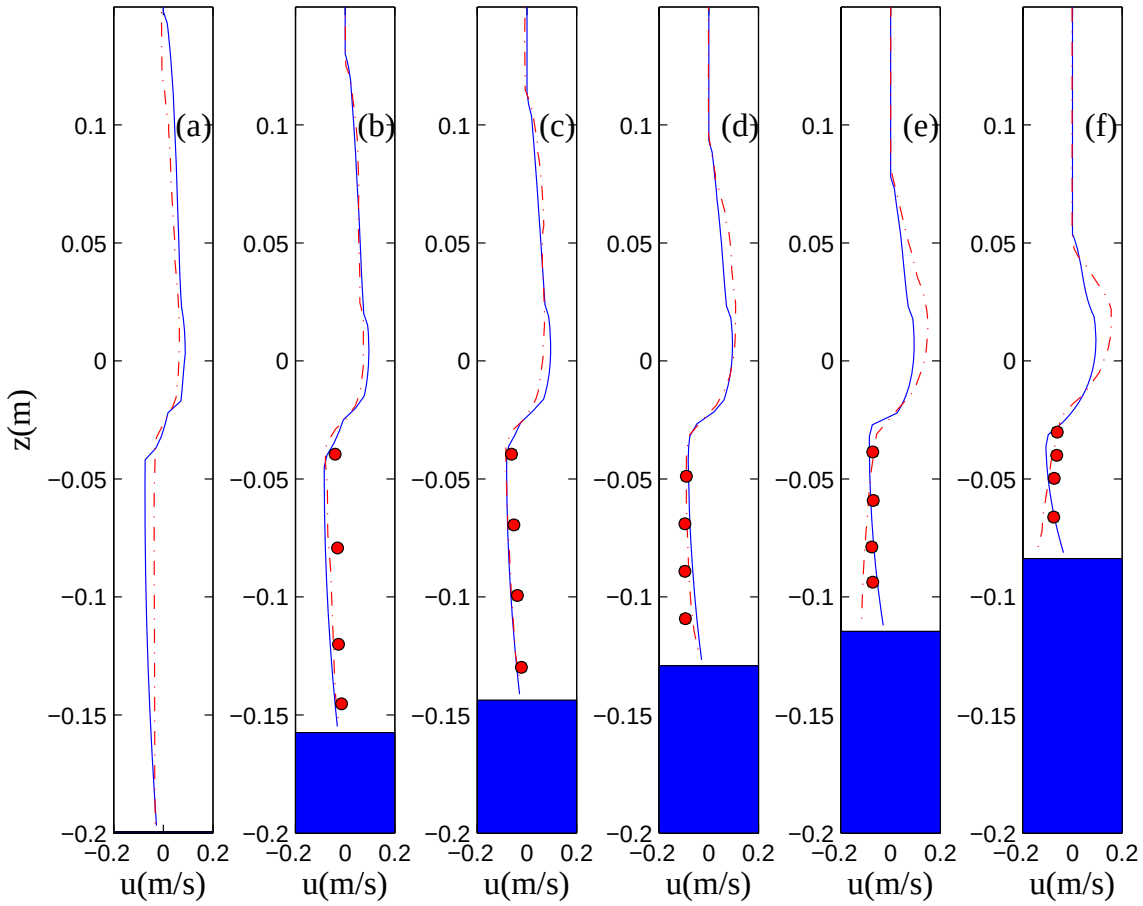


Figure 69. Vertical profiles of phase averaged horizontal velocity. (a)$x = 6.3m$, (b)$x = 7.8m$, (c)$x = 8.3m$, (d)$x = 8.8m$, (e)$x = 9.3m$, (f)$x = 10.4m$. Dots: experimental data (by Ting and Kirby, 1994). Solid line: numerical results. Dotted lines: Navier-Stokes equations model (by Lin and Liu, 1998).

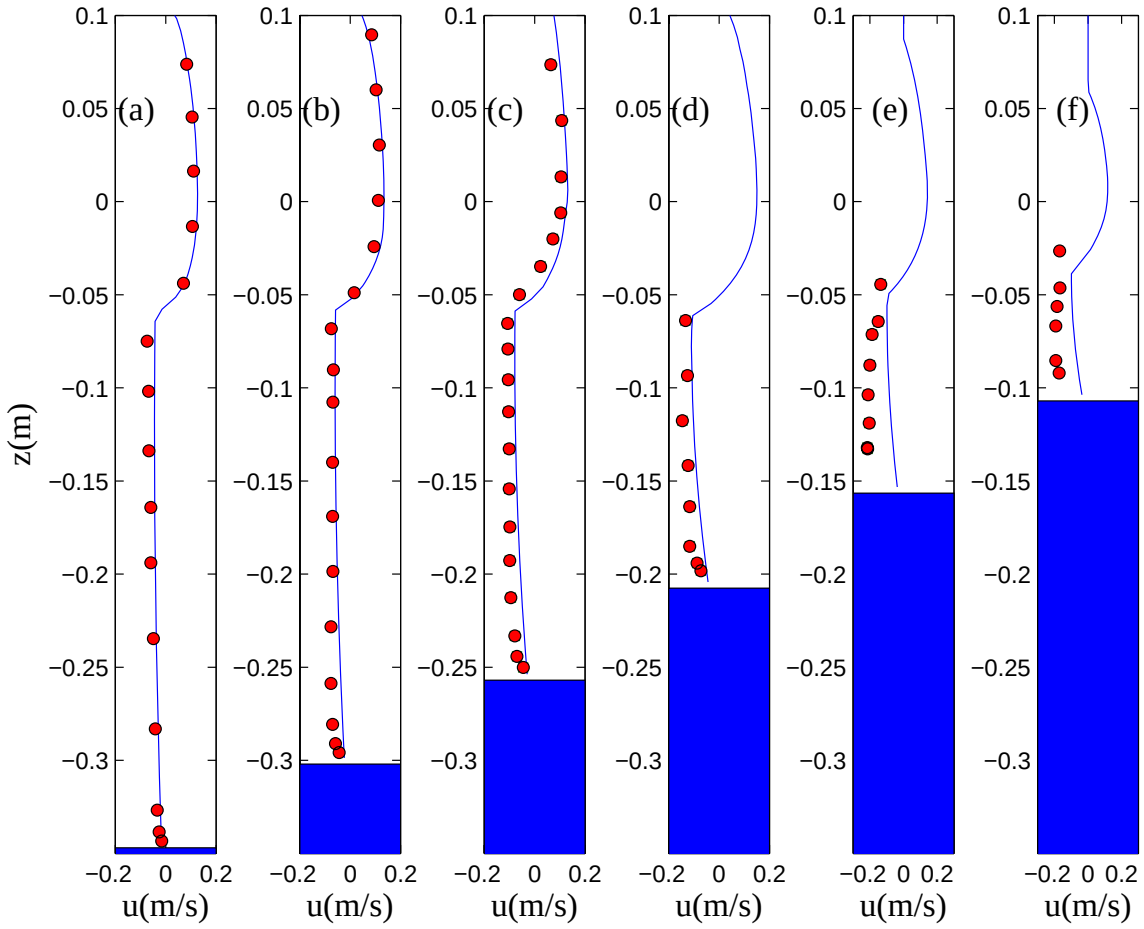


Figure 70. Vertical profiles of phase averaged horizontal velocity. (a)$x = 6.94m$, (b)$x = 6.04m$, (c)$x = 5.14m$, (d)$x = 4.14m$, (e)$x = 3.14m$, (f)$x = 2.14m$. Dots: experimental data (by Nadaoka and Kondoh, 1982). Solid line: numerical results.

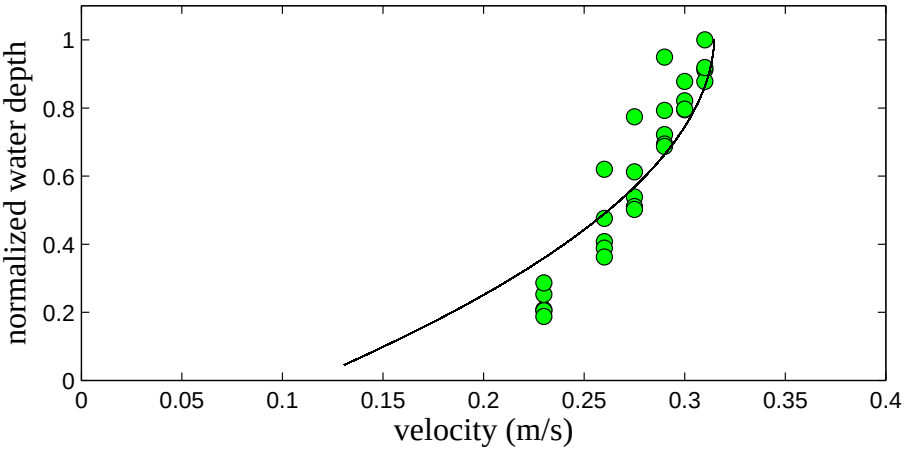


Figure 71. Time averaged velocity distribution, circle: experimental data (by Nokes and Wood, 1988), line: computational result.

ulations were described in the Figure 72. Definitely, the injection location affected to the concentration distribution greatly. The parabolic structures can be observed clearly in the figures, which are captured by the turbulence based on the stochastic BSM and the effects of the horizontal vorticity.

For the quantitative verification, time averaged concentration data at various locations and levels were compared. As in the Figure 73 and Figure 74, the measured concentration data and the computed concentration results are within very good agreements. Especially, even in the near field ($x/h <\sim 10$), the computational results are closely matched to the measured data, which is beyond of the inherent limitations of the 2D horizontal transport model. Therefore it can be concluded that the proposed $\sigma$-coordinated transport model coupled with the Boussinesq model is good for both near field and far field transport predictions.

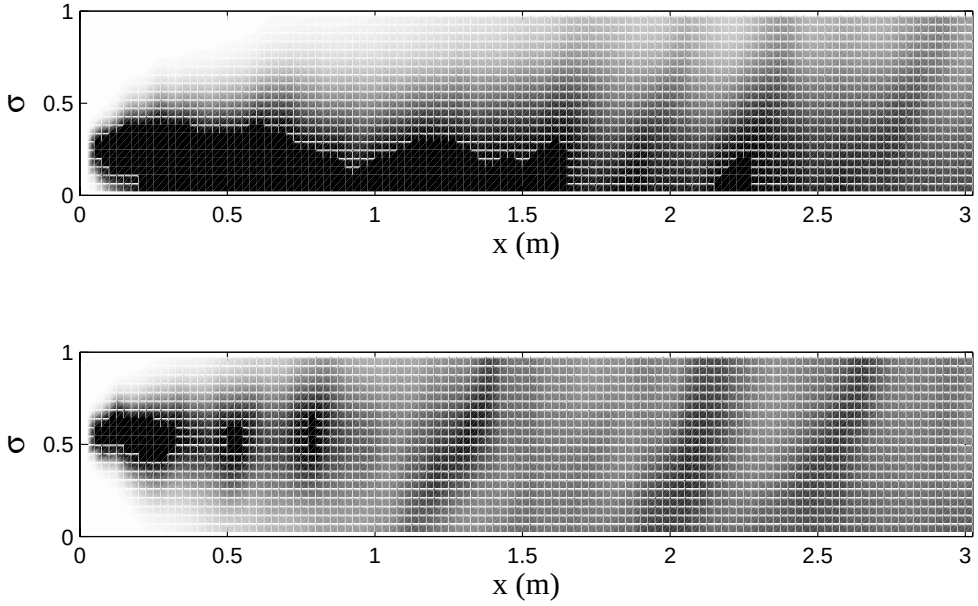


Figure 72. Instantaneous computed concentration distribution (black color means higher concentration). Upper: injection level $\sigma = 0.24$, lower: injection level $\sigma = 0.57$.

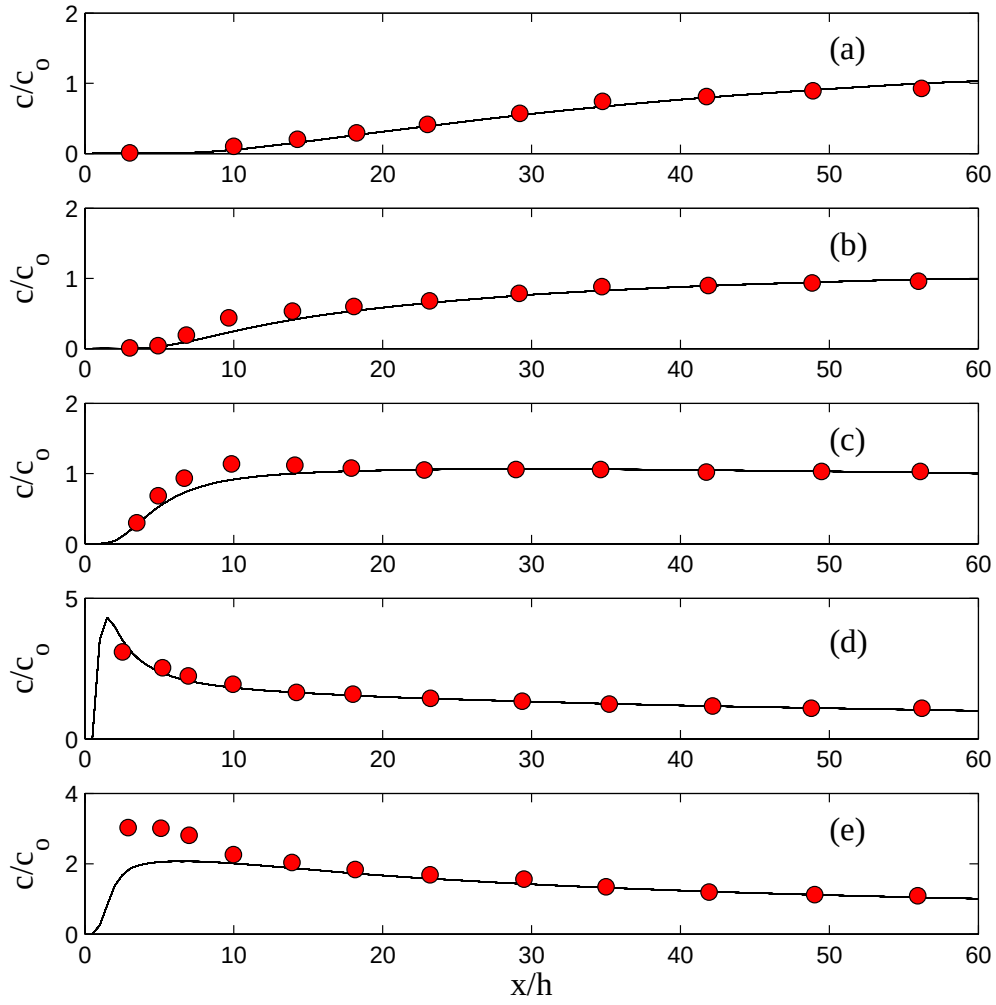


Figure 73. Time averaged concentration distributions at various level (source height $\sigma = 0.24$). (a) at $\sigma = 0.9$, (b) at $\sigma = 0.7$, (c) at $\sigma = 0.5$, (d) at $\sigma = 0.3$, (e) at $\sigma = 0.1$. Circle: measured data (Nokes and Wood, 1988). Line: computational results.

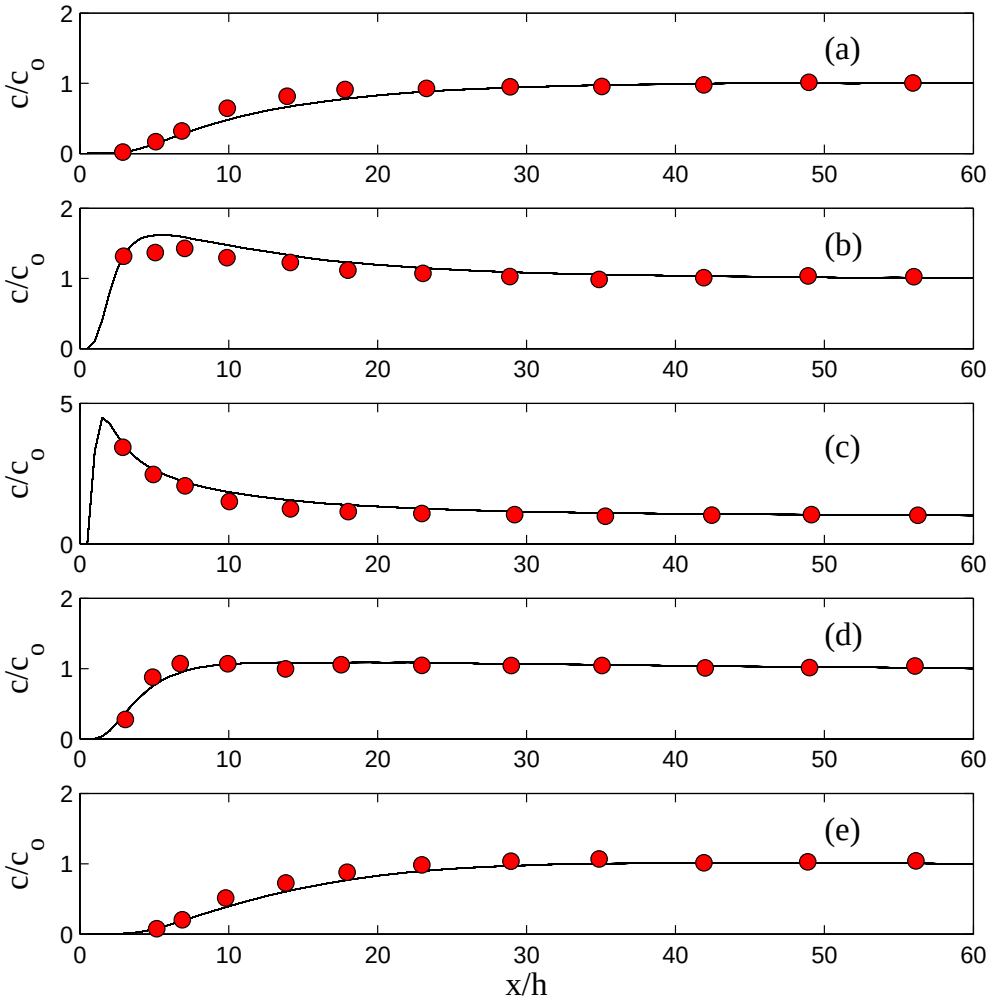


Figure 74. Time averaged concentration distributions at various level (source height $\sigma = 0.57$). (a) at $\sigma = 0.9$, (b) at $\sigma = 0.7$, (c) at $\sigma = 0.5$, (d) at $\sigma = 0.3$, (e) at $\sigma = 0.1$. Circle: measured data (Nokes and Wood, 1988). Line: computational results.

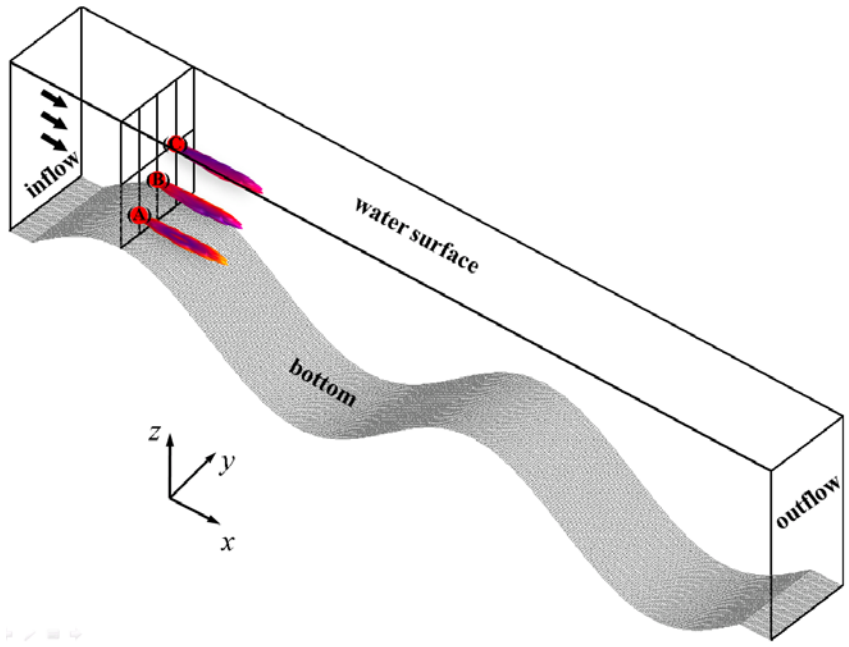


Figure 75. Schematic of sinusoidal bathymetry channel. Red spots are the sources of the passive scalar. (A) $\sigma = 0.16$, (B) $\sigma = 0.32$, (C) $\sigma = 0.48$.

### V.5.2. Transport Simulation in Open Channel with Wavy Bottom

For a test of computational aspect of the $\sigma$-coordinate, a similar test with the previous simulation is conducted on wavy bathymetry. The length of channel is $40h_o$ and the amplitude of the bottom bathymetry is $0.25h_o$, where the $h_o$ is the water depth at inlet section. A constant flow with $U = 0.12m/s$ is released at the upstream boundary, resulting in the Reynolds number $Re = 11800$. The scalar sources are released at three different levels on the first crest section as shown in the Figure 75.

The Figures 76 show the instantaneous concentration distribution of the numerical simulation. For the clear description of the results, the each of the iso-surfaces of concentration are sliced out above from $\sigma = 0.48$ (for the case C), from $\sigma = 0.32$

(for the case B), and from $\sigma = 0.16$ (for the case A). As can be seen clearly from the Figures 76, the depth dependent results, important characteristic of the near field mixing, were captured well by the proposed model.

### V.5.3. Transport in Surf Zone

In this section, the applicability to a surf zone of the proposed model is tested. The surf zone is composed of a beach with a constant slope of 1/35 and a horizontal plane with $h = 0.4m$. The wave source is located at $x = 10m$ and a sponge layer is installed at the left boundary, as shown in the Figure 77. Close to the breaking point, two initial contaminants are located at two different locations, one on the bottom (case A) and the other beneath the water surface (case B). The two cases are simulated separately.

A regular wave series with the $0.086m$ amplitude, the period of 3.33 second and the wave length of $L = 6.44m$ were generated at the source. For the calculations of the bottom friction terms, $k_s = 0.0001m$ was used. The breaking eddy viscosity term is added to the turbulent eddy viscosity terms for these simulations. The whole computational domain is composed of $600 \times 30$ cells. These input conditions resulted in the vertically varying flow structures as plotted in the Figure 78.

The Figures 79 show the computed scalar distributions for the case A. By the vertical velocity components the scalar is partially advected from the bottom to the water surface and carried toward the shore by the waves as can be seen at the Figures 79 (a), (c), (e) and (g). However, the scalar which is transported to the water surface by the advection and diffusion does not follow the progressive wave. Soon, as can be seen the Figures 79 (b), (d), (f) and (h), the cloud of the scalar is detached from the peaks of the waves. Near the bottom, the cloud of the scalar moved seaward direction in overall sense. Similar phenomenon was observed in the numerical simulation by

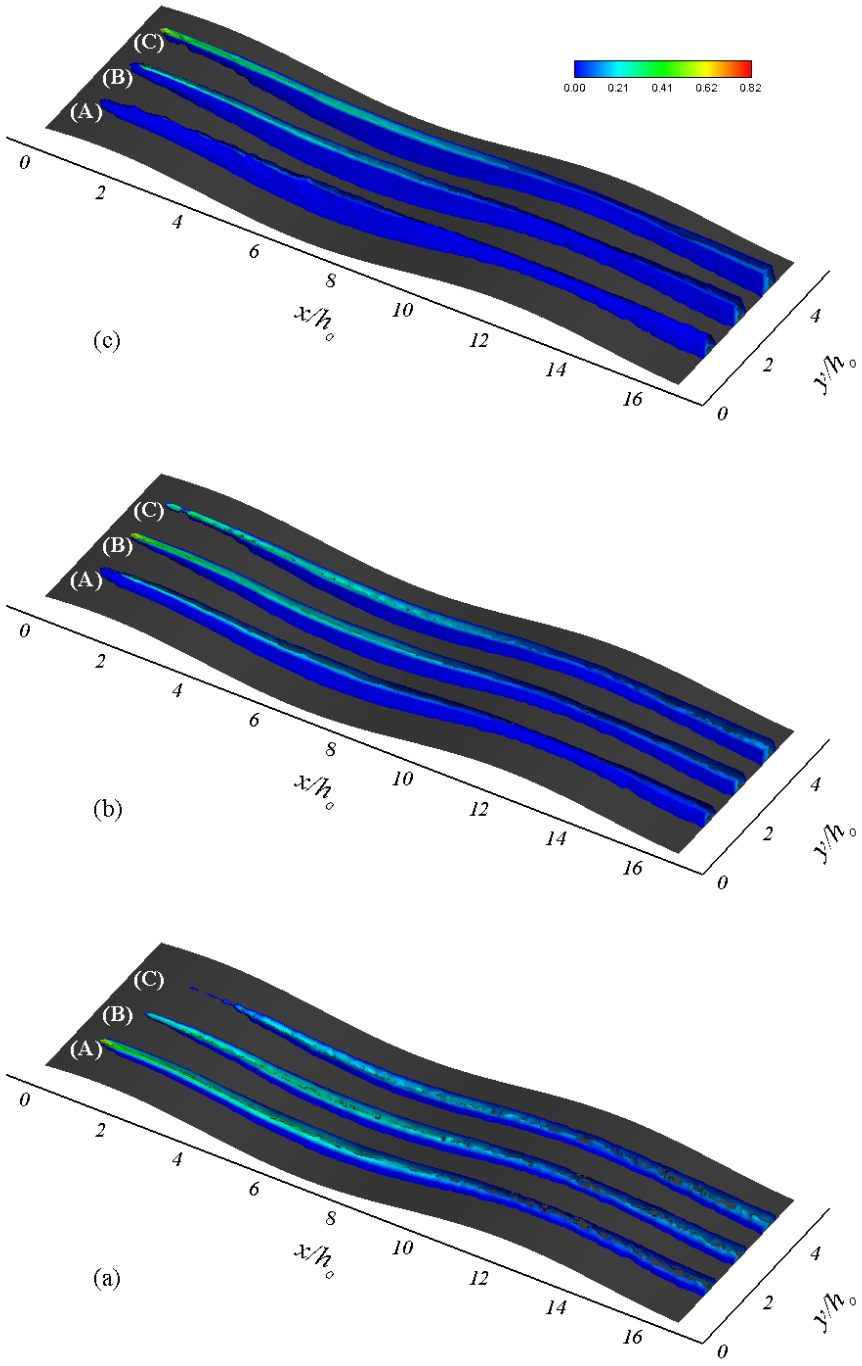


Figure 76. Instantaneous relative concentration ($C/C_{source}$). The iso-surfaces of concentration are sliced at (a) $\sigma = 0.16$, (b) $\sigma = 0.32$, (c) $\sigma = 0.48$.

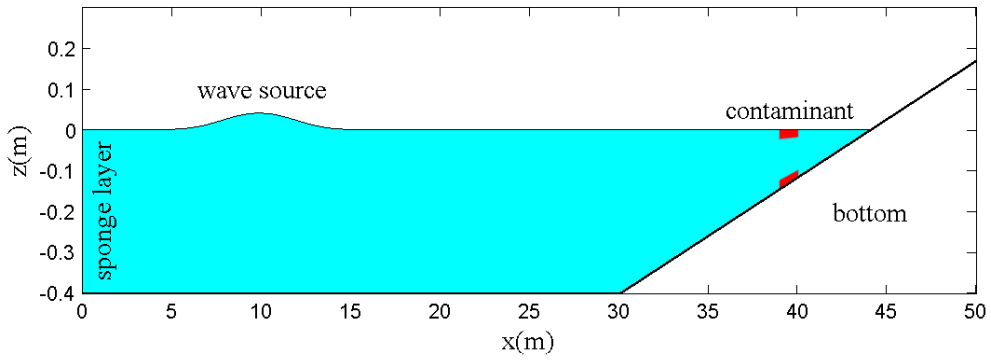


Figure 77. Schematic of the surf zone transport test problem.

a Navier-Stokes equations model with $k - \epsilon$ turbulence closure (Lin and Liu, 1998). For the case B, near the surface, the cloud of the scalar is transported to shoreline as shown in the Figure 80. These opposite movements of the case A and B could be expected by looking the velocity distributions in the Figure 69 and Figure 70. However, also in this case B, the scalar was detached from the progressive wave like the case A.

## V.6. Summary

For the accurate near field mixing prediction, a 3D $\sigma$-coordinate transport model coupled with Boussinesq equations model was developed. Basic advection test and advection-diffusion test showed good agreements with analytic solutions. The velocity information estimated by the Boussinesq equations model agreed with the measurements in open channel flow and surf zone reasonably. From the comparisons with the dispersion experiments data, quantitative verification of the proposed model for the near field and far field mixing was recognized. From the simulations in open channel

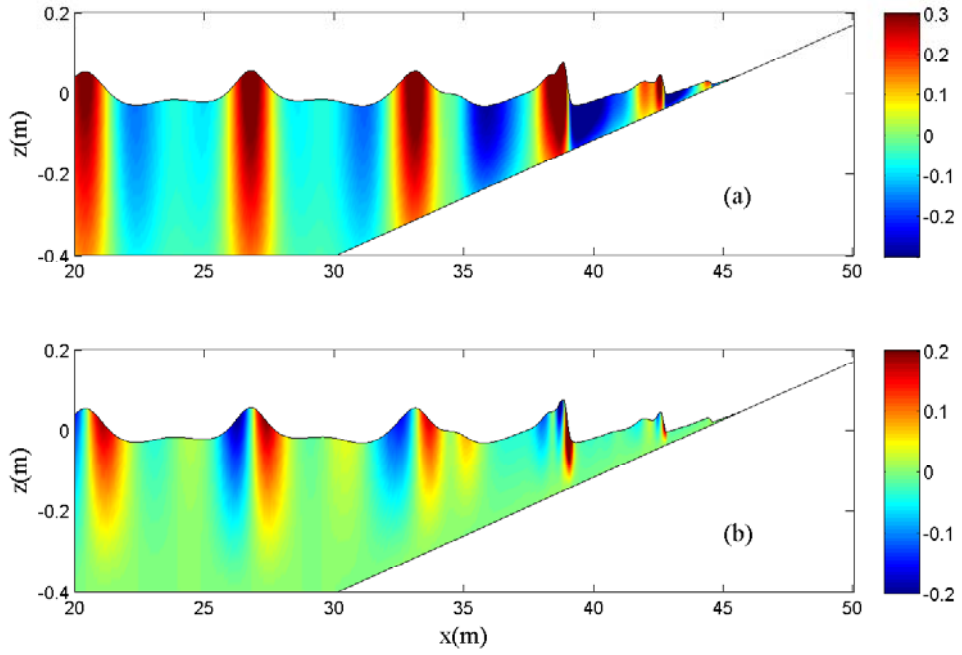


Figure 78. Snapshot of velocity distributions by Boussinesq equations model. (a) horizontal velocity $(m/s)$, (b) vertical velocity $(m/s)$. Positive value represents shoreward direction.

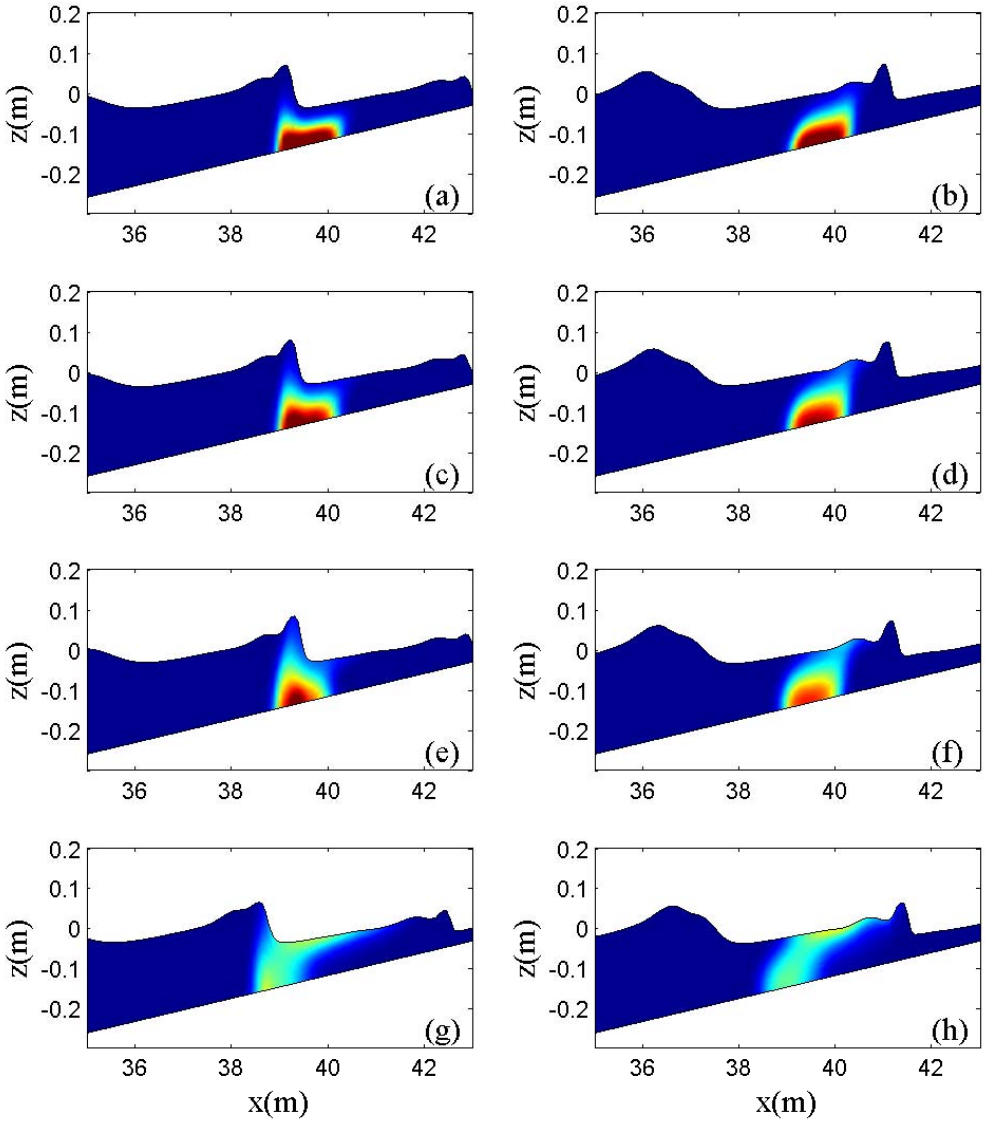


Figure 79. Scalar concentration by the numerical simulation for case A. (a)$t = 25.4s$, (b)$t = 27.0s$, (c)$t = 28.8s$, (d)$t = 30.4s$, (e)$t = 32.3s$, (f)$t = 33.8s$, (g)$t = 55.0s$, (h)$t = 57.3s$.

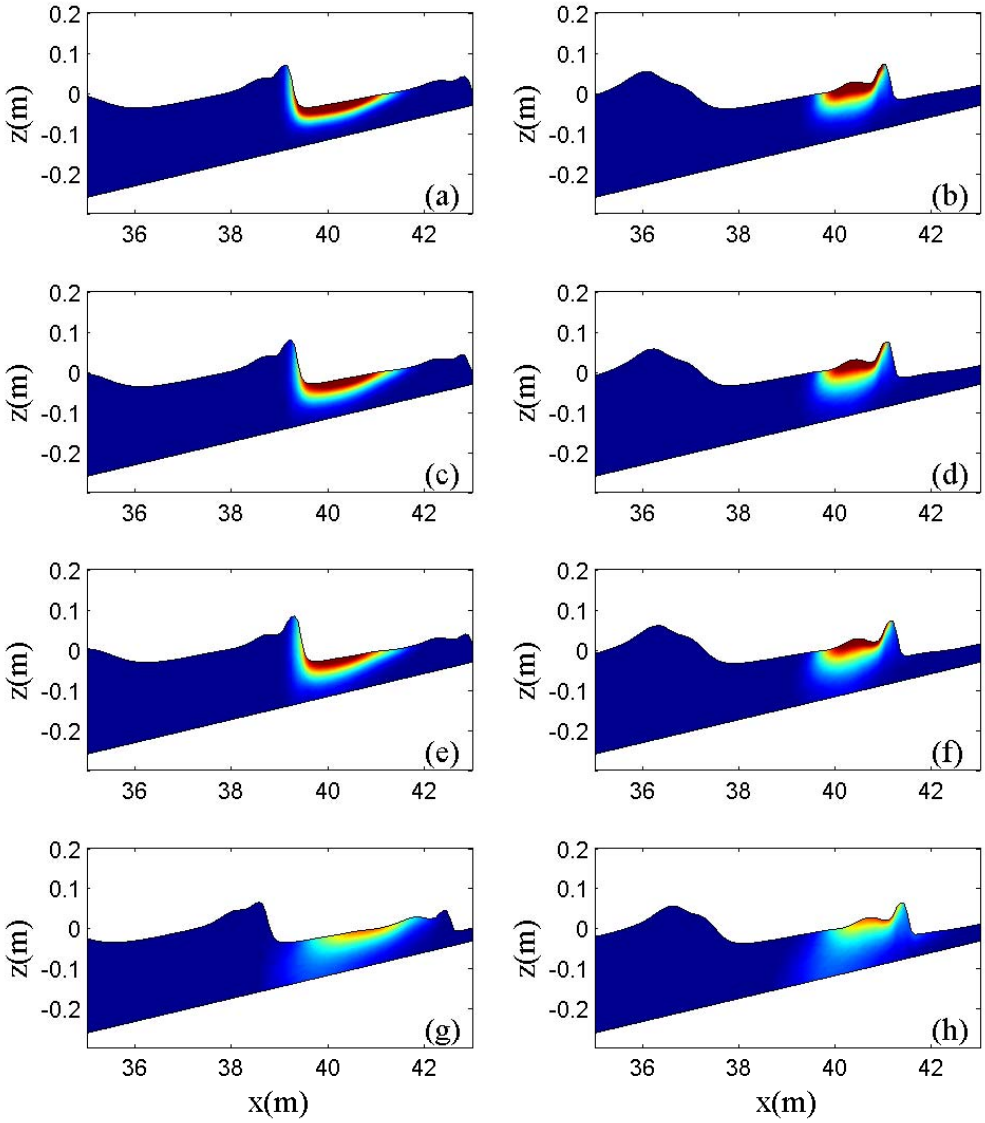


Figure 80. Scalar concentration by the numerical simulation for case B. (a)$t = 25.4s$, (b)$t = 27.0s$, (c)$t = 28.8s$, (d)$t = 30.4s$, (e)$t = 32.3s$, (f)$t = 33.8s$, (g)$t = 55.0s$, (h)$t = 57.3s$.

flow and surf zone, physically reasonable results were obtained. Therefore, it can be concluded that the proposed model is good for the near field and far field scalar transport predictions together.

# CHAPTER VI
# CONCLUSIONS AND FUTURE WORKS

## VI.1. Conclusions

In the first part of this dissertation a set of weakly dispersive Boussinesq equations, derived to include viscosity and vorticity terms in a physically consistent manner, was presented in conservative form. The model includes the approximate effects of bottom-induced turbulence, in a depth-integrated sense, as a high-order correction. Associated with this turbulence, vertical and horizontal rotational effects are captured. While the turbulence and horizontal vorticity models are simplified, a model with known physical limitations has been derived that includes the quadratic bottom friction term commonly added in an ad-hoc manner to the inviscid equations. An interesting result of this derivation is that one should take care when adding such ad-hoc models; it is clear from this study that:

(i) it is not necessary to do so - the terms can be included through a consistent derivation from the viscous primitive equations, that is Navier-Stokes equations.

(ii) one cannot properly add the quadratic bottom friction term without also adding a number of additional terms in the integrated governing equations.

To solve these equations numerically, a highly accurate and stable model was developed. The numerical method uses a fourth-order MUSCL-TVD scheme to solve the leading order (shallow water) terms. For the dispersive terms, a cell averaged finite volume method was implemented.

To verify the derived equations and the numerical model, four cases of verifications were given. First, solitary wave propagation was examined as a basic, yet fundamental, test of the models ability to predict dispersive and nonlinear wave

propagation with minimal numerical error. Vertical velocity distributions of spatially uniform flows were compared with existing theory to investigate the effects of the newly included horizontal vorticity terms. Other test cases include comparisons with experiments that generate obvious coherent structures by the change of bottom bathymetry as well as by tidal jets through inlet structures. Very reasonable agreements were observed for the four cases, and the results provide some information as to the importance of dispersion and horizontal vorticity.

For the simulations of the turbulent transport by long waves and currents, a depth-integrated model for turbulent flow and transport was presented. Based on the depth-integrated flow equations derived in the first part, the 3D turbulent effects were included by the consistent perturbation approach. The same approach was applied to derive a depth-integrated scalar transport equation based on the same scaling. The proposed transport equation was solved by a fourth-order accurate finite volume method. The numerical solver of transport equation showed very small error of numerical dispersion, dissipation and diffusion. The depth-integrated flow and transport models were applied to typical problems which have different mixing mechanisms. Four important conclusions were obtained from the numerical simulations:

(i) From the mixing layer simulation, it was revealed that the 3D turbulence effects implemented with a stochastic BSM played an important role for the energy transfer.

(ii) The proposed transport model coupled with the depth-integrated flow model can predict the passive scalar transport physically (based on the turbulent intensity) not by relying on an empirical constant.

(iii) The 2D horizontal transport model has an inherent limitation for near field mixing prediction.

(iv) In the mixing simulations by the topographical forcing, the effects of the 3D turbulence effects were less important relative to the other cases because the main mechanism of the instability were originated from the bottom topography.

To extend the applicable areas, a robust moving boundary scheme based on a simple physical condition was developed and verified. Several typical benchmark problems such as dam-break flows and tsunami wave fission were tested in the 1D and 2D spaces. Generally, the computed results by the Boussinesq equations model based on the nonhydrostatic pressure assumption seemed to be more accurate and physical than the results by the shallow water equations model based on the hydrostatic pressure assumption. One of the most challenging cases, the re-entrance flow into the lee side of a surfacing piercing structure showed very reasonable agreements with experimental data. In the Okushri tsunami simulations, complex physics and topography of the experiment were very well dealt with the proposed model. Therefore, it can be concluded that the proposed numerical model is able to provide very reliable results of the wave and current transformations including shocks and undular bores on complex bathymetry and topography.

For the near field mixing prediction, a $\sigma$-coordinate transport model coupled with Boussinesq equations model was developed. The irregular physical domain between the uneven bottom bathymetry and water surface are transformed to the rectangular shaped $\sigma$-coordinate. The velocity information estimated by the Boussinesq equations model agreed with the experimental data in open channel flow and surf zone reasonably. Basic advection test and advection-diffusion test were done and good agreements with analytic solutions were obtained. From the comparisons with the dispersion experiments, quantitative verification of the proposed model for near field and far field mixing was recognized. From the other simulations in open channel flow and surf zone, physically reasonable results were obtained. Finally, it can be

concluded that the proposed model is good for both the near field and far field scalar transport predictions.

## VI.2. Future Works

Numerous works can improve the products proposed by this study. In the view of physics, to add the mechanism of the stratified flow will be a valuable achievement. More general shear stress model including the boundary layer effects can make the vorticity effects physically meaningful much more. Possibly, it may be able to link to the development a new wave breaking mechanism for depth-integrated flow model.

To couple with a sediment transport and morphology change model will be a very interesting and practical topic.

In the view of computational methods, more robust and efficient numerical solver should be pursued. The numerical model using the boundary fitted grid system or unstructured grid system should be developed for the complex geometry applications. An explicit solver for the depth-integrate equations solution or the parallel solver can save the computational time greatly.

All these would require great efforts but appreciable greatly.

# REFERENCES

Alvelius, K. (1999) "Random Forcing of Three-Dimensional Homogeneous Turbulence." *Physics of Fluids*, 11, 1880-1889.

Babarutsi, S. and Chu, V. H. (1998) "Modeling Transeverse Mixing Layer in Shallow Open-Channel Flows." *Journal of Hydraulic Engineering*, 124, 718-727.

Blumberg, A.F. and Mellor, G.L. (1983) "Diagnostic and Prognostic Numerical Circulation Studies of the South Atlantic Bight." *Journal of Geophysics Research*, 88, 4579-4592.

Boussinesq, M.J. (1872) " Thorie des Ondes et des Remous Qui se Propagent le Long d'un Canal Rectangulaire Horizontal, en Communiquant au Liquide Contenu Dans ce Canal des Vitesses Sensiblement Pareilles de la Surface au Fond." *Journal de Mathmatique Pures et Appliques, Deuxime Srie*, 17, 55-108.

Carmer, C.F. (2005) "Shallow Turbulent Wake Flows: Momentum and Mass Transfer due to Large-Scale Coherent Vortical Structures." University of Karlsruhe. Germany.

Carmo, J.S., Santos, F.J., and Almeida, A.B. (1993) "Numerical Solution of the Generalized Serre Equations with the MacCormack Finite Difference Scheme." *International Journal for Numerical Methods in Fluids*, 16, 725-738.

Chaudhry (1993) "Open Channel Flow." Prentice Hall, London.

Chen, D. and Jirka, G.H. (1995) "Experimental Study of Plane Turbulent Wakes in a Shallow Water Layer." *Fluid Dynamics Research*, 16, 11-41.

Chen, Q. (2006) "Fully Nonlinear Boussinesq-Type Equations for Waves and Currents over Porous Beds." *Journal of Engineering Mechanics*, 132, 220-230.

Chen, Q., Kirby, J.T., Dalrymple, R.A., Kennedy, A.B., and Haller, C.M. (1999) "Boussinesq Modeling of a Rip Current System." *Journal of Geophysical Research*, 104, 20617-20637.

Chen, Q., Kirby, J.T., Dalrymple,R.A., Shi, F. and Thornton, E.B. (2003) "Boussinesq Modeling of Longshore Currents." *Journal of Geophysical Research*, 108, 3362-3380.

Dellar, P.J. and Salmon, R. (2005) "Shallow Water Equations with a Complete Coriolis Force and Topography." *Physics of Fluids*, 17, 106601.

Dodd, N. (1998) "Numerical Model of Wave Run-up, Overtopping and Regeneration." *Journal of Waterway, Port, Coastal, and Ocean Engineering*, 124, 73-81.

Elder, J.W., (1959) "The Dispersion of Marked Fluid in Turbulent Shear Flow." *Journal of Fluid Mechanics*, 5, 544-560.

Erduran, K.S., Ilic, S. and Kutija, V. (2005) "Hybrid Finite-Volume Finite-Difference Scheme for the Solution of Boussinesq Equations." *International Journal for Numerical Methods in Fluid*, 49, 1213-1232.

Fischer, H.B., List, E.J., Koh, R.C.Y., Imberger, J., and Brooks, N.H. (1979) "Mixing in Inland and Coastal Waters." Academic, New York.

French, R.H. (1994) "Open-Channel Hydraulics." McGraw-Hill, New York.

Haaland, S.E. (1983) "Simple and Explicit Formulars for the Friction Factor in Turbulent Pipe Flow." *Journal of Fluid Engineering*, 1, 89-90.

Haney, R.L. (1996) "On the Pressure Gradient Force over Steep Topography in $\sigma$-Coordinate Ocean Models." *Journal of Physical Oceanography*, 21, 610-619.

Hinterberger, C., Frohlich, J., and Rodi, W. (2007) "Three-Dimensional and Depth-Averaged Large-Eddy Simulations of Some Shallow Water Flows." *Journal of Hydraulic Engineering*, 133, 857-872.

Hsiao, S.C., Liu, P.L.F., and Chen, Y. (2002) "Nonlinear Water Waves Propagating over a Permeable Bed." *Proceedings of the Royal Society A*, 458, 1291-1322.

Hu, K., Mingham, C.G., and Causon, D.M. (2000) "Numerical Simulation of Wave Overtopping of Coastal Structure using the Non-linear Shallow Water Equation." *Coastal Engineering* 41, 433-465.

Hubbard, M., and Dodd, N. (2002) "A 2D Numerical Model of Wave Run-up and Overtopping." *Coastal Engineering*, 47, 1-26.

IMPACT (2004). www.impact-project.net.

Jirka, G.H. (2002) "Large Scale Flow Structures and Mixing Processes in Shallow Flows." *Journal of Hydraulic Research*, 39, 567-573.

Kennedy, A.B., Chen, Q., Kirby, J.T., and Dalrymple, R.A. (2000) "Boussinesq Modeling of Wave Transformation, Breaking, and Runup. I:1D." *Journal of Waterway, Port, Coastal, and Ocean Engineering*, 126, 39-47.

Kim, D.H., Cho, Y.S., and Kim, H.J. (2008) "Well Balanced Scheme between Flux and Source Terms for Computation of Shallow-Water Equations over

Irregular Bathymetry." *Journal of Engineering Mechanics*, 134, 277-290.

Kim, D.H., Cho, Y.S., and Kim, W.G. (2004) "Weighted Averaged Flux-Type Scheme for Shallow-Water Equations with Fractional Step Method." *Journal of Engineering Mechanics*, 130, 152-160.

Kim, D.-H., Lynett, P.J., and Socolofsky, S. (2009) "A Depth-Integrated Model for Weakly Dispersive, Turbulent, and Rotational Fluid Flows." *Ocean Modelling*, 27, 198-214.

Kobayashi, N., and Wurjanto, A. (1989) "Wave overtopping on coastal structures." *Journal of Waterway, Port, Coastal and Ocean Engineering*, 115, 235-251.

Kuipers, J.and Vreugdenhill, C.B. (1973) "Calculations of 2D horizontal flow." *Delft Hydraulics. Lab. Report*, S163, Part 1.

Lacor, C.A., Smirnov, S.A. and Baelmans, M. (2004) "A Finite Volume Formulation of Compact Central Schemes on Arbitrary Structured Grids." *Journal of Computational Physics*, 198, 535-566.

Lauber, G. and Hager, W.H. (1998) "Experiments to Dambreak Wave: Sloping Channel." *Journal of Hydraulic Research*, 36, 761-773.

Lee, S.O., Kim, S.J., Hwang, K.N., and Cho, Y.S. (2009) "Numerical Simulations of Scalar Transport with Full Diffusion Terms in the $\sigma$-Coordinate System." *Journal of Coastal Research*, SI 52, 141-148.

Lin, P., and Liu, P.L.F. (1998) "Turbulence Transport, Vorticity Dynamics, and Solute Mixing Under Plunging Breaking Waves in Surf Zone." *Journal of Geophysical Research*, 103, 15677-15694.

Lin, P., and Li, C.W. (2002) "A $\sigma$-Coordinate Three-Dimensional Numerical Model for Surface Wave Propagation." *International Journal for Numerical Methods in Fluids*, 38, 1045-1068.

Liu, P.L.F., Cho, Y.S., Briggs, M.J., Kanoglu, U., and Synolakis, C.E. (1995) "Runup of Solitary Waves on a Circular Island." *Journal of Fluid Mechanics*, 302, 259-285.

Lloyd, P.M., and Stansby, P.K. (1997a) "Shallow Water Flow around Model Conical Island of Small Slope. I: Surface Piercing." *Journal of Hydraulic Engineering*, 123, 1068-1077.

Lloyd, P.M., and Stansby, P.K. (1997b) "Shallow Water Flow around Model Conical Island of Small Slope. II: Submerged." *Journal of Hydraulic Engineering*, 123, 1068-1077.

Lynett, P.J. (2006) "Wave Breaking Effects in Depth-Integrated Models." *Coastal Engineering*, 53, 325-333.

Lynett, P.J., and Liu, P.L.F. (2004) "A Two-Layer Approach to Wave Modelling." *Proceedings of Royal Society of London A*, 460, 2637-2669.

Lynett, P.J., Melby, J., and Kim, D.H., (2009) "An Application of Boussinesq Modeling to Hurricane Wave Overtopping and Inundation." submitted to Ocean Engineering.

Lynett, P., Wu, T.-R., and Liu, P. L.-F. (2002) "Modeling Wave Runup with Depth-Integrated Equations." *Coastal Engineering*, 46, 89-107.

Madsen, P.A., Sorensen, O.R., and Schaffer, H.A. (1997) "Surf Zone Dynamics Simulated by a Boussinesq Type Model. Part I. Model Description and Cross-Shore motion of Regular Waves." *Coastal Engineering*, 32, 255-287.

Man, C., and Tsai, C.W. (2008) "A Higher-Order Predictor-Corrector Scheme for Two-Dimensional Advection-Diffusion Equation." *International Journal for Numerical Methods in Fluids*, 56, 401-418.

Matsuyama, M., Ikeno, M. Sakakiyama, T., and Takeda, T. (2007) "A Study of Tsunami Wave Fission in an Undistorted Experiment." *Pure and Applied Geophysics*, 164, 617-631.

Mignot, E., and Cienfuegos, R. (2008) "On the Application of a Boussinesq Model to River Flows including Shocks." *Coastal Engineering*, 56, 23-31.

Mohapatra, P.K., and Chaudhry, M.H. (2004) "Numerical Solution of Boussinesq Equations to Simulate Dam-Break Flows." *Journal of Hydraulic Engineering*, 130, 156-159.

Mingham, C.G., and Causon, D.M. (2008) "A Simple High-Resolution Advection Scheme." *International Journal for Numerical Methods in Fluids*, 56, 469-484.

Musumeci, R.E., Svendsen, I.A., and Veeramony, J. (2005) "The Flow in the Surf Zone: a Fully Nonlinear Boussinesq-type of Approach." *Coastal Engineering*, 52, 565-598.

Nadaoka, K., and Kondoh, T. (1982) "Laboratory of Measurements of Velocity Structure Field in the Surf Zone by LDV." *Coastal Engineering in Japan*, 25, 125-145.

Nadaoka, K., and Yagi, H. (1998) "Shallow-Water Turbulence Modeling and Horizontal Large-Eddy Computation of River Flow." *Journal of Hydraulic Engineering*, 124, 493-500.

NASA (2006) "Visible Earth", http://visibleearth.nasa.gov/.

Nicolau R.F. (2007) "Laboratory Studies of Eddy Structures and Exchange Processes through Tidal Inlets." MS thesis, Texas A&M University, College Station.

Nicolau R.F., Socolofsky, S.A., and Chang, K.A. (2009) "Structure and Evolution of Tidal Starting Jet Vortices at Idealized Barotropic Inlets." *Journal of Geophysical Research*, 114, c05024.

Nokes, R.I., and Wood, I.R. (1988) "Vertical and Lateral Turbulent Dispersion : Some Experimental Results." *Journal of Fluid Mechanics*, 187, 373-394.

Nwogu, O. (1993) "Alternative Form of Boussinesq Equations for Nearshore Wave Propagation." *Journal of Waterway, Port, Coastal, and Ocean Engineering*, 119, 618-638.

Peregrine, D.H. (1967) "Long Waves on a Beach." *Journal of Fluid Mechanics*, 27, 815-827.

Phillips, N.A. (1957) "A Coordinate System Having Some Special Advantages for Numerical Forecasting." *Journal of Meteorology*, 14, 184-185.

Rodi, W. (1980) "Turbulence Models and Their Application in Hydraulics - A State of the Art Review." IAHR, Netherlands.

Rummel, A.C., Socolofsky, S.A., Carmer, C.F., and Jirka, G.H. (2005) Enhanced Diffusion from a Continuous Point Source in Shallow Free-surface Flow with Grid Turbulence." *Physics of Fluids*, 17, 075105.

Shuto, N (1985), The Nihonkai-Chuubu Earthquake Tsunami on the North Akita Coast." *Coastal Engineering Journal*, JSCE, 28, 255-264.

Sitanggang, K. and Lynett, P, (2009) "Multi-scale Simulation with a Hybrid

Boussinesq-RANS Hydrodynamic Model." *International Journal of Numerical Methods in Fluids*, in press.

Smagorinsky, J. (1963) "General Circulation Experiments with Primitive Equations, I. the Basic Experiment." *Monthly Weather Review*, 91, 99-164.

Soares-Frazao, S. and Guinot, V. (2008) "A Second-Order Semi-Implicit Hybrid Scheme for One-Dimensional Boussinesq-Type Waves in Rectangular Channels." *International Journal for Numerical Methods in Fluids*, 58, 237-261.

Soares-Frazao, S. and Zech, Y. (1998) "Dam-break Flow through Sharp Bends Physical Model and 2D Boltzmann Model Validation." *Proceedings of the CADAM Meeting*. HR Wallingford, United Kingdom, 23 March.

Soares-Frazao, S. and Zech. Y. (2002a) "Dam Break in Channels with $90^o$ Bend." *Journal of Hydraulic Engineering*, 128, 956-968.

Soares-Frazao, S. and Zech. Y (2002b) "Undular Bores and Secondary Waves Experiments and Hybrid Finite-Volume Modelling." *Journal of Hydraulic Research*, 40, 33-43.

Stansby, P.K. (1997) "Semi-Implicit Finite Volume Shallow-Water Flow and Transport Solver with $k - \varepsilon$ Turbulence Model." *International Journal for Numerical Methods in Fluids*, 25, 285-313.

Stansby, P.K. (2003) "Solitary Wave Run Up and Overtopping by a Semi-Implicit Finite-Volume Shallow-Water Boussinesq Model." *Journal of Hydraulic Research*, 41, 639-647.

Stansby, P.K. and Zhou, J.G. (1998) "Shallow-Water Flow Solver with Non-Hydrostatic Pressure: 2D Vertical Plane Problems." *International Jour-*

*nal for Numerical Methods in Fluids*, 28, 541-563.

Synolakis, C.E. (1987) "The Runup of Solitary Waves." *Journal of Fluid Mechanics*, 185, 523-545.

Taylor, G. I. (1953) "Dispersion of Soluble Matter in a Solvent Flowing Slowly through a Tube." *Proceedings of the Royal Society of London, Series A*, 219, 186-203.

Ting, F.C.K., and Kirby, J.T. (1994) "Observation of Undertow and Turbulence in a Laboratory Surf Zone." *Coastal Engineering*, 24, 51-80.

Titov, V.V., and Synolakis, C.E. (1995) "Modeling of Breaking and Nonbreaking Long-Wave Evolution and Runup using VTCS-2." *Journal of Waterway, Port, Coastal and Ocean Engineering*, 121, 308-316.

Tonelli, M., and Petti, M. (2009) "Hybrid Finite Volume  Finite Difference Scheme for 2DH Improved Boussinesq Equations." *Coastal Engineering*, 56, 609-620.

Toro, E.F. (1997) *Riemann Solvers and Numerical Methods for Fluid Dynamics*. Springer-Verlag, London.

Toro, E.F. (2002) *Shock-Capturing Methods for Free-Surface Shallow Flows*, John Wiley & Sons, Singapore.

Treske, A. (1994) "Undular Bores (Favre-waves) in Open Channels - Experimental Studies." *Journal of Hydraulic Research*, 32, 355-370.

Vischer, D.L., and Hager, W.H. (1998) *Dam Hydraulics*, Wiley, Chichester, United Kingdom.

Wang, H., Dahle, H.K., Espedal, M.S., Ewing, R.E., Sharpley, R.C. and Man, S. (1999) "An ELLAM Scheme for AdvectionDispersion Equations in Two

Dimensions." *SIAM Journal on Scientific Computing*, 20, 2160-2194.

Wang, X., Wang., Z., Yu, M., and Li, D. (2001) "Velocity Profile of Sediment Suspensions and Comparison of Log-Law and Wake-Law." *Journal of Hydraulic Research*, 39, 211-217.

Wei, G., Kirby, J.T., Grill, S.T., and Subramanya, R. (1995) "A Fully Nonlinear Boussinesq Model for Surface Waves. Part 1. Highly Nonlinear Unsteady Waves." *Journal of Fluid Mechanics*, 294, 71-92.

Yamamoto, S., and Daiguji, H. (1993) "Higher-Order-Accurate Upwind Schemes for Solving the Compressible Euler and Navier-Stokes Equations." *Computers and Fluids*, 22, 259-270.

Yoon, S.B., and Liu, P.L.F. (1989) "Interaction of Currents and Weakly Nonlinear Water Wave in Shallow Water." *Journal of Fluid Mechanics*, 205, 397-419.

Yuan, H., and Wu, C.H. (2004) "A Two-Dimensional Vertical Non-hydrostatic $\sigma$ Model with an Implicit Method for Free-Surface Flows." *International Journal for Numerical Methods for Fluids*, 44, 811-835.

Zhou, J.G., Causon, D.M., Mingham, C.G., and Ingram, D.M. (2001) "The Surface Gradient Method for the Treatment of Source Terms in the Shallow Water Equations." *Journal of Computational Physics*, 168, 1-25.

Zhou, J.G., Causon, D.M., Mingham, C.G., and Ingram, D.M. (2004) "Numerical Prediction of Dam-Break Flows in General Geometries with Complex Bed Topography." *Journal of Hydraulic Engineering*, 130, 332-340.

# VITA

Dae Hong Kim was born in Seoul, Republic of Korea. He received his Bachelor of Science degree in 1997 from the Department of Civil Engineering of Hanyang University at Seoul, followed by his Master of Science degree in 1999 with emphasis in hydraulic experiment from the same department. He worked for seven years at the Korea Water Resources Corporation as a researcher and senior researcher and participated in many hydraulic engineering research projects. He returned to college at Texas A&M University in the Spring of 2006, where he pursued his doctoral studies that focused on the study of hydrodynamics, and graduated with his Ph.D. in August 2009.

He can be reached through: dhkimhyd@gmail.com or may be contacted at the Zachry Department of Civil Engineering, Texas A&M University College Station, TX, 77843-3136.